Helical edge transport and Fabry-Pérot interferometry in graphene quantum Hall effect

Corentin Déprez

Université Grenoble Alpes

THÈSE

Pour obtenir le grade de

DOCTEUR DE L'UNIVERSITE GRENOBLE ALPES

Spécialité : Physique de la Matière Condensée et du Rayonnement

Arrêté ministériel : 25 mai 2016

Présentée par

Corentin Déprez

Thèse dirigée par **Benjamin Sacépé**,

préparée au sein du **Laboratoire Institut Néel, CNRS**
dans **l'École Doctorale de Physique**

Transport hélical et interférométrie de Fabry-Pérot en régime d'effet Hall quantique dans le graphène

Helical edge transport and Fabry-Pérot interferometry in graphene quantum Hall effect

Thèse soutenue publiquement le **30 juin 2021**,
devant le jury composé de :

Monsieur Christopher Bäuerle
Directeur de recherche, Institut Néel, CNRS, Université Grenoble Alpes,
Président du jury

Monsieur Gwendal Fève
Professeur, Sorbonne Université, LPENS, Rapporteur

Monsieur Frédéric Pierre
Directeur de recherche, Centre for Nanoscience and Nanotechnology,
Rapporteur

Monsieur Moty Heiblum
Professeur, Weizmann Institute of Science, Examinateur

Monsieur Christian Schönenberger
Professeur, University of Basel, Examinateur

Abstract

Keywords: graphene, quantum Hall, helical edge transport, Fabry-Pérot interferometer.

In the quantum Hall regime, the Coulomb interactions lead to the emergence of various highly correlated electronic phases exhibiting striking statistical and topological properties. The recent development of high mobility graphene van der Waals heterostructures has opened up new opportunities for the study of these phases. In this PhD thesis, we developed new types of nanostructures that could enable to probe and exploit some of the unique properties of the correlated quantum Hall phases developing in graphene.

Using high-k dielectric $SrTiO_3$ substrates, we fabricated graphene devices where a phase exhibiting a helical edge transport develops at charge neutrality and at low magnetic fields. We show that this helical quantum Hall phase stems from the screening of the long-range Coulomb interaction by the substrate. We demonstrate that this helical edge transport survives over micron long distances and is robust up to a temperature of 110 K, thus providing a promising platform to investigate topological superconductivity.

We also successfully fabricated encapsulated graphene heterostructures equipped with quantum point contacts in series that operate as quantum Hall Fabry-Pérot interferometers. We demonstrate that these devices display gate-tunable oscillations that arise from the Aharonov-Bohm effect in remarkable agreement with theory. We investigate the quantum coherence of electron transport in these interferometers and the possibility to operate a coherent double Fabry-Pérot interferometer. We show that our graphene Fabry-Pérot interferometers also exhibit an intriguing transport regime where Aharonov-Bohm oscillations have a halved periodicity. We finally investigate the possibility to make interference in the fractional quantum Hall regime and we unveil the existence of phase jumps in Aharonov-Bohm oscillations which cannot be interpreted as signatures of anyonic statistics. Our work demonstrates that graphene devices offer a new platform to investigate the physics of quantum Hall Fabry-Pérot interferometers and open up new paths towards the probing of anyon physics emerging the fractional quantum Hall regime.

Résumé

Mots-clés: graphène, effet Hall quantique, transport hélical, interferomètre de Fabry-Pérot.

En régime d'effet Hall quantique, les interactions coulombiennes entrainent la formation de nombreuses phases électroniques hautement corrélées arborant des propriétés topologiques et des statistiques hors du commun. Le récent développement des hétérostructures de graphène de haute mobilité a offert de nouvelles opportunités pour l'étude de ces phases. Dans ce travail de thèse, nous avons développé de nouvelles nanostructures qui permettent de sonder et d'exploiter certaines des propriétés uniques des phases corrélées se développant en régime d'effet Hall quantique dans le graphène.

En utilisant des substrats de $SrTiO_3$ à haute constante diélectrique, nous avons fabriqué des dispositifs dans lesquels un transport hélical apparaît au point de neutralité et à bas champs magnétiques. Nous montrons que cette phase hélicale se développe grâce à l'écrantage de l'interaction coulombienne longue portée par le substrat. Dans cette phase le transport reste hélical sur des distances micrométriques et jusqu'à 110 K ce qui en fait un système de choix pour l'étude de la superconductivité topologique.

La seconde partie de cette thèse a consisté en la réalisation d'interféromètres de Fabry-Pérot en régime d'effet Hall quantique à base d'hétérostructures de graphène encapsulé équipées de contacts ponctuels quantiques. Nous démontrons l'existence, dans ces dispositifs, d'oscillations Aharonov-Bohm contrôlables par des grilles électrostatiques, en parfait accord avec les prédictions théoriques. Nous étudions la cohérence du transport électronique dans ces interféromètres ainsi que la possibilité de mettre en place un double interféromètre dans lequel le transport reste cohérent. Par ailleurs, nous montrons qu'il existe, dans ces interféromètres, un régime de transport particulier dans lequel les oscillations Aharonov-Bohm ont une périodicité réduite de moitié. Nous étudions, enfin, la possibilité de réaliser des expériences d'interférométrie en régime d'effet Hall quantique fractionnaire et nous mettons en évidence l'existence de sauts de phases dans les oscillations Aharonov-Bohm ne pouvant pas être interprétés comme des signatures de statistiques anyoniques. Notre travail montre que les dispositifs à base de graphène offrent de nouvelles opportunités pour l'étude des interféromètres de Fabry-Pérot en régime d'effet Hall quantique et ouvrent de nouvelles perspectives pour explorer la physique des anyons émergeant en régime fractionnaire.

Acknowledgements

A four-year PhD is a unique, thrilling but also exhausting experience. There was a long way to go until the end and I would not have achieved it without the help of my colleagues and friends. I wish to thank at least some of them if not all.

First of all, I would like to express my genuine gratitude towards my supervisor Benjamin Sacépé for his support, his management and his advices all along these years, up to the very end. I have learnt a lot about research and science while working with him. My work is a result of his investment, his experience and his daily support (weekends and holidays included).

I also would like to thank particularly Hermann Sellier. I greatly benefited from his knowledge, his explanations and very valuable discussions we had together during my PhD.

I acknowledge Gwendal Fève and Frédéric Pierre for writing the referee report for my PhD manuscript. Likewise, I also thank Christopher Bäuerle, Moty Heiblum and Christian Schönenberger for being member of my evaluation jury.

My work would not have been possible without the technical support provided by my colleagues from Néel Institute. First, I would like to thank the members of the Nanofab team for helping me with the fabrication of the samples, for their advices on the nanofabrication processes and for the friendly atmosphere they keep in the clean room where I spent so numerous hours. A special thank to Thierry Crozes for all his help with the ebeam lithography and his advices.

I would also like to thank Simon Le Denmat for his help with the atomic force microscopes and for all the hours he spent with me to trying to salvage some of my samples.

A special thank goes to Frédéric Gay and Florent Blondelle for their assistance with the cryogenics and the measurement set-up. They took care of the operation of the fridge, providing me a huge help with the set-up. Further, they were always ready to work with me to improve it. Their technical support was invaluable for the realization of my projects.

Likewise, I acknowledge Sylvain Dumont for the development and the fabrication of high stability DACs which were a key element to perform our measurements.

Regarding our project about graphene on $SrTiO_3$, I would like to thank Benjamin A. Piot for providing us some measurement slots in his cryostats at high field measurement facilities (LNCMI). It was a great opportunity for me to make measurements in such an incredible set-up. I also thank him for our fruitful discussions on the subject.

In the same lines, I also want to thank Zheng Han, aka Vitto, for his help during the measurements at high field lab, his advices on the device fabrications and his contribution to our discussions. I also thank Kenji Watanabe and Takashi Taniguchi for providing us the hexagonal boron nitride used to fabricate our heterostructures.

A PhD is not only a scientific adventure but also a human one. It's a great opportunity to meet people and develop new friendships. At Néel Institute, I had the chance to meet several non-permanents, to have nice time with them and to make very good friends.

I first would like to thank my two PhD partners, the scanning probe guys, Alexis Coissard and Marco Guerra who worked with me this last four years. We had great times together making fun of each other, having nice meals/drinks together, hiking (a bit but not too much) or playing board games. I am especially grateful to my mentor, Louis Veyrat, who taught me a lot about nanofabrication and measurements. He was a great working partner at the lab and he became a true friend. I really enjoyed the discussions we had together about science, books, history, baking and many other topics. I also particularly loved all the great times we had together while cooking and eating nice food.

I also thank his brother Arthur Veyrat for teaching me the fabrication of Van der Waals heterostructures and for the nice time we had when he was an intern in Benjamin's group. A huge thank goes to my padawan, Hadrien Vignaud, who will remain my duckling whatever he tells. I was really happy to teach him what I learnt and, with him, I found a very nice working partner as well as a very good friend. I will miss our morning coffee, our wisecracks, our discussions or our nice cheese-meals.

Likewise, I would like to thank old/new team members for the nice and friendly times we had working together: Johanna Seidemann, Kevin Le Calvez, Thibault Charpentier, David Perconte, Wenmin Yang, Bilal Kousar and Diego Fossion.

I also would like to thank Guilliam Butseraen and Goutham Nayak who became very good friends and with whom I had so much wonderful hikings and nice parties outside the labs. More generally, I wish to thank all the non-permanents from the Institute with whom I had good time (hiking, parties, ski trips, BBQ, cakes, etc.): Juliette Letellier, Nicolas Chauvet, Maëliss Ethys de Corny, Jorge Nacenta, Everton Arrighi, Alvaro Garcia Corral, Danial Majidi, David Wander, David Niegemann, Jun-Liang Wang, Michael Schöbitz, Maria Spies, Francesco Fogliano, Athanasios Gkountaras among many others.

I also would like to sincerely thank my childhood and college friends for their support all along my PhD, especially during the lockdown periods, and over the past years: Marine Le Blay and Pritish Luchoomun my two very good ESPCI friends; Camille Pluquet, Marie-Anne Duchemin, Madleen Bultez, Cécile Jacques, Valentin Baron, Thomas Cormont and Vianney Debavelaere my Faidherbard crew; and Victor Laborde my primary-school friend.

A special thank also to my physiotherapist, Jean-Baptiste Rance, who helps me to recover from my ski accident rapidly and to handle my daily back pain.

Last but not the least, I thank my family for their never ending help and support during all these years.

Contents

Dedicated to my parents, for their unwavering support . . .

A mes parents, pour leur soutien indéfectible . . .

Introduction

In 1980, K. von Klitzing and coworkers [1] discovered that two dimensional electron gas placed in strong perpendicular magnetic fields and at low temperatures have remarkable electronic transport properties. Investigating the transport in silicon MOSFET devices above 13 T, they observed the formation of transverse resistance R_{xy} plateaus appearing as they changed the carrier density in their sample. Surprisingly, these plateaus were in coincidence with cancellations of the longitudinal resistance R_{xx} and they were precisely quantized. Von Klitzing *et al.* indeed found that the conductance on these plateaus was an integer multiple of the conductance quantum e^2/h.[1] Soon after, in 1982, Tsui *et al.* [2] observed that such R_{xy} plateaus were also emerging at fractional values of e^2/h. These two novel phenomena were respectively named integer quantum Hall and fractional quantum Hall effects.

It was rapidly understood that electron-electron interactions would play a crucial role in the quantum Hall physics and that they would give rise to a wealth of highly correlated electronic phases having exciting properties. In particular, it was early predicted that the fractional quantum Hall states would host quasiparticles carrying fractional electric charges [3] and having anyonic statistics [4, 5], i.e. being neither bosons nor fermions. Likewise, some quantum Hall phases developing in the integer regime were predicted to host charged excitations having a skyrmionic spin textures [6]. The existence of such remarkable topological properties has driven research on quantum Hall physics for 40 years. It is still very active, as many questions remain unanswered, and it regularly leads to fundamental breakthroughs.

Since its discovery in 2004 [7] and the evidencing of its particular quantum Hall effect in 2005 [8, 9], graphene has revealed to be an interesting playground for the investigations of the physics of the integer and fractional quantum Hall effects [10–12] and the study of their topological properties [13]. In particular, the recent development of graphene Van der Waals heterostructures enabled to explore the coupling between quantum Hall effect and other condensed matter phenomena like Moiré superlattice physics [14] or superconductivity [15] which had not been addressed before. Many efforts are currently under way to implement elaborated gate-tunable (hybrid) devices, like quantum point contacts [16], in these heterostructures in the prospect of probing and manipulating the topological excitations developing in the graphene quantum Hall phases.

In this PhD work, we have successfully fabricated and investigated high mobility graphene devices dedicated to the study of correlated quantum Hall phases and the harvesting of their topological properties. We have studied them through transport measurements. The present manuscript is separated in two parts dedicated to the two types of samples studied during this thesis: graphene devices on $SrTiO_3$ and graphene devices with multiple split gates used as quantum Hall Fabry-Pérot interferometers.

In the first part, we present an approach that we have developed to induce the formation of the ferromagnetic quantum Hall phase in charge neutral graphene using $SrTiO_3$ substrates. In **chapter 1**, we review the physics of the integer quantum Hall effect in graphene and show that interactions lead to the formation of broken symmetry states. We discuss the consequences of this phenomena at charge neutrality describing the different competing ground states which exist and their properties. In **chapter 2**, we show that one can favour the formation of a helical quantum Hall phase in charge neutral graphene by using the dielectric screening provided by $SrTiO_3$ substrates.

[1] The resistance quantum $h/e^2 \simeq 25\,813\ \Omega$ is also known as the von Klitzing constant.

We present transport measurements demonstrating the robustness of the helical edge transport induced with such strategy. It offers a promising platform to probe topological superconductivity.

In the second part, we focus on quantum Hall Fabry-Pérot interferometers. In **chapter 3**, we review the physics and the functioning of these quantum Hall edge channel interferometers and explain how they allow to investigate the existence of anyons in the fractional quantum Hall regime. We also discuss previous experiments performed in such devices fabricated in GaAs/AlGaAs heterostructures and discuss the detrimental effect of Coulomb interactions in these interferometers. We then focus on graphene split-gated devices and show that they can be operated as such Fabry-Pérot interferometers. In **chapter 4**, we explain how we preliminary characterize the transport in graphene devices with multiple split gates before performing interferometry experiments. In **chapter 5**, we evidence that such devices behave as prototypical quantum Hall Fabry-Pérot interferometers in the integer regime. We show that they exhibit high-visibility Aharonov-Bohm interference in remarkable agreement with the non-interacting theory. Yet, in **chapter 6**, we show that it also exists a regime where Aharonov-Bohm oscillations display a halved periodicity. We discuss the manifestations of this regime in our graphene devices and its specificities. In **chapter 7**, we present the results of our theoretical and experimental investigations of coherent transport through a double quantum Hall Fabry-Pérot interferometer. Finally, in **chapter 8**, we discuss our attempts to make interference with fractional edge modes at fractional bulk filling factors but also in an unusual regime with quantum point contacts at fractional transmissions and with the bulk at integer filling. In this second configuration, we unveil the existence of peculiar transport regime where the Aharonov-Bohm oscillations display clear phase jumps that mimic the signatures expected for anyonic statistics.

Part I

Helical quantum Hall edge transport in charge neutral graphene

Chapter 1

Integer quantum Hall effect in monolayer graphene

Contents

In this first chapter, we present the physics of the integer quantum Hall (QH) effect in graphene. We begin a brief presentation of the basic electronic properties of graphene and of its QH effect in absence of interactions. We then consider the effect of electron-electron interactions in the integer QH regime focusing on the so-called quantum Hall ferromagnetism. Finally, we discuss the special case of the ground state of charge neutral graphene in magnetic field.

1.1 Quantum Hall effect of non-interacting Dirac fermions in graphene

In this section, we discuss the non-interacting quantum Hall effect emerging in graphene. We remind the basic electronic properties of graphene at zero magnetic field and then present how they evolve when graphene is placed in high magnetic field. We explain how the integer QH regime emerges from the Laudau quantization and what are its signature in graphene samples. The derivations of the results presented here, as well as further theoretical predictions, are reviewed for example in ref. [17–19].

1.1.1 Band structure and transport at zero magnetic field

Graphene is an atomic monolayer of carbon atoms arranged in a honeycomb lattice. The unit cell is composed of two atoms separated by $a = 0.142$ nm. The honeycomb lattice is usually decomposed in two different triangular sublattices A and B as shown in Fig. 1.1.A. The corresponding Brillouin zone also forms a honeycomb lattice with two inequivalent corner points labelled K and K'. The

electronic transport in graphene arises from the electrons occupying the out-of-plane $2p_z$ orbitals of carbon atoms. They are delocalized and, using tight binding methods, one can calculate the electronic band structure of graphene which is depicted in Fig. 1.1.B.

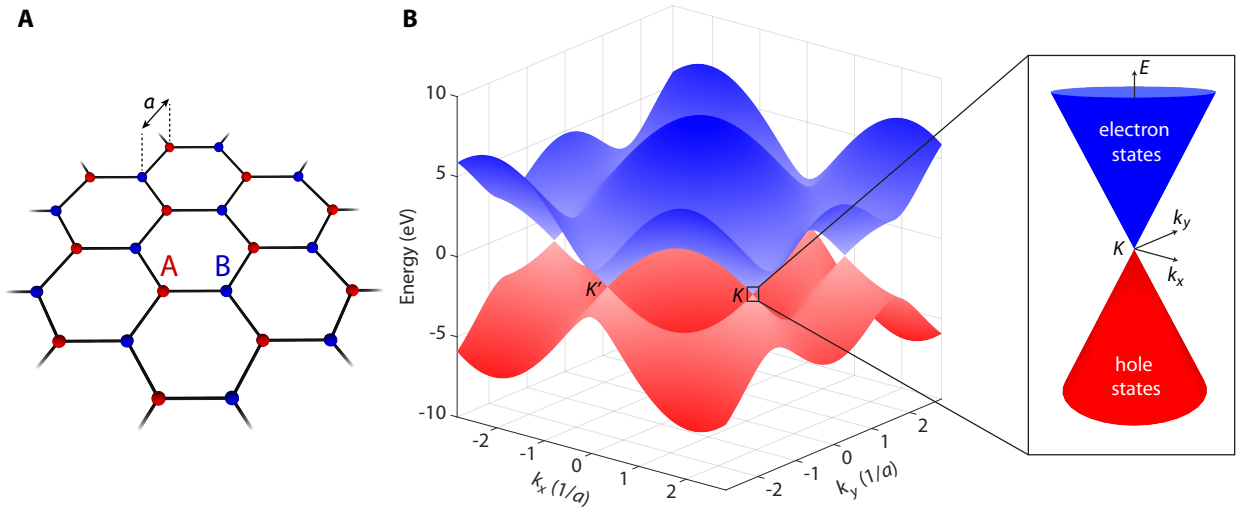

FIGURE 1.1: **Graphene basic electronic properties.** **A**, Carbon atoms organized in a honeycomb lattice forming a graphene sheet. The honeycomb lattice is decomposed in two triangular sublattices labelled A and B. **B**, Graphene band structure. Inset: Dirac cone at K point. Adapted from ref. [20].

It is composed of two symmetric bands, touching each others at points K and K'. Each carbon atom has only one electron in its $2p_z$ orbital which is either spin up or spin down. In contrast, each state of the electronic band structure is spin degenerate. Therefore, in undoped graphene, the valence band is completely filled whereas the conduction band is empty. The Fermi level thus lies at zero energy and the Fermi surface is reduced to the points K and K'. Physics at low energies is governed by the Dirac Hamiltonian and by the linear dispersion relation nearby these two points :

$$\epsilon = \pm \hbar v_F |\overrightarrow{q}|, \tag{1.1}$$

where $\overrightarrow{k} = \overrightarrow{q} + \overrightarrow{K}^{(\prime)}$ is the wave vector such that $|\overrightarrow{q}| \ll \overrightarrow{K}^{(\prime)}$ and $v_F = 10^6$ m/s is the Fermi velocity. In this expression, the signs $+$ and $-$ correspond to the conduction and valence band.

The Dirac cones originating from K and K' points are energy degenerate leading to an additional valley degeneracy on top of the usual spin degeneracy. The low energy spectrum can thus be considered as a single fourfold degenerate Dirac cone. Note that the band structure of graphene is associated with a non trivial π Berry phase [8].

As natural graphene is a gapless semi metal, it can be doped by field effect via application of a voltage on a metallic gate electrode. Application of a positive, respectively negative, gate voltage allows to accumulate, resp. deplete charges, in the flake populating the conduction, resp. valence band, with electrons, resp. holes. It enables to study the transport in both electron-doped and hole-doped regime but also to investigate how the transport within a sample is affected by changes of doping.

1.1.2 Graphene Landau levels

When graphene is placed in a perpendicular magnetic field, its band structure is modified and the Dirac cone splits into a discrete set of energy levels as sketched in Fig. 1.2.A. These energy levels are called Landau levels (LLs) and their energies are given by :

$$E_N = \pm v_F \sqrt{2\hbar e |N| B}, \tag{1.2}$$

where $N \in \mathbb{Z}$ is the Landau level index. In this expression, $\pm$ denotes the sign of N. It is positive, respectively negative, for electron-like and respectively hole-like LLs (i.e. LLs emerging from energy states respectively in the conduction and in the valence bands). The $N = 0$ LL equally belongs to both the conduction and the valence bands and it always lies at zero energy. It is usually said to be half composed of electron-like states and half composed of hole-like states.

The dispersion of LL energies with the magnetic field B is plotted in Fig. 1.2.B. It shows that the LLs are not equidistantly spaced in energy and that the spacing between adjacent LLs, i.e. the cyclotron gap $\hbar\omega_c$, decreases at higher values of $|N|$. This is a direct consequence of the $\sqrt{|N|B}$ scaling of LL energies.

Each LL is highly degenerate and its degeneracy n_{LL} is fixed by the density of magnetic flux $\Phi = BS$ threading the graphene sample of surface S. It is given by $n_{LL} = 4\frac{\Phi}{\Phi_0}$ where $\Phi_0 = \frac{h}{e}$ is the flux quantum and where the factor 4 accounts for the fourfold spin and valley degeneracies in graphene. Thus, there are four states available per flux quantum in each LL. Each of this state occupies a surface $\delta A = 2\pi l_B^2$ of the sample where:

$$l_B = \sqrt{\frac{\hbar}{eB}} = 26 \text{ nm at } 1 \text{ T}, \tag{1.3}$$

is the magnetic length i.e. the characteristic length scale governing the physics at high magnetic fields and the typical spatial extension of the wavefunctions in such regime.

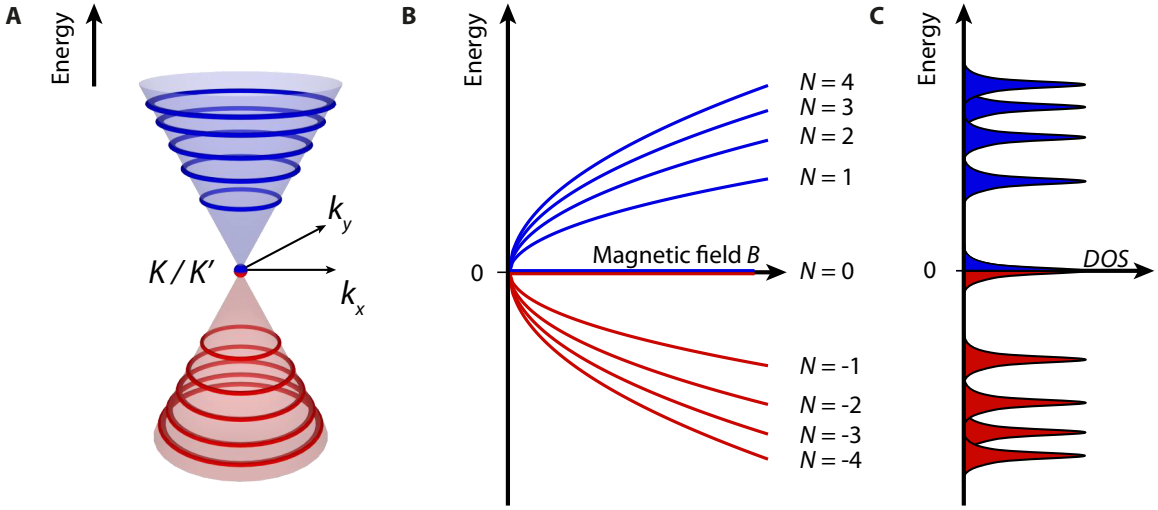

FIGURE 1.2: **Graphene Landau levels.** **A**, Splitting of the Dirac cones into both electron-like (blue) and hole-like (red) fourfold degenerate Landau levels in perpendicular magnetic field. Note the existence of a zero energy LL half electron-like and half hole-like. Adapted from ref. [20]. **B**, Dispersion of LL energies with magnetic field B. **C**, Density of states (DOS) of graphene LLs. In real samples, the LLs are broadened because of the potential disorder in the sample.

Importantly, the wavefunctions of valley degenerate eigenstates have spatial structures which depend on the LL index. In particular, in the $N = 0$ LL, the states in one valley reside only in one sublattice: their wavefunctions vanish on the other sublattice. Hence, there is a direct equivalence between the valleys and the sublattices in the $N = 0$ LL. In contrast, in the other LLs, eigenstates in a given valley have wavefunctions equally shared between both sublattices.

The filling of LLs can be characterized by the filling factor ν defined as:

$$\nu = \frac{n\Phi_0}{B} = 4\frac{nS}{n_{\mathrm{LL}}}, \tag{1.4}$$

where n is the charge carrier density in the sample. ν takes an integer value of $4(N+\frac{1}{2}) = 2(2N+1)$ when the N^{th} Landau level is completely filled with electrons and when the higher LLs are empty. This is a consequence of the existence of a zero energy LL equally shared between electrons and holes and of the fourfold degeneracy. Note that in this expression the $\frac{1}{2}$ shift also reflects the existence of the π Berry phase.

Considering their large degeneracy, one can ideally consider LLs as flat bands having a large density of state. Yet, in real samples, LLs are broadened by disorder as sketched in Fig. 1.2.C. When the LL broadening Γ is small compared to the cyclotron gap, $\Gamma \ll \hbar\omega_c$, the sample is in the QH regime where quantized resistance plateaus can be observed [21, 22]. This is the regime studied in this manuscript.

1.1.3 Graphene QH edge channels.

Landau levels nearby graphene edges: armchair and zigzag edges

The previous LL spectrum can be derived considering that the graphene sample is infinite. Yet, a real 2D sample always has finite dimensions delimited by some edges. They can be modelled by a strong confining potential which extends over a limited space region and which modifies the energy spectrum at the edges. In magnetic field, it leads to a bending of the LLs [22].

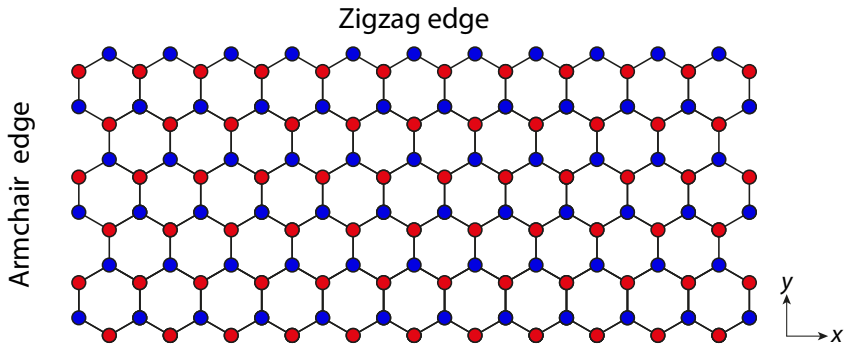

FIGURE 1.3: **Zigzag and armchair edges**

In graphene samples, the confinement actually depends on the form of the physical edges which can be either armchair or zigzag (see Fig. 1.3). To calculate the energy dispersion of graphene LLs nearby these edges, one needs to take into account the specific boundary conditions for the electronic wavefunctions in each case [23–25]. At an armchair edge, the last line of carbon atoms is composed of atoms belongings to both sublattices. Thus, the wavefunction should vanish on both sublattices at the edge. In contrast, at a zigzag edge, the carbon atoms of the last line all belong to the same sublattice. Thus, the wavefunction must only cancel on the other sublattice at the edge.

The LL dispersions were computed by Brey and Fertig [23, 27] using tight-biding model and by Abanin and Levitov [24, 25] using Dirac continuum model leading to similar results. We now discuss the results of second approach which are shown in Fig. 1.4. It displays the evolution of LL

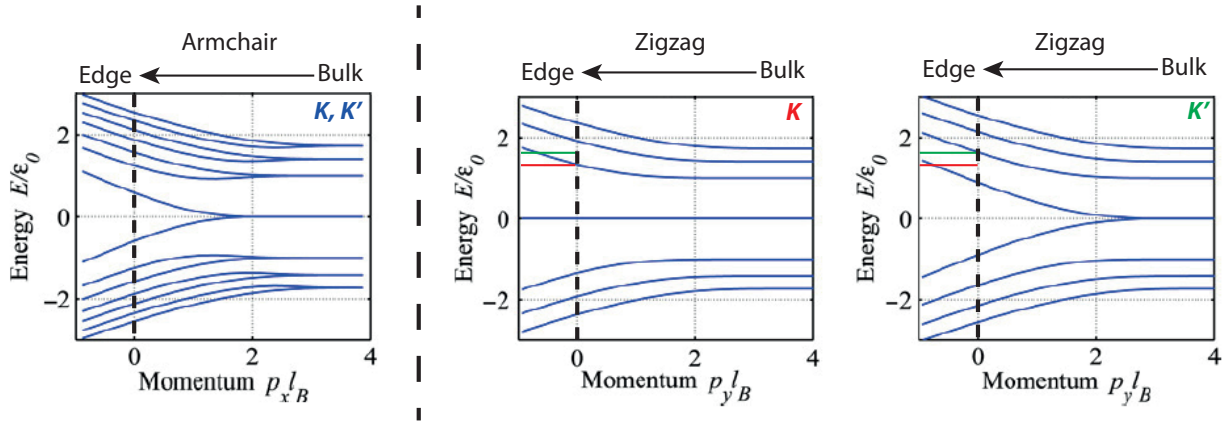

FIGURE 1.4: **Graphene LL bending at the edges.** LL bending approaching an edge in a graphene sample. The position of the edge is marked by the black dashed lines. In both cases, $N \neq 0$ electron/hole-like LLs disperse upward/downward as a result of the confinement. **A**, Nearby an armchair edge, the two valleys admixe and all LLs split in two dispersing spin degenerate branches. **B**, Nearby a zigzag edge, the valley degeneracy is lifted and the LL bending depends on the valley considered. For the $N = 0$ LL, the states in one valley form a single dispersionless branch whereas the states in the other valley form two branches dispersing in opposite directions. Red and green lines emphasize the energy difference between the states of the $N = 1$ LL in the two valleys (K in red and K' in green). Adapted from ref. [26].

energies for a half-infinite graphene plane approaching either an armchair edge at position $y = 0$ or a zigzag edge at position $x = 0$ marked by black dashed lines.[1]

In the armchair case, $N \neq 0$ electron-like, respectively hole-like, LLs bend upward, respectively downward and split into two branches approaching the edges. Likewise, the $N = 0$ LL splits into two branches dispersing in opposite direction. These splittings result from a lifting of the valley degeneracy. It is a consequence of the boundary condition at the edge which imposes that the two valleys admixe. All branches are spin degenerate.

In the zigzag case, one should distinguish the two valleys. Like in the armchair case, the $N > 0$ and $N < 0$ LLs bend respectively upward and downward approaching the edges. Yet, at a given position, the energy of each bent LL actually depends on the valley considered (see for example green and red lines corresponding to the energies of the $N = 1$ LL states respectively in K and K' valley at $p_y l_B = 0$) [28]. The valley degeneracy is also lifted at the edge.

For the $N = 0$ LL, the situation is more complex because of the mixing of this LL with dispersionless surface modes that exist along a zigzag edge. For one valley, the dispersion is similar to that of the armchair case edge: the $N = 0$ LL splits into two dispersing branches. For the other valley, the $N = 0$ LL remains at zero-energy because the bulk wavefunction naturally vanishes after the last line of carbon atoms (due to the valley-sublattice equivalence) and thus already satisfies the boundary condition. Note that in a zigzag ruban, the last carbons atoms of the two opposite edges belong to different sublattices. Hence, the spectra for the two valleys are exchanged at the two different edges.

[1]The dispersions are displayed in momentum space rather in real space. Yet, in the LL theory, there is a simple duality relation between momentum and position provided a suitable gauge choice. In a 2D geometry, infinite along y direction and finite along x direction, one can show that the eigenstate wavefunctions are plane waves propagating along y direction and spatially localized in the x direction. A state in the N^{th} LL with momentum $p_y = \hbar(k_y - K_y^{(\prime)})$ is centered around $x = k_y l_B^2$ and has a spatial extension about $\sqrt{2|N|+1}\, l_B$ in x direction. Hence, the LL dispersion in momentum space gives information about the LL dispersion in real space.

Formation of QH edge channels

This LL bending has deep consequences on the electronic transport and, in particular, it leads to the formation of one dimensional conductive edge channels. To explain it, we consider Fig. 1.5.A which shows a sketch of the LL dispersion for an armchair ruban infinite along the x direction and of finite width in the y direction.

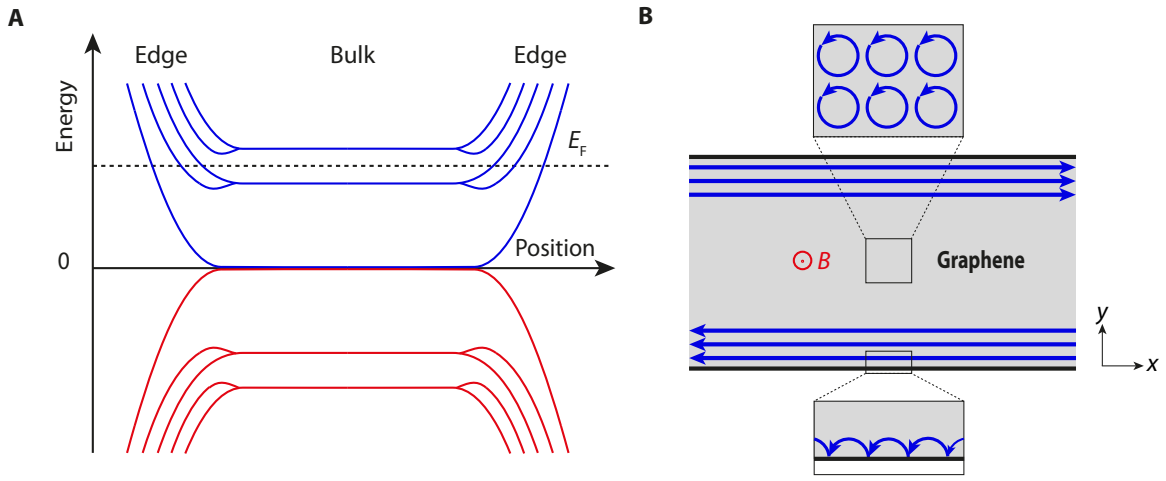

FIGURE 1.5: **Formation of graphene QH edge channels. A**, Schematic of the bending of graphene LLs in an armchair rubban. Electron-like LLs are represented in blue and hole-like LLs are represented in red. When the Fermi energy E_F lies between two adjacent LLs in the bulk, it crosses some of the bent LLs at the edges resulting in the formation of conductive edge channels. **B**, Semiclassical picture of QH edge channels. In the bulk, the charge carriers have a cyclotron orbital motion. 1D conductive channels formed by skipping orbits appear at the edges of the sample. Their propagation direction is imposed by the magnetic field.

When the Fermi energy E_F lies in the cyclotron gap between two adjacent LLs, the bulk of the sample is insulating. In contrast, at the edges, E_F crosses some of the bent LLs. Thus it exists low energy states all along each samples edges. They form one dimensional edge channels called QH edge channels. The carriers populating these channels have finite group velocities given by:

$$v_x = \frac{1}{\hbar}\frac{\partial \epsilon_N}{\partial k_x} = \frac{1}{eB}\frac{\partial \epsilon_N}{\partial y}, \tag{1.5}$$

where ϵ_N is the energy of the N^{th} bent LL. They propagate in opposite direction along opposite edges: they are chiral. The chirality of the charge carriers motion is actually imposed by the direction of the magnetic field. In a semi-classical picture, the QH edge channels can be seen as the results of the cyclotron orbital motion of electrons and the formation of so-called skipping orbits at the edges depicted in Fig. 1.5.B.

The edge states propagate along equipotential lines at the edges of the sample. As pointed by M. Buttïkker [29], the backscattering along a given edge is suppressed as all edge states propagate in the same direction. Backscattering can only occur if counterpropagating edge channels are brought sufficiently close such that electrons can tunnel from one edge to the other. This situation usually does not occur in real samples because the opposite edges are separated by several microns long distances. We note that hole-like and electron-like edge channels have opposite directions of propagation along a given edge.

According to the above section, in doped graphene, when E_F lies between the N and $N+1$ LL, there are $2(2N+1)$ of such chiral edge channels appearing at the edge of the sample. It does not matter whether the edge is zigzag, armchair or even a combination of both like in real samples.

1.1.4 Transport signatures of QH effect in graphene samples.

The QH effect is a direct consequence of the emergence of such chiral and conductive edge channels in an otherwise insulating bulk. Since backscattering is suppressed along a given edge, QH edge channels can be considered as unidirectional 1D conductive quantum channels having perfect transmissions [29]. Applying Landauer-Büttiker formalism to a six-terminal Hall bar geometry (Fig. 1.6.A), one can demonstrate that all the contacts on the upper arm of the Hall-bar have the potential of the source contact whereas all the contacts on the lower arm have that of the drain contact. Hence, we have:

$$G_{xy} = I/V_{xy} = M\frac{e^2}{h} \text{ and } R_{xx} = V_{xx}/I = 0, \tag{1.6}$$

where M is the number of edge channels along each edge which is fixed by the number of dispersing branches crossing the Fermi level at the edges. Similarly, in a two-terminal geometry (Fig. 1.6.B), one can show that:

$$G_{2t} = I/V_{2t} = M\frac{e^2}{h}. \tag{1.7}$$

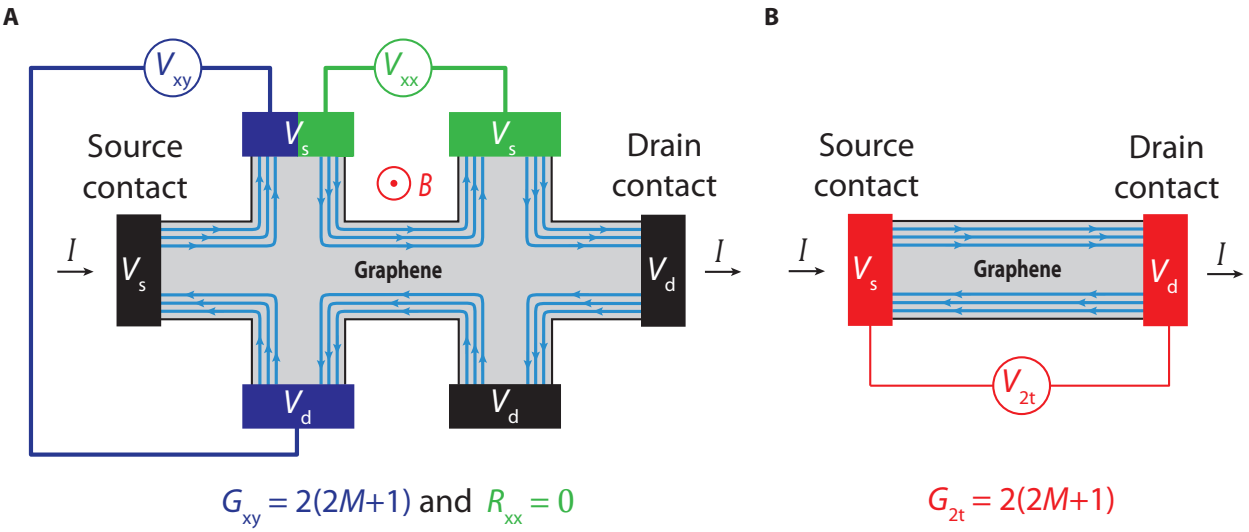

FIGURE 1.6: **QH signatures in various geometries of graphene samples. A**, Six-terminal Hall bar geometry. Due to the absence of backscattering, there is no potential drop, such that the voltage measured at the contacts on the upper edge, resp. on the lower edge, are the same than that of the source contact V_s, resp. of the drain contact V_d. The signatures of the QH effect are a quantization of G_{xy} together with a vanishing of R_{xx}. **B**, Two-terminal geometry. The signature of the QH effect is a quantization of the two-terminal conductance.

The quantized transport regime is observed when the Fermi level lies in the cyclotron gap between adjacent LLs. In contrast, when it lies in the middle of a LL, there are some bulk states extending in the sample and percolating between the two edges. They provide a backscattering mechanism and it results in a lose of quantization. Ideally, this last situation should always be observed. Indeed, the LLs should be perfectly flat bands and there should be no state in the cyclotron gap. The observation of a robust quantized transport regime may look surprising in this regard.

However, in real samples, the LLs are broadened because of the potential disorder and their density of states are peaks with a finite energy width (see Fig 1.7). The Fermi level can lie either

in the middle of the peaks or in the tails. In the first case, the situation is the same than the one described above and the transport is not quantized. In the second case, the bulk states at the Fermi level remain localized on small regions of the sample . There is no backscattering between the two edges and the transport remains quantized [22].

In graphene samples, one can continuously adjust the LL energies or the Fermi level by changing either the magnetic field or the carrier density with the back gate. In both cases, the relative position of E_F compared to that of the LLs is gradually changed and the Fermi level successively lies in different LLs. Hence, there is an alternation of quantized and not quantized transport regimes leading to the observation the famous QH resistance plateaus.

The direct consequence of the graphene relativistic LL spectrum [30], or equivalently of the LL dispersion at the edges of graphene, is that the QH plateaus followed a sequence given by:

$$G_{xy} = 2\frac{e^2}{h}(2M+1), \tag{1.8}$$

where the factor 2 arises from the spin degeneracy. The observation of such a sequence of QH plateaus in 2005 [8, 9] unambiguously demonstrated that the graphene low energy band structure is described by the 2D Dirac equation. It is worth noticing, that in graphene, the QH regime can be reached even at room temperature [31] due to the large cyclotron gap between $N = 0$ and $N = \pm 1$ LLs which is about 420 $\sqrt{B[\mathrm{T}]}$ K.

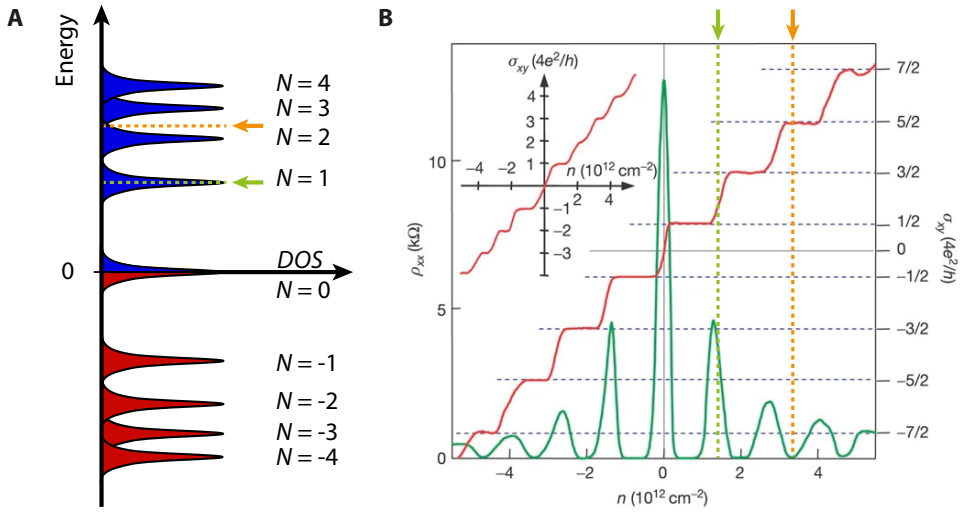

FIGURE 1.7: **Graphene QH plateaus. A**, Density of states (DOS) of graphene LLs. Each LL can be represented as a peak in the DOS with finite width. **B**, Typical signatures of graphene QH effect in six-terminal Hall bar geometry. When the Fermi level lies in the tail of a LL peak (orange dashed line), there is no backscattering in the sample and the transport is quantized. When the Fermi level lies in the middle of a LL (green dashed line), there is some backscattering in the sample and the transport is no longer quantized. Adapted from ref. [8].

1.2 Quantum Hall ferromagnetism in graphene

So far, we did not consider the effect of interactions which play a significant role in the QH physics. In this section, we include the interactions and present their main consequence in the IQH regime, that is, the emergence of the quantum Hall ferromagnetism. We discuss its effect on the transport properties. We conclude this section by considering specifically the case of the QH ground state at charge neutrality.

The effects discussed here are only visible in high mobility samples and at sufficiently large magnetic fields. These samples are fabricated either by using suspended graphene devices [10, 11], by putting graphene on top of a h-BN flake [32], or by encapsulating it between two h-BN flakes [33]. The origin of the mobility increase with the use of h-BN flakes are discussed in the Appendix 12.

1.2.1 Landau level degeneracy lifting induced by exchange interactions

In absence of interactions, the graphene LLs are fourfold degenerate and have an approximate SU(4) symmetry. It originates from both SU(2) spin and pseudospin = valley symmetries which can be combined and viewed as an effective SU(4) isospin [13, 18]. These degeneracies can be lifted by interactions and an initially fourfold degenerate LL can split into a set of sub-LLs with a lower or even no degeneracy. It leads to the appearance of IQH plateaus outside the sequence of eq. (1.8). When both the spin and valley degeneracies are lifted in every LL, we observe a QH plateau of transverse conductance for any integer multiple of $\frac{e^2}{h}$ as shown in Fig. 1.8. The QH states associated with these additional plateaus are referred as **broken symmetry states**.

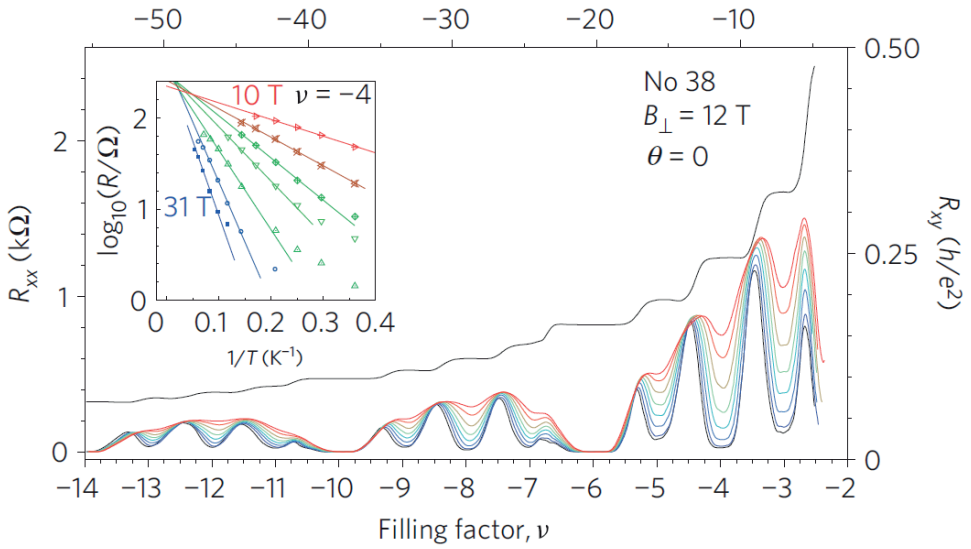

FIGURE 1.8: **Signatures of broken symmetry states in graphene devices.** In high mobility samples and at sufficiently large magnetic fields, QH plateaus of transverse resistance $R_{xy} = \frac{h}{e^2\nu}$ are observed for every integer values of ν. Plateaus outside the sequence of eq. (1.8) and the corresponding minima of R_{xx} mark the emergence of broken symmetry states. Increasing the temperature, these minima become rapidly less pronounced whereas the R_{xx} minima at $\nu = -2, -6$ and -10 do not evolve significantly. It shows that the gaps separating broken symmetry states are significantly smaller than the cyclotron gaps. Inset : Arrhenius plots for $\nu = -4$ at different magnetic fields showing that the transport gap increases with B and decreases with T. Taken from ref. [13].

The exchange interaction, i.e combination of both the repulsive Coulomb interaction and the Pauli exclusion principle, is at the origin of the degeneracy lifting. In spin degenerate electron system, it favours the formation of ferromagnetic ground states which have antisymmetric orbital wavefunctions mimizing the Coulomb energy. In particular, in fully ferromagnetic states, the spin component of the many-body wavefunction is completely symmetric. Therefore, the orbital part of the wavefunction must be fully antisymmetric and it naturally vanishes when electrons are brought close to one another. It lowers the Coulomb repulsion experienced by the electrons [34].

In metals, the exchange interactions can induce a ferromagnetic instability. It leads to a spontaneous electronic band splitting and a partial spin polarization of the system even in absence of magnetic field. Such spontaneous symmetry breaking can occur because it allows to lower the overall Coulomb energy. Yet, it is also accompanied by an increase of kinetic energy. Thus, ferromagnetism only appears when the gain in interaction energy overcomes the cost in kinetic energy. The spin polarization is only partial because of the competition between both effects.

Likewise, in the QH regime, the exchange interaction also leads to a spontaneous symmetry breaking and a splitting of the LLs into sub-LLs: this is the **quantum Hall ferromagnetism** (QHF). Compared to ferromagnetic materials, this effect is enhanced because the LLs are perfectly flat bands and thus there is no kinetic energy cost associated with the degeneracy lifting. In graphene, an initial spin-valley degenerate LLs splits into quartets of sub-LLs separated by interaction-induced exchange gaps.

The broken symmetry states that develop at integer filling factors have a finite polarization in the SU(4) isospin space. An example of such spontaneous symmetry breaking is represented in Fig. 1.9.A. In this example, all electrons in the lowest-sub LL have spin down and belong to the K valley while electrons in the second lowest sub-LL have spin down but belong to the K' valley. The overall broken symmetry state is therefore a spin-polarized valley-singlet state.

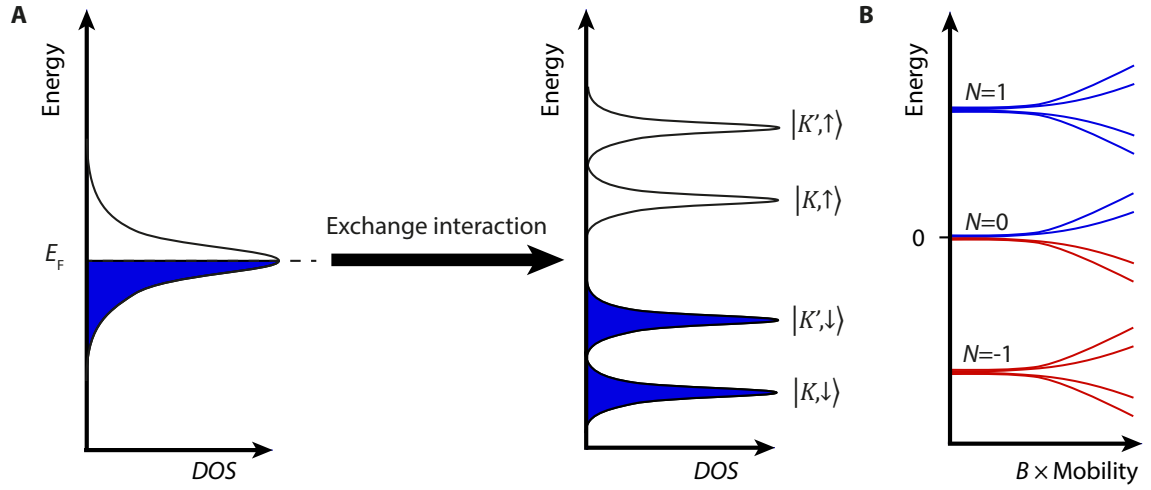

FIGURE 1.9: **Quantum Hall ferromagnetism in graphene. A**, Splitting of a half filled fourfold degenerate LL into a quartet of spin and valley-polarized sub-LLs due to exchange interactions. The polarisation of the broken symmetry states depends on the strength of the different symmetry breaking terms which lift spin or/and valley degeneracies. **B**, The QHF and the splitting of LLs into quartets of broken symmetry states can be observed when the magnetic field and the mobility are increased. The broken symmetry states appearing at half LL fillings are observed at lower fields/mobilities than those at quarter fillings.

The relevant energy scale quantifying the effect of exchange interactions is given by the long-range part of Coulomb interaction ϵ_C , i.e. its value evaluated for the average distance between the electrons [18, 35, 36]. Knowing that l_B is the characteristic distance between nearby electrons within a LL, we can estimate it as:

$$\epsilon_C = \frac{e^2}{4\pi\epsilon_0\epsilon_r l_B} \approx 162\sqrt{B[\mathrm{T}]}\,\mathrm{K}, \tag{1.9}$$

for encapsulated graphene devices assuming $\epsilon_r = \epsilon_{\mathrm{BN}} \approx 4$ (for graphene directly on silicon substrate $\epsilon_C \approx 130\sqrt{B[\mathrm{T}]}\,\mathrm{K}$ [35]).

Even though it is a large energy scale, the QHF has visible effects only in high mobility samples or at sufficiently large magnetic fields as sketched in Fig. 1.9.B. Indeed, the observation of broken

symmetry states requires that the exchange gaps become larger than the disorder broadening of LLs. It was demonstrated by K. Nomura and A. H. MacDonald [37], who also derived a Stoner criterion enabling to estimate the critical field above which the broken symmetry states could be observed for samples of an arbitrary mobility.

The detrimental effect of disorder explains why, in graphene on silicon devices, the first QHF signatures were only reported in the best samples and at very high magnetic fields ($B > 20$ T) [38, 39]. Comparatively, in later experiments, with suspended graphene devices [10, 11] or in graphene on h-BN samples [13], the first broken symmetry states were observed at magnetic fields of a few Teslas.

1.2.2 Symmetry breaking terms and polarization of broken symmetry states

If the long-range Coulomb interaction is driving the QHF, it does not favour any specific polarization in the spin-valley isospin space because the corresponding term in the Hamiltonian of the system is SU(4) symmetric [18, 35]. The precise polarization taken for each broken symmetry state is determined by a competition between other terms which do not conserve the SU(4) symmetry.

The first effect coming in mind is the Zeeman effect which promotes spin polarization. It favours a alignment of the spin opposite to the direction of the magnetic field. The corresponding energy scale is given by :

$$\epsilon_Z = g\mu_B B \approx 1.3\, B_{\text{tot}}[\text{T}]\ \text{K}, \tag{1.10}$$

where $g \approx 2$ is the Landé factor and $\mu_B = 0.67\ \text{K.T}^{-1}$ is the Bohr magneton and $B_{\text{tot}} = \sqrt{B_\perp^2 + B_\parallel^2}$ is the total magnetic field ($B_\perp$ is the out-of-plane component and $B_\parallel$ is the in-plane component).

The lattice-scale Coulomb interactions, especially the on-site repulsion and the nearest-neighbour repulsion, are also breaking SU(4) symmetry. They can favour both valley and/or spin orders depending on the relative strength of the different effects [18, 35, 36, 40–42]. In particular, one may expect that the on-site repulsion favours spin ordering. In contrast, the nearest-neighbour repulsion rather favours some valley polarization especially in $N = 0$ LL because of the valley-sublattice equivalence. The energy scale associated with the lattice-scale Coulomb interactions is given by [43]:

$$\epsilon_{\text{e-e}} \approx \frac{a}{l_B}\epsilon_C \approx 1\, B[\text{T}]\ \text{K}. \tag{1.11}$$

Finally, the electron-phonon interactions can also lead to a breaking of the valley symmetry. Optical phonons result in distorsions of the graphene lattice and they can drive a Peierls instability lowering the electronic energy. The most relevant phonons are the in-plane ones and in particular A_1 and B_1 modes which generate Kekulé distortions [44] i.e. a dimerization of one third of the electronic bonds (see Fig. 1.10.A). These distortions lead to a modulation of the nearest-neighbour hopping parameter [45] and they couple the two valleys as they are associated with a characteristic wavevector $\overrightarrow{G} = \overrightarrow{K} - \overrightarrow{K'}$ [18]. Therefore, Kekulé distortions break the valley degeneracy and they are expected to favour XY valley ordering in the $N = 0$ LL [46, 47]. The effect of these phonon-induced instabilities are further strengthened by the Coulomb interactions. D. M. Basko and I. L. Aleiner indeed demonstrated that the latter enhance the coupling with A_1 phonons [48]. Likewise, Hou and coworkers suggested that the nearest-neighbour Coulomb repulsion reinforces the Kekulé instabilities [45, 47]. The characteristic energy scale associated with Kekulé distortions is about [47]:

$$\epsilon_{\text{kek}} \approx\ 1.86\, \text{B}[\text{T}]\ \text{K}. \tag{1.12}$$

The out-of plane phonons were also predicted to induce a valley degeneracy lifting in $N = 0$ LL [49] but this effect is claimed to be weak compared to that of Kekulé distortions [36].

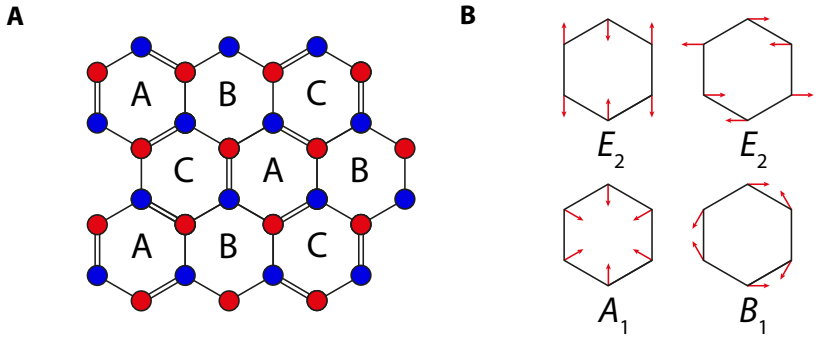

FIGURE 1.10: **Kekulé distortions and relevant in-plane optical phonons for graphene QHF. A**, Schematic of Kekulé distorsions. The dimerization occurs on one third of the bonds. They are shortened leading to a modulation of the nearest-neighbour hopping term. **B**, Relevant optical phonon modes for QHF [36] classified according to ref. [48]. The Kekulé distortions are due to A_1 and B_1 modes.

All these energy scales are two orders of magnitude smaller than the Coulomb energy ϵ_C and they are all really similar. Thus, the polarization of the broken symmetry states cannot be straightforwardly predicted and it actually depends on a delicate balance between the different symmetry breaking terms.

The development of high mobility graphene samples on h-BN allowed to probe experimentally the competition between the spin and valley polarizations in the different LLs. In ref. [13], A. Young and coworkers observed the full degeneracy lifting and well-defined broken symmetry states in all LLs at 14 T. Thus, they were able to measure the gaps between the broken symmetry states and studied their dependence with both out-of-plane and in-plane magnetic fields. They demonstrated that the broken symmetry states which develop at half-filling of $N \neq 0$ LLs are spin-polarized valley-singlet states. In contrast, they found a spin-singlet valley-polarized state at $\nu = 0$. The authors also measured the corresponding activation gaps and found that they were too large to be explained only by the Zeeman effect. Hence, they demonstrated that the gaps between broken symmetry states were indeed exchange-induced gaps.

Finally, Young et al. also showed that the field dependences of the gaps were consistent with a transport mediated by both spin and valley-textured skyrmions. It confirmed some of the theoretical predictions that were derived in the framework of graphene SU(4) QHF [35, 50].

1.3 Quantum Hall ferromagnetism at charge neutrality and helical quantum Hall phase

The consequences of the QHF in the $N = 0$ LL raised a lot of interests both theoretically and experimentally. In particular, the fate of the $\nu = 0$ broken symmetry state was extensively investigated because it can exhibit a helical edge transport. This is subject of this section. We first explain how such helical edge transport can emerge and why its existence is strongly related to the physics of QHF. We then show that it exists different ground states possible at charge neutrality and we review their properties based on past theoretical studies. We finally present the results of experimental investigations on the subject.

1.3.1 Helical edge transport at charge neutrality

In their early investigations of the LL dispersion in graphene, Abanin and Levitov [24] as well as Fertig and Brey [27] noticed that the QH transport at charge neutrality could be helical in presence of a spin splitting.

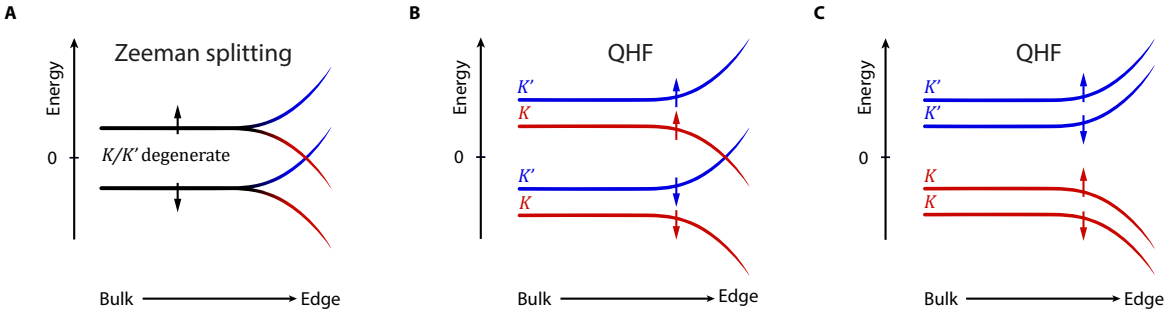

FIGURE 1.11: **Helical edge transport and possible scenarios of $N = 0$ LL splitting.** **A**, In absence of interactions, the Zeeman effect leads to the emergence of helical edge transport at charge neutrality. **B**, When interactions predominantly lift the spin degeneracy, the helical edge transport remains. **C**, When interactions predominantly lead to a lifting of the valley degeneracy, the graphene is insulating both in the bulk and at the edges.

In absence of interaction, it exists thanks to the Zeeman effect. The latter leads to a splitting of the zeroth LL into two spin-polarized valley degenerate sub-LLs as depicted in Fig. 1.11. Each of these sub-LL splits into one hole-like and one electron-like branch at the edges (we assumed here that the edges are armchair for simplicity). Hence, at charge neutrality, there is a crossing between two branches with opposite spins such that the graphene is insulating in the bulk but conductive at the edges. The sample indeed exhibits spin filtered counter propagative helical edge states, that are similar to those of the quantum spin Hall effect in 2D topological insulators [51–59], and it thus displays a finite quantized conductance [24, 51, 60, 61]. These helical edge channels are particularly interesting for practical applications like spintronics [62] but also for fundamental research to probe topological superconductivity and harvest of Majorana zero energy excitations [63, 64]. At first sight, inducing their formation in graphene seems straightforward.

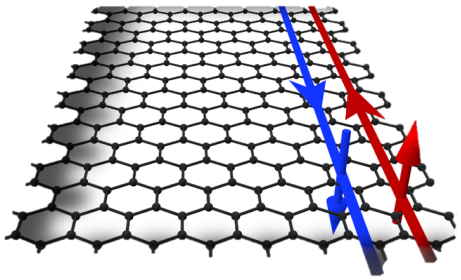

FIGURE 1.12: **Graphene helical edge states.** Counterpropagating spin filtered edge states which can appear at charge neutrality in graphene sample due to the QHF.

When one adds the effect interactions and thus of the QHF, the emergence of helical edge transport is no longer guaranteed. In a simplified picture [18, 65], the transport properties of the ground states actually depend on which degeneracy is predominantly lifted when the magnetic field is increased and whether the $\nu = 0$ ground state is preferably valley or spin-polarized. If the exchange gap opening at $\nu = 0$ is associated with the lifting of the spin degeneracy (Zeeman spin splitting enhanced by the exchange interactions) (Fig. 1.11.B), the situation is the same than the one described above: the bulk is insulating and helical edge channels appear. However, if the valley splitting is predominant (Fig. 1.11.C), there is no crossing of hole and electron-like branches at charge neutrality such that the sample is completely insulating both in the bulk and at the edges.

This shows that the QHF can give rise to very different QH states at charge neutrality depending on the balance between symmetry breaking terms. The competition between these states and the possible existence of a phase exhibiting a helical edge transport have motivated several research works.

1.3.2 Competing ground states at charge neutrality

Four possible ground states

The study of the $\nu = 0$ ground state was subject to many theoretical studies [35, 36, 40–42, 66, 67]. It was finally found that there are four possible many-body ground states [36] which are shown in Fig. 1.13.

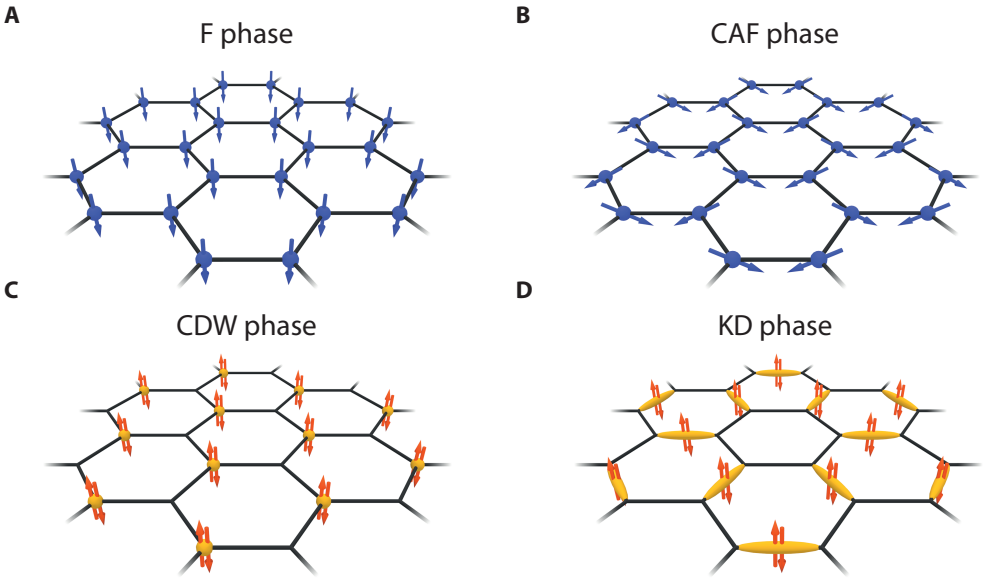

FIGURE 1.13: **Many-body ground states possible for charge neutral graphene in the QH regime. A**, The ferromagnetic phase (F) exhibits a helical edge transport. **B**, The canted antiferromagnetic (CAF), **C**, charge density wave (CDW) and, **D**, Kekulé distortions (KD) phases are insulating both in the bulk and at the edges. Adapted from ref. [20].

From the above discussion, we understand that the phase exhibiting helical edge transport appears when all electrons within the $N = 0$ LL have the same spin polarization. It corresponds to the ground state depicted in Fig. 1.13.A which is the ferromagnetic (F) phase. It is a spin-polarized valley-singlet state with one spin down electron above each carbon atom.

In three other cases, the sample is both gapped in the bulk and at the edges. The phase depicted in Fig. 1.13.B is named canted antiferromagnetic (CAF) phase and it exhibits a spin density wave order. In this case, there is one electron located above each carbon atom and the spins are canted with respect to the magnetic field direction. The electrons on different sublattices have spins with opposite canting angle such that the ground state has a partial spin polarization along the field direction. When the Zeeman effect is negligible compared to the other symmetry breaking terms, this phase tends to a purely antiferromagnetic (AF) phase where the spins on the different sublattices are anti-parallel and lie in the graphene plane [36, 61, 67].

The ground states depicted in Fig. 1.13.C and Fig. 1.13.D correspond respectively to the charge density wave (CDW) and Kekulé distorsions (KD) phases. They are fully valley-polarized spin-singlet states. In the first case, all charge carriers in the $N = 0$ LL reside on one sublattice and thus in one valley. In the second case, the electrons in the $N = 0$ LL are delocalized above one third of

the chemical bonds between carbons atoms thus the state has a $K + e^{i\theta}K'$ polarization in the valley Bloch sphere. It is an XY valley (pseudospin) ordered phase [46].

Competition between the ground states

We now summarize the results of these theoretical works regarding the impact of each symmetry breaking terms in determining the $\nu = 0$ ground state.

First, according to previous discussions, the Zeeman effect was found to favour the formation of the F phase [36, 41, 68]. In contrast, it was found that the coupling with the in-plane phonons [46, 47], respectively the out-of-plane phonons [49], promotes the formation of KD, respectively CDW phases.

On the other hand, the effect of the lattice-scale electron-electron interactions is more difficult to predict. Some early mean-field approaches found a promotion of the F phase by the on-site repulsion while the repulsion between the adjacent sites was found to induce the CDW order [35, 40]. Yet, some other theoretical and numerical investigations [41, 42] unveiled a competition between the AF and CDW phases depending on the balance between the lattice-scale repulsions. Therefore, it appeared that these lattice-scale electron-electron interactions had a non trivial effect in determining the $\nu = 0$ ground state.

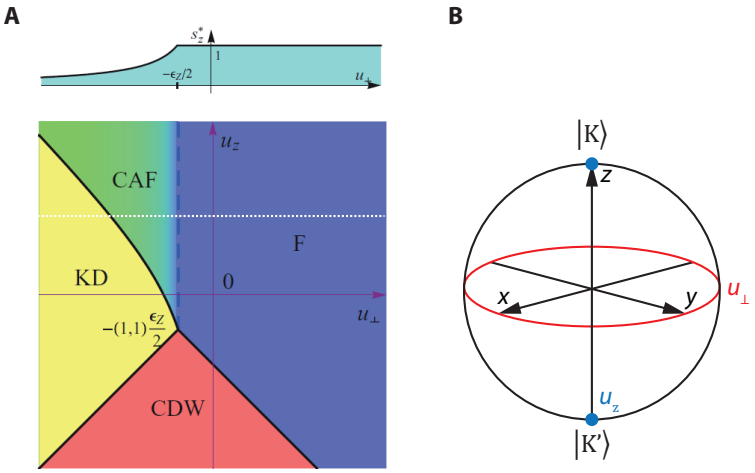

FIGURE 1.14: **$\nu = 0$ phase diagram.** **A**, Energetically favourable phase as a function of the valley anisotropies u_z and $u_\perp$. u_z and $u_\perp$ quantify the energy cost associated with a valley polarization respectively at the poles and in the equator of the valley/pseudospin Bloch sphere represented in **B**. Top panel in A: Evolution of the spin polarization along the magnetic field direction as a function of $u_\perp$ along the white dotted line. The spin polarization decreases in the CAF phase going away from the phase boundary with the F phase. Adapted from ref. [36].

To take account all effects together, M. Kharitonov proposed in 2012 a mean-field and extended theoretical model [36]. Thanks to it, he was able to draw the $\nu = 0$ ground state phase diagram showed in Fig. 1.14.A. He found that the phase favoured actually depends on the relative strength of the Zeeman energy ϵ_Z and of the valley anisotropies u_z and $u_\perp$. The latter are parameters quantifying the energy cost associated with valley polarization respectively at the poles and in the equator of the valley pseudospin Bloch sphere shown in Fig. 1.14.B.

Using his model, Kharitonov recovered the results of previous theoretical works. Yet, he also highlighted that the contributions of lattice-scale interactions to the anisotropies are strongly renormalized by the long-range Coulomb interaction. Kharitonov notices that such renormalization effect is so strong that it can lead to large changes in the amplitude of the valley anistropies and even changes of their sign. Considering that there is a large uncertainty on the bare values of

the on-site electron-electron interactions [35, 36, 40, 41], he claimed that it is impossible to predict which ground state emerges in real samples.

The phase diagram of Kharitonov was found to be correct beyond mean-field using exact diagonalization techniques [69]. It was also recovered very recently in an another approach allowing to investigate the skyrmionic excitations at $\nu = 0$ [70].

Edge dispersions

The four phases not only have different spin and valley polarizations but they also have different edge properties. In particular, looking at the simplified picture of section 1.3.1, we expect the F phase to have gapless spin-textured edge excitations whereas all the other phases must be gapped at the edges. It was actually confirmed by several theoretical investigations [27, 41, 67, 68].

M. Kharitonov calculated the energy dispersions in the AF, CAF and F phases approaching an armchair edge. For this purpose, he used his mean-field approach and he followed the ideas that had been developed to study the non-interacting case [67]. The three spectra that he calculated are displayed in Fig. 1.15. In the bulk, they are basically identical: they are all composed of two pairs of degenerate levels that are separated by an exchange gap Δ_{bulk}. At the edges, the dispersion are different for the three phases. In the AF phase, Fig. 1.15.A, the highest energy levels bend upward whereas the lowest energy levels bend downward such that $\Delta_{\text{edge}} \geq \Delta_{\text{bulk}}$.

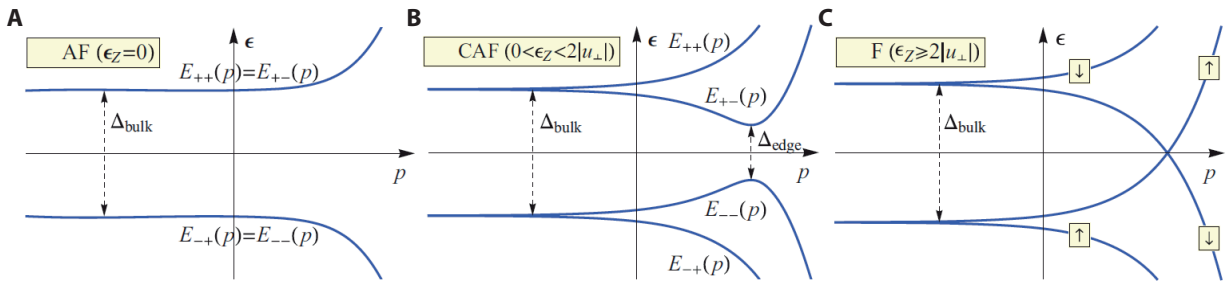

FIGURE 1.15: **Energy dispersions of the AF, CAF and F phase approaching the edges.** In the bulk, the spectra are composed of two pairs of degenerate levels, separated by a gap Δ_{bulk}. Approaching this edge, the dispersion of the degenerate pairs changes depending on the ground state. **A**, In the AF phase, the two pairs disperse in opposite directions. **B**, In the CAF phase, the pairs split into two branches. Two levels have a non-monotonic dispersion and the gap at the edges Δ_{edge} is smaller than in the bulk. **C**, In the F phase, the pairs also split into two spin-polarized branches with opposite bendings. Two levels cross at the edge which leads to a helical edge transport at charge neutrality. Adapted from ref. [67].

Adding a Zeeman splitting, the AF phase transforms into a CAF phase which leads to a modification of the edge dispersion as shown in Fig. 1.15.B. The degenerate pairs now split approaching the edges. In each pair, there is one level whose dispersion is not affected and a second level which have a non-monotonic dispersion. The second levels of each pair bend towards each other approaching the edges up to a point where their dispersions reverse. It leads to a reduction of the gap at the edges.

Due to this reduction of gap, the CAF phase exhibits an activated charge transport nearby charge neutral point mediated by some edge modes [67, 71] as shown in Fig. 1.16. These edge modes are formed of counterpropagating channels and they have some spin textures [61, 71–74]. Therefore, their properties are close to that of the helical edge channels but they are not protected against backscattering because their spin textures are not perfectly anti-aligned.

When the Zeeman energy reaches its threshold value, the CAF phase transforms into a F phase (Fig. 1.15.C). The gap closes at the edge and the energy dispersion is that of the non-interacting

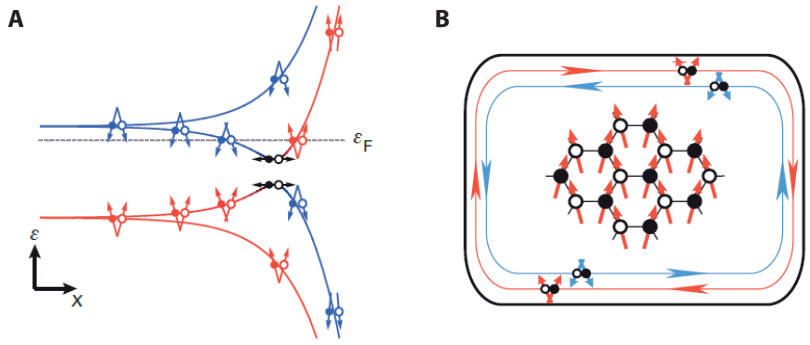

FIGURE 1.16: **Edge states in the CAF phase.** **A**, Schematic of the energy dispersion in the CAF phase approaching an armchair edge. The arrows represent the spin orientations and the open/filled circles represent the two sublattices. Nearby charge neutrality the system exhibits an edge transport mediated by spin-textured edge channels. The wavefunctions for edge states are equally shared between both sublattices because of the valley admixing. **B**, Schematic representation of the bulk and the edge polarization in such regime. Adapted from ref. [61].

theory with helical edge transport at $\nu = 0$. This work clearly evidenced the existence of a continuous phase transition between the F phase and the AF phase.

In 2015, A. Knothe and T. Jolicoeur calculated the edge dispersions in the KD and CDW phases extending Kharitonov's approach [73]. These dispersion actually correspond to that displayed in Fig. 1.11.C, i.e. four distinct levels with the two negative energy levels having an hole-like dispersion and the two positive energy levels having an electron-like dispersion. As expected for these two phases, the system is both insulating in the bulk and at the edges.

These calculations together with most of the previous studies [41, 68] actually get rid of the possible variation of the bulk order parameter approaching the edges. Yet, it may influence the edge properties. It was early pointed out by Fertig and Brey [27] who showed that, in the F phase, the system cannot sustain its bulk order parameter at the edges. It must form a domain wall, described by chiral Luttinger liquid theory, that supports gapless charged excitations.

Taking such effect into account, A. Knothe and T. Jolicoeur found that for some values of the Zeeman energy, the F phase could also be gapped in the sample [73, 75]. More surprisingly, they found that in the KD phase, there might be zero to four levels crossing at charge neutrality. Hence, their investigations suggest that the direct one-to-one correspondence between the transport properties and the identification of ground state may be impossible. Yet, these conclusions have to be taken with caution, as emphasized by the authors themselves, because their perturbative treatment lose its validity as we get closer to the edges.

1.3.3 Experimental investigations of the ground state at charge neutrality

In the experiments with a magnetic field perpendicular to the sample, a strong insulating phase is always observed in different types of samples [10–13, 16, 26, 38, 61, 76, 77]. Therefore, it seems that the F phase is usually not favoured and that one has to find specific strategies to induce its formation.

A. Young and coworkers implemented a remarkable solution. In ref. [61], they studied transport in graphene on h-BN samples and used a magnetic field with a large in-plane component to increase the relative strength of the Zeeman effect. Using this approach, they indeed managed to favour the F phase. They observed characteristic transport signatures of helical edge transport but only with an in-plane component exceeding 30 T. The authors observed a continuous increase of the conductivity at charge neutrality when they increased $B_{\parallel}$ (Fig. 1.17.B). Performing simultaneous capacitance measurements, they also noticed that this transition was not accompanied by a

closure of $\nu = 0$ bulk gap (Fig. 1.17.C). These features were interpreted as signatures of a transition from the CAF to the F phase driven by the increase of the Zeeman splitting.

More recently, Li and coworkers performed scanning tunnelling measurement on graphene on graphite and they made a direct imaging of a KD phase developing at $\nu = 0$ shown in Fig. 1.18.

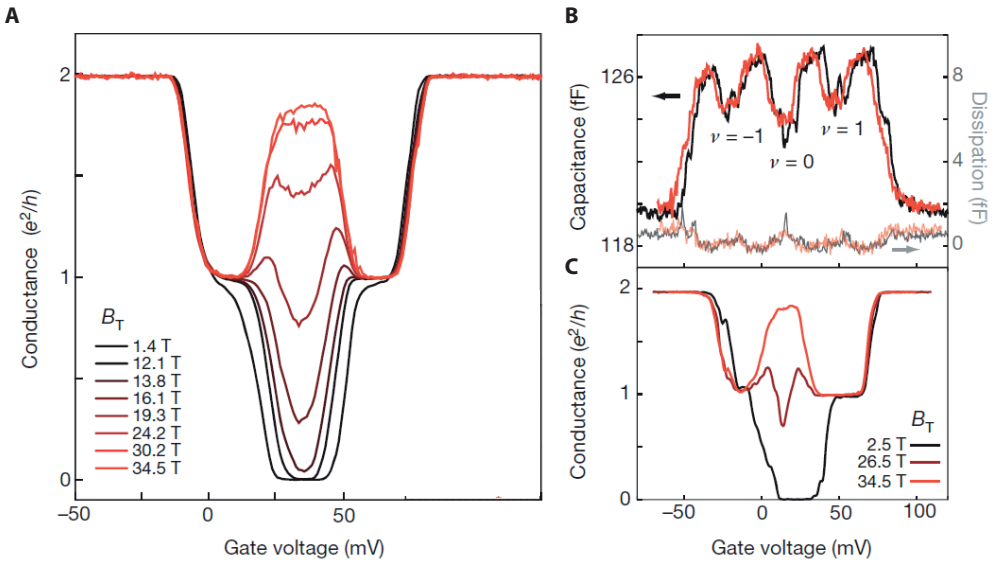

FIGURE 1.17: **Inducing the F phase by enhancement of the Zeeman effect. A**, Two-terminal conductance measurements in a graphene on h-BN sample with a tilted magnetic field. The out-of-plane component is kept constant at $B_\perp = 1.5$ T while the in-plane component is increased. QH plateaus at $G_{2t} = \pm 2, \pm 1\ e^2/h$ do not change wheareas the conductance at $\nu = 0$ continuously increases from 0 to approximately $2\ e^2/h$, the value expected for helical edge transport. **B**, Capacitance and, **C**, two-terminal transport measurements in a similar sample with fixed $B_\perp = 2.5$ T. The capacitance of the system shows dips when the bulk is gapped at integer filling factors. The sample at $\nu = 0$ becomes more conductive as the in-plane magnetic field is increased, whereas the capacitance does not change. It reveals that the bulk gap does not close during the transition. The finite conductivity can thus only arise from an edge transport. Adapted from ref. [61].

Therefore, the nature of the QH ground state at charge neutrality remains elusive and further investigations are needed. On the other hand, it would be interesting to find other strategies enabling to favour the helical quantum Hall phase and benefit from its specific transport properties. In the next chapter, we propose and study another solution to induce the F phase in monolayer graphene. It consists in modifying the effects of lattice-scale interactions and reducing their renormalization by the long-range Coulomb interactions via suitable substrate screening.

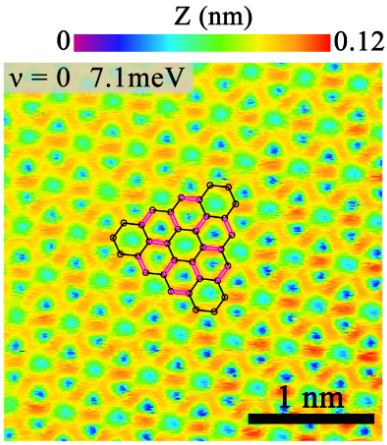

FIGURE 1.18: **Scanning tunnelling imaging of the KD phase at 9 T.** Adapted from ref. [78]

Chapter 2

Helical quantum Hall phase in charge neutral graphene on $SrTiO_3$

Contents

The ferromagnetic (F) ground state of charge neutral graphene in magnetic field, which exhibits helical edge transport, is experimentally difficult to induce. Indeed, the lattice-scale anisotropies usually favour other competing ground states. In this chapter, we demonstrate that the long-range Coulomb interactions in high mobility graphene heterostructures can be screened by a high-k dielectric substrate that enables to induce the formation of this helical QH phase.

After a discussion about the underlying mechanisms, we present the specificities of the a high-k dielectric substrate used: the strontium titanate oxyde $SrTiO_3$. We then detail how the nanofabrication processes should be adapted to benefit from its screening properties. We present several transport experiments performed in graphene devices on $SrTiO_3$ evidencing the existence of a helical quantum Hall phase in such systems at charge neutrality. Finally, we discuss its breakdown at high temperatures and high magnetic fields.

2.1 Use of $SrTiO_3$ substrate to induce the helical quantum Hall phase

2.1.1 Substrate screening of Coulomb interactions in the quantum Hall regime

According to ref. [36], the lattice-scale anisotropies which determine the ground state of charge neutral graphene in magnetic field, are strongly renormalized by the long-range Coulomb interactions. Therefore, to induce the formation of the F phase at charge neutrality, one can think about modifying the strength of the long-range Coulomb potential: it allows to affect these anisotropies indirectly by mitigating the renormalization effect.

As the Coulomb energy scale is given by $\epsilon_C = \frac{e^2}{4\pi\epsilon_0\epsilon_r l_B}$, it can be tuned by putting graphene on top of a substrate with a high dielectric constant ϵ_r. This strategy implies to have an efficient substrate screening and thus to place the graphene flake close enough to the high-k substrate. As we also need high mobility to get broken symmetry states emerging at few Teslas, we must fabricate graphene heterostructures with sufficiently thin bottom h-BN and deposit them on the substrate as depicted in Fig. 2.1.

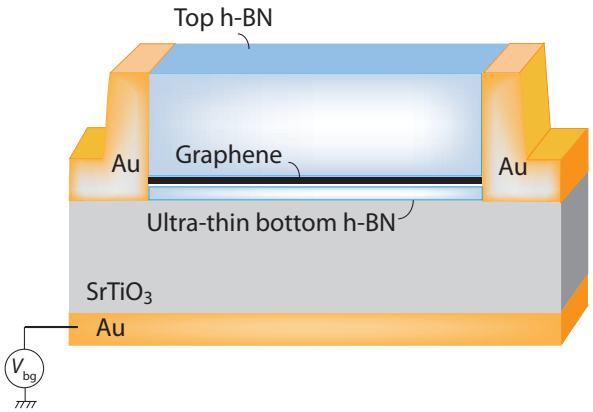

FIGURE 2.1: **Schematic of a typical high mobility graphene heterostructure on $SrTiO_3$.** The bottom h-BN is chosen such that $d_{BN} \leq 5$ nm. It allows to benefit from a strong substrate screening even at large magnetic fields. The graphene can be doped by applying a voltage on a back-gate electrode placed on the opposite face.

The condition on the thickness of the h-BN spacer separating the graphene from the substrate can be more quantitatively assessed by evaluating the Coulomb potential experienced by charge carriers in such heterostructures. Assuming that the bottom h-BN is thin, that the top h-BN is much thicker, such that it can be considered as infinitely thick, and that the substrate is also infinitely thick, the Coulomb potential reads [79]:

$$V(r) = \frac{e^2}{4\pi\epsilon_0\epsilon_{BN} r}\left(1 - \frac{\epsilon_S - \epsilon_{BN}}{\epsilon_S + \epsilon_{BN}} \frac{r}{\sqrt{r^2 + 4d_{BN}^2}}\right) = \frac{e^2}{4\pi\epsilon_0\epsilon_{BN} r} S(r/d_{BN}, \epsilon_S), \tag{2.1}$$

where r is the typical distance between charges carriers, ϵ_S the substrate dielectric constant and d_{BN} is the thickness of the bottom h-BN. Thus, we see that in such devices, the Coulomb potential is indeed reduced by a factor S providing $\epsilon_S > \epsilon_{BN} \simeq 4$. This factor decreases when the distance to the substrate decreases or when ϵ_S is increased as shown in Fig. 2.2.

Importantly, Fig. 2.2 also shows that the effect of the substrate dielectric constant is significant only when r is comparable or larger than d_{BN} in agreement with the previous discussion. Besides, we note that to reduce the Coulomb potential by one order of magnitude, one needs both to have $\epsilon_S \geq 100$ and $r/d_{BN} \geq 4$.

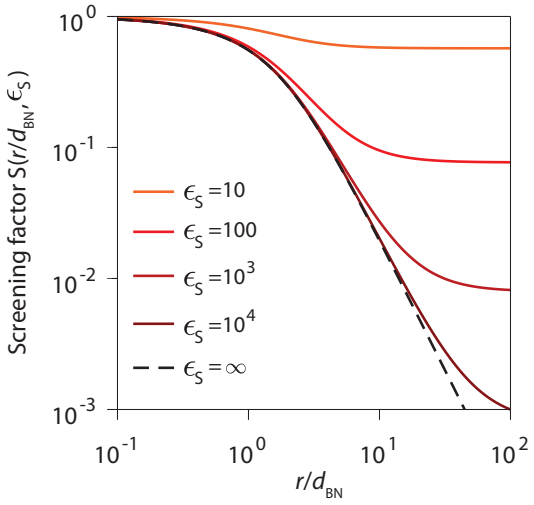

FIGURE 2.2: **Substrate induced screening.** Evolution of the screening factor $S(r/d_{\mathrm{BN}}, \epsilon_S)$ for various substrate dielectric constants ϵ_S with the ratio r/d_{BN} of the typical distance between charge carriers over the thickness of the bottom h-BN. The screening factor decreases with r/d_{BN} and ϵ_S. The effect of the substrate screening starts to be significant typically when $r/d_{\mathrm{BN}} \geq 1$. It converges at large r/d_{BN} values towards an asymptotic limit which decreases with ϵ_S. The saturation appears at smaller r/d_{BN} values when ϵ_S is smaller reducing the efficiency of the screening for intermediate ϵ_S values.

In the quantum Hall regime, the typical distance between charge carriers is given by the magnetic length $l_B = \sqrt{\frac{\hbar}{eB}}$ which is also the relevant length scale to consider for the screening of Coulomb interactions. In this regime, the reduced Coulomb energy scale reads as:

$$\epsilon_{\mathrm{C}}^{*} = \epsilon_{\mathrm{C}} \left(1 - \frac{\epsilon_{\mathrm{S}} - \epsilon_{\mathrm{BN}}}{\epsilon_{\mathrm{S}} + \epsilon_{\mathrm{BN}}} \frac{l_B}{\sqrt{l_B^2 + 4d_{\mathrm{BN}}^2}} \right) = \frac{e^2}{4\pi\epsilon_0\epsilon_{\mathrm{BN}} l_B} \left(1 - \frac{\epsilon_{\mathrm{S}} - \epsilon_{\mathrm{BN}}}{\epsilon_{\mathrm{S}} + \epsilon_{\mathrm{BN}}} \frac{l_B}{\sqrt{l_B^2 + 4d_{\mathrm{BN}}^2}} \right). \tag{2.2}$$

Considering that $l_B \leq 26$ nm above 1 T and decreases with the magnetic field, we see that the graphene must be placed only a few nanometers away from the underlying substrate to benefit from a significant substrate screening effect. Thus, if we hope to induce the formation of the F ground state using a high-k dielectric substrate, we must fabricate h-BN/graphene/h-BN heterostructures with only few nanometers thick bottom h-BN.

2.1.2 $SrTiO_3$: a very high-k dielectric of interest for graphene heterostructures

To benefit from a large substrate-induced screening, one can think about depositing the stack on a metallic material, like for example a graphite flake or a gold electrode, which virtually has an infinite dielectric constant. However, practically, it is extremely challenging to realize as we use of few nanometers thick bottom h-BN. It greatly increases the risk of connecting the graphene and the metallic plane underneath during the device fabrication, especially while etching for the contacts.

That's why we rather decided to use a high-k **insulating** substrate and focused our efforts on strontium titanate oxyde $SrTiO_3$. This material is a quantum paraelectric material where long-range ferroelectric ordering is destroyed by quantum fluctuations [80, 81]. It has a very large dielectric constant ϵ_{STO} which decreases with temperature and ranges typically from 10^2 at 300 K to 10^4 at 4 K [82]. This exceptional dielectric property has two advantages.

First, it allows the $SrTiO_3$ substrates to screen Coulomb interactions in the quantum Hall regime very efficiently provided that the bottom h-BN is thin enough (i.e. when $l_B > d_{BN}$). The mitigation of the Coulomb energy (see eq. (2.2)) is clearly evidenced in Fig. 2.3.A and Fig. 2.3.B where the evolution of ϵ_C^* with the magnetic field B is plotted for different thickness of bottom h-BN. The screening is particularly strong in samples with $d_{BN} \leq 5$ nm where a significant reduction of the Coulomb energy is observed. As evidenced in Fig. 2.3.B, ϵ_C^* varies strongly with B in these samples, much more than in standard dielectric environments (situation equivalent to $d_{BN} = \infty$). In particular, at low fields ϵ_C^* scales as $B^{3/2}$, whereas it scales as $B^{1/2}$ in standard samples. The substrate screening is then enhanced at low fields and ϵ_C^* even becomes smaller or of the same order of magnitude than the Zeeman energy in the samples with ultra-thin bottom h-BN.

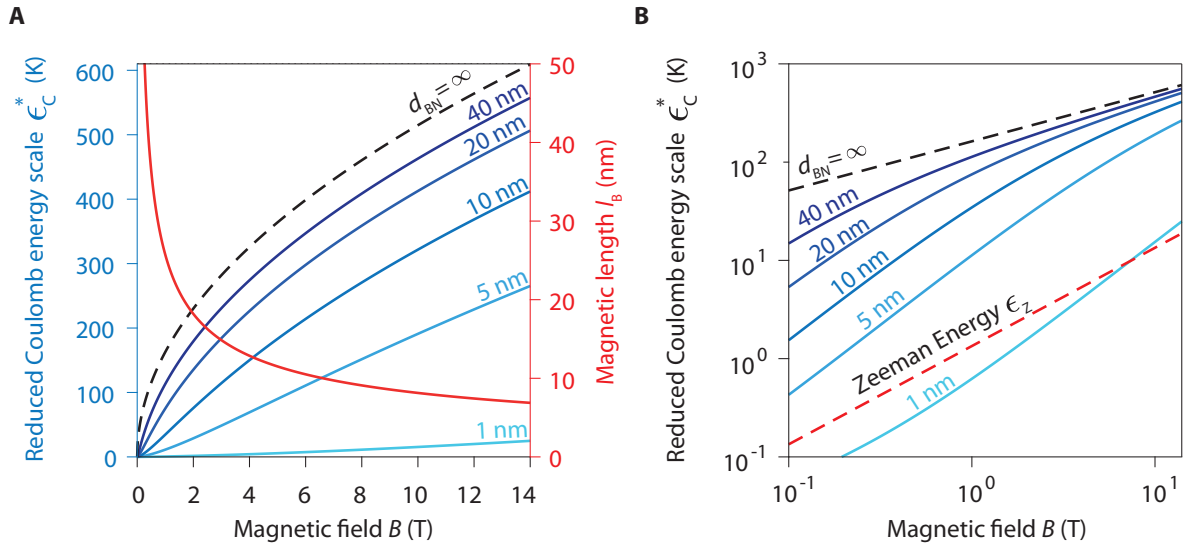

FIGURE 2.3: **Reduction of the Coulomb energy scale ϵ_C^* in graphene heterostructures on $SrTiO_3$.** Evolution of ϵ_C^* for different bottom h-BN thickness d_{BN}, **A**, in linear scale and, **B**, log-log scale . In A the evolution of the magnetic length l_B is displayed as an help to determine when $d_{BN} \leq l_B$. In B, the Zeeman energy ϵ_Z is reported to show that in samples with ultrathin h-BN it becomes comparable to ϵ_C^*. Note that the situation where $d_{BN} = \infty$ is equivalent to the case of standard devices on silicon substrates.

Second, the large dielectric constant of $SrTiO_3$ allows to use directly a 0.5 mm thick substrate as a back-gate dielectric even at high temperatures. To make a quantitative comparison, we can calculate the equivalent planar capacitance $C = \frac{\epsilon_0 \epsilon_r}{d}$ formed by a graphene flake on Si^{++}/SiO_2 substrate with $d = 300$ nm oxide thickness of dielectric constant $\epsilon_{SiO_2} = 3.9$ and compare it with the capacitance formed by a graphene flake on a $d = 0.5$ mm thick $SrTiO_3$ substrate with $\epsilon_{STO} \approx 10^4$. The corresponding capacitance, respectively $C_{SiO_2} = 1.2 \times 10^{-4}$ F/m^2 and $C_{STO} = 1.8 \times 10^{-4}$ F/m^2, are very similar confirming that a thick $SrTiO_3$ substrate can be used directly as a back-gate dielectric.

2.1.3 Fabrication of graphene heterostructures on $SrTiO_3$

We fabricated several high mobility graphene devices on $SrTiO_3$. The fabrication process is similar to that reported in Appendix 12 for devices on Si^{++}/SiO_2 substrate up to a few details.

First, according to previous discussions, the heterostructures must be fabricated using bottom h-BN with thicknesses $d_{BN} \lesssim 10$ nm. Once the heterostructures are assembled, they are deposited on the polished side of a 500 μm thick $SrTiO_3$ [100] substrate freshly cleaned with a hydrofluoric acid buffered solution (7:1 volume ratio) for 30 seconds [83].

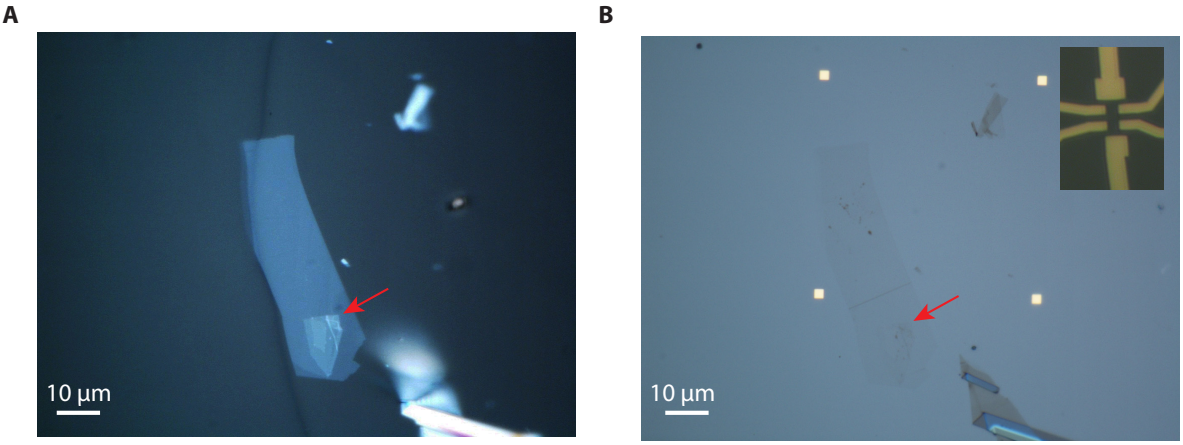

FIGURE 2.4: **Van der Waals heterostructures on $SrTiO_3$. A**, Image with enhanced contrast of a graphene heterostructure with a 3.3 nm bottom h-BN (indicated by a red arrow) on a stamp. **B**, Image of the same heterostructure after deposition on the $SrTiO_3$ substrate with normal contrast. The bottom h-BN and the graphene are hardly/not visible. Inset : Device fabricated after processing of the heterostructure.

To fabricate a device from the initial stack, e-beam lithography is used to have a good spatial resolution in the position and shape of the nanostructures. However, specific cares should be taken to perform e-beam lithography because the insulating nature of the thick substrate results in charge accumulations during the exposure. It leads to aberrations and distortions during the lithography. To prevent it, before the exposure, the e-beam resist can be covered by either a thin conductive resit films (Electra 92 AR-PC 5090) or a few nanometer thick gold film. These films help to drain the charges during the exposure and enable to perform reproducible and reliable e-beam lithographies on $SrTiO_3$. Before the e-beam resit development, the additional layers must be removed by rinsing the sample respectively in deionized water for one minute (Electra resist) or in a KI/I_2 solution for a few seconds (gold thin film).

The rest of the fabrication process (markerfield, deposition of electrical contacts and gate electrodes) does not differ from the one of devices on silicon substrate. Yet, we note that a careful processing of optical images of the devices is needed because of the very low contrast of graphene and ultra-thin h-BN on $SrTiO_3$ (see Fig. 2.4).

2.2 Samples studied and their transport characteristics at zero magnetic field

2.2.1 Devices studied

We fabricated several graphene devices on $SrTiO_3$ with thin bottom h-BN and characterized their transport properties. They are presented in Fig. 2.5 and their characteristics are summarized in Table 2.1. All the heterostructures were assembled with the Van der Waals pick-up method and for most of them we used bottom h-BN with thicknesses below 5 nm. Sample BNGrSTO-09 was purposely made with a 61 nm thick bottom h-BN to confirm the necessity of having a thin h-BN to benefit from $SrTiO_3$ screening in the quantum Hall regime. The contacts in BNGrSTO-04, 05, 07 and 09 samples were made in a single step by a direct etching of the stack in the resist lines immediately followed by a Cr/Au evaporation. For BNGrSTO-VH02 and VH-03 samples, the contacts were made in two steps. First, the heterostructures were etched into a Hall bar geometry using a hardened HSQ resist mask and on a second lithography step, a Cr/Au bilayer was deposited on the etched graphene edges.

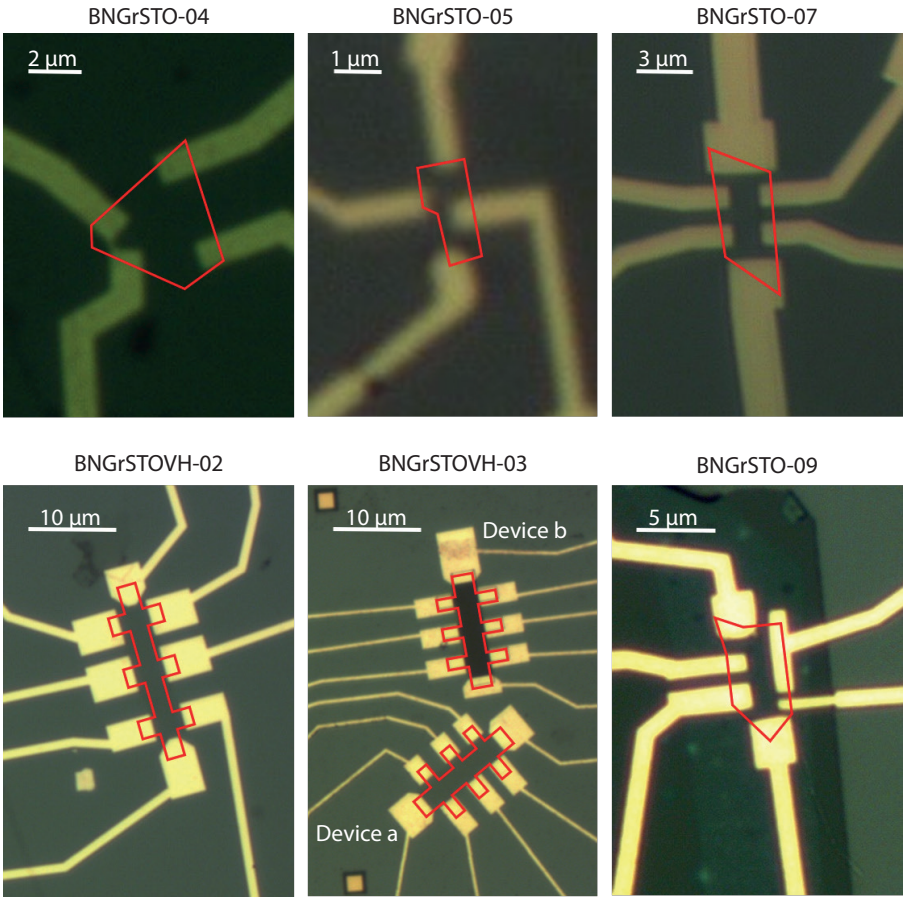

FIGURE 2.5: **Optical images of the samples on $SrTiO_3$ studied.** The edges of the graphene flakes (pristine or etched) are represented by red lines.

Sample	Contacts number	Graphene dimensions (μm)	Bottom h-BN thickness (nm)	Mobility ($cm^2.V^{-1}.s^{-1}$)
BNGrSTO-04	3	4×5	5	75 000
BNGrSTO-05	4	1.6×2.2	3.3	20 000
BNGrSTO-07	6	6×3	3.2	40 000
BNGrSTOVH-02	8	15×2	5	130 000
BNGrSTOVH-03a	8	15×3	4	50 000
BNGrSTOVH-03b	8	15×3	4	50 000
BNGrSTO-09	6	8×3	61	200 000

TABLE 2.1: **Characteristics of samples on $SrTiO_3$ studied.**

2.2.2 Hysteresis of back-gate sweeps for devices on $SrTiO_3$

Below 35 K, $SrTiO_3$ is a quantum paraelectric material composed of several microscale to nanoscale ferroelectric-like domains [84–88]. They can influence the transport properties in graphene especially because they move when the back-gate voltage is changed [86]. Similarly, it exists dipoles on the surface of $SrTiO_3$ which are sensitive to changes of back-gate voltage. Both the dynamics of the domains and of the dipoles relaxation are very long with typical time scales of several minutes or even hours, and they are strongly dependent on the strength of the electric field applied [89].

All of this results in non-linearities and in an hysteresis of the dielectric constant of $SrTiO_3$ [90] appearing while performing back-gate voltage sweeps. This leads to a shift in the position of Dirac point between upward and downward sweeps. Likewise, the Dirac point can be shifted if the voltage range spanned is changed [89]. To limit this hysteresis, upward and downward sweeps are always performed within the same voltage range (typically from 0 to 30 V at 4 K) and under the same conditions. It allows to have reproducible sweeps, to stabilize the position of the Dirac point and it ensures that the density, at a given back-gate voltage, is the same for different sweeps performed in the same direction.

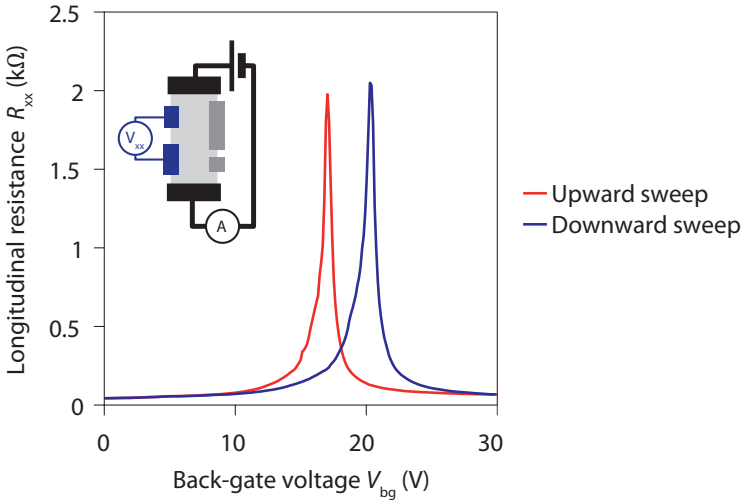

FIGURE 2.6: **Back-gate hysteresis.** Evolution of the longitudinal resistance with back-gate voltage in sample BNGrSTO-09. The Dirac peak appears respectively at 17 and 20.4 V for upward and downward sweeps because of the strong dielectric hysteresis of the substrate. Inset : Contact configuration during the measurements. Contacts in grey are floating.

2.2.3 Characterization of the devices at zero and low magnetic fields

Mobility of the devices

Before studying the devices in the quantum Hall regime, we preliminarily study transport at zero/low magnetic fields. In particular, we characterize their Hall mobility μ and the dielectric constant ϵ_{STO} of the $SrTiO_3$ substrates which are relevant quantities to consider for the study of the formation of the helical quantum Hall phase.

Both can be extracted from classical Hall measurements and back-voltage sweeps at zero magnetic field. The evolution of the Hall resistance R_{xy} with back-gate voltage V_{bg} allows to evaluate n the charge carrier density (positive for electrons and negative for holes) at fixed V_{bg} as $n = \frac{B}{R_{xy}\, e}$

where B is the magnetic field at which Hall measurements are performed. [1] An example of such estimation of the charge carrier density based on Hall measurements is given in Fig. 2.7.C. The resulting Hall mobility, given by $\mu = \frac{1}{n\, e\, R_\square}$ with $R_\square$ the longitudinal sheet resistance, is displayed in Fig. 2.7.D.

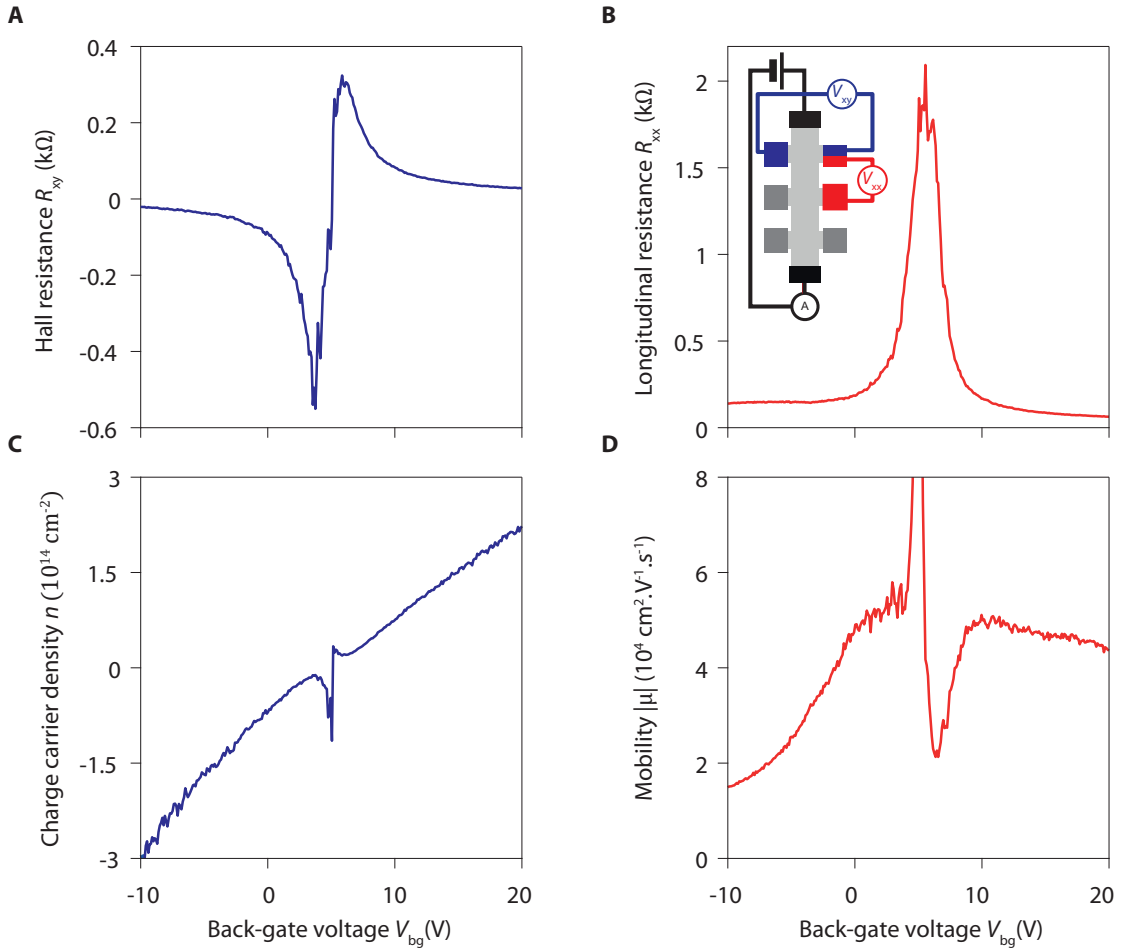

FIGURE 2.7: **Extraction of the charge carrier density and mobility based on Hall measurements. A**, Evolution of the anti-symmetrized Hall resistance R_{xy} with the back-gate voltage V_{bg} at $B = \pm 0.1$ T in sample BNGrSTOVH-03a. **B**, Evolution of the longitudinal resistance R_{xx} with the back-gate voltage V_{bg} at zero magnetic field. Inset: Contact configuration during the measurements. Contacts in grey are floating. **C**, Charge carrier density n calculated from B. **D**, Hall mobility calculated from B and C after polynomial fitting of n.

The resulting mobilities are summarized in Table 2.1 and displayed Fig 2.8. Most of the samples with thin bottom h-BN have a mobility above 40 000 cm^2.V^{-1}.s^{-1} at high carrier density which is sufficient to observe the formation of broken symmetry states at intermediate magnetic fields of a few Teslas.

The samples BNGrSTO-04 and BNGrSTO-05 do not have a geometry or contacts that allow to perform Hall measurements. Thus to estimate the mobility, we use the sheet resistance 10 V away from the Dirac point and an estimate of the density at such voltage based on Hall measurements performed in other devices with a more suitable geometry.

[1] For a proper evaluation, we anti-symmetrize the value of the Hall resistance with respect to B to get rid of the geometry of the device.

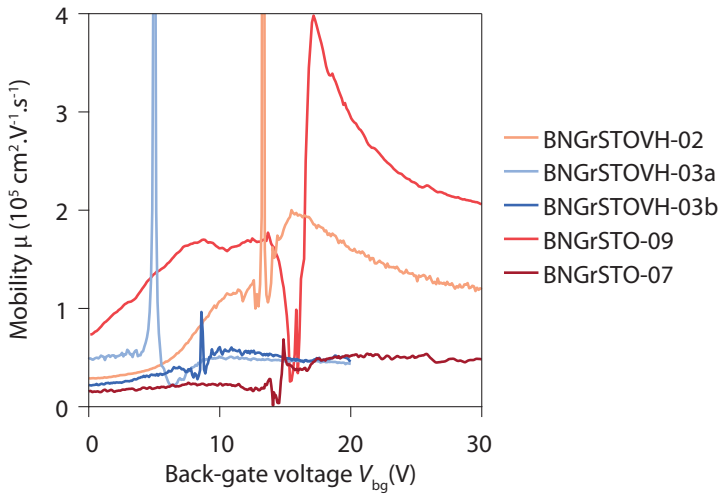

FIGURE 2.8: **Mobility of the samples on $SrTiO_3$ with a Hall bar geometry**

Substrate dielectric constant at 4 K

The Hall measurements also enable us to estimate the dielectric constant of each $SrTiO_3$ substrate using the graphene devices as charge sensors through the Hall effect. The density n in the graphene flake is given by:

$$n = \frac{C_{bg}}{e}\Delta V_{bg}, \tag{2.3}$$

where $\Delta V_{bg} = V_{bg} - V_{bg}^{CNP}$ is the voltage applied on the back-gate shifted by the voltage where charge neutral point (CNP) is reached and where C_{bg} is the equivalent planar capacitance. The latter can be decomposed as a sum of two contributions arising from bottom h-BN and $SrTiO_3$ substrate capacitance such that:

$$\frac{1}{C_{bg}} = \frac{d_{STO} + d_{BN}}{\epsilon_r} = \frac{1}{C_{STO}} + \frac{1}{C_{BN}} = \frac{d_{STO}}{\epsilon_{STO}} + \frac{d_{BN}}{\epsilon_{BN}}, \tag{2.4}$$

where d_{STO} and d_{BN} are the thicknesses of the $SrTiO_3$ substrate and bottom h-BN flake and where ϵ_{STO}, ϵ_{BN} and ϵ_r are the dielectric constant of the $SrTiO_3$ substrate, bottom h-BN flake and of the overall system. Considering that $d_{BN} \ll d_{STO}$, we can express ϵ_r as:

$$\epsilon_r = \frac{\epsilon_{STO}}{1 + \frac{d_{BN}}{d_{STO}}\frac{\epsilon_{STO}}{\epsilon_{BN}}} \tag{2.5}$$

At low temperatures, $\epsilon_{BN} \approx 3 - 4$ and $\epsilon_{STO} \sim 10^4$ and for the samples with a few nanometers thick BN spacer $\frac{d_{BN}}{d_{STO}}\frac{\epsilon_{STO}}{\epsilon_{BN}} \lesssim 0.1$. Thus, in these devices, the effective back-gate capacitance is mainly determined by ϵ_{STO} and $\epsilon_r \approx \epsilon_{STO}$. Even in BNGrSTO-09 where $d_{BN} = 61$ nm, $\frac{d_{BN}}{d_{STO}}\frac{\epsilon_{STO}}{\epsilon_{BN}} \lesssim 1$ and thus ϵ_r provides a good order of magnitude for ϵ_{STO} (as $\frac{\epsilon_{STO}}{2} \leq \epsilon_r < \epsilon_{STO}$)

The dielectric constants at 4 K measured in the different devices are shown in Fig. 2.9. ϵ_r varies between the different substrates and typically ranges between 5000 and 70000 in agreement with previous measurements for ϵ_{STO} at low temperatures. ϵ_{STO} varies significantly with the back-gate voltage depending on the sample as a result of the non-linear dielectric properties of $SrTiO_3$. Surprisingly, ϵ_{STO} values in BNGrSTOVH-03 sample are quite different for the two devices and

the device BNGrSTOVH-03b displays an exceptionally high dielectric constant exceeding 70000 at $V_{bg} = 0$ V.

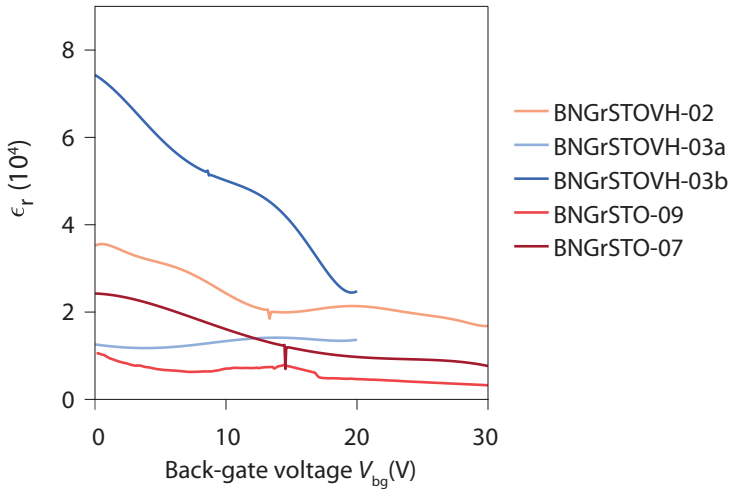

FIGURE 2.9: **Dielectric properties of $SrTiO_3$ substrate at 4 K.** Relative dielectric constants of the plane capacitance formed by the graphene and the back-gate electrode for samples on $SrTiO_3$. ϵ_r values are computed from the same Hall measurements than the ones used to evaluate the mobilities μ of the devices.

2.3 Helical quantum Hall edge transport at CNP in samples with thin bottom h-BN

We now discuss the transport in the quantum Hall regime for devices on $SrTiO_3$ and show that a helical edge transport emerges at charge neutrality in devices with a thin bottom h-BN. To facilitate the comparison between different experiments and different samples, all the plots displaying evolution of resistances with back-gate voltages are shifted such that CNP lies at $V_{bg} = 0$ V. Most of the measurements presented are performed at 4 K, otherwise the temperature during measurements is explicitly mentioned.

2.3.1 Evidence of non-local helical edge transport in BNGrSTO-07 sample

The effects of $SrTiO_3$ screening, and the emergence of the helical quantum Hall phase in samples with thin bottom h-BN, appear by measuring resistance of the devices in two-terminal configurations at intermediate magnetic fields (typically around 2 T). To illustrate it, we start by focussing on the sample BNGrSTO-07 which shows characteristic features.

Fig. 2.10.A displays the evolution of the two-terminal resistance in this device with both the magnetic field B and the back-gate voltage V_{bg} for a given contact configuration drawn in inset. We see that in this device the quantized resistance plateaus $\nu = \pm 2$ and $\nu = \pm 6$, characteristic of the QH effect in graphene, appear above 1 T whereas the $\nu = 1$ broken symmetry state emerges above 5 T. It is consistent with the sample's mobility.

Remarkably, the device displays a finite conductance at charge neutrality which remains constant over a long range of magnetic field from 1.5 T to about 4 T as we can see in Fig. 2.10.B and Fig. 2.10.C. At higher fields, the resistance approximately increases exponentially with B but remains below 100 kΩ at 14 T. This is in sharp contrast with the transport characteristics measured in devices on silicon substrate where a strong insulating phase develops with the magnetic field before the emergence of broken symmetry states at $\nu = \pm 1$ [12, 13, 76]. This observation indicates

that some conduction occurs in the sample at charge neutrality suggesting that the ground state could be the F phase.

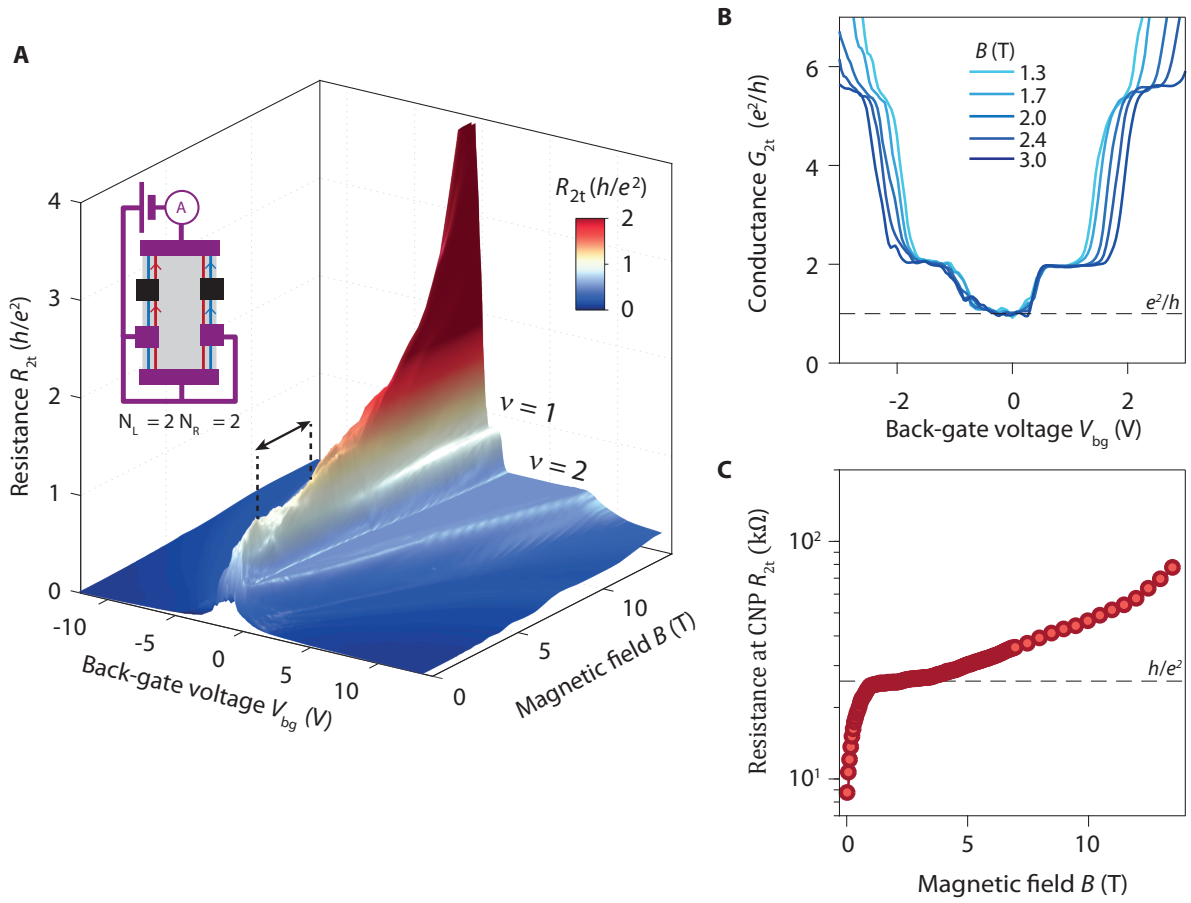

FIGURE 2.10: **Helical quantum Hall plateau at charge neutrality in BNGrSTO-07 sample. A**, Evolution of the two-terminal resistance R_{2t} in BNGrSTO-07 sample with respect to back-gate voltage V_{bg} and magnetic field B at 4 K. On top of the standard $\nu = 1$, 2 plateaus, an anomalous quantized $\frac{h}{e^2}$ resistance plateau arises at CNP between 1.5 and 4 T (delimited by dashed lines). Inset: Schematic of the contact configuration considered. Black contacts are floating. The red and blue arrows on the helical edge channels indicate the direction of the current between contacts, and A indicates the ampmeter. **B**, Two-terminal conductance $G_{2t} = \frac{1}{R_{2t}}$ versus V_{bg} extracted from A for different magnetic fields. In addition to the $\pm\frac{2e^2}{h}$ and the $\pm\frac{6e^2}{h}$ characteristic of graphene QH effect, a clear $\frac{e^2}{h}$ plateau develops at CNP consistent with the value expected for helical edge transport (dashed line). The $\frac{6e^2}{h}$ plateau actually appears around $5.6\frac{e^2}{h}$ because of the wire resistance. **C**, Resistance at CNP versus magnetic field extracted from A evidencing the presence of a resistance plateau between 1.5 T and 4 T. At higher magnetic fields, R_{2t} increases with B but remains below 100 kΩ at 14 T contrary to standard samples on silicon substrate which usually display a very strong insulating phase.

Even more surprisingly, the constant conductance at charge neutrality is quantized to $\frac{e^2}{h}$ as shown in Fig. 2.10.B. We now show that this value is consistent with a helical edge transport regime.

Along a free sample edge, backscattering between the counterpropagating edge channels of single helical pair is fully suppressed because the two edge channels have opposite spin polarization. The transmission of helical edge states is supposedly perfect along a free edge. In contrast, in a metallic contact, the carriers lose their spin coherence and thus the two helical edge channels

are equilibrated at the contacts [60, 61]. Therefore a helical edge section between two contacts can be seen as single resistor of quantized resistance $R_Q = \frac{h}{e^2}$ as represented in Fig. 2.11.A [61].

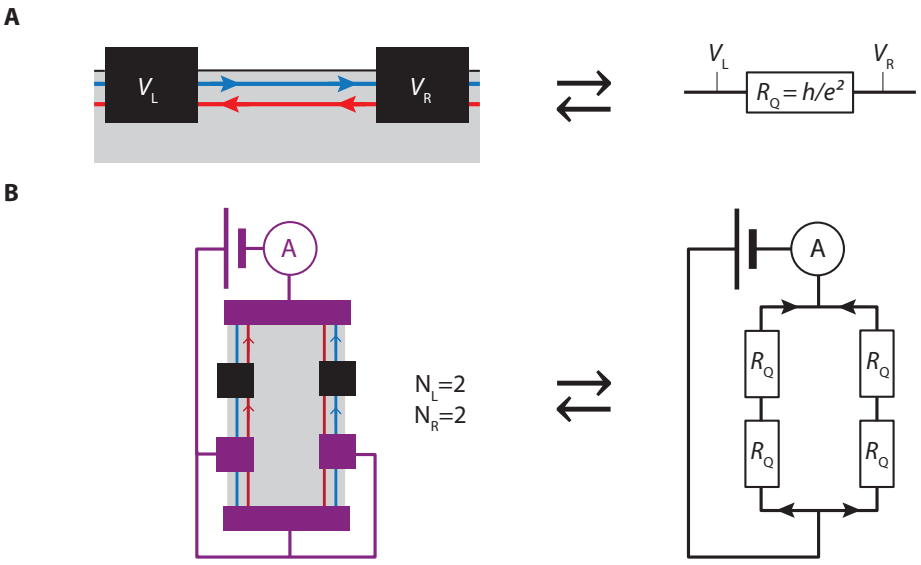

FIGURE 2.11: **Equivalence between a contact configuration and an electric circuit in the helical edge transport regime. A**, A helical edge section between adjacent contacts, respectively at electric potential V_L and V_R, can be modelled by a resistor $R_Q = \frac{h}{e^2}$. **B**, A given contact configuration can be modelled by an electric circuit composed of two branches of R_Q resistors in series. Each branch represents an edge of the device between the source and drain contacts. The numbers of resistors in each branch, N_L and N_R, are respectively given by the numbers of helical edge sections on the left (L) edge and on the right (R) edge of the device.

The two-terminal resistance value in the helical edge transport can then be calculated by modelling the device by the equivalent resistor network. It is composed of two branches representing the left and right edges connecting the source and drain contacts and which both contribute to the transport. Each branch is composed of N resistors in series which represent the N helical edge sections between the source and drain contact along the edge considered. Therefore, the two terminal resistance R_{2t} is given by:

$$R_{2t} = \frac{h}{e^2}\left(\frac{1}{N_L} + \frac{1}{N_R}\right)^{-1}, \tag{2.6}$$

where N_L and N_R are respectively the number of helical edge sections between source and drain contacts on the left (L) edge and on the right (R) edge of the device [61, 91] (see also Appendix 9 for derivation). Fig. 2.11.B displays the equivalent circuit corresponding to the contact configuration used for measurements of Fig. 2.10. We note that, that in this case, the resistance measured at charge neutrality is fully consistent with the expected value $R_{2t} = \frac{h}{e^2}\left(\frac{1}{2} + \frac{1}{2}\right)^{-1} = \frac{h}{e^2}$.

Similarly, this formula can be used to demonstrate the existence of a helical edge transport by changing N_L and N_R and seeing if the resistance varies accordingly. Fig 2.12 shows R_{2t} measured at 2.5 T for other contact configurations, with different source/drain contacts and different number of edge sections. At CNP, the value of two-terminal resistance measured fits with the value calculated from eq. (2.6) evidencing that the transport is indeed mediated by helical edge states at charge neutrality.

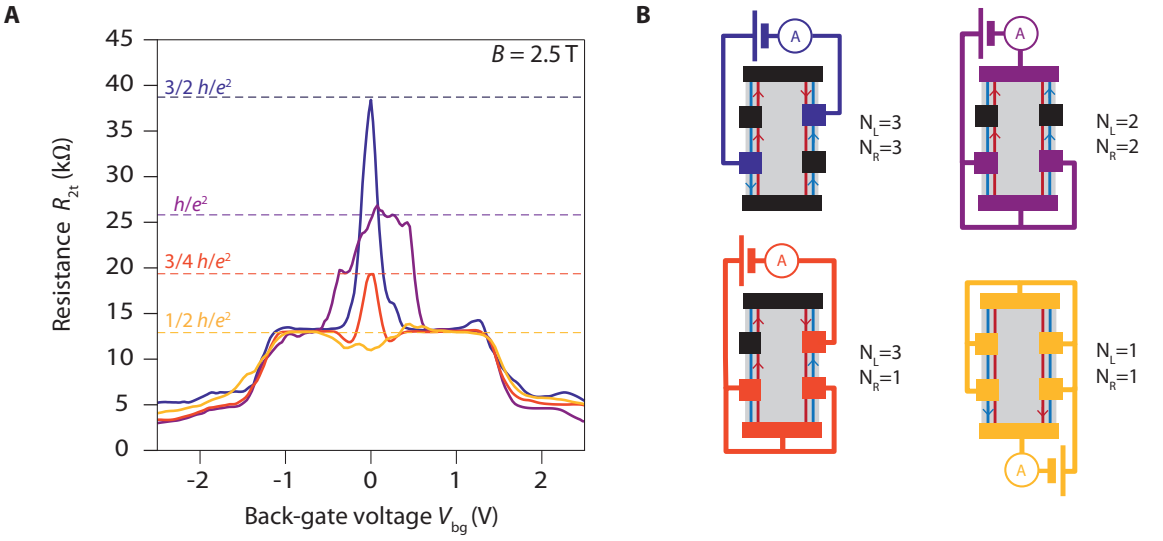

FIGURE 2.12: **Dependence of the quantized resistance at CNP with the contact configuration. A**, Evolution of the two-terminal resistances R_{2t} in BNGrSTO-07 sample with back-gate voltage V_{bg} at 2.5 T for different contact configurations. At CNP, R_{2t} reaches values expected for helical edge transport, indicated by coloured dashed lines, in all the displayed configurations. **B**, Schematics of the contact configurations. Black contacts are floating. The red and blue arrows on the helical edge channels indicate the direction of the current between contacts, and A indicates the ampmeter. N_L and N_R indicate the number of helical edge sections between the source and drain contacts respectively on the left and the right edge of the device.

As helical edge channels drive the current all along the edge of the devices, the device should display a finite resistance even when the voltage probes are far from the source and drain contacts. In four-terminal contact configuration, we thus expect to measure a non-local resistance given by:

$$R_{NL} = R_{2t}\frac{N_V}{N_I}, \tag{2.7}$$

where N_V is the number of helical edge sections between the two voltage probes and N_I is the number of helical edge sections between the source and drain contacts on the side where the voltage probes are put [91] (see also Appendix 9). Fig 2.13.A displays the evolution of both R_{2t} and R_{NL} with the back-gate voltage for the non-local configuration sketched in inset at 2.5 T. At charge neutrality, both resistances reach a value consistent with the ones expected for helical edge transport.

Notably, R_{NL} is not negligible only at CNP, where its exceeds 5 kΩ. It cannot be explained by a diffusive transport in the device for which the non-local resistance is given by:

$$R_{NL} \approx R_{\square}\exp(-\pi\frac{L}{w}), \tag{2.8}$$

where L is the distance between the source/drain contacts and the voltage probe and w is the width of the graphene flake [92]. Considering the device geometry, it would result in only a few tenth of Ohms non-local resistance inconsistent with the large non-local signal measured at CNP. We must also note that both R_{NL} and R_{2t} values at CNP stay constant over the same field range as shown in Fig 2.13.B and thus the two plateaus seem correlated. All these features give further evidences that transport is mediated by helical edge channels at charge neutrality in the intermediate magnetic field regime.

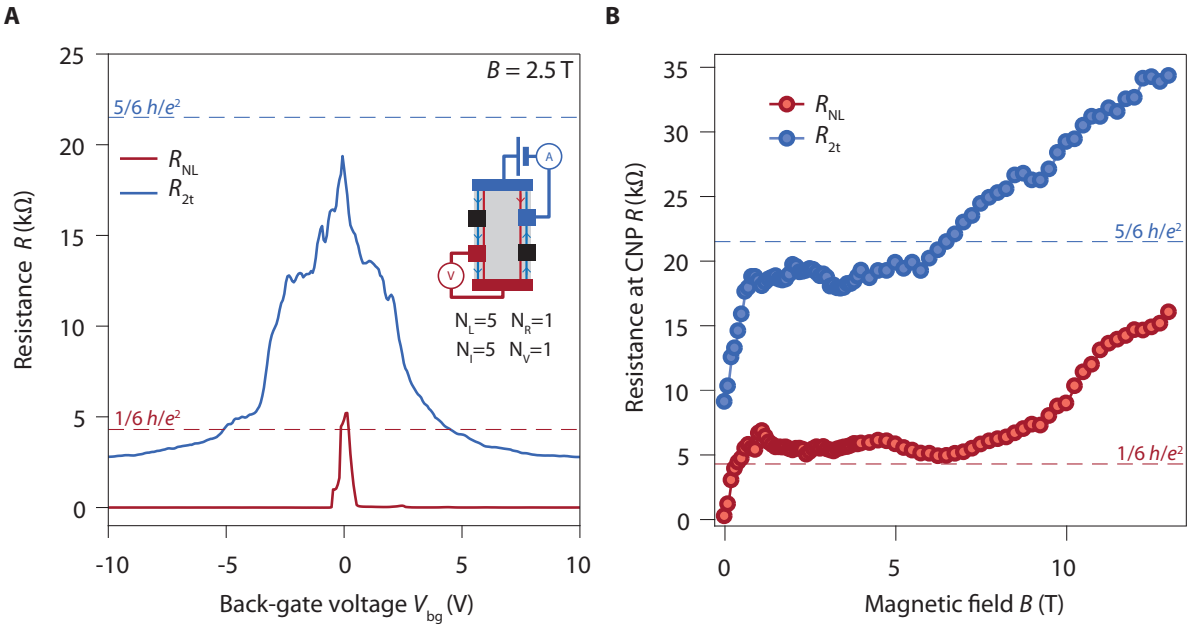

FIGURE 2.13: **Evidence of non-local edge transport. A**, Evolution of the two-terminal R_{2t} and of the non-local resistances R_{NL} in BNGrSTO-07 sample with V_{bg} at 2.5 T. At CNP, both resistances display large values consistent with helical edge transport. $R_{NL} > 5$ kΩ indicative that the transport is non diffusive at CNP. **B**, Evolution of R_{2t} and R_{NL} with magnetic field B at CNP. Both resistances show a helical resistance plateau between 1.5 and 6 T. Inset: Schematic of the contact configuration. N_L and N_R indicate the number of helical edge sections between the source and drain contacts respectively on the left and the right edge of the device. N_V and N_I indicate the number helical edge sections respectively between the voltage probes and between the source and drain contacts on the edges where the voltage probes are placed.

2.3.2 Evidence of non-local helical edge transport in other samples

Similar signatures of helical edge transport were also observed in the other samples at charge neutrality and low/intermediate magnetic fields. The systematic observation of such features in different samples shows that the use of $SrTiO_3$ substrate screening allows to induce the formation of the F phase at $\nu = 0$ in a reliable and reproducible way.

BNGrSTO-04 sample

Fig. 2.14 presents two-terminal transport measurements performed in BNGrSTO-04 sample in a similar fashion than Fig. 2.10. In this sample, a $\frac{2}{3}\frac{h}{e^2}$ plateau appears at charge neutrality between 1 and 3 T (see Fig. 2.14.A and Fig. 2.14.C) consistent with the expected value for helical edge transport given the contact configuration. At higher magnetic fields, the resistance departs from its expected value and increases with B. In the field range where helical edge transport is observed, a change of the contact configuration results in a change of the resistance measured at CNP which displays a value consistent with helical edge transport as shown in Fig. 2.14.D.

BNGrSTO-05 sample

Fig. 2.15 presents two-terminal transport measurements performed in BNGrSTO-05 sample in a similar fashion than Fig. 2.10. A $\frac{3}{4}\frac{h}{e^2}$ resistance plateau appears at charge neutrality between 1 and 2.6 T (Fig. 2.15.B. and Fig. 2.15.C) as expected for helical edge transport given the contact configuration considered.

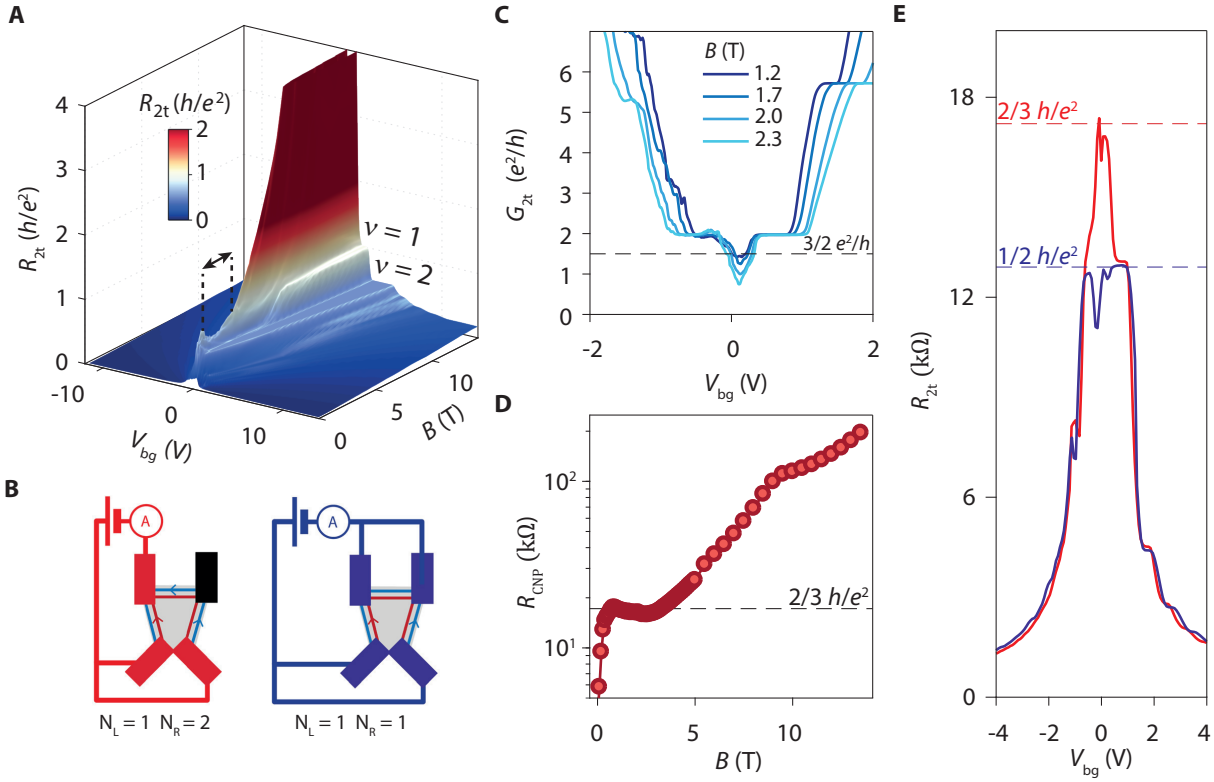

FIGURE 2.14: **Evidence of helical edge transport in BNGrSTO-04 sample.** **A**, Evolution of the two-terminal resistance R_{2t} with back-gate voltage V_{bg} and magnetic field B at 4 K (red contact configuration in B). On top of the standard $\nu = 1$, 2 plateaus, an anomalous quantized $\frac{2h}{3e^2}$ resistance plateau arises at CNP between 1 and 3 T (delimited by the dashed lines). **B**, Contact configurations studied. A, C, and D, are obtained in the configuration depicted in red. **C**, Two-terminal conductance G_{2t} versus V_{bg} extracted from A for different magnetic fields. G_{2t} displays $\pm\frac{2e^2}{h}$ and $\frac{6e^2}{h}$ plateaus characteristic of graphene QH effect and reaches approximately $\frac{3e^2}{2h}$ at CNP, consistent with the value expected for helical edge transport (dashed line). **D**, Resistance at CNP versus B extracted from A evidencing the presence of a $\frac{3e^2}{2h}$ resistance plateau between 1 T and 3 T. At higher magnetic fields, R_{2t} increases with the magnetic field almost exponentially with B but remains below 200 kΩ at 14 T. **E**, Evolution of R_{2t} with V_{bg} for the two contact configurations depicted in B. At CNP, the resistances reach the values expected for helical edge transport in both cases.

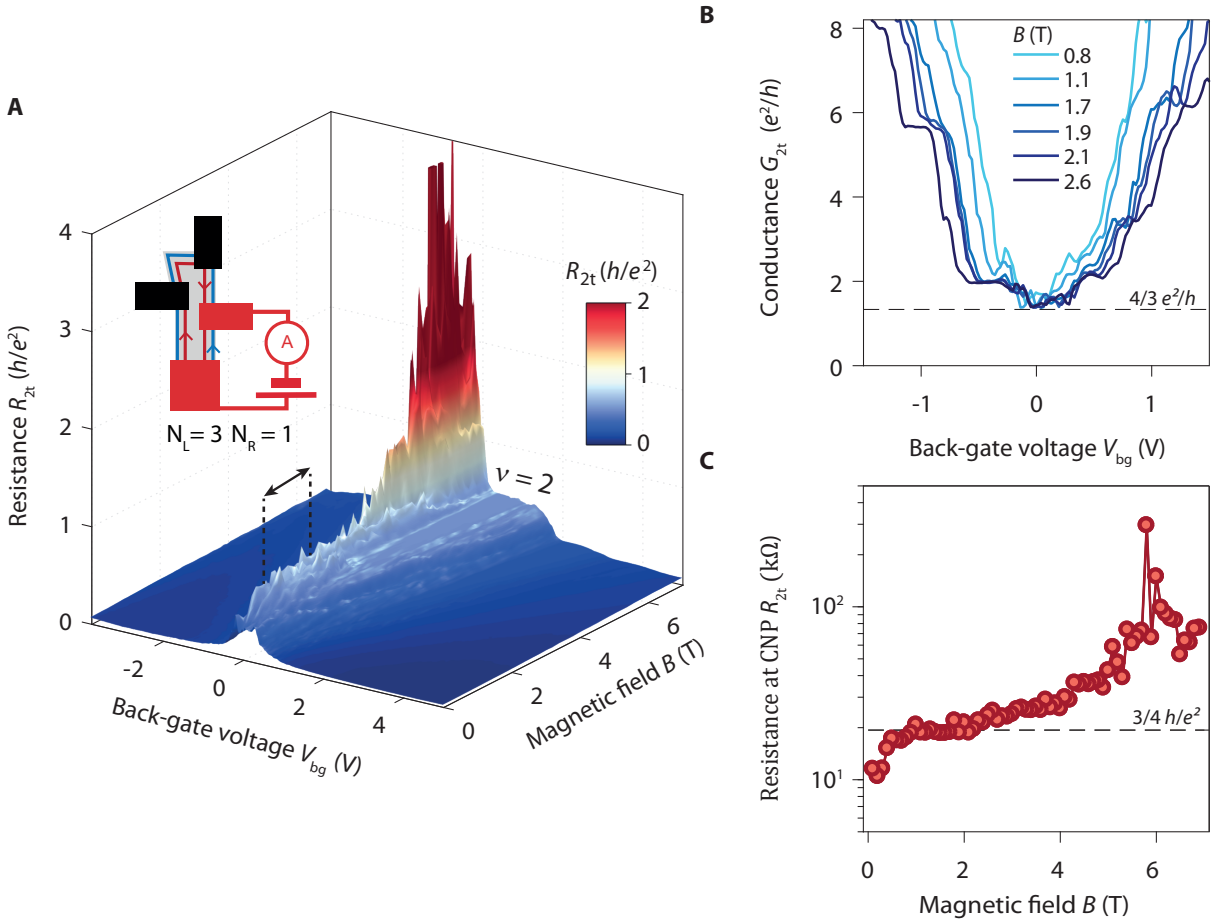

FIGURE 2.15: **Evidence of helical edge transport in BNGrSTO-05 sample.** **A**, Evolution of the two-terminal resistance R_{2t} with back-gate voltage V_{bg} and magnetic field B at 4 K. On top of the $\nu = 2$ plateau, an anomalous quantized $\frac{3h}{4e^2}$ resistance plateau arises at CNP between 1 and 2.5 T (delimited by the dashed lines). Inset: Contact configuration considered. **B**, Two-terminal conductance G_{2t} versus V_{bg} extracted from A for different magnetic fields. The conductance displays plateaus at $\pm\frac{2e^2}{h}$ and $-\frac{6e^2}{h}$ characteristic of graphene QH effect and reaches approximately $\frac{4e^2}{3h}$ at CNP consistent with the value expected for helical edge transport (dashed line). **C**, Resistance at CNP versus magnetic field extracted from A evidencing the presence of a resistance plateau between 1 T and 2.5 T consistent with the value expected for the helical edge transport (dashed line). At higher magnetic fields, R_{2t} increases with B almost exponentially with the magnetic field but remains below 300 kΩ at 14 T.

BNGrSTOVH-03a sample

Fig. 2.16 presents the evolution of the two-terminal resistance R_{2t} with B and V_{bg} for a given contact configuration (depicted in inset). Contrary to previous data, the measurements presented were performed in dilution fridge at a temperature of 70 mK and with an ac-voltage excitation of 100 μV.

In this sample, a finite conductance plateau of approximately $\frac{2e^2}{3h}$ appears at charge neutrality point between 2.5 and 7 T marking the formation of the helical phase. Above 7 T, the resistance increases exponentially with the magnetic field up to about 10 MΩ at 14 T. Note that the resistance measured at high magnetic fields is larger than in previous measurements because of the lower temperature during the measurements.

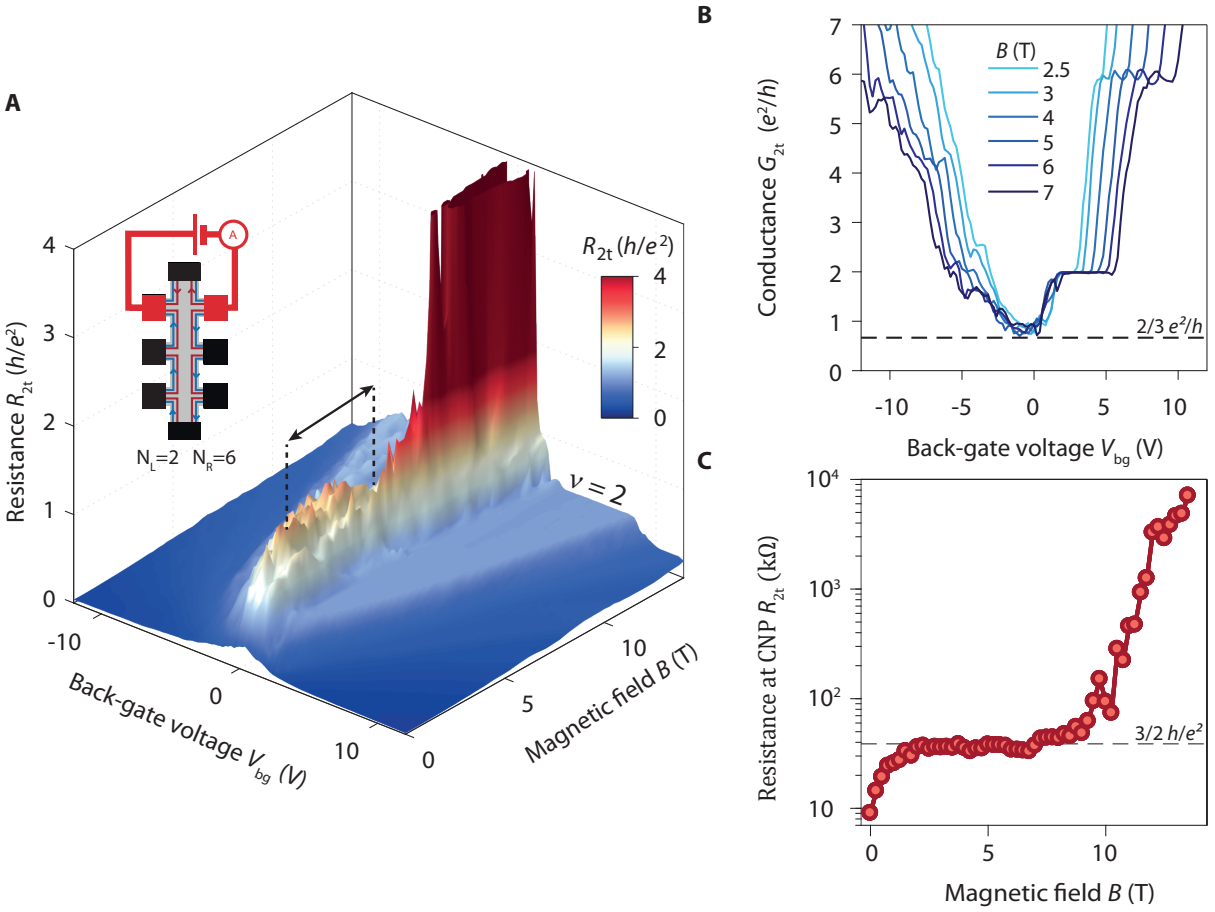

FIGURE 2.16: **Evidence of helical edge transport in BNGrSTOVH-03a sample. A**, Evolution of the two-terminal resistance R_{2t} with back-gate voltage V_{bg} and magnetic field B at 70 mK. A finite resistance plateau, indicated by the dashed line, arises at CNP between 2.5 and 7 T with a value close to $\frac{3h}{2e^2}$ the expected value helical edge transport. Inset: Contact configuration considered. **B**, Two-terminal conductance G_{2t} (after subtraction of wire resistance) versus V_{bg} extracted from A for different magnetic fields. G_{2t} displays $\pm\frac{2e^2}{h}$ and $\pm\frac{6e^2}{h}$ plateaus characteristic of graphene QH effect and shows a $\frac{2e^2}{3h}$ plateau at CNP consistent with the value expected for helical edge transport (dashed line). **C**, Resistance at CNP versus B extracted from A evidencing the presence of a resistance plateau between 2.5 T and 7 T consistent with the value expected for the helical edge transport (dashed line). At higher magnetic fields, R_{2t} increases with B exponentially.

The observation of helical edge transport signatures in these measurements provide us further information. Considering the voltage excitation used and the temperature, we should be able to resolve edge gaps of about 1 K. This is much smaller than the reduced Coulomb energy scale in this sample that is already $\epsilon_C^* \approx 27$ K at 2.5 T. Thus, we can reasonably assume that the exchange gap at $\nu = 0$ is larger than 1 K for $B > 2.5$ T. In this regard, the helical edge transport signatures observed can hardly be attributed to an activated transport at the edges of a CAF phase. It would imply that the edge gap would be smaller than 1 K even at 7 T and hence that the CAF phase would be very close to the transition. This is rather unlikely.

Likewise, one may argue that we could not resolve the edge gap because the sample would have a high amount of disorder in the sample. This hypothesis seems unlikely considering its mobility and the fact that we observe signatures of broken symmetry states at $\nu = 1,\ 3,\ 4$ at 14 T in this sample as shown in Fig. 2.17.

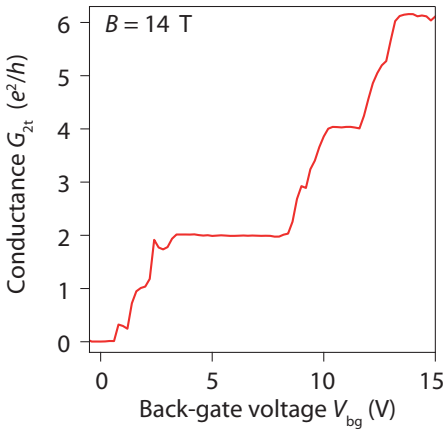

FIGURE 2.17: **Broken symmetry states in BNGrSTOVH-03a at 14 T.** Broken symmetry states develop at $\nu = 1,\ 3,\ 4$ and potentially at $\nu = 5$ in the sample consistent with its mobility.

BNGrSTOVH-02 sample

Finally, Fig. 2.18 presents the evolution of the two-terminal resistance measured at charge neutrality in BNGrSTOVH-02 sample for measurements performed at 1.5 T with different contact configurations.

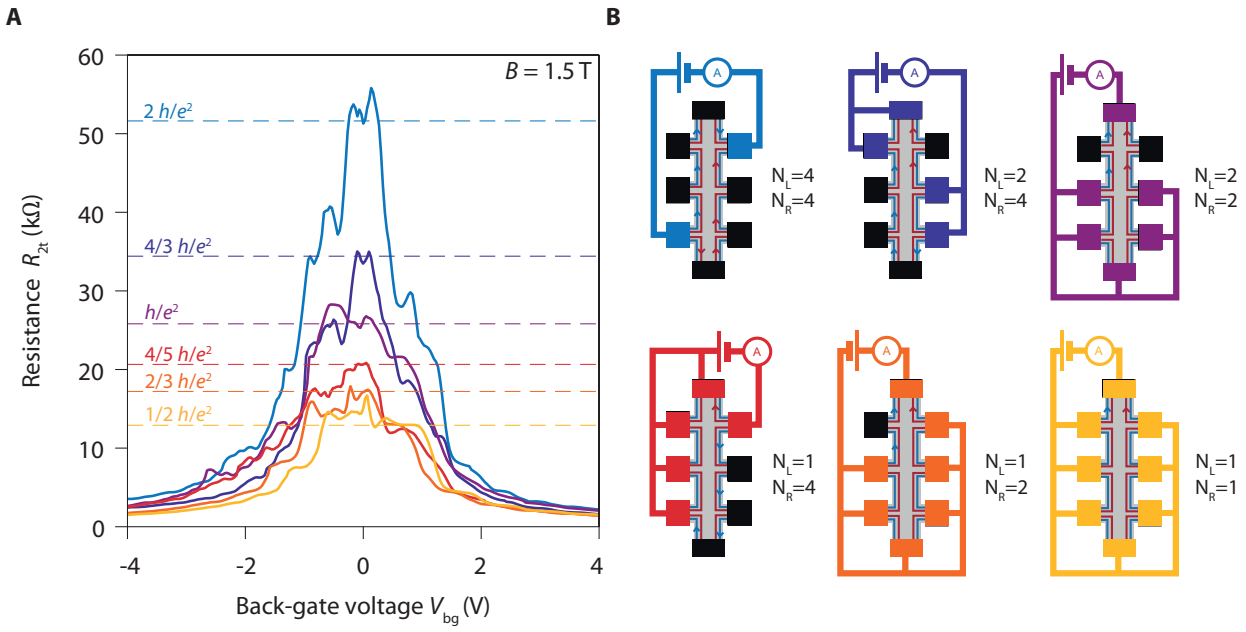

FIGURE 2.18: **Evidence of helical edge transport in BNGrSTOVH-02 sample. A**, Evolution of the two-terminal resistances R_{2t} with back-gate voltage V_{bg} at 1.5 T for different contact configurations. At CNP, R_{2t} reaches the values expected for helical edge transport, indicated by coloured dashed lines, in all the displayed configurations. **B**, Schematics of the contact configurations. Black contacts are floating. The red and blue arrows on the helical edge channels indicate the direction of the current between contacts, and A indicates the ampmeter. N_L and N_R indicate the numbers of helical edge sections between the source and drain contacts respectively on the left and the right edge of the device.

For the six configurations presented, the resistance at charge neutrality reaches the value expected for helical edge transport. Contrary to the samples presented above, this device was etch-defined such that the graphene edges are not pristine. It shows that the edge roughness induced by the plasma etching does not hinder the appearance of the helical edge transport regime.

2.4 Evidencing the origin of the helical quantum Hall phase

As demonstrated above, in graphene samples on $SrTiO_3$ substrate with thin bottom h-BN, a clear helical edge transport regime arises in the quantum Hall regime and at charge neutrality. The observation of this specific transport regime unambiguously points towards the formation of a F ground state at $\nu = 0$ in this type of device. Yet, one may still wander if indeed it arises because the substrate provides a strong screening or because of a different effect. To discard this second possibility, we must investigate the importance of the screening. Also one must verify that the ground state is gapped in the bulk as expected for the F phase.

2.4.1 Key role of the substrate screening

To check that the helical edge transport arises because of the screening provided by the $SrTiO_3$ substrate, we purposely fabricated a sample, BNGrSTO-09 with a 61 nm thick h-BN spacer substrate. With such a thick bottom h-BN, the distance between the graphene and the substrate is too far from the latter to provide a significant screening ($l_B \geqslant 60$ nm when $B \leqslant 0.18$ T) such that the Coulomb energy is not reduced as shown in Fig. 2.3.

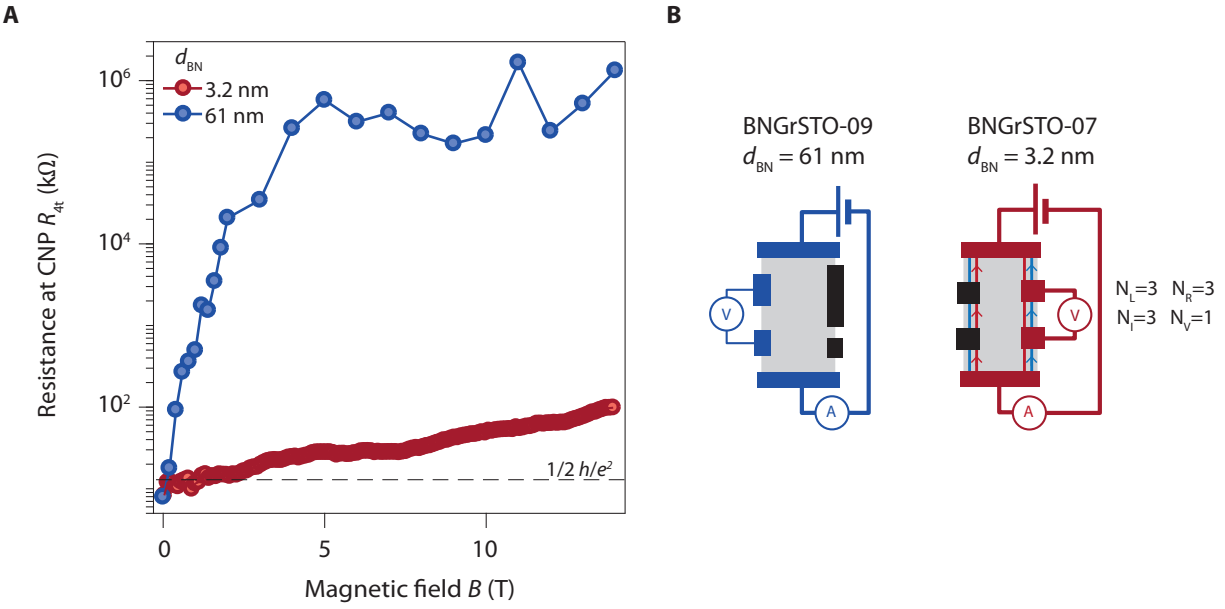

FIGURE 2.19: **Influence of bottom h-BN thickness on the substrate screening. A**, Evolution of the four-terminal resistance R_{4t} at CNP with B in samples with two very different bottom h-BN thicknesses d_{BN}. BNGrSTO-07 have a thin bottom h-BN and exhibits a resistance plateau (dashed line) at intermediate magnetic fields consistent with a helical edge transport. It departs to a weak insulating phase at higher fields. In contrast, BNGrSTO-09, which have a thick h-BN, displays a very strong insulating phase even at low/intermediate magnetic fields. Note that above 5 T, we have a saturation as we reach the noise level of our current amplifier. **B**, Contact configurations considered for both samples.

The evolution of the four-terminal longitudinal resistance in this sample is displayed in Fig. 2.19 as well as the evolution of the resistance for a similar configuration in sample BNGrSTO-07. Contrary to the samples with thin bottom h-BN, in BNGrSTO-09 sample, the resistance diverges very rapidly the B and exceeds 100 kΩ above 1 T. It marks the formation of a strong insulating phase which develops with the magnetic field as already reported in other measurement performed in high mobility devices on SiO_2. Above 4 T, the resistance saturates above 100 MΩ because of the noise level of the current amplifier. These stark differences show that the insulating phases developing in each case are fundamentally different. These two samples must have different ground states at $\nu = 0$ one being insulating at the edges, the other being the F phase which displays a helical edge transport. It clearly shows that the substrate screening of Coulomb interactions is indeed at the origin of the formation of the helical quantum Hall phase.

2.4.2 Existence of a bulk gap

To complement previous experiments, it is necessary to probe the existence of bulk gap at CNP in the helical regime. For this purpose, the devices with a Hall-bar like geometry are not suitable since the bulk is short-circuited by the edge channels. We thus fabricated a device with a Corbino geometry following ref. [93, 94], where the graphene is contacted in the middle of the flake allowing to probe only bulk transport and to get rid of any contribution from the edges.

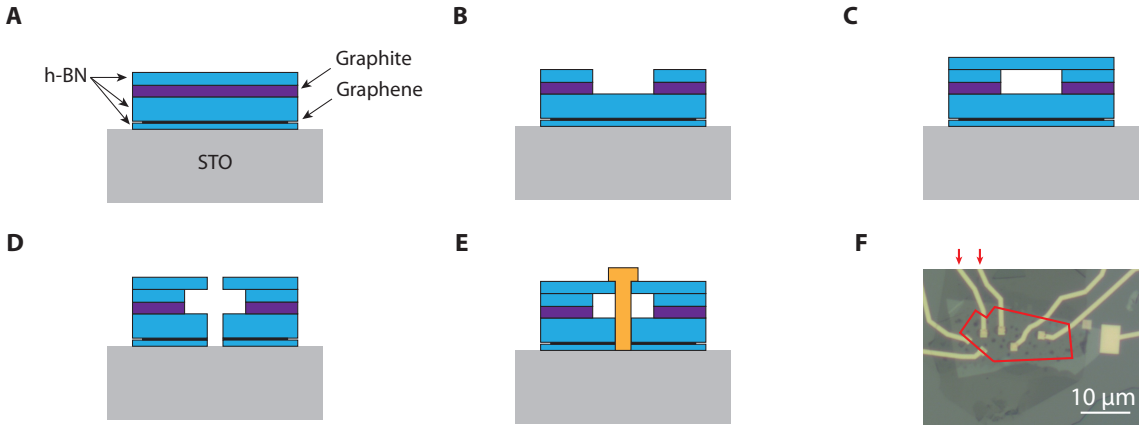

FIGURE 2.20: **Fabrication of a device with Corbino geometry on $SrTiO_3$ subsrate. A**, Initial Van der Waals heterostructure. **B**, Etching of large holes in the top h-BN/graphite flakes. **C**, Deposition of an additional h-BN flake. **D**, Etching of smaller holes, down to the bottom h-BN, in the center of the first set of holes. **E**, Deposition of a Cr/Au bilayer to make contacts with graphene. **F**, Optical image of a Corbino device studied in Fig. 2.21 (two-terminal measurements are performed between contacts denoted by red arrows). Graphene edges are indicated by the red line.

The fabrication of such sample is presented in Fig. 2.20. First, a thin h-BN/graphene/h-BN heterostructure is first placed on $SrTiO_3$ substrate and then covered by an additional graphite/h-BN layer (Fig. 2.20.A). The latter graphite flake is used as a screening layer and allows to get rid of the local doping induced by the deposition of metal on the capping h-BN. Without this layer, the graphene doping below the contact lines connected to the inner contacts would be different from the rest of the flake. It would result in the formation of pn or nn' junctions and thus some QH edge channels would connect the graphene edges to the inner contact. A serie of holes are then etched in the top h-BN and the graphite layer at positions where the graphene will be contacted (Fig. 2.20.B). Another h-BN flake is deposited on top of the etched heterostructure (Fig. 2.20.C) and a second set of holes, with a smaller radius, is then etched in the overall heterostructure, down to the bottom h-BN, exactly at the same position than the first set. (Fig. 2.20.D). Finally, a Cr/Au

bilayer is deposited in the small holes to make one-dimensional contacts (Fig. 2.20.E). The prior etching of the graphite/h-BN layer into larger holes prevents from having connections between the graphite and the graphene flakes. An optical image of the device fabricated following this process is presented in Fig. 2.20.F.

Measurements of the two-terminal resistance with B and V_{bg} in this device are shown on Fig. 2.21 in form of a Landau fan diagram. They were performed between both contacts denoted with red arrows in Fig. 2.20.F.

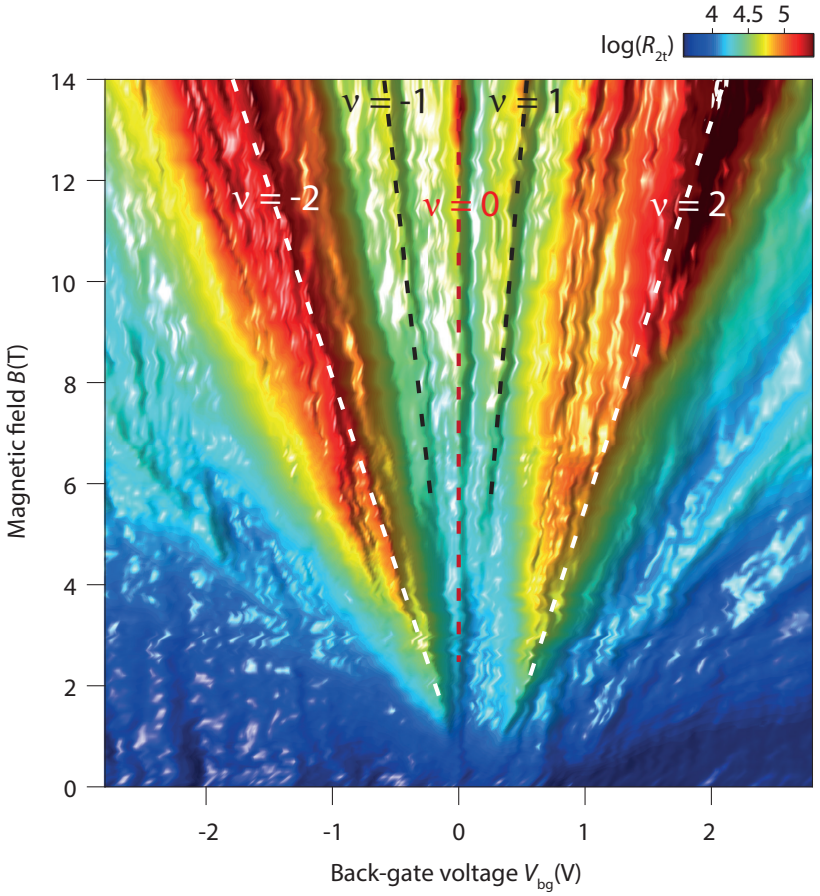

FIGURE 2.21: **Transport in Corbino geometry.** Evolution of the two-terminal resistance R_{2t} in the Corbino device shown in Fig. 2.20.F measured between the contacts marked with red arrows. Two main resistance peaks (white dashed lines), indicative of the gap opening at $\nu = \pm 2$, appear starting from 1.5 T. An additional central peak (red dashed line) is observed and indicates the presence of a bulk gap at $\nu = 0$ in the field range where the helical edge transport is observed. Above 5 T, the gaps corresponding to the $\nu = \pm 1$ broken symmetry states also open.

We observe the emergence of two main insulating peaks dispersing with magnetic field starting from approximately 1.5 T. In a Corbino geometry, the resistance peaks mark the opening of gaps in the density of states between Landau levels or broken symmetry states. Thus the two main insulating peaks, which disperse in opposite gate direction, can be easily identified as the opening of the cyclotron gaps between $N = 0$ and $N = \pm 1$ Landau levels (filling factors $\nu = \pm 2$). Between these two peaks, a central peak also emerges above 1.5 T and it does not disperse with the magnetic field. This peak marks the opening of a gap at $\nu = 0$. Finally, two additional satellite peaks, dispersing with B, also appear above 5 T between $\nu = \pm 2$ and $\nu = 0$ states. They correspond respectively to the broken symmetry states at $\nu = \pm 1$.

Importantly, we note that the gap at $\nu = 0$ appears at similar magnetic field than the helical edge transport plateaus in the other samples and it does not close when the magnetic field is increased. It shows that in the helical regime, the charge transport only occurs at the edges and not in the bulk of the graphene flake. It reinforces the demonstration that the $\nu = 0$ ground state in our screened graphene devices on $SrTiO_3$ is indeed the F phase gapped in the bulk and gapless at the edge.

2.5 Robustness of the helical edge transport

We now investigate the robustness of the helical phase against the magnetic field and the temperature and discuss its breakdown at high magnetic fields or temperatures.

2.5.1 Phase diagram of helical edge transport

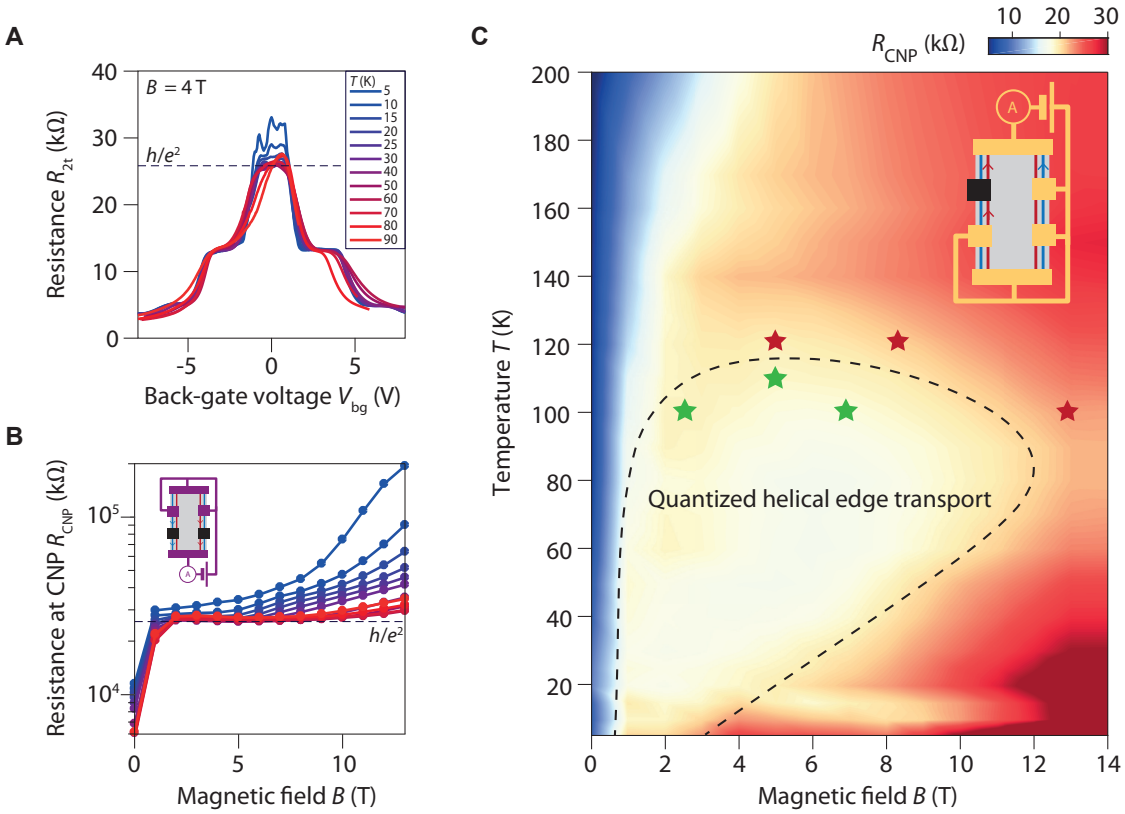

FIGURE 2.22: **Phase diagram of quantized helical edge transport regime in BNGrSTO-07 sample. A**, Two-terminal resistance R_{2t} versus back-gate voltage V_{bg} measured at various temperatures and a magnetic field of $B = 4$ T. Note that the back-gate voltage is renormalized using the position of the $\nu = \pm 2$ plateaus to compensate the temperature-dependence of the substrate dielectric constant. **B**, Two-terminal resistance at CNP, R_{CNP}, for the same data as in A. Inset: Contact configuration used for data in A and B figures. **C**, Two-terminal resistance R_{CNP} at the CNP versus magnetic field B and temperature T for the contact configuration shown in the inset. The resistance reaches the value expected for helical edge transport $\frac{2e^2}{3h}$ over a large range of temperatures and magnetic fields. The stars indicate the points of the phase diagram where R_{CNP} has been checked by measuring different contact configurations. The green stars indicate when R_{CNP} is matching the quantized helical edge transport value while the red stars indicate that R_{CNP} does not match the expected value (see Fig. 2.23). The dashed curve is a guide for the eyes showing the approximate limits of the regime of helical edge transport.

We studied the evolution of the quantized resistance at CNP with respect to both the temperature T and the magnetic field B in BNGrSTO-07 sample. Two relevant examples are given in Fig. 2.22.A and Fig. 2.22.B. At fixed magnetic field $B = 4$ T, the resistance at CNP remains close to the expected value for helical edge transport on a very large of temperature from 5 to 90 K as shown in Fig. 2.22.A. More surprisingly, when the temperature is increased, the resistance at CNP departs from its expected value towards insulation at higher magnetic fields and even survives up to 10 T at 90 K.

Similarly, Fig. 2.22.C shows the evolution of the two-terminal resistance at CNP over both large temperature and field ranges for another contact configuration. R_{CNP} retains its expected value over a wide range of temperature and magnetic field delimited approximately by the black dashed line. To ascertain this boundary, the value of the two-terminal resistance was checked at different points of the phase diagram indicated by stars. In the helical edge transport region (green stars), the resistance at CNP reaches its expected helical value for the three different contact configurations investigated while outside it (red stars) R_{CNP} is above the value expected for helical transport as shown in Fig. 2.23.

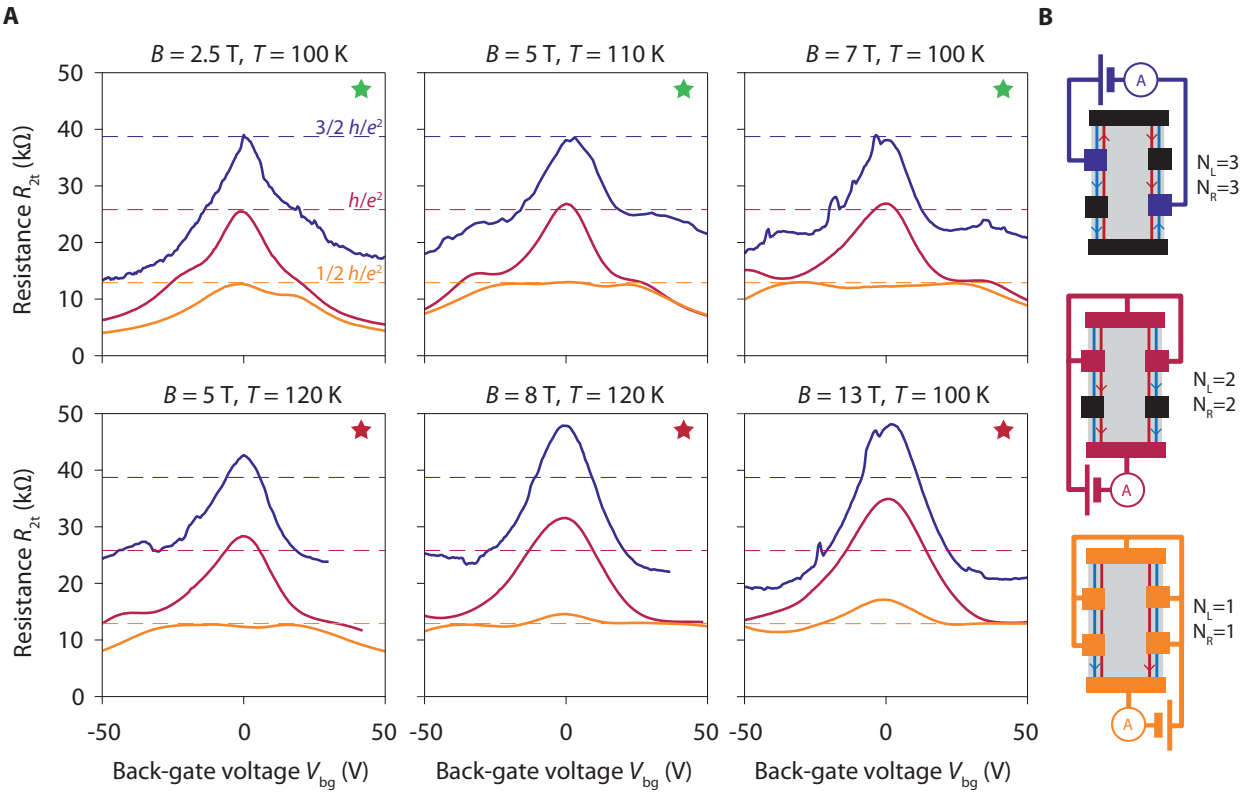

FIGURE 2.23: **Resistance at CNP at the boundary of the helical transport regime**. **A**, Two-terminal resistance R_{CNP} at charge neutrality for different points of the (B, T) phase diagram (stars in Fig. 2.22.C) nearby the boundary of the region where quantized helical edge transport is observed. In the helical regime (green stars), R_{CNP} reaches its expected helical values for the different configurations considered (dashed lines) whereas outside this region (red stars) R_{CNP} is notably above the expected value. **B**, Corresponding contact configurations.

Above 110 K, the quantization of the helical edge transport is no longer observed. We can therefore infere that helical edge states retain their topological protection against backscattering over 1.1 μm (edge section's length in the device studied) at 110 K and thus over longer distances at lower temperatures. The helical edge transport regime is particularly robust especially compared to the one observed in standard topological insulator. For examples, in HgTe/CdHgTe quantum

wells, the helical edge transport was observed in micron long distance but at temperatures of only a few Kelvins [56] while in WTe_2, quantum spin Hall transport signatures were observed up to 100 K but only over 100 nm distances [58]. The helical quantum Hall phase in graphene seems to have a much longer inelastic scattering length than the ones measured in time-reversal symmetric topological insulator.

The breakdown of the quantized helical edge transport with the temperature increase cannot be attributed to the lowering of the $SrTiO_3$ dielectric constant. Indeed, the latter remains sufficiently high, $\epsilon_{STO} \sim 10^3$ above 100 K [82], such that the screening provided by the substrate is only weakly affected in samples with thin h-BN (see Fig. 2.2). Thermal activation of bulk charge carriers can also be discarded as it would lead to a decrease of the resistance at CNP with increasing temperatures contrary to what we observe experimentally. Therefore, the helical transport regime most likely breaks at high temperatures due to an activation of inelastic processes.

A possible explanation might be provided by the work of J. L. Lado and J. Fernández-Rossier. In ref. [95], they numerically investigate the spatial evolution of the magnetic properties of the AF/CAF/F phases in finite size samples with both armchair and zigzag edges. According to them, there are some localized magnetic moments at graphene zigzag edges which result from the presence of the surfaces states. They found these local spin moments can induce spin-mixing and that they can generate inelastic backscattering of the helical edge channels depending on their orientations. At higher temperatures, we expect these spin moments to fluctuate which would enhance their effect on the backscattering. Such scenario would explain the dependence observed experimentally and could be relevant as a graphene edge is composed of several patches of zigzag terminations.

2.5.2 Breakdown of helical edge transport with magnetic field

In Fig. 2.22.C, it is worth inspecting at the boundaries of the helical edge transport regime with the magnetic field. The low field limit is virtually constant with the temperature ($B \approx 0.7$ T) and is most probably fixed by the mobility of the sample that limits the observability of the $\nu = 0$ broken symmetry state [37]. On the other hand, the high field limit shows a rather unexpected behaviour as it increases linearly with T.

This second trend is confirmed when studying the evolution of resistance at charge neutrality away from helical edge transport regime in BNGrSTOVH-02 sample. Fig 2.24.A displays the Arrhenius plots of the four-terminal resistance of the device for different magnetic fields. For $1 < B \leq 6$ T the device exhibits helical edge transport signatures and R_{CNP} stays constant with both B and the temperature between 4.2 and 7.1 K (a temperature range where ϵ_{STO} is almost constant). For $B \gtrsim 6$ T, the sample is outside the helical regime and R_{CNP} shows an activated temperature dependence. The activation gaps Δ, computed from these plots, evolves linearly with B as displayed in Fig. 2.25. Such scaling is consistent with the behaviour observed in the previous phase diagram.

This linear dependence differs from the theoretical expectations which predict that the charge activation gap is set by the Coulomb energy and scales as $\sqrt{B}$ [18]. This last scaling is actually recovered rather quantitatively when similar measurements are performed on sample BNGrSTO-09 which has a thick bottom h-BN. In this case, the activation gap, calculated from Ahrrenius plots in Fig 2.24.B, shows a clear $\sqrt{B}$ dependence which can be fitted with a disorder-free activation gap $\Delta^* \approx 0.4\,\epsilon_C$ consistent with an activation energy set by the long-range Coulomb interaction.

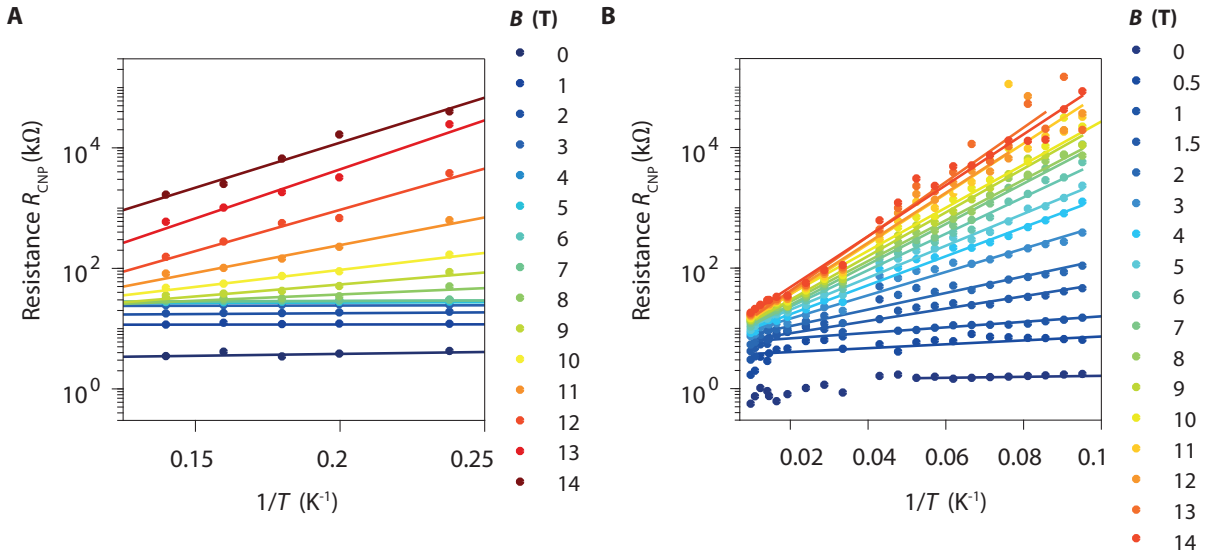

FIGURE 2.24: **Arrhenius plots at CNP in two types of devices on $SrTiO_3$.** Evolution of the four-terminal longitudinal resistance at the charge neutrality R_{CNP} versus inverse temperature $1/T$ for different magnetic field values. Arrhenius plots are respectively measured for sample BNGrSTOVH-02 in **A** and for sample BNGrSTO-09 in **B**. The first has a thin bottom h-BN and displays helical edge transport at intermediate magnetic fields. The latter has a thick bottom h-BN and shows a strongly insulating behaviour (see Fig. 2.19). Note that measurements in A were performed on a temperature range where the dielectric constant of the substrate is almost constant.

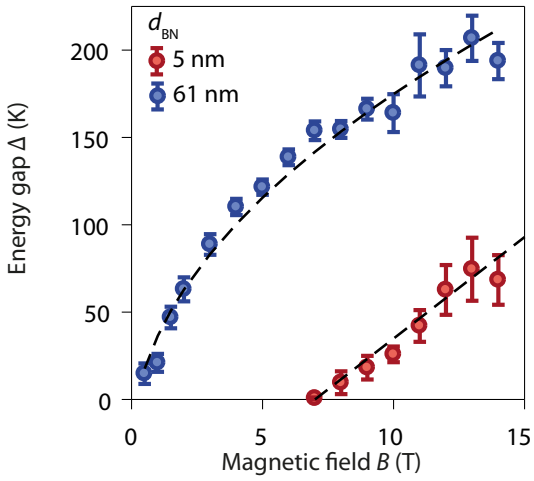

FIGURE 2.25: **Evolution of intercation-induced opening with magnetic field.** Activation energy gap Δ extracted from Ahrrenius plot presented in Fig. 2.24 for the two samples with different bottom h-BN thickness d_{BN}. The sample with a thick bottom h-BN (blue dots) shows an activation energy which scales as $\sqrt{B}$ while the sample with a thin bottom h-BN shows an activation energy scaling linearly with B outside the helical edge transport regime translating the opening of an edge gap. Dashed lines are respectively fits of the linear and of the $\alpha\sqrt{B} - \Gamma$ dependence. The fitted parameter $\alpha = 64$ K.T$^{-1/2}$ correspond to a disorder-free activation energy gap $\Delta^* \simeq 0.4\,\epsilon_C$ consistent with an activation energy set by the long-range Coulomb interaction. The intercept $\Gamma = 28$ K gives an estimation the disorder-broadening of Landau levels.

The breakdown of the helical edge transport could originate from an opening of a gap in the edge excitation similar to that happening at the CAF/F transition. Different scenarios can explain such opening. First, it may arises from a phase transition from the F phase to another ground $\nu = 0$ ground states especially the CAF phase [61]. It may occur because the substrate screening is less efficient at higher magnetic fields as l_B decreases. Such a transition should occur without the closure of the bulk gap [36]. It is consistent to what we observe in devices with a Corbino geometry (see Fig. 2.21) where the $\nu = 0$ bulk gap emerges at 1.5 T and remains visible up to 14 T. Likewise, the interactions terms breaking U(1) symmetry can drive a phase transition from the F phase to phases with gapped edge excitations while increasing the magnetic field [74].

Other scenarios involving helical Luttinger nature [27] of the gapless edge modes of the F phase may also be envisioned. Tikhonov and coworkers indeed demonstrated that the coupling between the helical edge modes and the 2D bulk spin waves may lead to some backscattering [71]. Similarly, Huang and Cazalilla found that the combination of disorder and electron-electron interactions in the helical edge channels can lead to their backscattering [96]. One can also speculate, by analogy with predictions made for 2D topological insulators, that the enhancement of electron-electron interactions with the magnetic field may lead to the emergence of two-particles backscattering processes [51, 97]. Further investigations are needed to understand the underlying mechanisms behind the breakdown of the helical phase with the magnetic field.

2.6 Conclusion

In this chapter, we have demonstrated that the helical edge transport in charge neutral graphene under perpendicular magnetic field can be favoured by using a $SrTiO_3$ high-k dielectric substrate. Provided the bottom h-BN is thin enough, it allows to reduce significantly the Coulomb interactions within the graphene flake and restore the predominance of the spin splitting over the valley splitting in the graphene QHF at $\nu = 0$. Such strategy allows to fabricate graphene heterostructures exhibiting a robust helical edge transport at low-intermediate magnetic fields up to 110 K and over micron long distances.

This helical quantum Hall phase is particularly promising further applications as well as fundamental research. Efforts to couple it to superconductivity in the prospect of investigating Majorana zero-energy modes physics are under way [98]. On the other hand, the substrate engineering strategy presented here offers new opportunities to tune electronic interactions in Van der Waals heterostructures and provides a tool to study a wealth of physics phenomena in such systems.

Part II

Quantum Hall Fabry-Pérot interferometry in high mobility graphene devices

Chapter 3

Probing anyon physics with quantum Hall Fabry-Pérot interferometers

Contents

The major part of this PhD work was dedicated to the experimental study of QH Fabry-Pérot (FP) interferometer in high mobility graphene heterostructures. In this introduction chapter, we focus on these devices and explain how QH FP interferometers allow to probe the properties of the quasiparticles forming the QH edge channels.

We begin by discussing the specificities of anyonic quasiparticles emerging in the fractional regime. We then present the QH FP interferometers and we explain how the investigation of quantum interference in these devices enable to evidence the properties of anyonic quasiparticles. Afterwards, we make a review of past experimental and theoretical studies of such devices focussing on the consequences of charging effects. We then present recent achievements that led to major breakthroughs in the field. We conclude this chapter by discussing the possibility to perform QH interferometry in graphene heterostructures.

3.1 Anyons in the fractional quantum Hall effect

In this section, we present a specific type of quasiparticles called anyons, which emerge in the fractional regime. A very recent review on the subject can be found in ref. [99].

3.1.1 Concept of anyons

In quantum mechanics it is usually said that there are only two types of particles with different statistics namely the bosons and the fermions. The above assumption is valid in 3D system whereas in 2D systems it exists some quasiparticles whose exchange statistics is neither bosonic nor fermionic [100]. These quasiparticles are called anyons [101].

The essence of anyons is readily captured with their unusual exchange statistics. In the simplest case, when two anyons are exchanged, their two-particles wavefunctions Ψ acquired a non trivial phase factor. It can be written as:

$$\Psi(\overrightarrow{r_2}, \overrightarrow{r_1}) = e^{i\theta}\Psi(\overrightarrow{r_1}, \overrightarrow{r_2}), \tag{3.1}$$

where $\overrightarrow{r_i}$ are the anyon positions and θ is the statistical phase. θ is different from 0 or $\pm\pi$ such that after a double exchange of the two anyons (two successive exchanges in the same direction of rotation), the wavefunction does not return to its original value contrary to what happens with bosons or fermions. Note that such a double exchange is equivalent to the rotation of one anyon around the other as depicted in Fig. 3.1, and it is usually referred as a braiding operation. In a system of several anyons with such statistics, the many-body wavefunction picks up a total phase of $e^{2iN\theta}$ when one anyon is moved along a close loop enclosing N other anyons. Likewise, the phase factor acquired after M successive braidings performed in the same direction is $e^{2iM\theta}$. It actually does not depend on the exact order followed to perform the braiding operations. Therefore, the anyons following such statistics are referred as **Abelian anyons**.

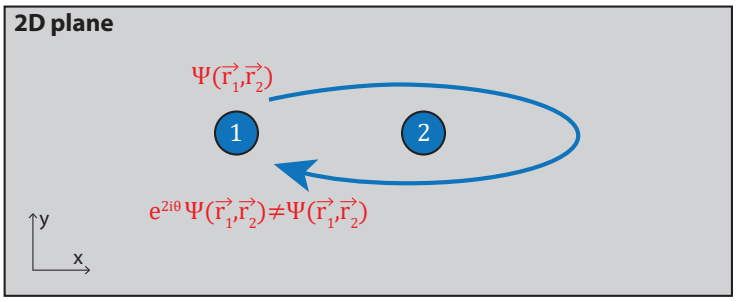

FIGURE 3.1: **Abelian anyonic statistics.** The braiding of one Abelian anyon around another leads to the appearance of a non trivial statistical phase in the two-particle wavefunction.

It also exists anyons with even more complex statistics: **the non-Abelian anyons**. In a system composed of non-Abelian anyons at given positions, there are several quasi-degenerate low-energy eigenstates possible for the system. The eigenstates form a Hilbert space [99, 102, 103]. Each braiding operation is associated with an unitary transformation within the Hilbert space (provided it is performed fast enough compared to the vanishingly small energy difference between eigenstates). These transformations can be different from simple multiplications of the many-body wavefunction by a phase factor and thus they do not necessarily commute with each others. That's why it is said that these anyons follow non-Abelian statistics.

These last anyons are particularly interesting for topological quantum computation [103, 104]. Indeed, as the quasi-degenerate eigenstates form a Hilbert space, one can encode information on the eigenstate taken by the system. The operations can then be performed by making braiding operations. Such system is intrinsically protected against decoherence because it undergoes a non-trivial evolution only when the anyons are braided. Likewise, it is protected against unitary errors

occurring while performing gate operations. Indeed, the braidings only depend on the topology of the quasiparticles trajectories and are insensitive to their exact geometry or the dynamic of the quasiparticles.

Evidencing the existence of such quasiparticles is thus of particular interest both for fundamental research and potentially for applied research on a long term perspective.

3.1.2 Emergence of anyons in the fractional quantum Hall effect

The transport signatures appearing in the fractional quantum Hall (FQH) regime cannot be explained in the non-interacting LL framework. Similarly to the QHF, they rather indicate the openings of interaction-induced gaps inside partially-filled LLs and the formation of highly correlated electronic phases. The lowest-energy excitations of these phases are expected to be anyons and supposed to carry fractional charges.

It was first suggested by R. Laughlin in 1983. In ref. [3], he studied the FQH phases developing at filling factors $\nu = \frac{1}{m}$, where m is an odd integer, and he proposed a many-body wavefunction to describe them. With numerical simulations, he demonstrated that this wavefunction was particularly relevant to describe the ground-state properties at such filling fractions. Thanks to that, he showed that these FQH phases are incompressible quantum fluids whose elementary excitations carry a fractional charge $-e^* = -\frac{e}{m}$. Following this work, Halperin together with Arovas and coworkers demonstrated that these fractionally charged quasiparticles are also Abelian anyons characterized by an exchange phase $\theta = \frac{\pi}{m}$ [4, 5]. These conclusions were then extended to many other odd-denominator fractions observed experimentally (see Fig. 3.2.A) [4, 5, 105–109].[1]

Few years after the observation of odd-denominator fractions [116], clear QH signatures were observed at $\nu = \frac{5}{2}$ in high mobility GaAs/AlGaAs heterostructures [117]. This state has raised a lot of interests because the first theoretical investigations [118] predicted that its low energy-excitations could be non-Abelian anyons usable for topological quantum computation [103, 119, 120]. Yet, the exact nature of this state still remains under debate. Likewise, other even-denominator states were observed in GaAs/AlGaAs heterostructures [121] and some of them can be non-Abelian states.

Therefore, probing the properties of FQH states is particularly relevant in order to investigate the physics of anyons.

3.1.3 Experimental evidence of anyons properties in the fractional QH regime

Theoretical investigations also demonstrated that FQH states support chiral gapless edge modes [124] which are similar to the IQH edge channels [125, 126]. The low-energy excitations of these edge modes are actually the fractionally charged anyons discussed above [127]. The existence of these edge channels gives rise to the quantized transport regime [128] but it also enables to probe the properties of the anyons via suitable transport measurements.

In particular, shot noise measurements performed with gate-tunable quantum point contacts (QPCs) [129] were early proposed as a way to probe the existence of fractional charges [130, 131]. These experiments were rapidly implemented in GaAs/AlGaAs heterostructures by two groups from Weizmann Institute and CEA-Saclay [132, 133]. They demonstrated that the FQH edge channels appearing at $\nu = \frac{1}{3}$ are indeed composed of quasiparticles with an effective charge $-e^* = -\frac{e}{3}$. Since that, similar experiments evidenced the existence of fractionally quasiparticles at different filling fractions, for instance, $-e^* = -\frac{e}{3}$ at $\nu = \frac{2}{3}$ [134], $-e^* = -\frac{e}{5}$ at $\nu = \frac{2}{5}$, $-e^* = -\frac{e}{7}$ at $\nu = \frac{3}{7}$ [135] and $-e^* = -\frac{e}{4}$ at $\nu = \frac{5}{2}$ [136]. Likewise, current noise measurements perfomed in more elaborated devices [137–139] were also proposed to probe the fractional statistics of anyons.

[1] The description of the different theories developed to describe the FQH effect (hierarchy theory [4, 110], composite fermions theory [111, 112], etc.) are beyond the scope of this manuscript. They are reviewed and explained for example in ref. [102, 113–115]. These references also discuss the case of the state developing at $\nu = \frac{5}{2}$.

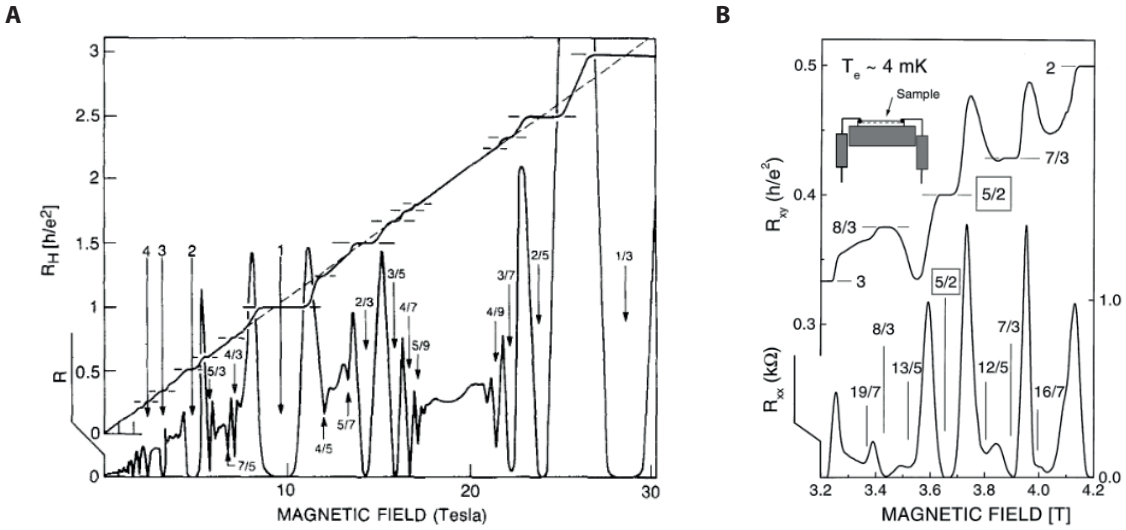

FIGURE 3.2: **Fractional quantum Hall effect in GaAs/AlGaAs heterostructures.** **A**, Typical signatures of FQH states measured GaAs/AlGaAs heterostructures. Many odd-denominator fractions are observed. Taken from ref. [122]. **B**, QH signatures at $\nu = \frac{5}{2}$. Taken from ref. [123].

One of these experiments was implemented recently by Bartolomei and coworkers providing a first direct measure of the $\frac{\pi}{3}$ exchange phase of Laughlin quasiparticles of the $\nu = \frac{1}{3}$ state [140].

On the other hand, the non-Abelian statistics of $\nu = \frac{5}{2}$ quasiparticles in GaAs heterostructures have also been probed indirectly via heat transport measurements by Banerjee and coworkers. In ref. [141], they measured the thermal conductance at filling factor $\nu = \frac{5}{2}$ and found that it was $\kappa \simeq 2.5\,\kappa_0 = 2.5\frac{\pi^2 k_B}{3h}$. According to the authors, such value, that is a half integer multiple value of the thermal conductance quantum κ_0, demonstrates the existence of Majorana modes at the edges of the $\nu = \frac{5}{2}$ state. They are expected to appear only in non-Abelian ground states.

In graphene, the proofs demonstrating the existence of fractionally charged anyons remain scarce most probably due to the difficulty to fabricate fully gate-tunable QPCs (see section 3.4.2). Yet, studying tunnelling in QH antidots, Mills and coworkers measured the charge of quasiparticles emerging at $\nu = \pm\frac{1}{3}$ and they found that is was approximately $-\frac{e}{3}$ [142].

Thus, there are already several evidence that quasiparticles developing in the FQH effect are anyons carrying fractional charges.

3.2 Quantum Hall Fabry-Pérot interferometers

In parallel to these approaches, Chamon, Freed, Kivelson, Sondhi and Wen proposed another strategy to study the properties of anyons appearing in the FQH regime [143]. It consists in studying quantum interference arising in a mesoscopic physics device called quantum Hall Fabry-Pérot (FP) interferometer which is the experimental system studied during this PhD work.

This section is devoted to QH FP interferometers. In the first part, we present the theory of QH FP interferometers and explain how they allow to probe the property of the quasiparticles forming the QH edge channels. In the second part, we make a review of both theoretical and experimental investigations of QH FP interferometry in GaAs/AlGaAs heterostructures.

3.2.1 A multiple path electronic interferometer

The QH FP interferometer proposed by Chamon and coworkers is schematized in Fig 3.3.A. It is composed of two sets of contacts (yellow) separated by a FP cavity formed by two quantum point contacts (QPCs) in series (red). The device is also equipped with a plunger gate which is placed between the two QPCs just along the edges of the 2DEG.[2] It can also have a back gate that enables to tune the charge carrier density in the device. Fig 3.3.B shows a real device, fabricated in GaAs/AlGaAs heterostructures by the Harvard group, illustrating the concept.

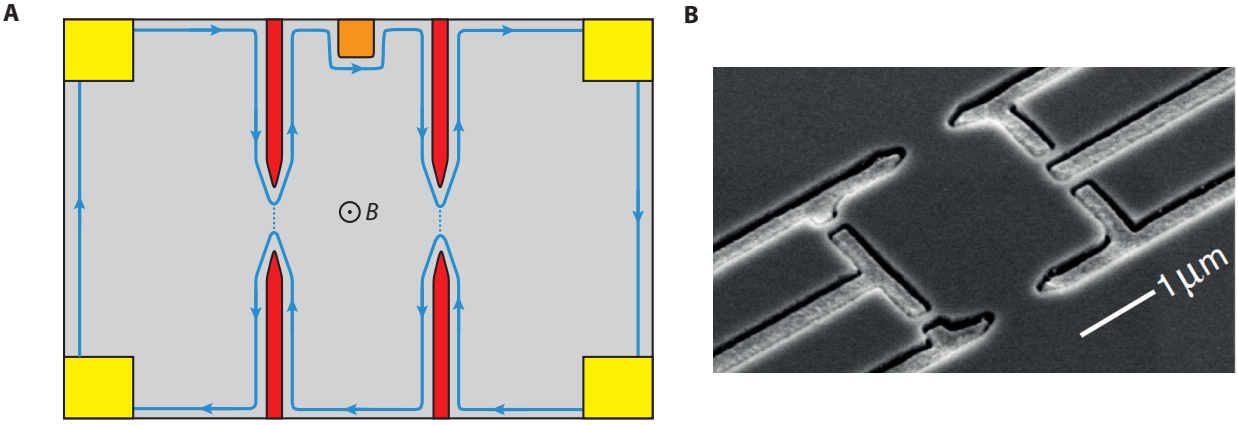

FIGURE 3.3: **Quantum Hall Fabry-Pérot interferometer.** **A**, Schematic of a QH FP interferometer. The contacts are coloured in yellow, the QPCs in red and the plunger gate in orange. The interfering electron edge channel (blue line) follow the edges of the 2DEG and the edges of the gates. It is partially reflected by the two QPCs and the quasiparticles can tunnel from one edge to the other (blue dotted line). **B**, Scanning electron micrograph of a QH FP interferometer fabricated in GaAs/AlGaAs heterostructures studied in Harvard group. Adapted from ref. [144].

The QPCs are defined by split gates deposited above the 2DEG. The resulting constriction in the 2DEG can be tuned by changing the voltage applied on the gate-electrodes [129]. In the QH regime [145], they act as tunable beamsplitters for the edge channels and they allow to tune the number of bulk edge channels passing through the constrictions. One can also adjust the transmission of a given edge channel by changing the voltage V_{QPC} applied on the gate electrodes to tune the potential/filling factor in the constriction [129]. An example is depicted in Fig. 3.4.

The two QPCs are in series and they partially reflect the same QH edge channel. As a result, the quasiparticles in this edge channel can follow different paths: they can either be transmitted directly through both QPCs or they can make one or several loop(s) inside the cavity before leaving it. The transmission of the device is then the result of the interference between these different trajectories. The QH FP interferometer, like its optical analogue, is therefore a multiple-path interferometer contrary to the QH Mach-Zehnder interferometer [146] which is a two-path interferometer.

The transmission of the QH FP interferometer T_{FP} was calculated by Chamon *et al.* within a non-interacting theory using the scattering matrix formalism [143]. It can be written as:

$$T_{\mathrm{FP}} = \frac{T_1 T_2}{1 + R_1 R_2 - 2\sqrt{R_1 R_2}\cos(\varphi)}, \tag{3.2}$$

[2]Such a plunger gate was actually absent in the original paper of Chamon and coworkers [143]. Instead, they propose to use a central gate placed above the bulk of the FP cavity that allows to deplete or accumulate locally charges in the bulk of the FP interferometer. The current devices mostly have plunger gates rather than central gates.

where T_i are the transmission coefficients of the QPCs, $R_i = 1 - T_i$ their reflection coefficients and where φ is the phase accumulated when the quasiparticles make a winding inside the cavity. In weak backscattering limit, that is $R_i \ll 1$, it simplifies to:

$$T_{FP} = 1 - R_1 - R_2 + 2\sqrt{R_1 R_2}\cos(\varphi). \tag{3.3}$$

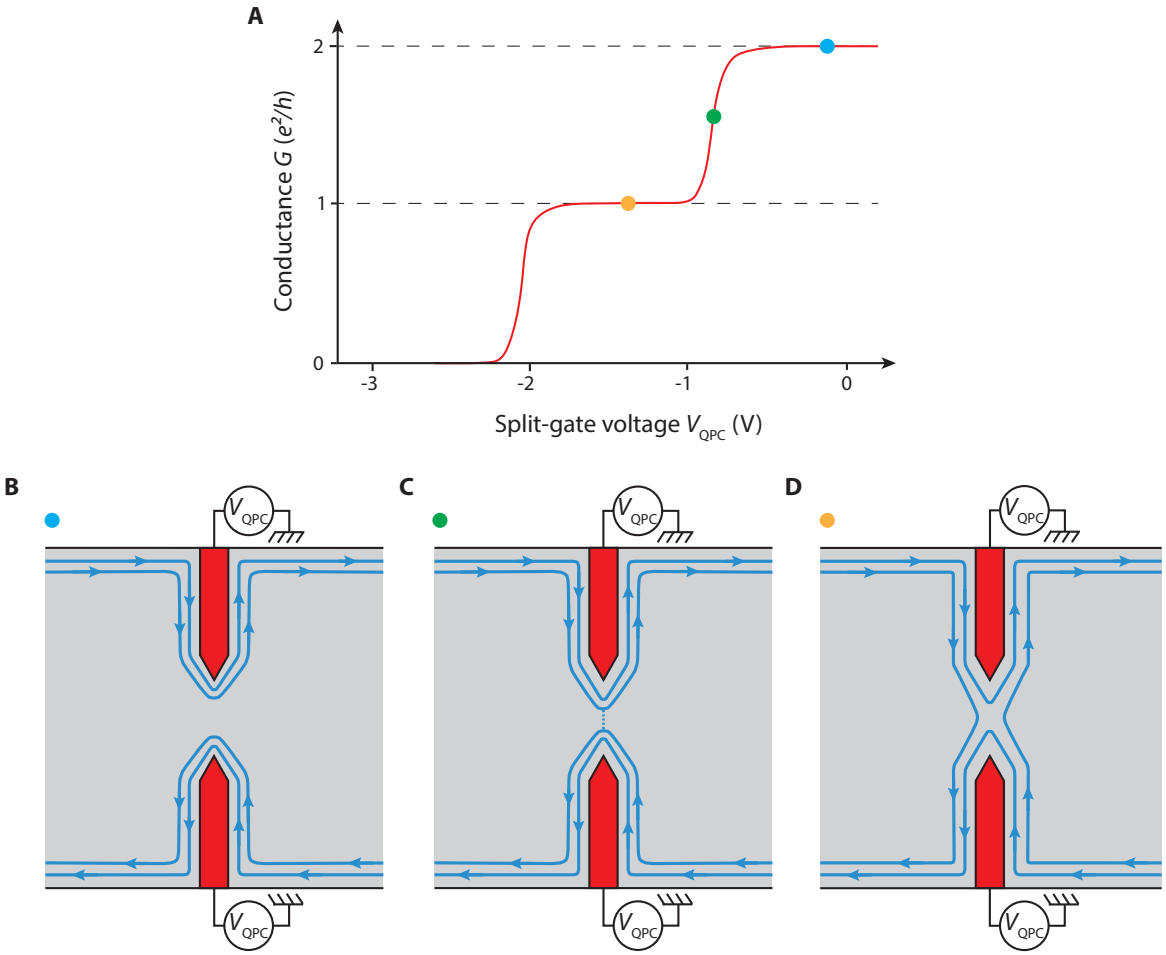

FIGURE 3.4: **Quantum point contact in the QH regime. A**, Evolution of conductance or equivalently of the edge channel transmission with the split-gate voltage $V_{QPC} < 0$ V. **B**, **C**, **D**, Edge channel configurations nearby the QPC for the three split-gate voltages indicated by the color dots on the transmission curve.

3.2.2 Aharonov-Bohm interference

The first effect at the origin of interference in the QH FP interferometer is the Aharonov-Bohm (AB) effect. Indeed, when quasiparticles make a loop inside the FP cavity, they accumulate an AB phase φ_{AB} because of the applied magnetic field B. This AB phase reads as:

$$\varphi_{AB} = \frac{2\pi\Phi}{\Phi_0^*} = \frac{2\pi BA}{\Phi_0^*}, \tag{3.4}$$

where $\Phi_0^* = \frac{h}{e^*}$ is the effective magnetic flux quantum experienced by the quasiparticles with effective charge $-e^*$ and A is the area enclosed by the trajectory of the interfering edge channel inside the FP cavity.

Experimentally, one can observe AB interference in FP interferometer by measuring the evolution of the resistance/conductance of the device with φ_{AB}. The first way to tune the AB phase is to change the magnetic field. The corresponding oscillations period $\Delta B = \frac{\Phi_0^*}{A}$ is basically constant and independent of the average magnetic field value but it depends on the effective charge of the quasiparticles. φ_{AB} can also be tuned by applying a negative voltage V_{pg} on the plunger gate. It changes the local potential at the edges, modifies the edge channel trajectories in the vicinity of the plunger gate and thus it enables to tune the effective surface A of the interferometer as shown in Fig. 3.5. Assuming that the change of surface is proportional to the change of plunger-gate voltage [147–149], one expects the gate-voltage period of AB oscillations to scale as $1/B$. These two parameters allows a fine tuning of φ_{AB} and to make precise studies of AB oscillations in QH FP interferometers.

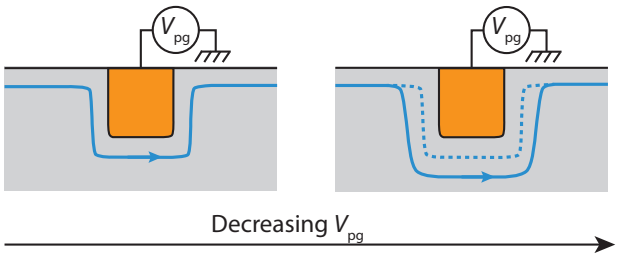

FIGURE 3.5: **Tuning of electron edge channel trajectory with a plunger gate.** Evolution of an edge channel trajectory nearby the plunger gate with the voltage $V_{pg} < 0$ V applied on it. Decreasing V_{pg} allows to repel the edge channel away from the gate and to reduce the effective interferometer surface.

3.2.3 Effect of exchange statistics

At fractional filling factors, the presence of quasiparticles localized inside the bulk of the interferometer also leads to a shift of the phase accumulated along the interfering loop. This phase shift arises because the anyons in the interfering edge channel are braided around the localized ones (see Fig. 3.6). Assuming that they are N_{qp} Abelians quasiparticles localized in the bulk of the FP interferometer, one may write the effective AB phase as [143, 148, 150, 151]:

$$\varphi_{AB} = \frac{2\pi BA}{\Phi_0^*} + \delta\varphi_{stat} = \frac{2\pi BA}{\Phi_0^*} + 2N_{qp}\theta, \tag{3.5}$$

where $\delta\varphi_{stat}$ is the statistical phase term and θ is the exchange phase of the anyonic quasiparticles (see eq. (3.1)). This formula is valid both in the integer and fractional regimes. In the former case, $\delta\varphi_{stat} = 2\pi$ such that the contribution of the statistical phase in the AB oscillations is unobservable. In the fractional regime, $\delta\varphi$ may be different from 2π (e.g. $\theta = \frac{\pi}{m}$ for Laughlin states $\nu = \frac{1}{m}$) leading to the appearance of discrete phase jumps in the AB oscillations each time N_{qp} changes. Such a change may occur irregularly in experiments when the magnetic field or the plunger-gate voltage are slightly varied.

Thus, as anticipated by Chamon and coworkers [143], the study of AB oscillations in the QH FP interferometers provides an experimental way to unveil both the fractional statistics and the effective charge of anyons. The former could be unveiled by observing and measuring phase jumps in AB oscillations with fractional edge channels. The latter could be evidenced by comparing the field periods of AB oscillations in the integer and fractional regimes. Yet, the authors mentioned that this study must be performed at fixed bulk filling factor (requiring the presence of a back gate in the device). Otherwise, the bulk QH droplet may adjust its area or additional quasiparticles

may localize in the bulk to accommodate the flux change and to keep the filling fraction constant such that a flux period of $\Phi_0 = \frac{h}{e}$ would be restored.

Later theoretical works focusing on the $\nu = \frac{5}{2}$ demonstrated that the study of AB interference in QH FP interferometers also allows to evidence non-Abelian anyonic statistics. They should manifest as successions of regimes where AB oscillations can be measured and of regimes where no interference can be observed depending on the parity of the number of localized quasiparticles [103, 150, 152–155]. This is the so-called "even-odd" effect.

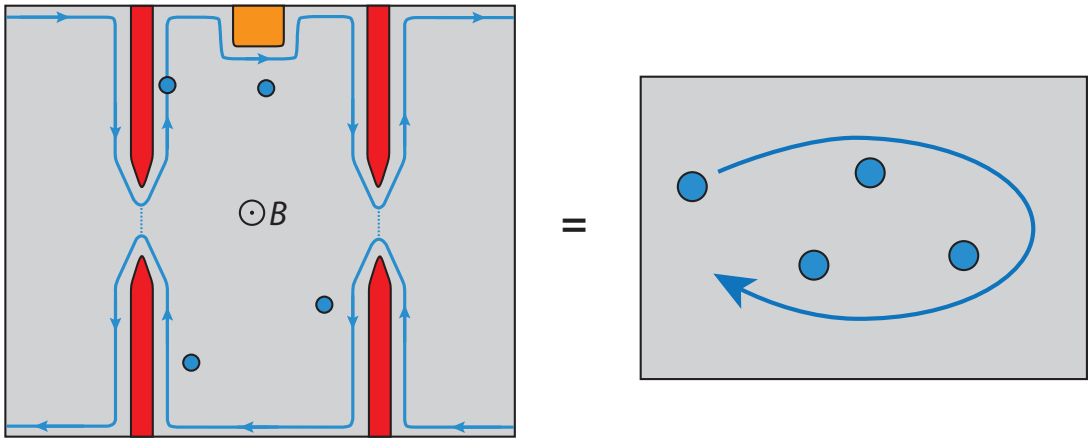

FIGURE 3.6: **Anyon braiding in a QH FP interferometer.** When the QH FP interferometer is operated in the fractional regime, the quasiparticles (blue dots) in the interfering edge channel make loop around the ones localized in the bulk of the FP cavity. The Fabry-Pérot geometry naturally allows to make anyon braiding.

3.2.4 Bias-induced oscillations

In a QH FP interferometer, quantum interference can also emerge from the modification of the energies of the interfering quasiparticles. Indeed, an energy change of $\delta\epsilon$ with respect to the Fermi energy translates into a shift of the quasiparticles wavevector given by $\delta k = \delta\epsilon/\hbar v$, where v edge-excitation velocity. It then results in the accumulation of a dynamic phase shift $\delta\varphi_{\mathrm{dyn}}$ which adds to the AB phase. It can be written as:

$$\delta\varphi_{\mathrm{dyn}} = \frac{2L\delta\epsilon}{\hbar v}, \tag{3.6}$$

where L is the average distance between the two QPCs ($2L$ is the perimeter of the cavity). Hence, the tuning of $\delta\varphi_{\mathrm{dyn}}$ allows to unveil additional quantum oscillations.

Experimentally, these oscillations can be probed by the application of a source-drain dc-voltage bias V_{dc}. When such bias is applied, the incident wavepackets no longer have a fixed and well-defined energy. They rather have a finite energy bandwidth of $e^* V_{\mathrm{dc}}$ and thus they can be decomposed into spectral components with different energies. Each spectral component carries a part of the total current flowing through the device and its contribution depends on the FP transmission at the corresponding energy. Therefore, the oscillations of the FP transmission with the quasiparticles energy $\delta\epsilon$ translate into oscillations of the total conductance of the device with V_{dc}.

Chamon and coworkers calculated the integrated transmission and thus the conductance of the FP interferometer in such configuration. They indeed found that both quantities oscillate with V_{dc} but they also highlighted the existence of a decay of the oscillations amplitude with the bias. This fading actually results from the internal dephasing between the different energy

components of a single wavepacket. The typical period of bias-induced oscillations and the energy scale associated with the amplitude fading were found to be fixed by the Thouless energy $E_{\mathrm{Th}} = \frac{hv}{L}$ that is the typical energy associated with the travel of the quasiparticles between QPCs.

Likewise, Chamon *et al*. predicted an exponential decay of oscillations amplitude with the temperature on a scale fixed by E_{Th} because of thermal smearing. The exact scalings of these two decays were found to depend on the properties of the QH edge channels enabling to probe the chiral Luttinger liquid nature of fractional edge channels [124].

In the integer regime, the study of bias-induced oscillations allows to extract interesting information about the edge channel properties in the device. In this case, the differential conductance δG can be expressed as:

$$\delta G = \delta G_0 \cos\left(2\pi\frac{\Phi}{\Phi_0}\right)\cos\left(2\pi\frac{eLV_{\mathrm{dc}}}{hv}\right), \tag{3.7}$$

where δG_0 is the oscillations amplitude. Then, one can measure the edge-excitation velocity v from the period of bias-induced oscillations. v describes the sharpness of the edge potential in the FP interferometer. It also characterizes the robustness of the quantum interference against intrinsic dephasing mechanisms according to the above discussion.

Therefore, the study of bias-induced oscillations in QH FP interferometers provides complementary information about edge channels physics and the coherence of the quantum transport in both the integer and fractional regimes.

3.3 QH FP interferometry in GaAs/AlGaAs heterostructures

In this section, we make a review of the research work on QH FP interferometers. We mainly focus on the effect of Coulomb interactions that have long hindered the observation of fractional statistics and that have been deeply studied in GaAs/AlGaAs heterostructures. We explain how the electrostatic interactions can lead to conductance oscillations and discuss how they prevent the observation of anyonic signatures based on previous experiments and theoretical investigations. We then describe what were the strategies found to mitigate these charging effects. We finally discuss the status of QH FP interferometry in the fractional regime.

3.3.1 Aharonov-Bohm vs Coulomb-dominated oscillations

Unexpected magnetic field periods in early experiments

The first observation of AB-like oscillations in FP geometry and in the integer regime is anterior to the original proposal of Chamon *et al*. It was reported in 1989 by B. J. Van Wees and coworkers [156] who studied the transport through a large dot. The latter was defined by two QPCs shown in Fig. 3.7.A and 3.7.B and subjected to a perpendicular magnetic field. In this device, Van Wees and coworkers observed conductance oscillations with the magnetic field arising only when the two QPCs were partially pinched (Fig. 3.7.C-E) as one would expect in such geometry.

However, the authors measured oscillation periods ΔB which were inconsistent with the AB period expected considering the size of their device. They also found some surprising dependences of ΔB with the magnetic field or with the interfering edge channel (ΔB varied by a factor 4 between interference with the second edge channel and interference with the fifth edge channel). Such features were not expected within the AB framework but they were observed in different studies performed in quantum dots [157, 158].

Likewise, in the first experiments aiming purposely to perform QH FP interferometry [159–161], similar features were also observed. Indeed, in the integer QH regime, Camino and coworkers observed AB-like oscillations and they found a proportionality between $1/\Delta B$ and the constriction filling factor inconsistent with the non-interacting theory.

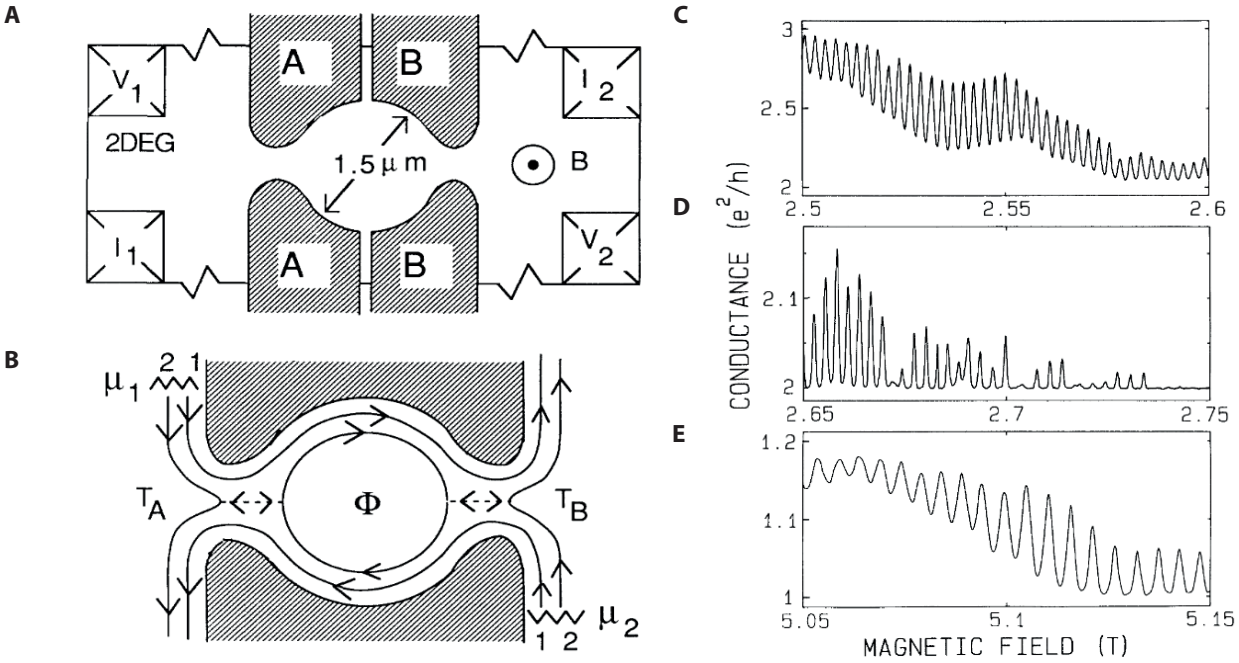

FIGURE 3.7: **First observation of AB-like oscillations in Fabry-Pérot geometry. A**, Schematic of the device studied in ref. [156]: it is composed of a small 2DEG disk defined by two QPCs. **B**, Zoom on the dot with the edge channels configuration. The two QPCs are pinched to partially reflect the inner edge channel. **C**, **D**, **E**, AB-like conductance oscillations. The period of the oscillations largely changes depending on the interfering edge channel pinched or on the magnetic field which is not expected in the theory of non-interacting QH FP interferometers. Adapted from ref. [156].

These unexpected observations were poorly understood at that time. They were actually the first evidence of charging effects in the small FP interferometer whose consequences had not been anticipated initially by Chamon and coworkers.

A simple model evidencing the role of charging effects

The first theoretical explanations were provided in ref. [162] by B. Rosenow and B. I. Halperin. They demonstrated that Coulomb-blockade effects could also lead to resistance oscillations with magnetic field in QH FP interferometers. To draw their conclusions, the authors proposed an instructive model describing how the electrostatic couplings in the FP cavity affect the QH transport. We now follow their approach to get an insight of the effect of Coulomb interactions.

We consider a QH FP interferometer operating in the integer regime with the innermost edge channel interfering and equipped with a back gate.[3] We assume that the filling factor of the constrictions f_c is an integer and that the bulk is at higher filling factor f_b such that $f_c < f_b < f_c + 1$. Then, there are f_c filled and one partially filled LLs in the bulk of the FP cell. These bulk LLs form a compressible island located in the center of the device which is separated from the edge channels by an incompressible region [163]. This island is supposed to be quasi-isolated i.e. weakly tunnel coupled to both the interfering edge channel and the leads (red and blue dashed lines in Fig. 3.8). Thus the island charge must be discrete and it has a finite charging energy E_C. We expect the conductance of the FP interferometer to depend on this charging energy because of the electrostatic coupling between the island and the interfering edge channel.

[3]Most of the results derived in this part hold for a plunger gate.

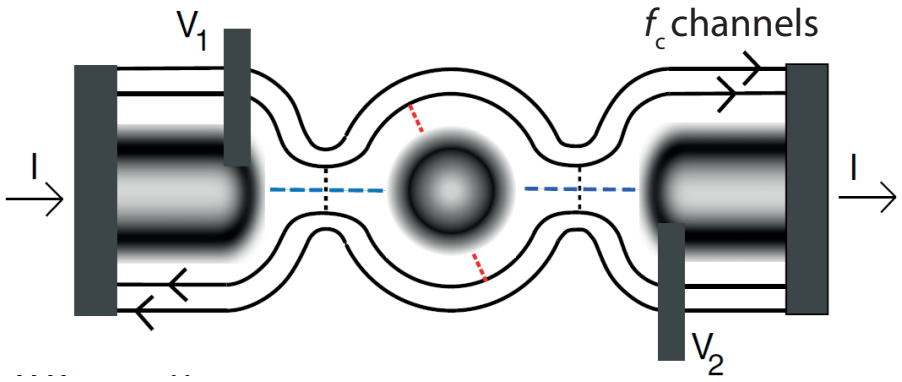

FIGURE 3.8: **Simplified model describing transport in QH FP interferometer in presence of charging effects.** Sketch of QH FP interferometer operating with the innermost edge channel. The shaded regions represent compressible regions. They are f_c edge channels transmitted through the constriction and a partially filled $(f_c+1)^{\text{th}}$ LL. In the center of the cavity, they form a quasi-isolated island whose charge is discrete. The island is electrostatically coupled to the interfering edge channel and to a back gate (not represented here). Transport through the device is the result of a balance between three types of tunnelling events: forward tunnelling between the leads and the island (horizontal blue dashed lines), backward tunnelling between opposite edge states through the island (diagonal red dashed lines) and backward tunnelling across the constrictions (vertical black dashed lines). Adapted from ref. [162].

The key aspect of this model is that E_C depends on the magnetic flux in the FP cavity. Any increase of the flux $\delta\Phi$ results in an increase of the LL degeneracy and thus leads to the addition of electrons in the f_C filled bulk LLs. There is a net flow of electrons through the incompressible stripe towards the island. These extra electrons create a charge imbalance that leads to an increase the island charging energy. It can be compensated if electrons tunnel out from the island or by an increase of the back-gate voltage. In particular, if the flux is increased by Φ_0, there are f_c electrons added to the filled LL and we expect f_c electrons to tunnel outside the island.

With similar considerations, Rosenow and Halperin calculated the island charging energy. It can be written as:

$$E_C = \frac{e^2}{2C_i}(f_c\frac{\delta\Phi}{\Phi_0} + N - N_{\text{gate}})^2, \tag{3.8}$$

where C_i is the capacitance of the island, N is the number of extra-electron added into the island by tunnelling processes and where $N_{\text{gate}} = \frac{C_i}{e}V_{\text{gate}}$ is the number of electrons attracted to the island by changing the gate voltage V_{gate}. In this expression, $f_c\frac{\delta\Phi}{\Phi_0} + N - N_{\text{gate}}$ is the total charge imbalance in the island.

Looking at eq. (3.8), it readily appears that an electron can tunnel outside the island each time the flux is increased by $\delta\Phi = \frac{\Phi_0}{f_C}$ and that E_C oscillates with the magnetic field with a period $\Delta B = \frac{\Phi_0}{Af_c}$.

These oscillations generate periodic variations of the electrostatic potential in the FP cavity. Thus, they lead to a periodic modulation of the energy-dependent phase shift acquired by the interfering quasiparticles. Taking into account this effect, Rosenow and Halperin demonstrated that the oscillations of conductance in the QH FP interferometers could be written as:

$$\delta G \sim \left\langle \cos\left(2\pi\frac{\Phi}{\Phi_0} - 2\pi\frac{2\Delta_X}{E_{\text{Th}}}(f_c\frac{\delta\Phi}{\Phi_0} + N_i - N_{\text{gate}})\right)\right\rangle_N, \tag{3.9}$$

where Δ_X is a parameter describing the energy shift associated with the addition/removal of one electron in the island. In this expression, $\langle ...\rangle_N$ is an appropriate thermal average other the number of extra charges in the island N that is weighted by the Boltzmann factor associated with the corresponding charging energies $E_C(N)$.

This model therefore predicts two oscillation regimes. In the low-coupling regime, that is $\frac{2\Delta_X}{E_{Th}} \ll 1$, the oscillations observed have a Φ_0 periodicity and correspond to the non-interacting AB oscillations. In the strong-coupling regime, that is $\frac{2\Delta_X}{E_{Th}} \approx 1$, the oscillations have a $\frac{\Phi_0}{f_c - 1}$ periodicity[4] and mainly arise from Coulomb interactions in the FP cell. In this case, the gate period ΔV_g of the conductance oscillations is constant and fixed by the island capacitance. This second regime was actually the one observed in early experiments discussed in section 3.3.1. It explains the scaling of the magnetic field periods with the constriction filling factor f_c reported at that time.

This model shows that the Coulomb interactions between localized states and the interfering edge channel can significantly impact the transport through a QH FP interferometer. It also highlights the competition between the standard AB oscillations and the so-called Coulomb-dominated oscillations, which are more likely to emerge in small interferometers.

Rosenow and Halperin also extended their model to the fractional regime. Assuming that the filling factor in the QPCs was $f_c = \frac{r}{s}$ and that quasiparticles tunnelling had an effective charge $-e^* = -\frac{e}{s}$, they found a charging energy:

$$E_C^* = \frac{e^2}{2C_i}\frac{1}{s^2}(r\frac{\delta\Phi}{\Phi_0} + N_i - sN_{gate})^2. \tag{3.10}$$

This expression shows that the gate period of the oscillations with fractional quasiparticles $\Delta V_g^* = \frac{\Delta V_g}{s}$ is reduced compared to that measured with electrons. It provides a way to evidence the existence of fractional charges experimentally.

Two competing oscillation regimes

Following this theory, the competition between the two regimes was investigated into details in the IQH effect. Several interferometry experiments were carried out at Harvard university [147] and at Weizmann Institute [164]. They were performed using QH FP interferometers having different sizes (varying from 2 to 20 μm^2), different gate designs and several edge channels configurations were studied. Thanks to their investigations, both groups were able to confirm the existence of two oscillation regimes and they also recovered the theoretical predictions of the above model.

Importantly, the two groups demonstrated that it was possible to distinguish experimentally the origin of the resistance oscillations by studying their evolution with both B and V_{pg}: oscillations were found to form lines with negative slopes in the AB regime whereas they were found to form lines with positive (or zero) slopes in the Coulomb-dominated regime (see Fig. 3.9).

These two different behaviours can be readily understood. In the first case, the constant resistance lines correspond to constant AB phase / constant flux lines. Therefore, to keep the device resistance constant, one needs to maintain the flux enclosed by the interfering edge channel constant. It requires to compensate any increase of the magnetic field by a lowering of the interferometer surface, as $\delta\Phi \simeq \delta B A + B\delta A$, and thus to lower the plunger-gate voltage such that the constant resistance lines have a negative slope (see Fig. 3.9.A).

In the Coulomb-dominated regime, the constant resistance lines correspond to constant charging energy lines. Considering eq. (3.8), we see that the charging energy is kept constant by increasing simultaneously the flux and the gate voltage such that constant resistance line have a positive slope (see Fig. 3.9.A). Ofek and coworkers [164] suggested that, in this regime, small increases of the magnetic field were accompanied by a shrinkage of the surface enclosed by the interfering edge state. This shrinkage is driven by the Coulomb interactions: the system adapts its area to keep the magnetic flux constant preventing any increase of the charging energy [164].

In 2011, an extended theoretical model was developed by Halperin, Stern, Neder and Rosenow [148] to describe the transport in QH FP interferometers in presence of electrostatic interactions. The

[4] Equivalently a $\frac{\Phi_0}{f_T}$ periodicity where f_T is the number of fully transmitted edge channels.

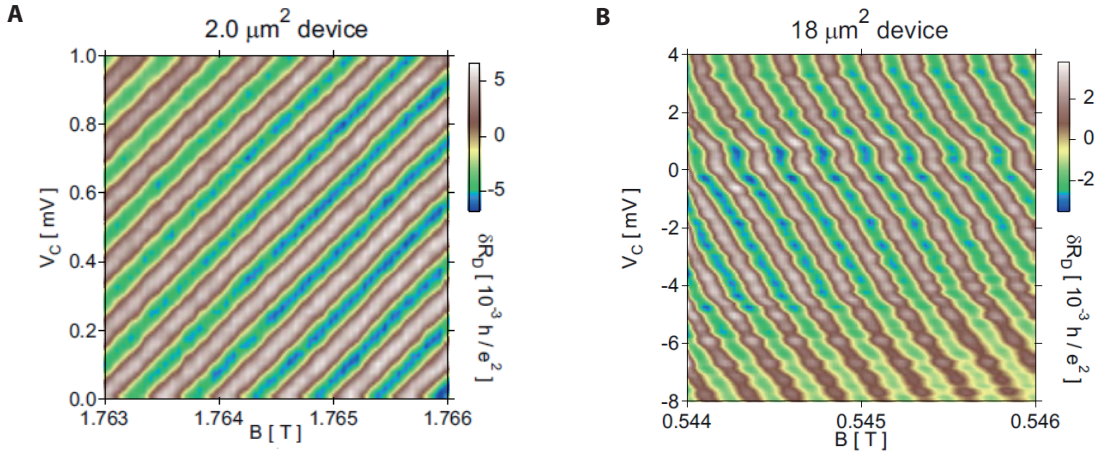

FIGURE 3.9: **Experimental signatures of Aharonov-Bohm and Coulomb-dominated oscillations.** Evolution of the resistance with magnetic field B and gate voltage V_C in two different GaAs/AlGaAs QH FP interferometers. **A**, The 2.0 μm^2 device operates in the Coulomb-dominated regime where the resistance oscillations draw lines with a positive slope. **B**, The 18.0 μm^2 device operates in the Aharonov-Bohm regime where the resistance oscillations draw lines with a negative slope. Adapted from ref. [147].

model treats both AB and Coulomb-dominated oscillations in a common framework. Halperin and coworkers showed that the oscillation regime of a given FP device is actually determined by a ratio of capacitances:

$$\xi = \frac{C_{eb}}{C_{eb} + C_b}, \tag{3.11}$$

where C_b is the capacitance between states localized in bulk of the FP cavity and the gate, and C_{eb} is the effective capacitance characterizing the coupling between localized states and the interfering edge channel. Halperin *et al*. thus demonstrated that there is a transition from the AB regime ($\xi \ll 1$) to the Coulomb-dominated regime ($\xi \sim 1$) with a full range of intermediate cases where both types of oscillations coexist as shown in Fig 3.10. With their new theory, they were able to recover the predictions of the first theoretical model as well as the experimental signatures observed in the two extreme regimes, in particular, the opposite slopes of constant resistance lines in the $B - V_{pg}$ plane. Similar conclusions were also obtained in another theoretical work by S. Ngo Dinh and D. Bagrets [165].

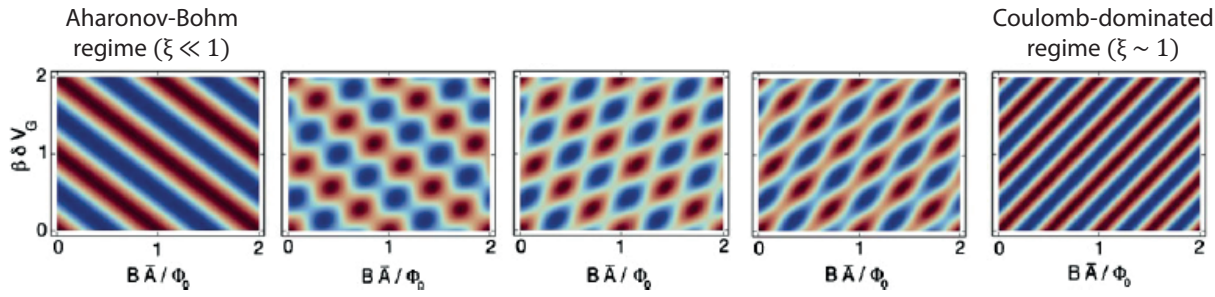

FIGURE 3.10: **Transition from Aharonov-Bohm oscillations to Coulomb-dominated oscillations in QH FP interferometers.** Evolution of the 2D pattern formed by the resistance oscillations in the magnetic field/gate voltage plane depending on the value of ξ . Pure AB oscillations ($\xi \ll 1$) form lines with negative slopes while Coulomb-dominated oscillations ($\xi \sim 1$) form lines with positive slopes. A transition exists between the two extreme regimes where both types of oscillations coexist. Intermediate regimes are characterized by 2D rhombis lattice patterns. Adapted from ref. [148].

Halperin and coworkers also generalized the model for interference with Abelian anyons in fractional regime. Importantly, in weak backscattering limit, **they showed that to probe anyonic statistics, the QH FP interferometer must be operating in the AB regime** (or potentially in a less-favoured intermediate regime). In the Coulomb-dominated regime, the phase shifts were predicted to be unobservable. In this case, the addition/removal of one quasiparticle in the bulk generates a modulation of the effective interferometer surface. Both effects modify the phase accumulated by the interfering quasiparticles and Halperin and coworkers found that the total phase shift was actually 2π. It prevents to measure the contribution of the statistical phase in the Coulomb-dominated regime.

Mitigation of charging effects using elaborated device designs

In experiments performed at Harvard university [147] and at Weizmann Institute [164], the AB regime was only observed in large devices having areas exceeding 15 μm^2. Unfortunately, such interferometers were not operating in the fractional regime because the interfering path lengths were too large compared to the limited phase coherence lengths in FQH edge channels. It rapidly appeared necessary to find solutions enabling to fabricate smaller devices operating in the AB regime.

A lot of efforts have been made to fabricate GaAs/AlGaAs FP interferometers with elaborated designs mitigating charging effects. The first solution proposed was to cover the FP cavity with a top gate (see Fig 3.11.A) in order to increase the bulk capacitance C_b and to screen the Coulomb interactions. Such strategy was actually already used in ref. [147, 164] but it was found to be inefficient when the devices had areas below 12 μm^2 [166]. Another solution proposed by the Weizmann group [149] was to put an ohmic contact (Fig 3.11.B) in the center of the FP. It reduces the device charging energy but it also allows the charge in the bulk to vary continuously rather than discretely. Such strategy was found to be efficient in the IQH effect enabling to operate few micron squares devices in the AB regime. Yet, no AB interference in the fractional regime have been reported with such devices.

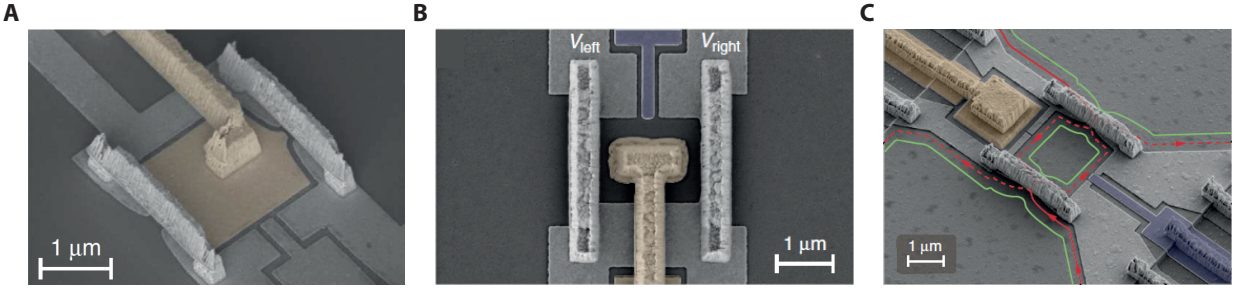

FIGURE 3.11: **Implementation of advanced screening strategies in GaAs QH FP interferometers.** Scanning electron micrographs of QH FP interferometers fabricated in AlGaAs/GaAs heterostructures with designs mitigating charging effects. **A**, Small top-gated devices operate in the CD regime despite an enhanced bulk capacitance. Adapted from ref. [166]. **B**, Devices with a central grounded ohmic contact operate in the AB regime. Adapted from ref. [149]. **C**, Devices with a nearby grounded ohmic contact operate in the intermediate regime. Adapted from ref. [149].

Likewise, some other designs where the ohmic contact was placed at the edges of the FP cavity (Fig 3.11.C), were also implemented [149]. Such designs led to FP interferometers operating in the intermediate regime [149]. Studying these last devices, Sivan and coworkers confirmed that the Coulomb interactions are responsible of periodic changes of the effective interferometer area [149].

In 2019, Manfra's group in Purdue university finally found an efficient solution [167] to work in FQH regime. Using multilayer GaAs/AlGaAs heterostructures (Fig. 3.13.A), they fabricated small

FP interferometers in quantum wells which were encapsulated between two screening layers. These layers were placed only a few tenths of nanometers away from the central quantum well and were providing a significant screening of interactions in the FP interferometers. Using such devices, Nakamura and coworkers observed, for the first time, AB oscillations in the fractional regime [167] some of them displaying phase jumps consistent with the signatures expected for anyonic statistics [151].

3.3.2 Interferometry in the fractional regime

Although, interferometry with fractional edge states was long limited to the study of the Coulomb-dominated regime, it has provided several interesting informations about quasiparticles in the FQH effect. In this section, we make a short review of experiments performed in such regime and discuss their conclusions.

The first experiments were carried out by Camino *et al.* using the same device they had used to study the integer regime [160, 161] and therefore most probably in the Coulomb-dominated regime. Working at filling factor $\nu = \frac{1}{3}$, they observed oscillations having a gate periodicity of about one third of the one they measured at $\nu = 1$. Hence, they showed that the interfering quasiparticles had effective charges $-\frac{e}{3}$ as one would expect at $\nu = \frac{1}{3}$ [168]. Thus, they were able to confirm the results of shot noise measurements with their interferometry experiments. Camino *et al.* also investigated other configurations in the FQH regime but their other results still remain not understood [159, 169].

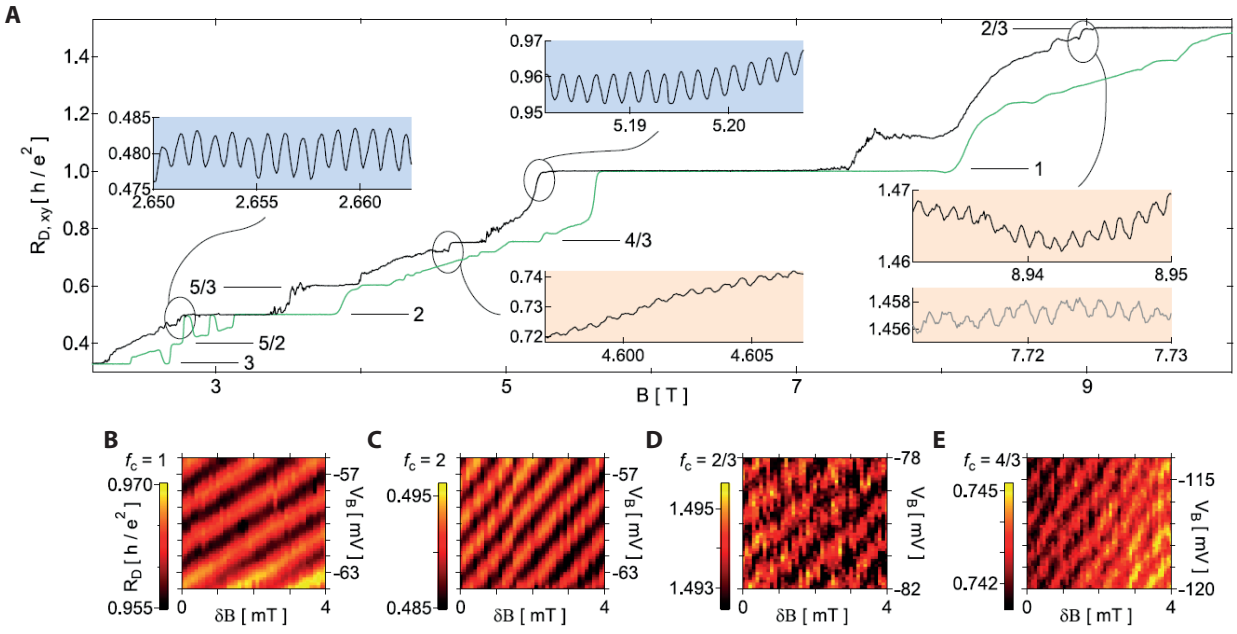

FIGURE 3.12: **Coulomb-dominated oscillations with fractional edge channels in GaAs in QH FP interferometers. A**, Evolution of the diagonal resistance R_D (black line) and transverse resistance R_{xy} with the magnetic field B. Resistance oscillations appear at the edges of both integer (blue insets) and fractional (orange insets) R_D plateaus. **B**, **C**, **D**, **E**, Evolution of R_D with magnetic field variation δB and plunger-gate voltage V_B displaying Coulomb-dominated oscillations respectively at constriction filling factors $f_c = 1, 2, \frac{2}{3}$ and $\frac{4}{3}$. Adapted from ref. [144].

Few years after, the Weizmann [164] and Harvard groups [144] reported the observation of Coulomb-dominated oscillations with $\nu = \frac{1}{3}$ and $\frac{2}{5}$, respectively $\nu = \frac{1}{3}, \frac{2}{3}, \frac{4}{3}$ and $\frac{5}{3}$, edge channels interfering (see Fig. 3.12). They inferred the existence of fractionally charged quasiparticles from

the gate-voltage periods of the oscillations. In particular, McClure and coworkers [144] demonstrated the existence $-\frac{e}{3}$ charged quasiparticles in the $\nu = \frac{1}{3}, \frac{2}{3}, \frac{4}{3}$ and $\frac{5}{3}$ edge channels by comparing the gate-voltage periods measured in both the integer and fractional regimes. Similar conclusions were drawn more recently by the study of Coulomb resonances in a large quantum dot operated at filling factors $\nu = \frac{1}{3}$ and $\frac{2}{3}$ [170].

McClure and coworkers also studied the temperature dependence of the oscillations in the two regimes [144]. In both cases, they observed an exponential decay of the amplitude of the oscillations. The fractional oscillations were found to decay much faster with temperature highlighting their fragility and their sensitivity to dephasing mechanisms.

The observation of AB oscillations with fractional edge channels interfering by Nakamura and coworkers complemented the previous results but also unveiled new puzzling features.

In ref. [167], Nakamura and coworkers reported the observation of oscillations with $\nu = \frac{1}{3}$ and $\frac{2}{3}$ edge channels interfering. In the first case, they reported a gate period consistent with the existence of charged $-\frac{e}{3}$ quasiparticles confirming previous results performed in Coulomb-dominated regime [167]. More surprisingly, they measured a magnetic field period $\Delta B = 22.2$ mT for experiments performed with $\nu = \frac{1}{3}$ interfering anomalously large compared to the one measured in the integer regime $\Delta B = 5.7$ mT. Such difference may be partially explained assuming that their AB oscillations had a $\Phi_0^* = 3\Phi_0$ periodicity although the experiments were not performed at fixed filling factor: the observation of such magnetic field superperiod can indeed be expected in devices with screening layers [171]. Yet, even with this assumption, the period measured at $\nu = \frac{1}{3}$ remains surprisingly large compared to that measured in the integer regime.

Contrastingly, in experiments with the $\nu = \frac{2}{3}$ edge channel interfering, Nakamura *et al.* measured a magnetic field period of 5.5 mT nearly equal to that measured in the integer regime. They also measured a gate-voltage period consistent with quasiparticles having a charge $-e$. Therefore, it appeared that their oscillations at $\nu = \frac{2}{3}$ were arising from electron tunnelling contrary to previous measurements performed in Coulomb-dominated devices at the same filling factor. Such discrepancy was explained by the complex edge structure of the $\nu = \frac{2}{3}$ state that can host several edge modes depending on the edge potentials and on reconstruction effects. The signatures observed were actually consistent with the edge structure predicted by A. H. MacDonald where the edge is supposed to be composed of one $-e$ charged mode and a counter-propagating $\frac{e}{3}$ charged mode [125].[5] The existence of several edge modes might also explain the reduction of the visibility observed for interference at $\nu = \frac{2}{3}$ compared to that of interference at $\nu = \frac{1}{3}$.

In ref. [151], Nakamura and coworkers performed additional interferometry experiments at $\nu = \frac{1}{3}$ in another device and they observed discrete $\frac{2\pi}{3}$ phase jumps in the AB oscillations (see Fig. 3.13.C). These phase jumps were consistent with the signatures expected for the localization of Laughlin quasiholes providing the first direct measurement of braiding statistics in FP interferometers. In addition to this ground-breaking finding, Nakamura and coworkers also highlighted the possible existence of dephasing mechanisms specific to anyon physics thanks to both temperature dependence and out-of-equilibrium transport measurements. Such mechanisms may explain the difficulty to observe interference in the fractional regime.

Finally, we mention the earlier results of Willet and coworkers who focussed mostly on performing FP interferometry experiments at $\nu = \frac{5}{2}$ [174]. They managed to make interference at this filling factor and they observed both gate-induced and magnetic-field induced oscillations. They were attributed to interference arising from either charged $-\frac{e}{4}$ quasiparticles or charged $-\frac{e}{2}$ quasiparticles [175, 176] and alternations between the two oscillations regimes within same device were also reported. These results seem consistent with transport signatures expected for some $\nu = \frac{5}{2}$ non-Abelian ground states [150, 152, 154, 155]. However, they remain controversial notably due to

[5] Other structures involved either a $-\frac{2e}{3}$ charged edge mode with a counter-propagating charge neutral mode [172] or two $-\frac{e}{3}$ charged mode [173].

absence of 2D plots demonstrating that the devices were operating in the AB regime and because the analysis of the authors is based on study of oscillations with poorly defined periods.

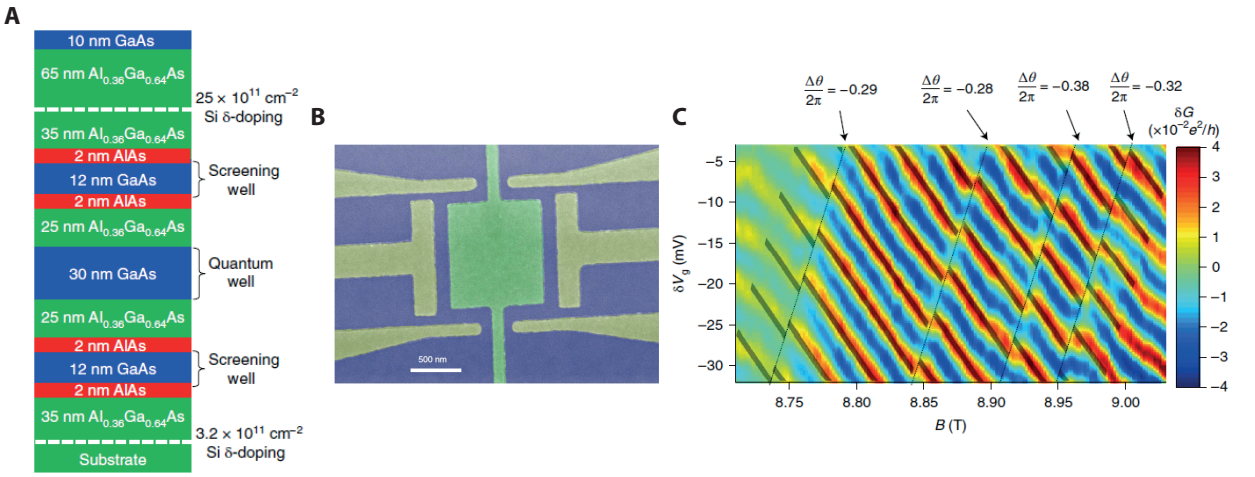

FIGURE 3.13: **AB interference with fractional edge channels and evidence of anyonic statistics in QH FP interferometers. A**, Multilayer GaAs/AlGaAs heterostructures used in Manfra's group to fabricate small QH FP interferometers showing AB oscillations in the fractional regime. The FP interferometer is fabricated in the central well and the two other wells are used as screening layers mitigating charging effects in the interferometer. Adapted from ref. [167]. **B**, Scanning electron micrograph of one interferometer fabricated in such heterostructure. A top gate (green) covers the sample to further reduce charging effects. Adapted from ref. [167]. **C**, AB oscillations measured at $\nu = \frac{1}{3}$ in such device. Discrete $-\frac{2\pi}{3}$ phase jumps (diagonal dashed lines) appear in the oscillations. They are consistent with additions of quasiholes in the bulk of the FP interferometer. Adapted from ref. [151].

3.3.3 Turning to another material

The previous investigations in GaAs/AlGaAs heterostructures have revealed that the QH FP interferometers are powerful tools to probe the properties of the fractional edge channels. Yet, they have also showed that the Coulomb interactions have a detrimental effect in small FP interferometers preventing the observation of anyonic statistics. Mitigating these charging effects in GaAs/AlGaAs devices has proven to be particularly challenging and it requires the implementation of elaborated device designs or the growth of complex multilayer heterostructures. On the other hand, the fractional QH edge channels in GaAs/AlGaAs heterostructures are subject to edge reconstructions [163, 177–179]. It gives rise to the emergence of neutral modes [172, 173, 180–182] which may hindered QH interferometry [182, 183] or generate additional dephasing mechanisms [184].

Therefore, it seems necessary to explore QH FP interferometry in other 2DEGs that exhibit different configurations of electrostatics or edges. It would possibly enable to investigate the physics of FP interfermeters in systems where charging effects have a reduced impact. It would also enable to confirm the universality of anyon physics in the FQH effect that is supposed to emerge in any material.

3.4 QH FP interferometry in graphene

As we have seen in the previous chapters, monolayer graphene in Van der Waals heterostructures is a particularly interesting material for the study of QH effect. It naturally appears as an alternative platform to fabricate and study QH FP interferometers. Indeed, as we show in the first part

of this section, the 2DEG in encapsulated graphene devices exhibits all the necessary features to perform QH interferometry experiments. Yet, until now, QH interferometry has remained little addressed in graphene because the fabrication of gate-tunable QPCs has proven to be particularly challenging. We also discuss this issue in the following and explain how one can solve it.

3.4.1 A material of interest for QH FP interferometry

Many aspects of high-mobility encapsulated graphene heterostructures make them particularly suitable and interesting candidates for QH interferometry.

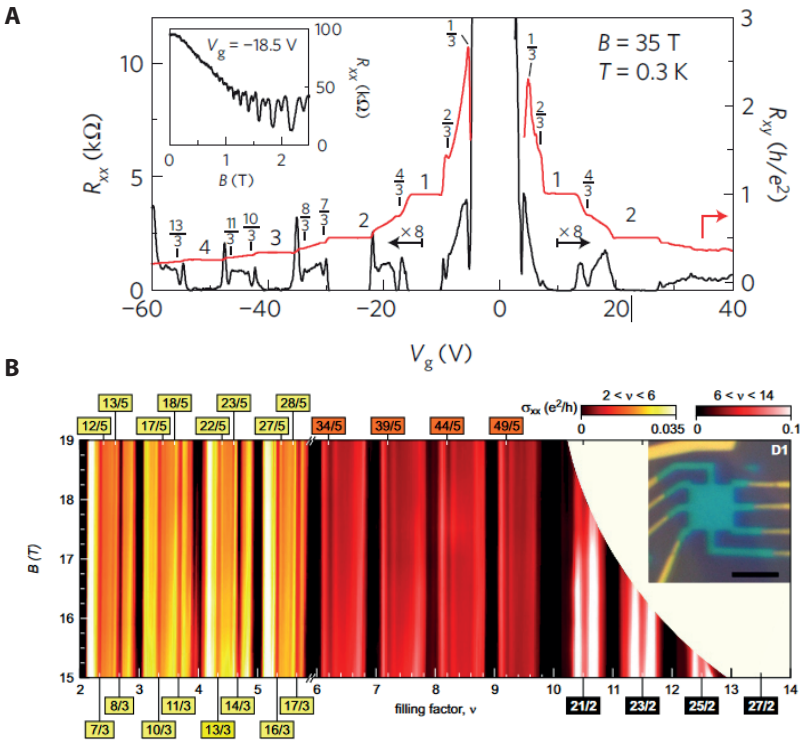

FIGURE 3.14: **Fractional quantum Hall effect in graphene heterostructures. A**, Signatures of $\nu = \frac{k}{3}$ fractional QH states in graphene on h-BN devices. Taken from ref. [12]. **B**, Observation of fractional QH states with even denominator fractions in $N = 2$ LL in encapsulated graphene devices. Taken from ref. [185].

First, the quality of state of the art graphene devices fabricated nowadays enables to observe a rich variety of highly-correlated QH states. All broken-symmetry states [13] were already observed in graphene on h-BN devices [32] as well as many $\nu = \frac{k}{3}$ fractional states [12] as illustrated in Fig. 3.14.A. The use of graphite back gate in these devices then allowed to observe these fractional states, even at intermediate magnetic field (down to 5 T), as well as additional odd-denominators fractions [76] demonstrating the robustness of FQH states in graphene Van der Waals heterostructures. Likewise, encapsulated graphene devices were found to display several FQH states [16] especially when they are equipped with a graphite back gate and/or graphite top gates [93, 94, 186]. These last devices also enabled to unveil the existence of even-denominator fractional quantum Hall states [185, 187] which can possibly host non-Abelian quasiparticles excitations (Fig. 3.14.B). Hence, these encapsulated graphene devices seem particularly interesting for anyons physics.

Furthermore, the valley degree of freedom, together with the SU(4) LL symmetry, give rise to rich physics at fractional fillings and allow the existence of a large variety of possible FQH

states [18, 188, 189]. Some of them are expected to have no analogous in GaAs/AlGaAs heterostructures [190, 191]. It might be interesting to probe their properties with FP interferometers.

On the other hand, the edge channel reconstruction may be limited in graphene heterostructures with graphite back gate. Scanning tunnelling microscopy experiments were performed by Li and coworkers in graphene on graphite substrate [192]. They revealed an absence of QH edge channel reconstruction that is characteristic of atomically sharp confinement. It was attributed to the very close-proximity between the 2DEG and the metallic substrate. Therefore, one may envision to limit the fractional edge channel reconstruction in encapsulated graphene heterostructures using a graphite back gate and a thin bottom h-BN. It would potentially enable to observe AB oscillations with fractional edge channels more easily.

Finally, these encapsulated graphene devices also allow to study the coupling between superconductivity and QH effect [15, 193] or to induce non-local superconducting correlations in the QH edge channels [194, 195]. It offers the possibility to generate Majorana zero-energy modes in such heterostructures that are of interest for topological quantum computation [196, 197]. They might be conveniently manipulated with QH FP interferometers.

3.4.2 The challenge of fabricating QPCs in graphene

Despite these different assets, the fabrication of QH interferometers in graphene has long suffered from the difficulty to fabricate fully tunable QPCs. It requires to have high mobility samples where equilibration between QH edge channels is limited.

Edge channel mixing and equilibration

In standard 2DEGs, the application of a negative voltage on a gate depletes the electron gas beneath by rejecting the Fermi level in the band gap. This property is used to force the edge channels to pass in the constriction of a QPC. In contrast, in gapless graphene, the application of a negative gate voltage generates a hole doping and the formation of pn interfaces. In the QH regime, it leads to an accumulation of localized hole-like edge channels beneath the gate electrodes which circulate along the gate-electrode edges in the same direction than the bulk electron edge channels (see Fig. 3.15). The presence of these hole edge channels can lead to a short-circuiting of the QPCs in low mobility samples.

Indeed, in such samples, there is no valley degeneracy lifting in the bulk. Thus, at the pn junctions, the electron-like and the hole-like edge channels of the $N = 0$ LL hybridize and form one single valley degenerate electron-hole interface state [198].[6] Therefore, there are some current redistribution and some charge transfers between the $N = 0$ electron edge channels and hole edge channels at the pn junctions.

Hence, in a npn geometries, a part of the current injected in the $N = 0$ electron edge channels at one side of the junction is transferred into the edge channels at the other side of the junction via the localized $N = 0$ hole edge channels of the p region. Consequently, one cannot pinch completely the $N = 0$ LL edge channels with a QPC or control completely their transmissions.

This mode mixing is actually not limited to the $N = 0$ LL in disordered samples. Indeed, in early investigations of the QH transport across top-gated [199–202] or split-gated [203], unexpected quantized resistance plateaus were observed in the bipolar regime. Abanin and Levitov demonstrated theoretically that these plateaus were arising from a complete mode mixing at the pn junctions [204]. It leads to equilibration of the chemical potentials of the QH edge channels and thus to some current redistributions at the pn interfaces which forbid to operate a split gate as a full-fledged QPC.

[6] Note that although the valley degeneracy is lifted at a physical edge, it is preserved at the pn junctions (provided it is smooth on the scale of the lattice constant)

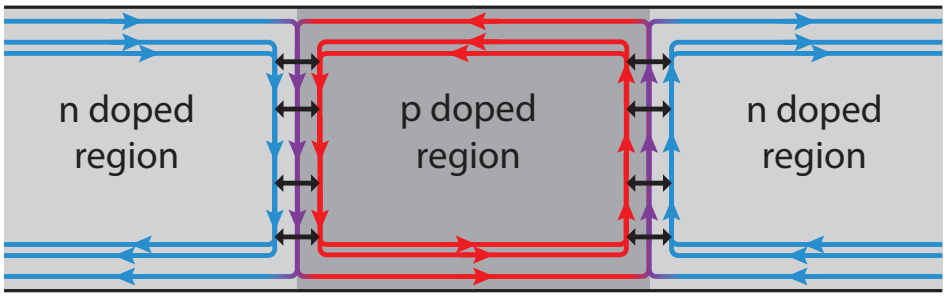

FIGURE 3.15: **Mode mixing at a disordered graphene npn junction.** The spin degenerate electron-like (blue lines) and hole-like (red lines) edge channels propagate along the same direction at the pn interfaces. The valley degeneracy, which is lifted along physical edges, is restored at the pn junctions. In the zeroth LL, electron and hole edge channels hybridize and form a single valley degenerate mode (violet line). Other edge channels also mix such that equilibration and charge transfers occur between the electron and the hole edge channels (black arrows).

Theoretical investigations were conducted to understand in more details how such mode mixing arises [205–208]. They showed that the latter is enhanced by disorder and by the dephasing occurring when charges are scattered between edge states. It explains why a complete mode mixing was observed in the first devices on silicon oxide: there was a high level of disorder in these devices.

Limited equilibration in high mobility samples

Fortunately, in higher quality devices with lower amounts of disorder, mode mixing and equilibration are reduced. It was first evidenced by Amet and coworkers who studied QH transport in graphene on h-BN samples having suspended top gates [209]. Taking advantage of the quality of their devices, they manage to study them in the regime of full degeneracy lifting and they observed that the equilibration processes were limited to the broken symmetry states with the same spin polarization. They also reported, that at high magnetic fields, equilibration was strongly suppressed supposedly due to the formation of an insulating $\nu = 0$ stripe at the pn interface separating electron and hole edge channels. The existence of such insulating stripe was confirmed soon after by Morikawa and coworkers in encapsulated graphene devices [210]. It was used to make a coherent AB interferometers.

Following a similar approach, our group studied the QH edge channel transport across high mobility encapsulated graphene samples equipped with split gates [16, 211]. Equilibration at pn interfaces was found to be spin-selective, limited to the $N = 0$ LL in the bipolar regime and reduced at higher magnetic fields. Furthermore, our group demonstrated that split gates could be used in h-BN/graphene/h-BN graphene heterostructures to make fully gate-tunable QPCs operating with both the IQH and FQH channels without equilibration [16, 211]. This work opened the path towards the fabrication of elaborated QH interferometers.[7]

3.4.3 Current status of QH interferometry in graphene

Up to now, the QH interferometry in graphene has remained very little investigated hindered by the difficulties in fabricating QPCs.

[7] A graphene QPC can also be operated in a unipolar regime where the filling factor below the gate electrodes is lower than that of the bulk. In such configuration, some of the outer electron edge channels can cross the gated region while the inner ones are forced to pass in the QPC constriction.

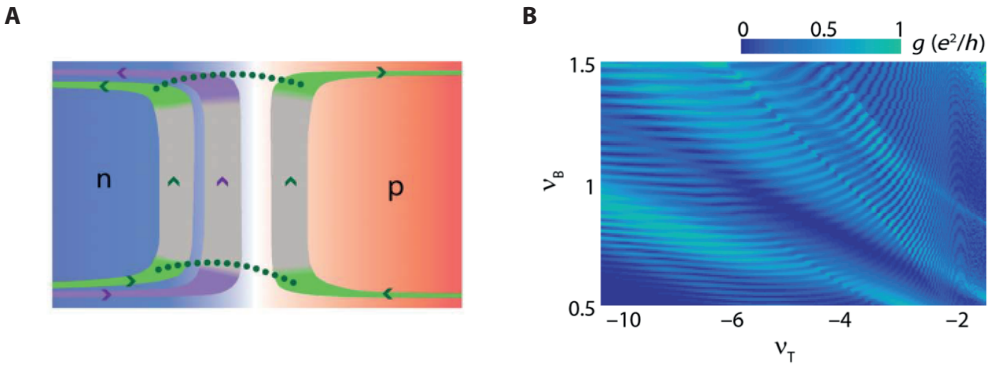

FIGURE 3.16: **Graphene Mach-Zehnder QH interferometer using pn junction. A**, Schematic of a Mach-Zehnder interferometer fabricated in encapsulated graphene heterostructure using a pn junction and the selective equilibration in the $N = 0$ LL. The different spin states are indicated by different colors of edge states (green or violet). In ultraclean pn junctions, intervalley scattering and equilibration (dashed line) only occur at points where the pn junction meets the edges of graphene flake. These points act as two beamsplitters defining an effective Mach-Zehnder interferometer. **B**, Transconductance oscillations measured in a graphene Mach-Zehnder interferometer as a function of filling factors ν_B and ν_T of the n and p regions at 9 T. Adapted from ref. [212].

Following the pioneer work of Morikawa and coworkers [210], most of the experiments focussed on the use of pn junctions in encapsulated graphene heterostructures. Wei and coworkers confirmed that, in ultraclean pn junctions, equilibration was indeed limited to edge channels in the $N = 0$ LL having the same spin. They also demonstrated, that in such samples, the charge transfers were only occurring at the points where the pn junctions meet the physical edges of graphene. They used this property to realize Mach-Zehnder interferometers formed by the copropagating electron and hole edge channels of the zeroth LL (see Fig. 3.16).

Similar results were recovered shortly after by P. Makk and coworkers. Yet, they also demonstrated that the coherent AB oscillations in these devices are likely to coexist with other incoherent magnetoconductance oscillations complicating the interpretation of transport measurements [213]. More elaborated and gate-tunable versions of such Mach-Zehnder interferometers were implemented recently by P. Brasseur and coworkers to investigate the physics of magnons in the integer QH regime [214, 215].

At the same time, only one group reported the fabrication of a graphene QH FP interferometer [216]. The device, that is shown in Fig. 3.17.A, was made from disordered CVD grown graphene transferred on silicon oxide substrate and etched to define split gates (the device does not have plunger gate). Zhang *et al.* observed a few Coulomb-dominated oscillations in their device (Fig. 3.17.B and Fig. 3.17.C). The data they presented clearly suffer from the low mobility of the sample and the absence of degeneracy lifting. This work is only a very first step towards the study of QH FP interferometers in graphene samples and one needs to make higher quality samples to perform such experiments.

Using the expertise of our group in the fabrication of gate-tunable QPC in encapsulated graphene devices, we succeed to fabricate and study some high mobility QH FP graphene interferometers. In the next chapters, we present the results of our investigations of QH transport in such devices.

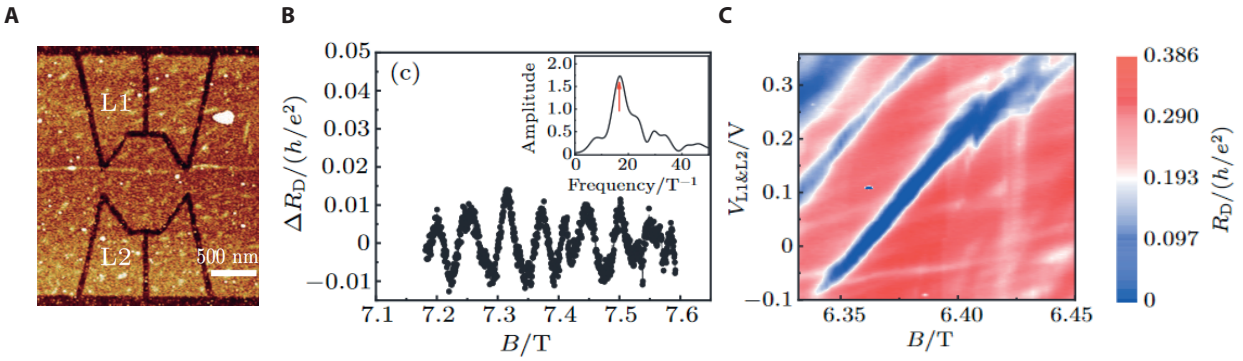

FIGURE 3.17: **QH FP interferometer in CVD graphene. A**, AFM image of a QH FP interferometer made out of CVD graphene flake which was selectively etched. **B**, Diagonal resistance variations ΔR_D as a function of magnetic field B revealing oscillations arising from quantum interference with QH edge channels. Inset: Fourier transform of oscillations. **C**, Evolution of the resistance of the device with B and the voltage $V_{L1\&L2}$ applied on the QPC showing that the device operates in the Coulomb-dominated regime. Adapted from ref. [216].

Chapter 4

Characterisation of a graphene device with multiple split gates

Contents

Following the fabrication process described in Appendix 12, we fabricated several high mobility graphene devices equipped with split gates in series. These devices were aimed at performing QH FP interferometry experiments. In this chapter, we present how we preliminarily characterize such split-gated devices before operating them as QH FP interferometers. In particular, we detail the transport measurements performed both at zero and high magnetic fields that allow to show that the split gates indeed act as QPCs. We also present in this chapter the experimental set-up. Most of the results presented in thesis were obtained on a sample, BNGr74, that showed good performances in the IQH effect. Therefore, we focus here only on this sample.

4.1 Presentation of BNGr74 sample and of the experimental set-up

We begin by the presentations of BNGr74 sample, of the experimental set-up and of the measurement procedures.

The Van der Waals heterostructure

Fig 4.1 presents optical images of the graphene heterostructure used to fabricate BNGr74 device. It is composed of a h-BN/graphene/h-BN stack deposited on top of a thin graphite flake used as a back gate.

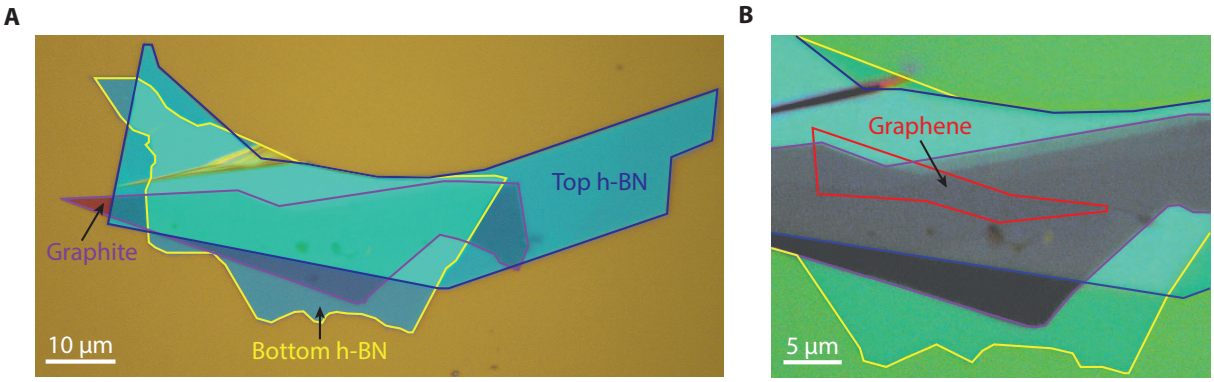

FIGURE 4.1: **BNGr74 Van der Waals heterostructures.** Optical images, **A**, of the full graphite/h-BN/graphene/h-BN heterostructure with a zoom, **B**, on the part where the graphene flake is located. In B, the substrate is covered with PMMA to enhance the visibility of the graphene flake.

The respective flake thicknesses are summarized in Table 4.1. Fig 4.1.B presents an alternative image of the stack which was covered with PMMA resist enhancing the visibility of the graphene. Its position is marked by the red line. A part of the graphene is going outside the graphite back gate and thus the device was fabricated only on the part lying above the graphite flake.

Sample	Top h-BN thickness (nm)	Bottom h-BN thickness (nm)	Graphite thickness (nm)
BNGr74	22	18	4

TABLE 4.1: **Thicknesses of the flakes used.** The thicknesses of the h-BN and graphite layers are measured by atomic force microscopy.

A multiple QH FP interferometer device

From this heterostructure, we fabricated a device displayed in Fig 4.2 and schematized in Fig. 4.3. It is composed of two sets of three ohmic contacts which are separated by three split gates in series used as QPCs. We respectively labelled them $QPC_{1,2,3}$ from the left to the right (see Fig. 4.2).

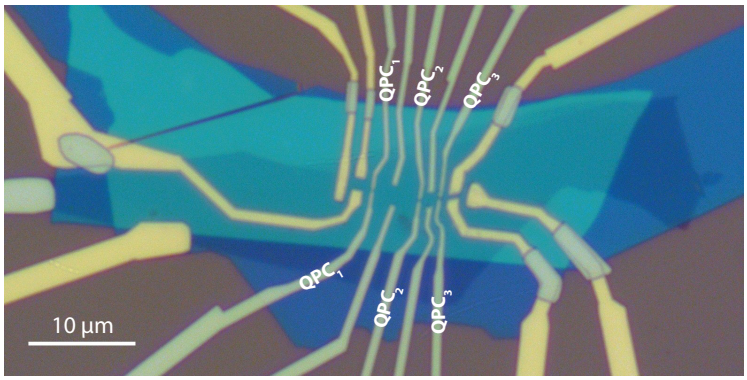

FIGURE 4.2: **BNGr74 multiple QH FP interferometer.** Optical image of the multiple QH FP interferometer fabricated from the BNGr74 stack. 1D Cr/Au ohmic contacts appear in yellow and Pd gate electrodes deposited on top of the capping h-BN appear in light grey. The graphite flake is contacted both by a 1D contact and by a 2D surface contact made on a purposely uncovered part.

To be able to operate the split gates as QPC, one should be careful about the design of the gate electrodes and especially the size of the gap separating them. Indeed, the larger is the gap between the split-gate electrodes the higher is the voltage required to pinch the QPC. Hence, QPCs with very large gap may be impossible to close with reasonable voltages. On the other hand, QPCs with very narrow gaps may have poorly define saddle point potential and thus may be very delicate to tune.

In samples with graphite back gate, the split gates and the back gate are typically at the same distances from the graphene plane. The gates and the graphene are separated by h-BN in the two cases. Hence, the existence of a saddle point potential depends on the ability of the back gate to screen the electric field generated by the split-gates electrodes. In this sample, the graphite back gate is only 18 nm away from the graphene imposing stringent conditions for the design of the split-gate electrodes.

Suitable sizes for the QPCs gaps can be determined by making self-consistent electrostatic numerical simulations. In ref. [217] (Supplementary Information section 1), our group showed that one can compute the spatial evolution of the electrostatic potential $V(x,y)$ and of the charge density $\sigma(x,y)$ in graphene split-gated devices with given geometries. These calculations, repeated for different split-gate V_{sg}/back-gate V_{bg} voltages, can be used to extract the local capacitance $C_{sg}(x,y)$ to the split gates that is given by $\sigma(x,y) = -C_{bg}(V_{bg} - V(x,y)) - C_{sg}(V_{sg} - V(x,y))$ where C_{bg} is the geometric capacitance to the back gate.[1] It allows to extract the capacitance in the QPC constriction and to study its evolution with the gap width.

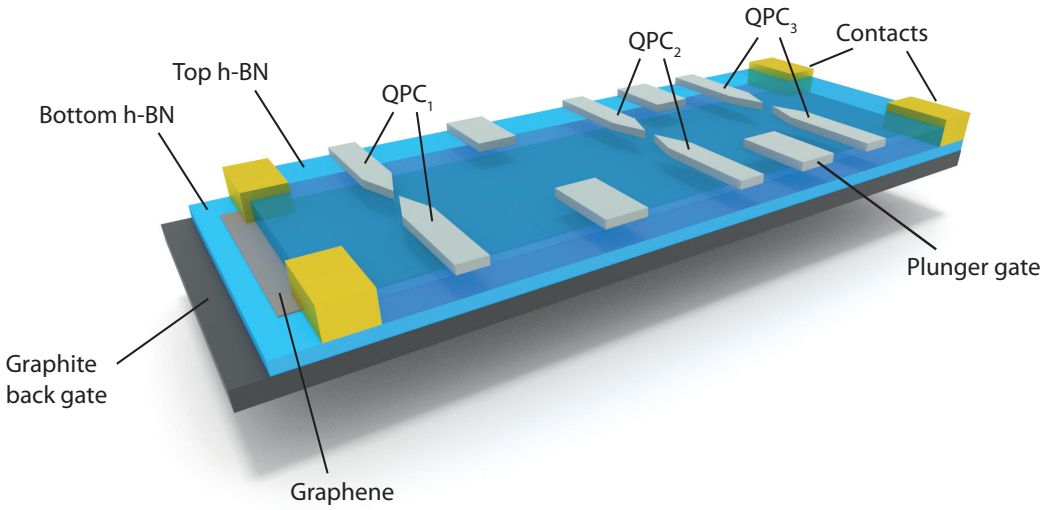

FIGURE 4.3: **Schematic of BNGr74 heterostructure and of the multiple QH FP interferometer device.**

Hermann Sellier, a member of QuNES team, carried out such simulations for different QPC gap widths in geometries close to that of our sample. He found, that to obtain a split-gate over QPC capacitances ratio of about 2, which is suitable in practise, the gap should be about few tenths of nanometers (typically between 20 and 60 nm). This is more restrictive and more difficult to realize than fabricating QPCs in devices with silicon oxide back gate. Indeed, in the these last devices, split-gate gaps of about 150 nm allow to operate the QPCs [16, 217–219].

Scanning electron micrograph of the three QPCs are presented in Fig. 4.4. There is a 20 nm gap between the electrodes defining QPC_2 and QPC_3 whereas the two electrodes forming in QPC_1 are unintentionally connected. This short-circuit does not hinder the QPC operation as demonstrated in section 4.4.

[1] Further explanations are provided in chapter 5 where similar simulations were used to study the plunger gate electrostatics.

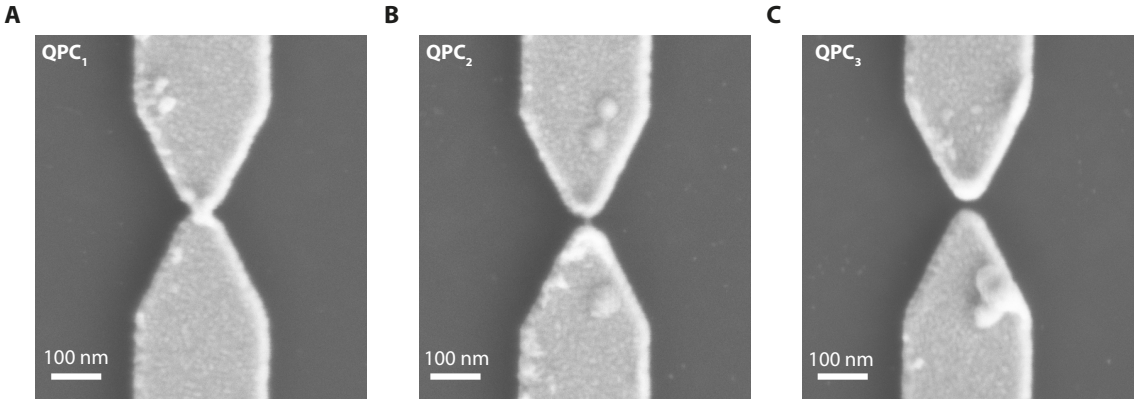

FIGURE 4.4: **QPCs of BNGr74 device.** SEM images of the three QPCs of BNGr74 devices. Split-gates electrodes forming QPC_1 are connected while the gaps between QPC_2 and QPC_3 electrodes are respectively of 21 and 20 nm.

The three QPCs define three FP interferometers with different sizes which can be operated by partially closing two of the three QPCs. We name small, medium and large interferometer, the FP cavities defined by respectively closing QPC_2/QPC_3, QPC_1/QPC_2 and QPC_1/QPC_3 whose geometric characteristics are summarized in Table 4.2. In this device, one can also study the coupling between two QH FP cavities in series using the three QPCs simultaneously. In this configuration, we say that the device operates as a double QH FP interferometer.

QH FP interferometer	QPCs used	A_{geo} (μm^2)	L (μm)
Small	QPC_2/QPC_3	3.1 ± 0.4	4.3 ± 0.5
Medium	QPC_1/QPC_2	10.7 ± 1.2	7.2 ± 0.5
Large	QPC_1/QPC_3	14.7 ± 1.8	9.0 ± 0.5
Double	$QPC_1/QPC_2/QPC_3$	13.8 ± 1.6	11.5 ± 0.9

TABLE 4.2: **Characteristics of the different QH FP interferometers in BNGr74 sample.** The QPCs used in each interferometers are reported. Geometrical areas A_{geo} and average interfering path length L (i.e half of the FP cavity's perimeter $2L$) are estimated from the lithographic design and optical images. The uncertainties on the values of A_{geo} and L reflect the uncertainty $\delta x \simeq \pm 150$ nm we have on the exact position of the graphene's edges on the optical images.

Inside each FP cavity, additional gate electrodes are placed above the pristine edges of graphene to define the plunger gates used to shift the edge channel trajectory and modulate the surface enclosed by the interfering one (see Fig. 4.5).

Experimental set-up and measurement procedure

All transport measurements were performed in a dilution fridge (Fig. 4.6.A) reaching a base temperature of 10 mK equipped with a superconducting solenoid (Fig. 4.6.B) enabling to generate a maximum perpendicular magnetic field of 16 T. The dilution fridge used was highly filtered. Its wiring is shown in Fig. 4.7. It was designed such that the thermal noise in the wires remains lower than the noise level of our voltage amplifiers ($0.7\ nV/\sqrt{Hz}$). The wiring also enables to filter the thermal radiations between the different cooling stages.

To study the transport in this sample, we used a low-frequency ac-voltage excitation, ranging typically from 5 μV for interferometry experiments to 50 μV for the characterization. We measured

the current I flowing in the sample as well as the diagonal V_D, longitudinal V_{xx} and Hall V_{xy} voltage drops according to the contact configuration displayed in Fig. 4.5 using standard lock-in measurements. For simplicity, we do not distinguish longitudinal resistances R_{xx} calculated from V_{xx} or V_{xx2} as they are equivalent especially in the QH regime.

The voltage and current signals were amplified using room-temperature amplifiers placed in a home-made box (Fig. 4.6.C and Fig. 4.6.D) thermoregulated with a chiller at $25 \pm 0.1°$ C. It allows to get rid of thermal offsets in the input voltages. The QPCs and the back gate were polarized using high-stability voltage sources whereas plunger gates were polarized using a DAC with 21 bits resolution. The set-up was used to study all the graphene QH FP interferometers presented in the manuscript.

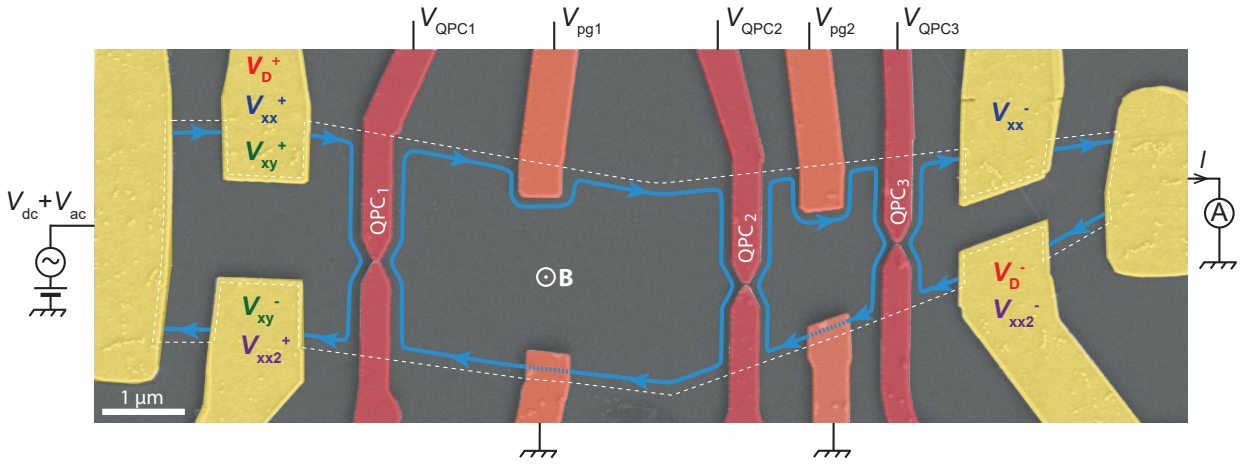

FIGURE 4.5: **SEM image of the multiple QH FP interferometer and contact configuration.** False-coloured electron micrograph of BNGr74 device. The contacts, the QPCs and the plunger gates are respectively coloured in yellow, orange and red. The edges of the graphene flakes are represented by white dashed line and the trajectory of an interfering electron edge channel is represented in blue. The different gate voltages applied during interferometry experiments are noted in black. The sample is measured in voltage polarization by application of a 5 μV ac-voltage excitation on top of which a dc-voltage bias can be added. The current is measured at the drain contact with a current amplifier. The position of the voltage probes used to measure the diagonal $R_D = V_D/I$, longitudinal $R_{xx} = V_{xx}/I$ or $R_{xx} = V_{xx2}/I$ and Hall resistances $R_{xy} = V_{xx}/I$ are labelled with four distinct colors.

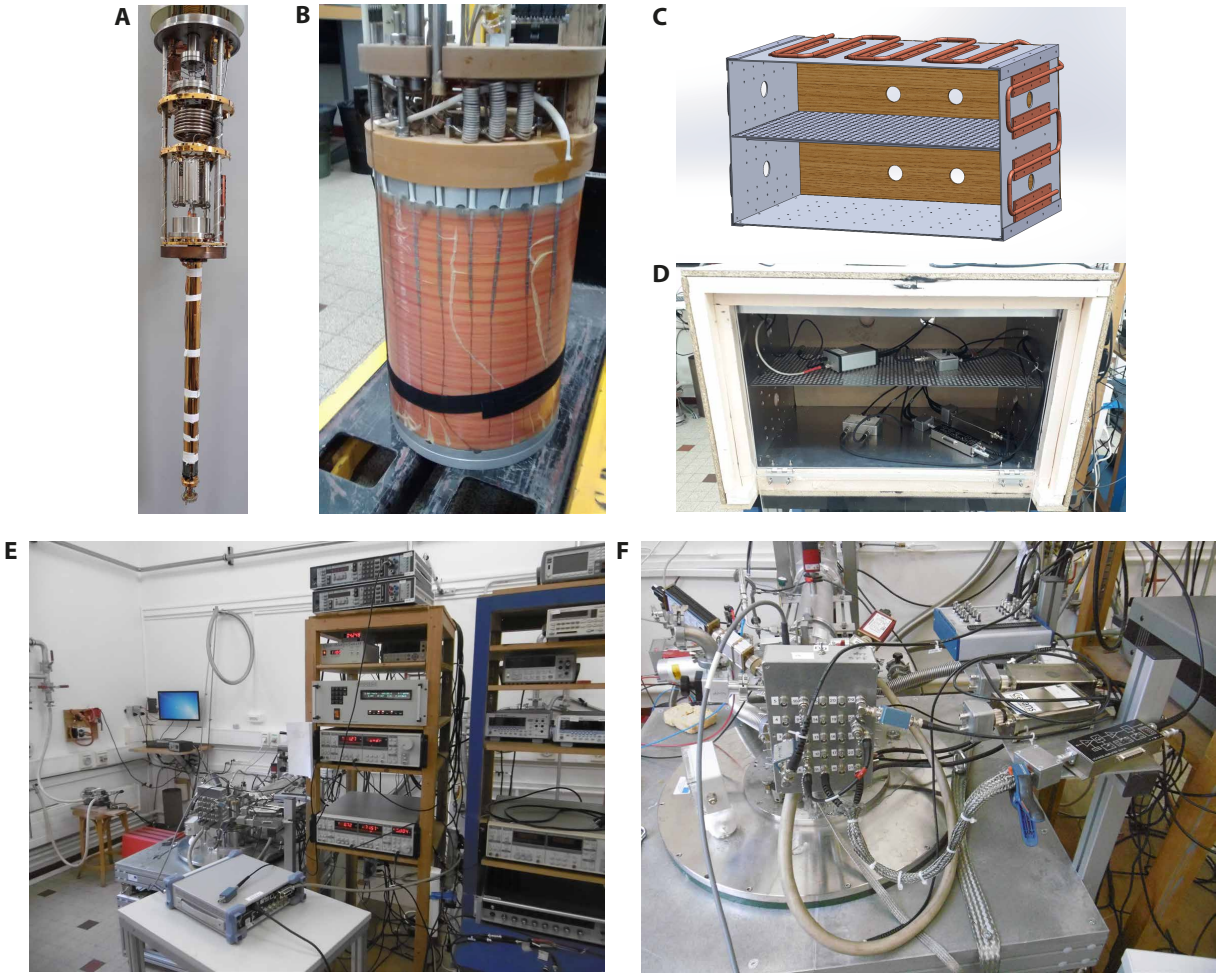

FIGURE 4.6: **Measurement set-up.** **A**, Dilution fridge. **B**, Superconducting solenoid **C**, 3D design of the metallic structure of the home-made thermoregulated box. The metallic structure is cooled via cooper pipes which are filled of water thermalized by a chiller. Design by Florent Blondelle. **D**, Image of the home-made thermoregulated box. The amplifiers are placed inside the box during the interferometry experiments to get ride of thermal offset drifts. The metallic structure is fully surrounded by thick polystyrene slabs allowing to isolate the thermoregulated part of the box. **E**, **F**, Photos of the set-up during transport measurements.

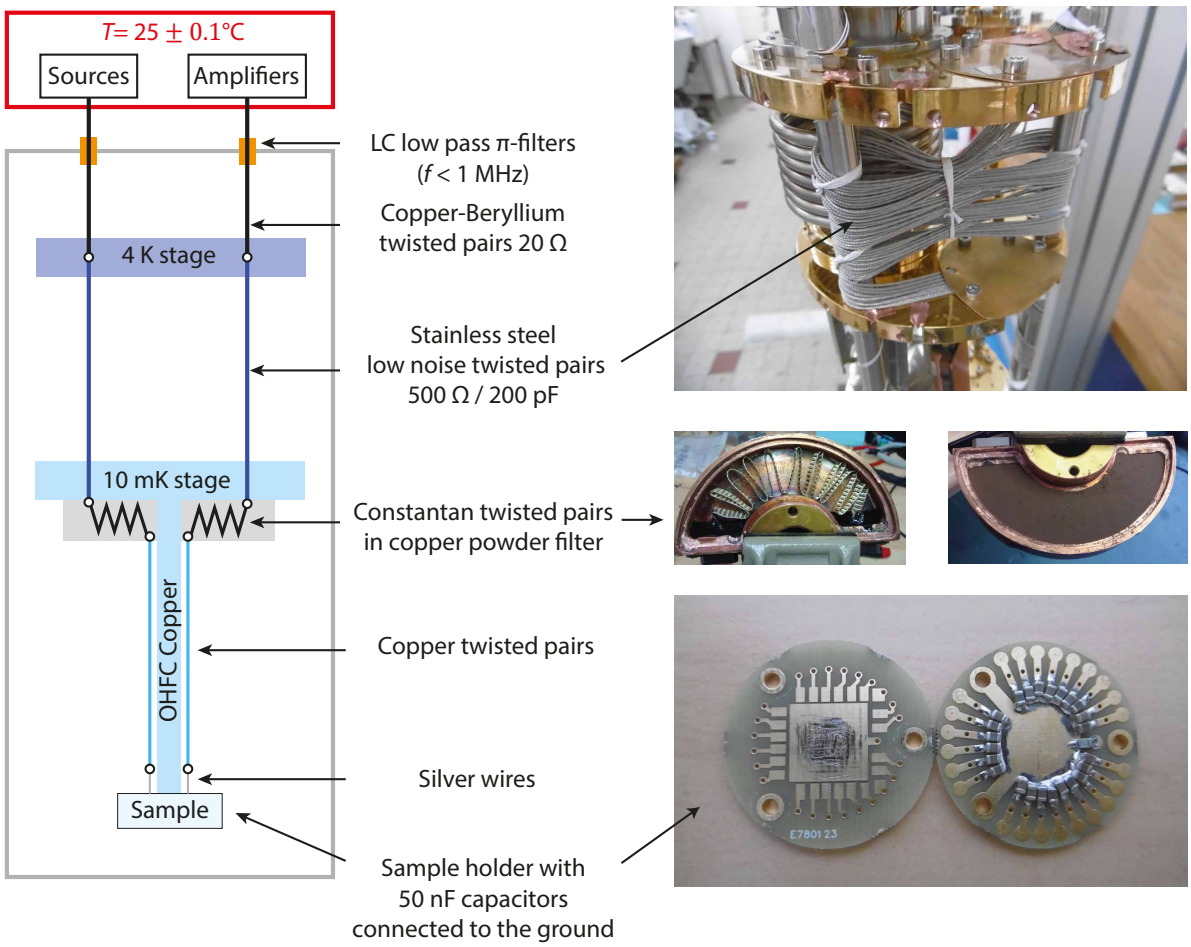

FIGURE 4.7: **Dilution fridge wiring and filtering.** Before entering in the cryostat all signals are filtered using LC π-filters that reject the radiofrequency noise. There is 25 lines in the fridge. One is used to apply a voltage on the silicon back gate. The 24 others can be used either for measurements or to apply voltages on the gates of the samples. Up to the 4 K stage, the wires are made of highly conductive copper-beryllium alloy to limit thermal noise. Between the 4 K and 10 mK, the wires are made of stainless steel that are graphitized to reduce electric noise coming from friction. They also limit thermal conduction between 4 K and 10 mK stages. Before going to the samples, the twisted pairs pass in a RF copper powder filter. It filters thermal radiations coming from sources at higher temperatures. The lowest part of the dilution fridge is made of oxygen-free high thermal conductivity copper to ensure a good thermalization of the sample. For the same reason, the last wires connecting the sample to the lines are made of silver. The signal is further filtered on the sample holder thanks to capacitors connected to the ground.

4.2 Device characterization at zero magnetic field

We begin with the characterization of the transport properties at zero magnetic field.

4.2.1 Field effect characteristic

Fig 4.8 displays the evolution of R_{xx} in the device with back-gate voltage V_{bg}. R_{xx} exhibits two resistance peaks reaching a few tenths of kilo-Ohms : a main peak at $V_{bg} = -70$ mV and a second one at $V_{bg} = 30$ mV. It contrasts with the usual transport characteristics observed in standard Hall-bar graphene devices (for example Fig 2.6 of Chapter 2) where a single peak at CNP is observed. The second Dirac point actually reflects the existence of a graphene region where the doping is different from that of the rest of the sample.

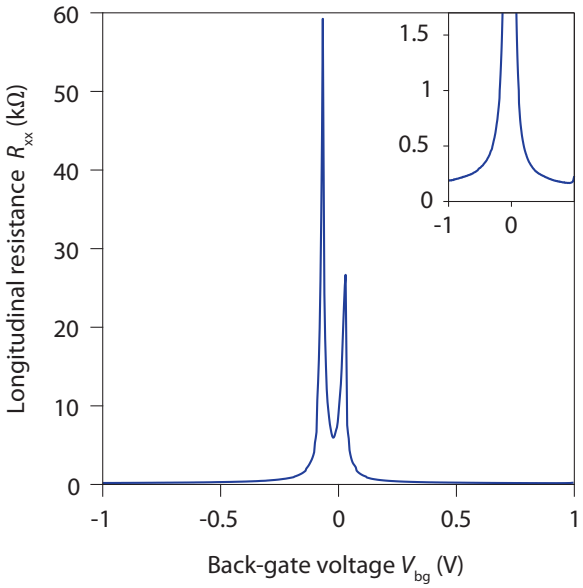

FIGURE 4.8: **Zero magnetic field transport characterisation.** Evolution of the longitudinal resistance of the device R_{xx} with the back-gate voltage V_{bg} at 4 K. The sample displays two resistance peaks around $V_{bg} = -70$ mV and $V_{bg} = 30$ mV in contrast with standard transport characteristics in graphene. All the top gates are floating. Inset: Zoom on the low resistance part of the plot.

From this measurement, we can have a first indication of the quality of the sample. At large electron doping for $V_{bg} = 1$ V, R_{xx} drops to 170 Ω leading to a sheet resistance $R_{\square} = 42.5$ Ω (assuming there are four squares between the voltage probes). This relatively low value is a hint of the good quality of the sample.

4.2.2 Characterization of the split gates

The origin of the doping inhomogeneities clearly appears by studying the transport through the split gates at $B = 0$ T. Fig 4.9 displays color-coded maps of the evolution of R_{xx} with both V_{bg} and V_{QPC} the voltage applied on one given split gate while the others are kept floating.

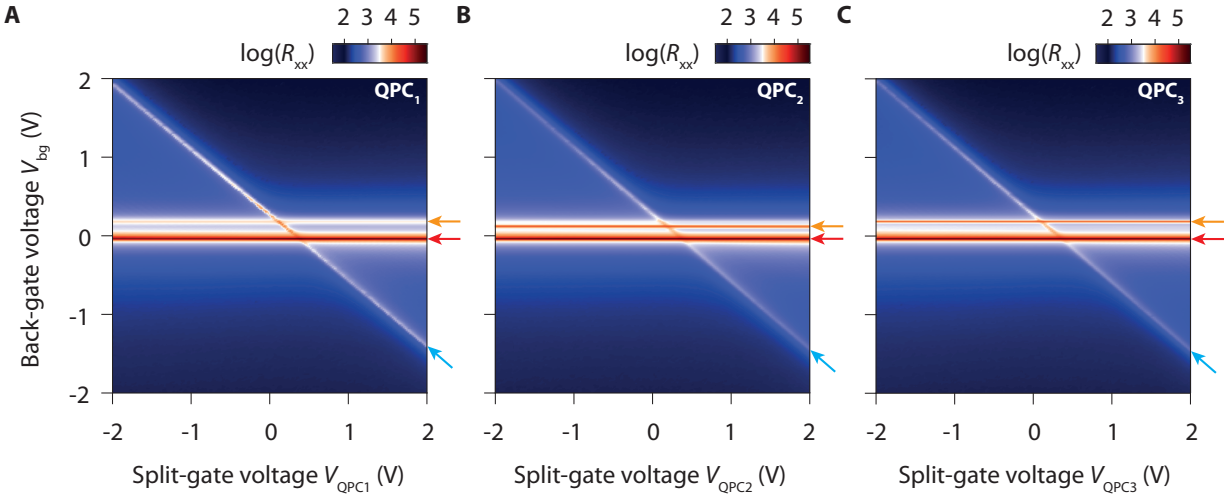

FIGURE 4.9: **Split-gate characterization at zero magnetic field. A**, **B**, **C**, Evolution of the longitudinal resistance of the device R_{xx} with the back-gate voltage V_{bg} and the split-gate voltage $V_{QPC1,2,3}$ at 4 K. The horizontal lines at $V_{bg} = -40$ mV (red arrows) correspond to the CNP in the bulk graphene, whereas the diagonal lines (blue arrows) correspond to the CNP in the graphene beneath the active split gate. They intersect at $(V_{QPC}, V_{bg}) \simeq (0.38\text{ V}, -0.04\text{ V})$ as a result of the local hole doping induced by the palladium electrodes. The second horizontal lines (orange arrows), appearing at $V_{bg} = 0.18,\ 0.12,\ 0.18$ V, evidence the existence of a local doping beneath non-active split gates resulting in a shift of the CNP.

All the maps display four quadrants separated by two horizontal lines and a diagonal line. The most resistive horizontal line (red arrow), which appears at $V_{bg} = -40$ mV in all the three maps, corresponds to the CNP of the graphene bulk. The diagonal line (blue arrow) corresponds to the CNP in the graphene region beneath the active split gate in agreement with previous studies of graphene devices equipped with a single top gate (see ref. [16, 217, 218, 220, 221] for example). They intersect respectively at positive split-gate voltage values (see Table 4.3) reflecting the local doping induced by the split-gate electrodes. It arises from the difference between the work functions of palladium and graphene [222]. The slopes of the diagonal lines provide the ratios C_{sg}/C_{bg} of the capacitances between the active split gate and the back gate which are reported in Table 4.3.

QPC	Position of CNP beneath the QPC (V_{QPC}, V_{bg})	Capacitance ratio C_{sg}/C_{bg}
QPC_1	$(0.38\text{ V}, -0.04\text{ V})$	0.83
QPC_2	$(0.4\text{ V}, -0.04\text{ V})$	0.86
QPC_3	$(0.36\text{ V}, -0.04\text{ V})$	0.86

TABLE 4.3: **QPC characteristics at zero field**

The second horizontal line (orange arrow), already highlighted in Fig. 4.9, is usually not observed in devices with a single top gate. It results from the contribution of the graphene regions located beneath the two floating palladium split gates. Even though they are not active, they shift locally the position of the Dirac point resulting in the second horizontal resistance line. Its position varies between $V_{bg} = 0.12$ V and 0.18 V in the three maps reflecting a sensitivity to the past charging states of the floating gate electrodes and the intrinsic differences between the gates.

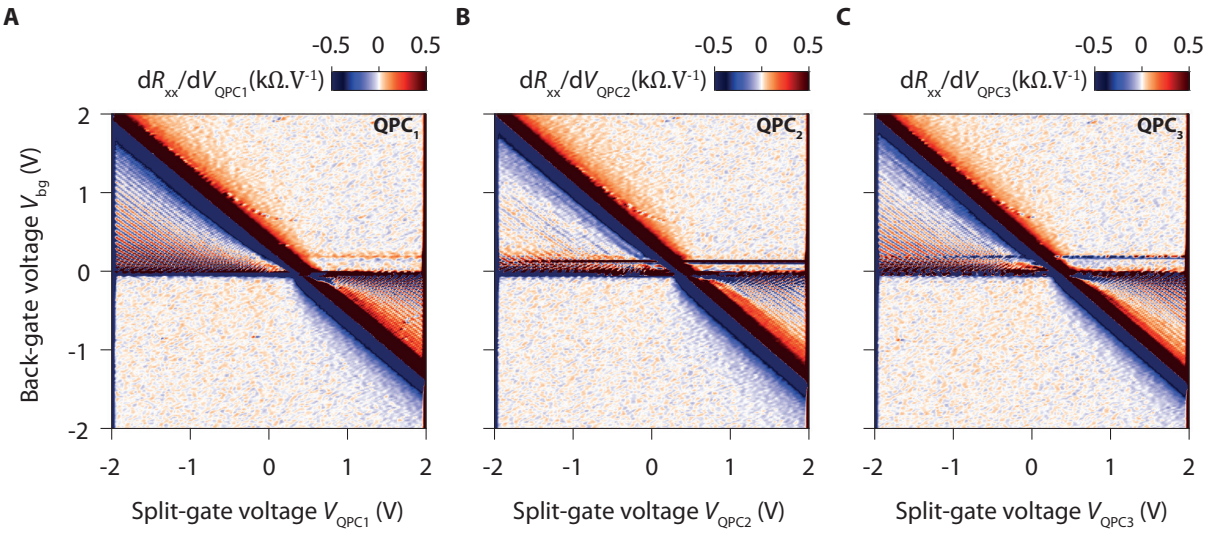

FIGURE 4.10: **Fabry-Pérot interference beneath the split gates at zero field.** Evolution of the derivative of longitudinal resistance dR_{xx}/dV_{QPC} with the back-gate voltage V_{bg} and the split-gate voltage V_{QPC}. At fixed V_{bg}, oscillations in dR_{xx}/dV_{QPC} with V_{QPC} clearly appear. They disperse with V_{bg} and V_{tg}. It shows the existence of FP oscillations characteristic of ballistic transport in the region beneath the active split gate.

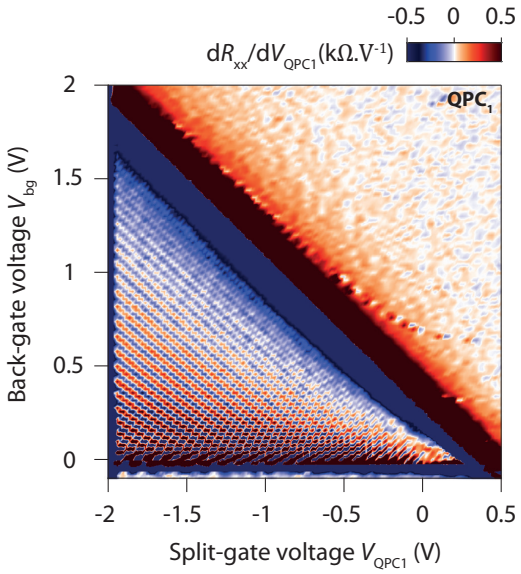

FIGURE 4.11: **Fabry-Pérot interference beneath QPC$_1$.** Zoom on Fig. 4.10.A map.

Fig. 4.10 displays color-coded maps of the derivative of the longitudinal resistance with respect to the split-gate voltage dR_{xx}/dV_{QPC} for the three QPCs. The three maps, are almost identical and exhibit the same typical features in the bipolar regimes (see also Fig. 4.11).

They highlight the existence of pseudo-periodic resistance oscillations appearing in the bipolar regimes at fixed V_{bg}. These oscillations disperse both with V_{QPC} and V_{bg} and are usually referred as FP oscillations. They arise from quantum interference between ballistic electron trajectories in the top-gated regions. The observation of well-defined FP oscillations in each maps demonstrates that the transport beneath the three split gates, which are about 300 nm wide, is ballistic [202, 217, 220, 223–226].

4.3 Transport characterization in the quantum Hall regime

We now focus on the magneto-transport characteristics of the device and especially the transport in the QH regime.

4.3.1 Bulk Landau fan diagram

Fig. 4.12 presents the evolution of R_{xx} and $1/R_{xy}$ in the device in the form of a Landau fan diagram measured at 20 mK. During the measurement, a $V_{QPC} = 0.3$ V voltage was applied on each QPCs to compensate most of the hole doping induced by the palladium electrodes and ensure a quasi isodensity in the graphene flake. The sample displays typical QH features starting from 0.5 T with the robust graphene QH states corresponding to filling factors $\nu = 2\frac{e^2}{h}(2N+1)$ firstly appearing followed by the formation of broken symmetry-states at higher magnetic fields. The latter is marked by the apparition of additional minima in R_{xx}. The full degeneracy lifting occurs above 5 T and 3 T respectively for electron-type and hole-type broken symmetry states and a very strong insulating phase develops at CNP even at low magnetic field. In the zeroth Landau level, the $\nu = \pm 1$ broken symmetry states develops above 4 T.

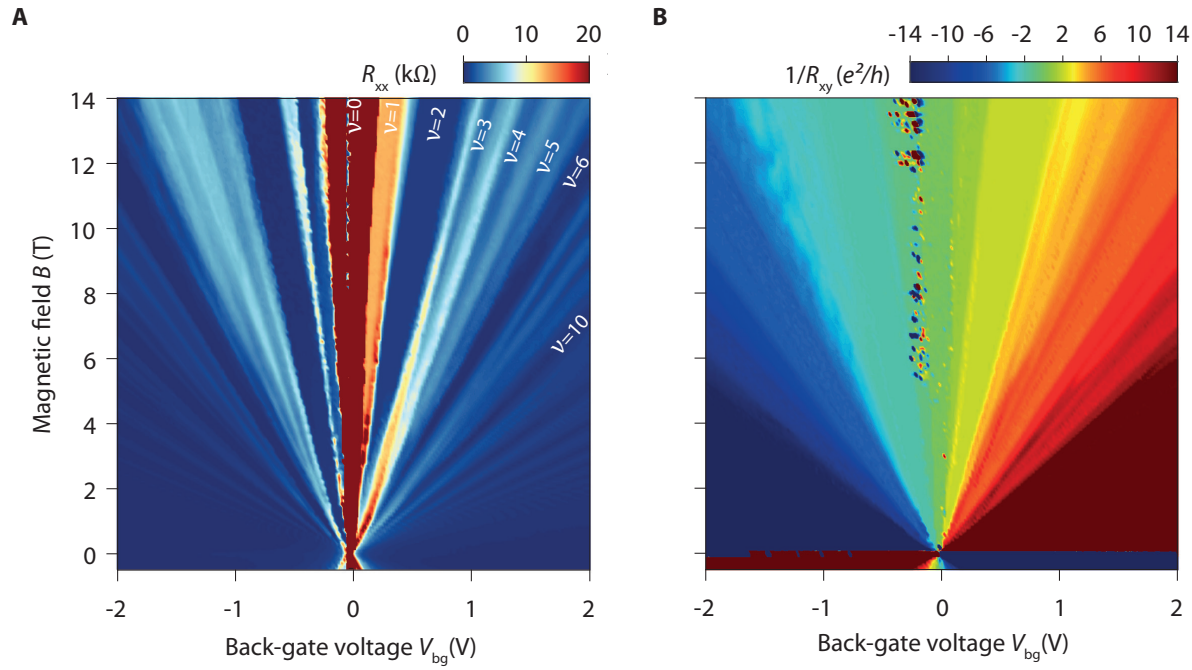

FIGURE 4.12: **Landau fan diagram.** **A**, Evolution of R_{xx} and, and **B**, $1/R_{xy}$ with B and V showing clear QH features in the device. QH signatures appear starting from 0.5 T and broken-symmetry states develop above 2 T with a full degeneracy lifting above 5 T. In A, some of the electron integer QH states developing with the magnetic field are labelled. Measurements performed at 20 mK with 5 μV ac-voltage excitation.

It is worth noticing that, despite the full degeneracy lifting, the Hall conductance is not well quantized or does not display clear plateaus in $|N| \geqslant 1$ LLs. It is especially visible for broken-symmetry states as shown in Fig. 4.13. It results from the existence of a residual backscattering in the sample which may arise from the incomplete compensation of the doping induced by the QPC electrodes. The quantization of R_{xy} for the broken symmetry states is better on the electron side than on the hole side, especially for $\nu = \pm 1$ states thus we decided to focus only on the first for interferometry experiments.

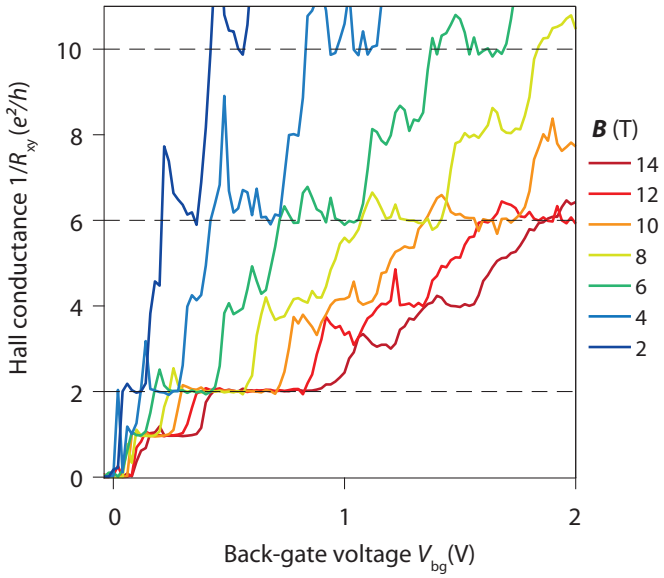

FIGURE 4.13: **Quantized Hall conductance.** Linecuts of the fan diagram displayed in Fig. 4.12.B. Features characteristic of QH effect appear clearly with more robust plateaus at values characteristic of monolayer graphene QH effect (black dashed lines). Signatures of $\nu = 1$ broken-symmetry state appear starting from 4 T while plateaus corresponding to other broken-symmetry states develop at higher fields. Quantization in $N = 1$ LL is imperfect even at high magnetic fields because of the existence of a residual backscattering.

4.3.2 Estimation of back-gate capacitance and mobility

The Hall measurements performed at $B = \pm 0.1$ T allow to estimate the charge carrier density n and the mobility μ in the device which are displayed in Fig. 4.14. In Fig. 4.14.A, we note that n displays a non-linear dependence to V_{bg}. It may arise from the incomplete compensation of the doping induced by the palladium electrodes ($V_{QPC} = 0.3$ V for the measurement whereas $V_{QPC}^{CNP} = 0.38$ V). From this measurement, we can obtain an estimation of the back-gate capacitance C_{bg} which ranges between 1.46 and 2.0 mF/m^2. It gives a h-BN dielectric constant ranging from 3.0 and 4.1 consistent with previous measurements [227]. In Fig. 4.14.B, we see that μ reaches 130 000 cm^2.V^{-1}.s^{-1} at a carrier density of $n = 10^{12}$ cm^{-2} density.

In a Landau fan diagram, the dispersion of the R_{xx} minima provides another way to evaluate C_{bg}. Assuming that the latter does not depend on B and V_{bg} and remembering that $\nu = \frac{n\Phi_0}{B}$ and $n = \frac{C_{bg}}{e}(V_{bg} - V_{bg}^{CNP})$, we can write the relation:

$$\frac{\nu Be}{\Phi_0} = C_{bg}(V_{bg}^{\nu} - V_{bg}^{CNP}), \tag{4.1}$$

which gives the back-gate voltage V_{bg}^{ν} to apply to reach filling factor ν at given field. This relation can be used with $\nu = 2, 6, 10$ states to estimate C_{bg} based on the positions of R_{xx} minima/cancellations in the fan diagram as they mark when the corresponding integer filling factors are reached.

We performed this analysis for similar measurements performed at 4 K. Fig. 4.15.A displays the positions of the R_{xx} minima/cancellation for filling factors $\nu = 2, 6, 10$. For a given QH state, R_{xx} minima occur at V_{bg}^{ν} values which scales linearly with B in agreement with eq. (4.1). The data are rearranged in Fig. 4.15.B where the evolution of $\frac{\nu Be}{\Phi_0}$ versus $(V_{bg}^{\nu} - V_{bg}^{CNP})$ is plotted.

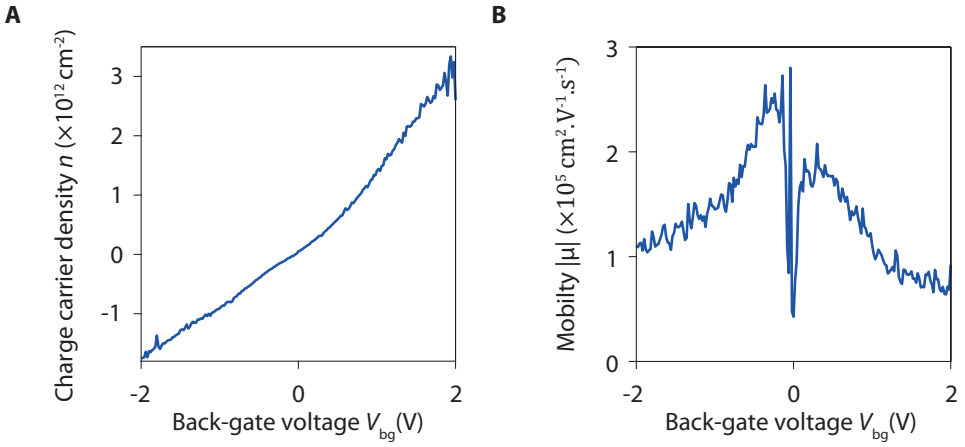

FIGURE 4.14: **Charge carrier density and mobility.** **A**, Charge carrier density n and **B**, mobility μ of the sample computed from the Hall measurements of Fig. 4.12 performed at $B \pm 0.1$ T. In A, the mobility shows non-linear V_{bg} dependence which may arise from the effect of the residual doping induced by the gate electrodes.

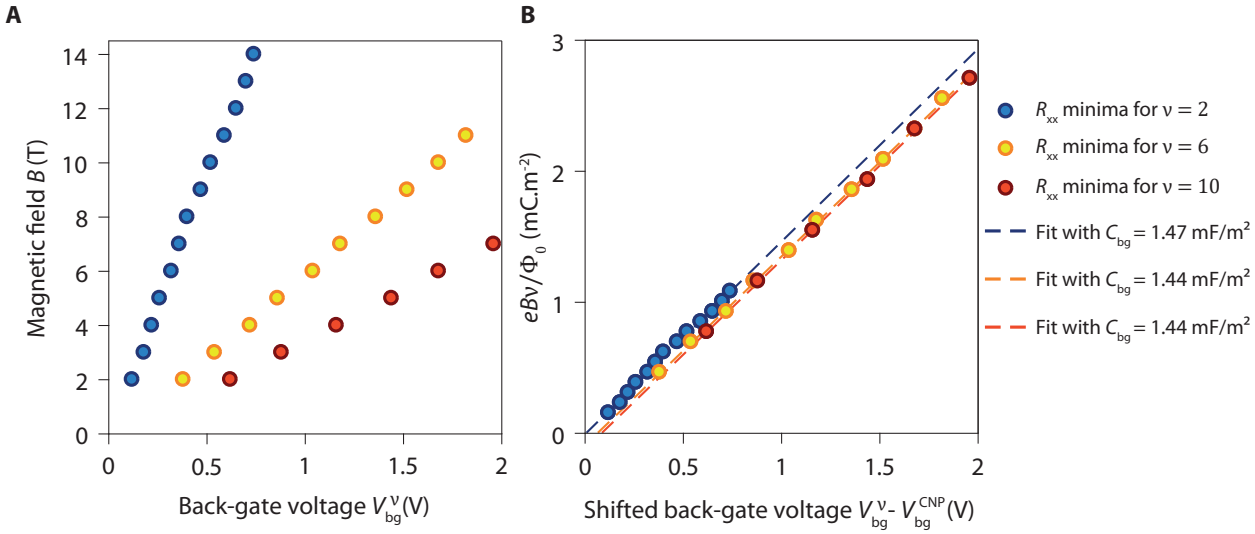

FIGURE 4.15: **Back-gate capacitance estimation from the positions of QH features in Landau fan diagrams.** **A**, Position of R_{xx} minima or of the center of the $R_{xx} = 0\ \Omega$ plateaus for $\nu = 2$, 6, 10 QH states in a Landau fan diagram measured at 4 K. **B**, Same data after suitable rescaling based on eq. (4.1). All data points almost fall on a single straight line. Linear fits for each QH states allow to estimate an average back-gate capacitance $C_{bg} = 1.45\ \mathrm{mF/m^2}$.

We see that all the data points almost collapse on a single line consistent with eq. (4.1). Linear fits for each QH state enable to estimate an average value of the back-gate capacitance $C_{bg} = 1.45\ \mathrm{mF/m^2}$ in agreement with the lower bound obtained with previous method. We note that for $\nu = 6$ and 10 states the linear fit do not pass by the origin at $B = 0$ T but rather at $(V_{bg}^{\nu} - V_{bg}^{\mathrm{CNP}}) = 0.06$ and 0.08 V quantitatively consistent with the small mismatch between the doping in the bulk and below the gate electrodes. Comparatively, the fit for $\nu = 2$ pass by the origin and leads to a slightly large value of C_{bg}. The differences observed simply reflect the fact that the $\nu = 2$ appears at a lower density and closer to the CNP. It is thus more sensitive to the incomplete doping compensation. For latter analysis, we keep this last value of back-gate capacitance $C_{bg} = 1.45\ \mathrm{mF/m^2}$ obtained as it is directly estimated from the QH physics.

4.4 QPC characterization at 14 T

We conclude this chapter by presenting the characterization of the transport through the three QPCs at 14 T. For this purpose, we measured for each QPCs the evolution of the diagonal conductance $G_D = I/V_D$ in the device with respect to both V_{bg} and V_{QPC}. During these measurements the non active split-gate were kept floating.

4.4.1 Evidence that the split gates operate as QPCs

Fig. 4.16 displays the evolution of G_D with V_{QPC} and V_{bg} at 14 T in form of color-coded maps on top of which two series of lines are reported. Horizontal lines indicate the back-gate voltages where integer bulk filling factors ν_b are reached, while diagonal lines indicate points in the $V_{QPC} - V_{bg}$ plane where integer filling factors ν_{sg} are reached beneath the active split gate. These two sets of lines were plotted using the positions of CNP below each split-gates extracted from Fig. 4.9, the capacitance ratios C_{sg}/C_{bg} of Table 4.3 and the back-capacitance C_{bg} estimated from the positions of QH plateaus.

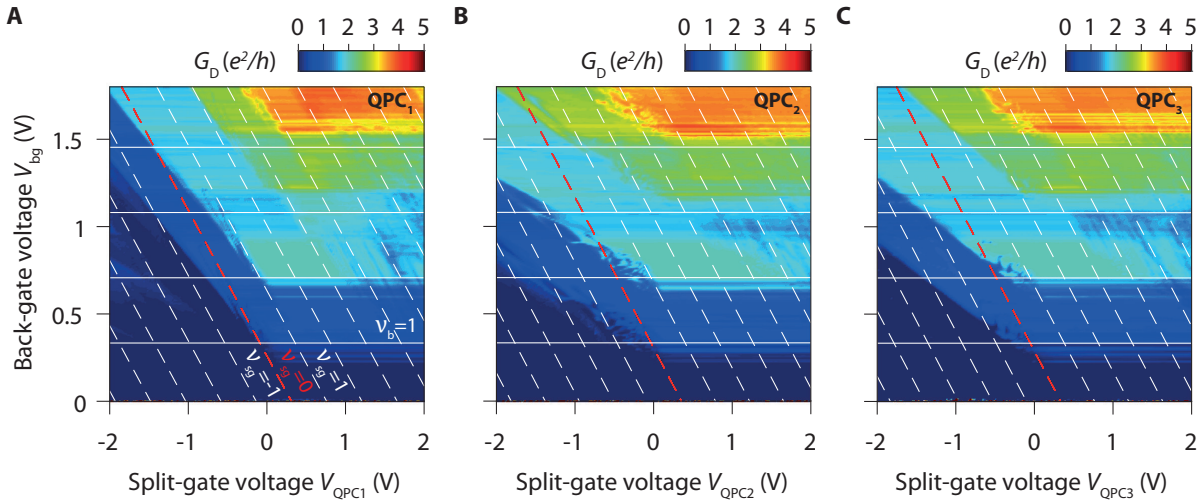

FIGURE 4.16: **QPC conductance maps at 14 T. A, B, C**, Diagonal conductance G_D versus split-gate voltages, V_{QPC}, and back-gate voltages, V_{bg}, for the three QPCs of the device. During a measurement, only one QPC is studied and the two other split gates are kept floating. Lines corresponding to integer bulk filling factors ν_b and integer filling factors beneath the split gate ν_{sg} are reported. The slope of the diagonal stripes corresponds to the capacitance ratio between the QPC constriction and the back gate. This slope is 2.7 and 2.4 times smaller than the zero-field slope for QPC_2 and QPC_3. It is 1.4 smaller for QPC_1 because of the absence of gap between the two split-gates electrodes.

The three maps display all the characteristic features of graphene QPCs operating in the QH regime [16, 211]. In particular, they show diagonal stripes of nearly constant and quantized G_D appearing at $V_{QPC} \leqslant 0$ V. They have smaller slopes than that of the constant ν_{sg} lines. It highlights the existence of smaller capacitive couplings in the constrictions. These couplings can be characterized by capacitance ratios C_{QPC}/C_{bg} (see Table 4.4) which are indeed lower than the ones measured at zero field. Hence, the diagonal stripes identified the gate voltages where it exits a saddle point potential that is characteristic of split gates operating as QPCs [129]. It is worth noticing that such saddle point potential exists even in the QPC_1 despite the short-circuit between split-gate electrodes.

QPC	C_{QPC}/C_{bg}
QPC_1	0.58
QPC_2	0.31
QPC_3	0.36

TABLE 4.4: **QPC characteristics at 14 T**

In the gate-voltages ranges where G_D shows diagonal stripes, we can readily interpret the value of G_D as a measure of the edge channel transmission. Indeed, according to Büttiker, in the QH regime [29]:

$$G_D = \frac{e^2}{h} N_{QPC}, \tag{4.2}$$

where N_{QPC} is number of bulk edge channels transmitted through the QPC constriction. Hence, we see that the latter can be controlled by changing the gate voltages. In particular, one can induce the successive reflections of each bulk QH edge channel by decreasing V_{QPC} at fixed V_{bg}.

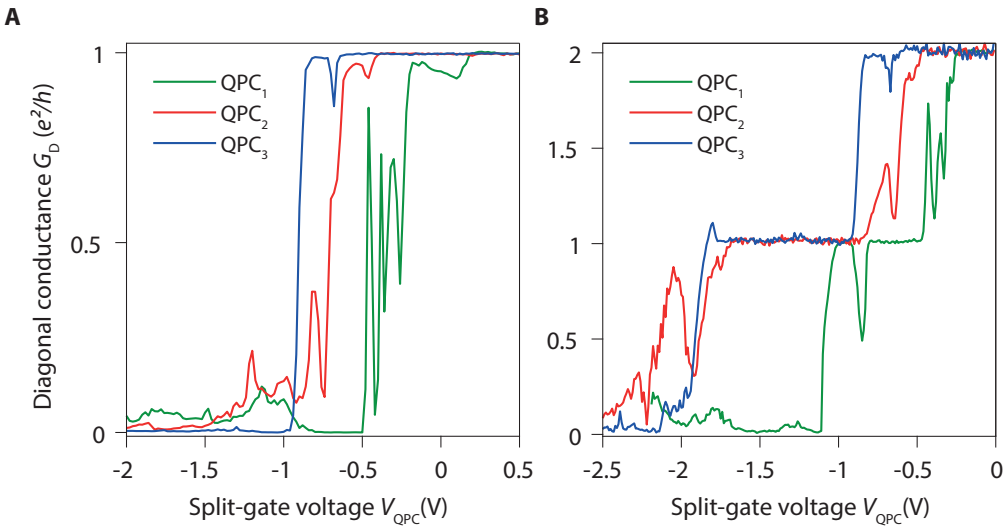

FIGURE 4.17: **QPC transmission curves at 14 T.** Evolution of the diagonal conductance G_D as a function of split-gate voltages V_{QPC} at fixed back-gate voltage V_{bg} of 0.54 V in **A**, and 0.88 V in **B**. During each measurement, only one QPC is active and the two others are either floating or grounded. Quantized conductance plateaus appear after each reflection of a QH edge channel by the active QPC.

Some examples of individual QPC transmission plots obtained at fixed $V_{bg} = 0.54$ V and 0.88 V (bulk filling factors of $\nu_b \simeq 1.6$ and 2.5) are displayed in Fig. 4.17. In Fig. 4.17.A, we see that, for each QPC, G_D displays a $\frac{e^2}{h}$ plateau for $V_{QPC} \geqslant 0$ and drops continuously down to zero when V_{QPC} is lowered below a certain threshold. It shows that, we are able to tune the transmission of the $\nu = 1$ edge channel in each QPC by adjusting the corresponding gate voltage. It allows to set interferometry experiments with this edge channel in all FP cavities. Similarly, in Fig. 4.17.B, $G_D = \frac{2e^2}{h}, \frac{e^2}{h}$ and $G_D \simeq 0$ plateaus appear when V_{QPC} is lowered evidencing the successive reflections of the two edge channels of the zeroth Landau level in each QPC.

4.4.2 Effect of non-active split gates

A more detailed analysis a G_D map and its comparison with the Hall conductance map $1/R_{xy}$ enable to unveil the effect of the floating gate electrodes in the QH regime. In Fig. 4.18.A, when $V_{QPC} \gtrsim 0$ V, the diagonal quantized G_D stripes become horizontal bands. They mark the voltage

ranges where the active QPC is not inducing any backscattering and thus they should coincide with bulk QH plateaus. This is not what we observe we observe in Fig. 4.18.A and Fig. 4.18.B. The horizontal G_D stripes instead appear to be shifted towards higher bulk filling factors.

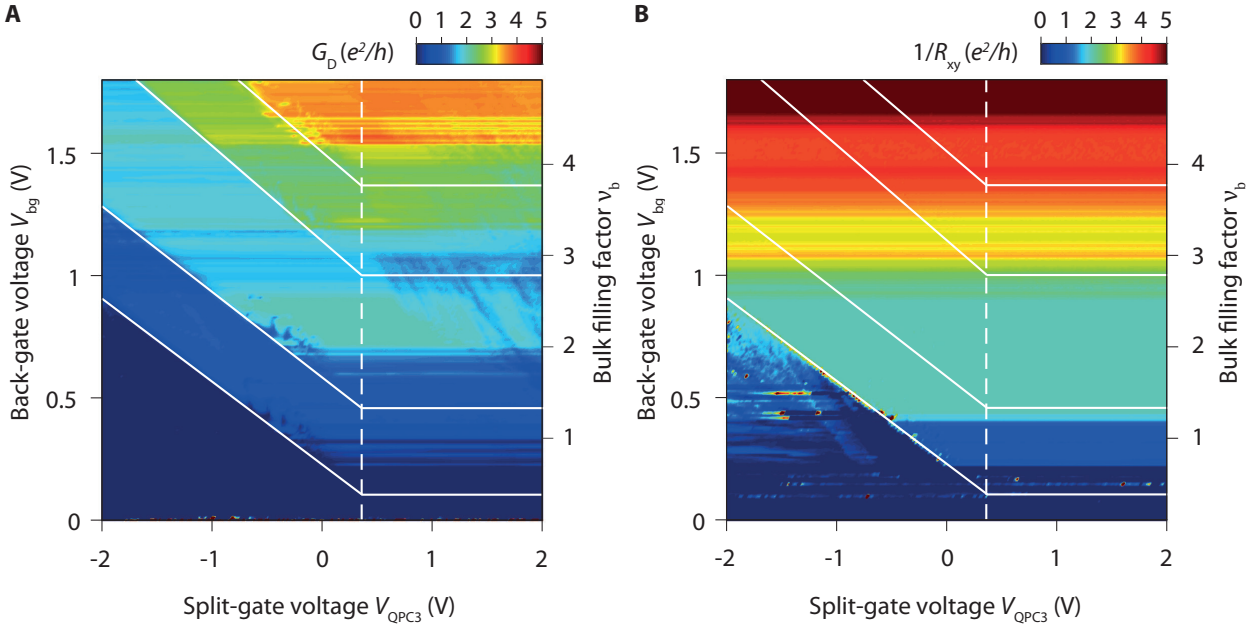

FIGURE 4.18: **QPC_3 map compared to the Hall conductance map at 14 T. A**, Diagonal conductance G_D versus split-gate voltage, V_{QPC}, and back-gate voltage, V_{bg}, for QPC_3. **B**, Inverse of the transverse Hall resistance $1/R_{xy}$ versus V_{QPC} and V_{bg}. The vertical dashed white line indicates the split-gate voltage that compensates the hole doping induced by the split-gate electrodes (isodensity in the bulk and beneath the active split gate) determined from Fig. 4.9. The diagonal lines delineate the diagonal bands of constant G_D in the QPC map that are conductance plateaus given by the number of transmitted edge channels through the QPC. For a single QPC, these lines should become horizontal when they intersect the isodensity line and they should delimit the bulk QH plateaus. The shift between the actual position of the horizontal G_D stripes and their expected positions (given by the plain white lines) reflects the existence of a backscattering induced by the hole-doping below non active split-gates.

This shift can also be evidenced by a simple geometric construction. For a single QPC, the crossover between the diagonal and horizontal bands should occur at split-gate voltages corresponding to the isodensity condition [16, 211], i.e at $V_{QPC3} = 0.36$ V here (white horizontal dotted line). So, by following the transitions between diagonal G_D bands, we can plot the expected positions for the horizontal G_D stripes, represented by white plain lines in Fig. 4.18.A. They indeed coincide with the bulk QH plateaus or integer filling factors as we can see in Fig. 4.18.B.

This construction shows that the shift in the position of horizontal G_D bands is a consequence of having multiple QPCs in series. It can be expected because G_D is measured across the whole device. Hence, its value is also affected by the transmission of non-active split gates and gives the number of edge channels transmitted through the whole device rather than only through the active QPC.

From zero field characterization in section 4.9, we know that the graphene is hole-doped below the non-active QPCs. It induces a backscattering of the innermost QH edge channel at integer ν_b and it consequently results in a lowering of G_D value. This backscattering can be suppressed with a sufficient increase of the whole graphene doping. This is consistent with the upward shift of the horizontal bands what we observed experimentally. We can then assess that this shift originates from the hole-doping below the non active split-gates.

4.4.3 Consequences for interferometry experiments

Considering the above analysis, one must be careful while setting an interferometry experiment because the non-active split gates can generate undesirable backscattering for the interfering edge channel. To prevent it, one must either compensate the induce hole-doping by application of a suitable split-gate voltage or work at high enough back-gate voltages.

For all interferometry experiments presented in the next chapters, we worked at back-gate voltage where the QPC transmission plots show well-quantized plateaus despite the contribution of the two non-active split gates. More particularly, for the experiments performed at 14 T, we used back-gate voltages close to $V_{\mathrm{bg}} = 0.54$ V and 0.88 V where the transmission plots displayed in Fig. 4.17 were measured. In both cases, we measured $1/R_{\mathrm{xy}} = \frac{2e^2}{h}$ indicating that two edge channels were propagating in the bulk. At $V_{\mathrm{bg}} = 0.54$ V the inner edge channel was fully back-reflected by the non active QPC while at $V_{\mathrm{bg}} = 0.88$ V it was fully transmitted. In each case, the non-active QPC did not have influence on the AB interference measured by partially closing the two other QPCs.

Chapter 5

Graphene QH Fabry-Pérot interferometry in the integer regime

Contents

In this chapter, we demonstrate that high mobility graphene devices equipped with QPCs in series can be operated as QH FP interferometers in the integer regime. We present typical interferometry experiments evidencing the existence of quantum interference. We further show that graphene QH FP interferometers operate in the AB regime even when they have few micron squares areas. We then investigate the robustness of the quantum interference through the study of bias-induced oscillations and of the temperature dependence of AB oscillations.

All the measurements presented in this chapter were obtained on BNGr74 sample, presented in previous chapter, except the results discussed in section 5.1.4.

5.1 Aharonov-Bohm interference in graphene QH FP interferometers

In this section, we demonstrate the existence of AB interference in graphene split-gated devices and discuss the absence of Coulomb-dominated oscillations even in the small size devices.

5.1.1 Gate-induced oscillations

We first focus on experiments where quantum interference are unveiled by sweeping the plunger-gate voltage at fixed magnetic field. We show typical results obtained in the three interferometers. We then discuss the electrostatics of the plunger gate and show that it gives first indications of the origin of the oscillations.

High visibility plunger-gate-induced oscillations

We begin by presenting a typical experiment performed at 14 T in the small FP interferometer of BNGr74 sample. The back-gate voltage was set to 0.533 V corresponding to a bulk filling factor $\nu_b = 1.5$ and the transmissions of the outer edge channel through the QPC_2 and QPC_3 were respectively set to 60 % and 47 %. Fig. 5.1 displays the evolution the diagonal resistance R_D with the voltage V_{pg2} applied on one of the two plunger gate between the two QPCs (see Fig. 4.5).

In Fig. 5.1.C, we see that a continuous decrease of V_{pg2} induces clear resistance oscillations. These oscillations appear starting from $V_{pg2} \simeq -0.3$ V and persist over the full range of voltage spanned down to $V_{pg2} = -4$ V. They evidence the existence of quantum interference in the device whose origin remains to determine. Thus, we see that the device indeed operates as a QH FP interferometer. The observation of more than 280 oscillations in Fig. 5.1.C shows that the interferometer is very stable and widely tunable with the plunger gate. The oscillations have a large amplitude of several tenths of kiloOhms evidencing the high level of coherence in the device. It can also be assessed from the visibility $\mathcal{V}$ of the oscillations given by:

$$\mathcal{V} = \frac{R_D^{max} - R_D^{min}}{R_D^{max} + R_D^{min}}, \tag{5.1}$$

where R_D^{max} are respectively the resistance minimum and maximum value. $\mathcal{V}$ is larger than 40 % in this experiment demonstrating that the quantum transport is highly coherent in this device.

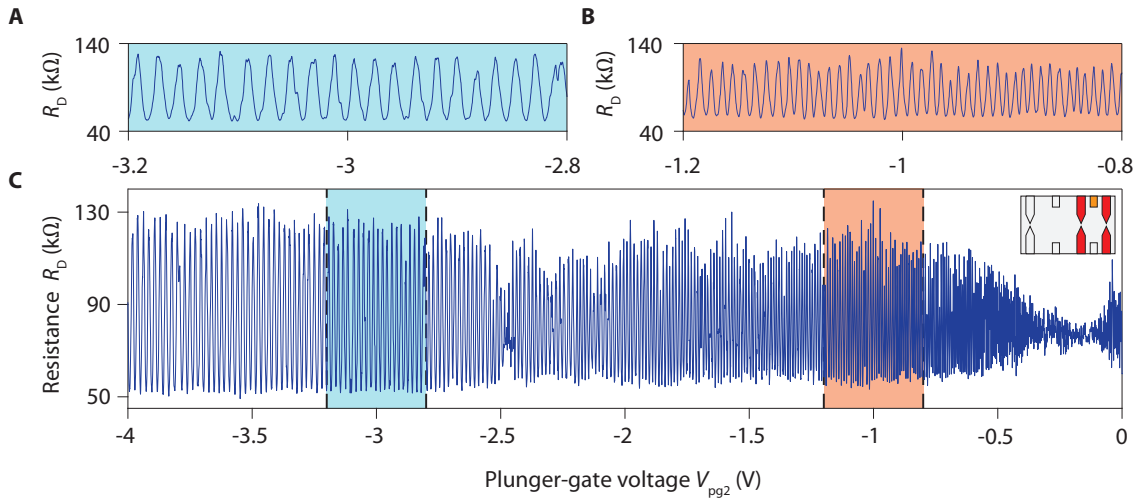

FIGURE 5.1: **High visibility gate-tunable quantum interference in the small FP interferometer. A, B, C,** Diagonal resistance oscillations observed with change of plunger-gate voltage V_{pg2} for an interferometry experiment performed in the small FP interferometer at 15 mK and 14 T. The back-gate voltage is set to $V_{bg} = 0.533$ V corresponding to a bulk filling factor $\nu_b = 1.5$ and the QPCs partially reflect the outer edge channel. In A and B, resistance oscillations observed over small V_{pg2} ranges. In C, oscillations over the full range of voltage spanned. Inset: Schematic of the gates configuration. Active QPCs and plunger gates are respectively represented in red and orange.

Such large resistance oscillations persisting all along a large range of plunger-gate voltage can also be observed in the medium and large FP interferometers as displayed in Fig. 5.2. They demonstrate that the two other devices are also operating as QH FP interferometers. The visibility of the oscillations in each case is smaller than in the experiment with the small FP cavity but it remains relatively high as it reaches respectively about 20 % and 15 % for the medium and the large interferometers. A quantitative analysis of the influence of the FP dimensions on the coherence is addressed in section 5.3.3.

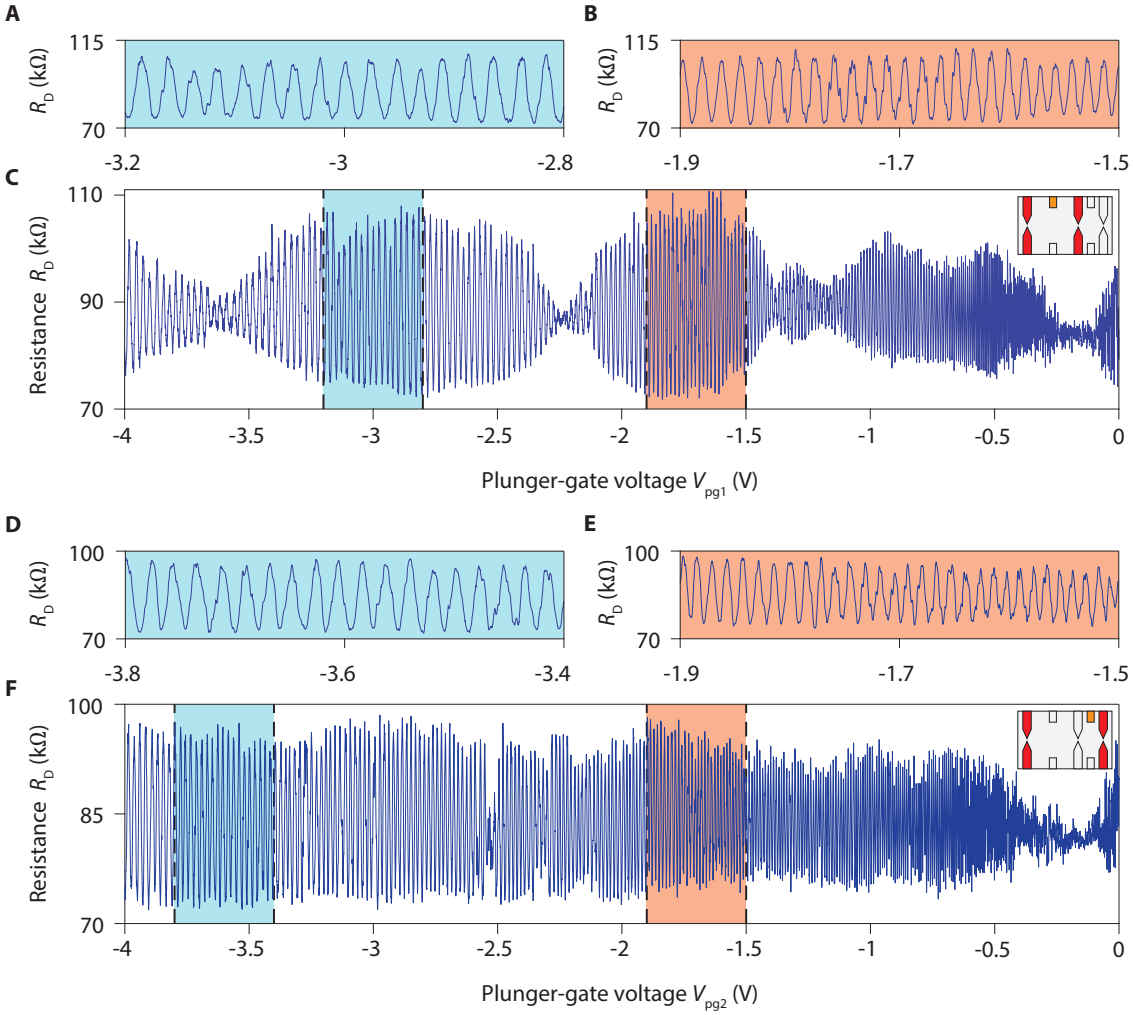

FIGURE 5.2: **High visibility gate-tunable quantum interference in the medium and large FP interferometers.** Diagonal resistance oscillations observed versus plunger-gate voltages V_{pg} for interferometry experiments performed in **A**, **B**, **C**, the medium and in **D**, **E**, **F**, the large interferometers (same experimental conditions than Fig. 5.1). Insets: Schematics of the gates configuration. Active QPCs and plunger gates are respectively represented in red and orange.

Evolution of the frequency of the oscillations with the plunger-gate voltage

In Fig. 5.1.C, we see that the period of the oscillations ΔV_{pg2} increases when V_{pg2} is lowered. This observation is corroborated by looking at the oscillations on smaller voltage ranges in Fig. 5.1.A and Fig. 5.1.B. Similar evolutions are also observed in experiments performed in the two other interferometers shown in Fig. 5.2.

The evolution of the oscillations period can be tracked by computing the Fourier transform of the oscillations restricted to a small V_{pg2} window that is slid over the entire V_{pg2} range. The evolution of the resulting Fourier amplitude as a function of the plunger-gate voltage V_{pg2} and the plunger-gate-voltage frequency is shown in Fig. 5.3.

In this color-coded map, a clear peak at $f_{pg2} = 1/\Delta V_{pg2}$ is observed all along the voltage range spanned together with an additional peak corresponding to the second harmonic mostly visible at large negative V_{pg2} (see individual linecut in inset of Fig. 5.3). We note that the emergence of

the oscillations at $V_{pg2} \simeq -0.3$ V coincides with the charge neutrality below the plunger-gate (red dashed line).

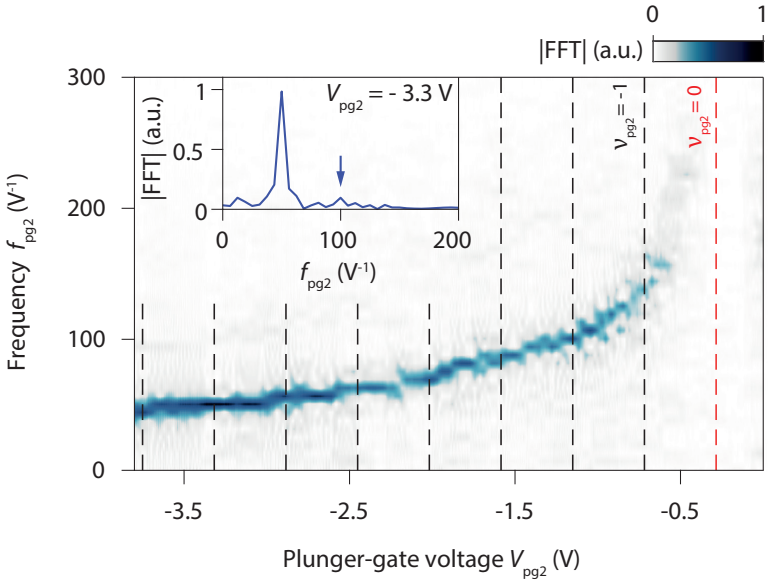

FIGURE 5.3: **Fourier transform of gate-induced oscillations.** Evolution of the Fourier amplitude of the resistance oscillations shown in Fig. 5.1.C with the plunger-gate voltage V_{pg2} and the plunger-gate-voltage frequency f_{pg2}. The vertical dashed lines indicate when the filling factor beneath the plunger gate ν_{pg2} is an integer. Oscillations with a small voltage period emerge at $V_{pg2} \simeq -0.3$ V corresponding to the CNP below the plunger gate. Inset: Linecut at $V_{pg2} = -3.3$ V evidencing the presence of a second harmonic (blue arrow).

The frequency f_{pg2} of the main peak in Fig. 5.3 clearly decreases when V_{pg2} is lowered confirming the tendency previously observed. The frequency drops fastly around $V_{pg2} \simeq -0.3$ V and it continues to decrease as V_{pg2} is lowered but more and more slowly. This evolution can be intuitively understood assuming the device is operating in the AB regime.

Initially, at $V_{pg2} = 0$ V, the interfering outer edge channel propagates below the plunger gate along the graphene edges as shown in Fig. 5.4.A. As V_{pg2} is decreased, the CNP is reached below the plunger gate at $V_{pg2} \simeq -0.3$ V and the interfering outer edge channel is expelled out from the area beneath the plunger gate. This expulsion occurs within a small V_{pg2} range and leads to a rapid change of the area enclosed by this edge channel. It results in fast oscillations.

At lower plunger-gate voltages, holes are accumulated below the gate and the interfering edge channel propagates along the pn interface which follows the gate edges (Fig.5.4.B and Fig.5.4.C). The oscillations then arise because a decrease of V_{pg2} leads to a smooth displacement of the pn junction inward the FP cell. The progressive distancing (Fig.5.4.C) of the pn junction from the gate edges also results in a reduction of the capacitive coupling that explains the continuous decrease of the oscillations frequency observed. Therefore, the V_{pg2}-dispersion of the oscillations frequency simply reflects the plunger-gate electrostatics.

We systematically observed such dispersions for experiments performed in different samples (see section 5.1.4) and for experiments performed with different conditions within the same FP interferometer. As an example, Fig. 5.5 displays the Fourier amplitude maps obtained for measurements performed in the small FP interferometer, at different magnetic fields and with different interfering edge channels. They all display the same typical features. It evidences the common origin of such dispersion. Importantly, we observe that at fixed V_{pg2}, the frequency f_{pg2} of the oscillations increases with the magnetic field B.

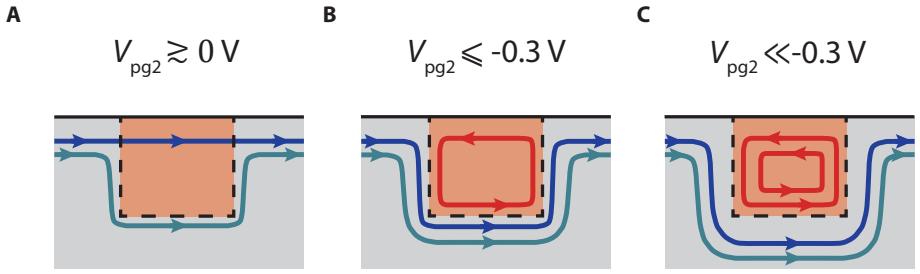

FIGURE 5.4: **Tuning of the edge channel trajectory with the plunger-gate at negative voltages.** Schematics of edge channel trajectories in the vicinity of the plunger gate. **A**, When $V_{pg2} \gtrsim 0$ V, the filling factor below the plunger gate is $\nu_{pg2} \lesssim 0.7$. Hence, the interfering outer edge channel (navy blue line) can propagate along the graphene edges (plain black line) beneath the plunger gate (orange) while the inner edge channel (green-blue) must circulate outside the gated region following the gate edges. **B**, As the CNP is reached below the plunger gate ($V_{pg2} \simeq -0.3$ V), the outer channel is expelled outside the gated region and propagates close to the gate edges. **C**, At more negative voltage, the interfering edge channel circulates further away from the gate edges because the pn junction shifts towards the bulk of the interferometer.

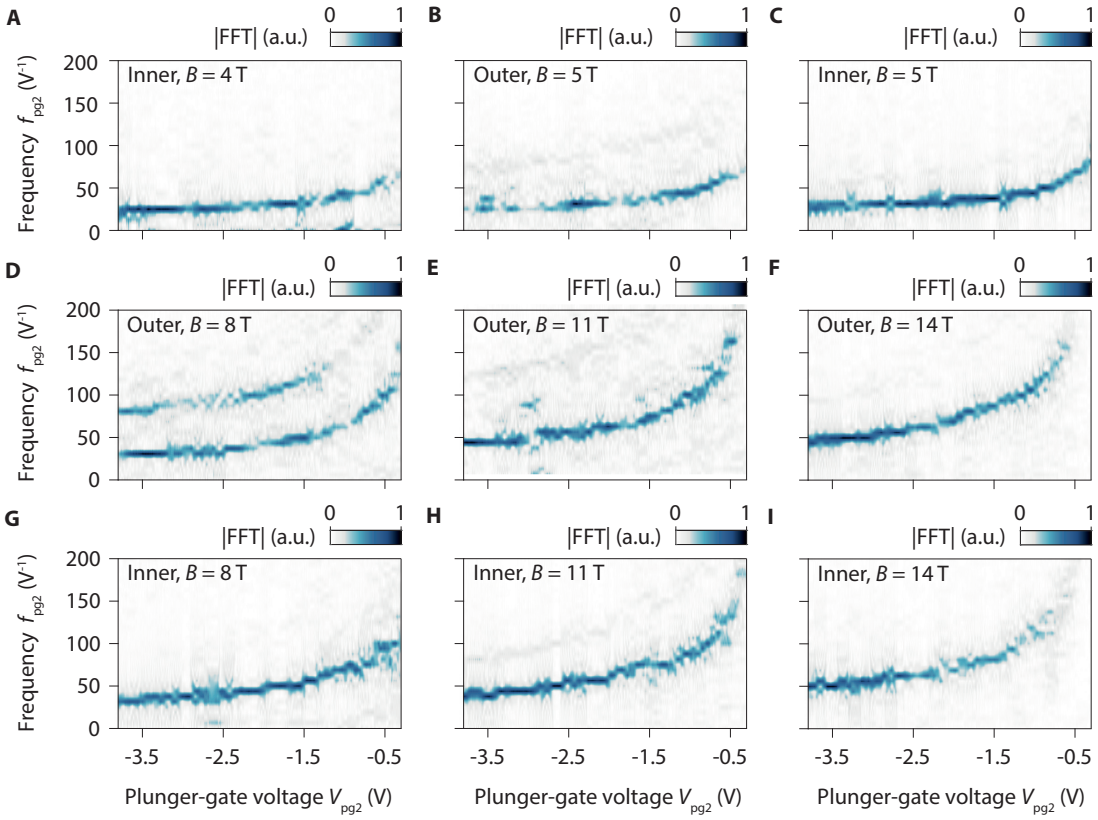

FIGURE 5.5: **Fourier transforms of resistance oscillations for different experimental conditions.** Fourier amplitudes of the resistance oscillations observed in the small interferometer for different configurations of magnetic field and interfering edge channel.

The study of the magnetic-field dependence of the oscillations period allows to probe their origin. In pure AB regime, the only effect of the plunger gate is to modulate the effective surface A of the interferometer and a voltage period $\Delta V_{pg2} = 1/f_{pg2}$ corresponds to change of AB area

by $\Delta A = \frac{\Phi_0}{B}$. Besides, we can assume that the area variation scales linearly with the plunger-gate voltage in the limit of small voltage changes [148, 149]. Thus, we can write $\Delta A = \alpha \Delta V_{pg2}$ where α is the gate lever arm which accounts for the evolution of the area enclosed by the interfering edge channel with the plunger-gate. Hence, in the AB regime, we expect:

$$\frac{f_{pg2}}{B} = \frac{\alpha}{\Phi_0}. \tag{5.2}$$

As a consequence, all the frequencies normalized by the magnetic field should collapse on the same curve. In Fig. 5.6, the evolution of the rescaled frequencies f_{pg2}/B is plotted as a function of $\tilde{V}_{pg2} = V_{pg2} - V^*_{pg2}$, i.e. the plunger-gate voltage shifted by V^*_{pg2} the voltage associated with expulsion of the outer or inner edge channel from the area beneath the plunger gate (i.e. $\nu_{pg2} = 0$ or 1 respectively). All the data points corresponding to the different experiments indeed collapse into a single curve, except for the experiments at 4 T and 5 T which are shifted to higher rescaled frequencies. It is in good agreement with the above predictions and it provides a first indication that the device operates in the AB regime. It also shows that the plunger-gate allows to tune the magnetic flux in the FP interferometer over wide ranges of both plunger-gate voltages and magnetic fields.

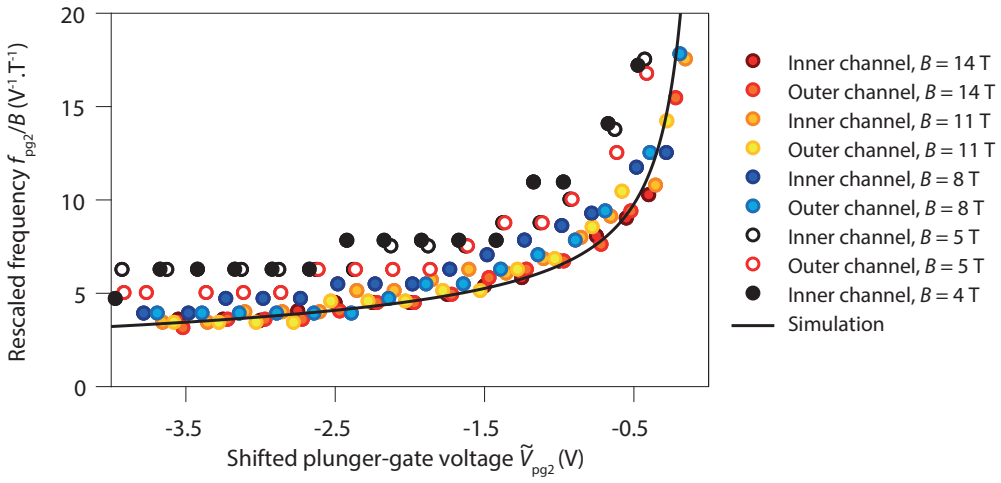

FIGURE 5.6: **Magnetic field dependence of the frequency of gate-induced oscillations.** Evolution of the main peak frequency f_{pg2} rescaled by the magnetic field B as a function of $\tilde{V}_{pg2}$, the plunger-gate voltage shifted with respect to the voltage that expels the interfering edge channel in several experiments. The data points for different interferometry experiments collapse onto a single curve, except for the low field data. The solid black line is an electrostatics simulation of the pn junction displacement with the plunger-gate voltage.

Plunger-gate electrostatics

The evolution of the lever arm α with the plunger-gate encodes the displacement of the pn junction with the lowering of V_{pg2}. To evidence it, we present in Fig. 5.7 the results of 2D electrostatic simulations carried out by Hermann Sellier a member of QuNES team. These simulations consist in computing the electrostatic potential $V(x)$ in a graphene sheet nearby a plunger gate in the 2D geometry depicted in Fig. 5.7.A. They were performed for different values of the plunger-gate voltage V_{pg} and at fixed back-gate voltage V_{bg} allowing to determine the evolution of the position of the pn interface x_{pn} with V_{pg}.

For a given set of gate voltages V_{pg} and V_{bg}, the solution $V(x)$ can be calculated self-consistently assuming that the local charge density $\sigma(x)$ is given by:

$$\sigma(x) = -e\,\mathrm{sign}\big(V(x)\big)\,\frac{e^2V(x)^2}{\pi\hbar^2v_F^2}, \tag{5.3}$$

where $v_F = 10^6$ m/s is the Fermi velocity in graphene. Once the solution is computed for a given couple of voltages (V_{pg}, V_{bg}), one can extract the local plunger-gate capacitance $C_{pg}(x)$ (which includes quantum capacitance contribution) that is given by:

$$\sigma(x) = -C_{bg}\left(V_{bg} - V(x)\right) - C_{pg}(x)\left(V_{pg} - V(x)\right), \tag{5.4}$$

where $C_{bg} = \epsilon_0\epsilon_{BN}/d_b$ is the back-gate geometric capacitance that is fixed by the bottom h-BN thickness d_b and its dielectric constant ϵ_{BN}.

This local plunger-gate capacitance $C_{pg}(x)$ is actually independent of the values taken for V_{pg} and V_{bg} in the simulation. Therefore, one can use the vale of $C_{pg}(x)$ extracted from one simulation to calculate $V(x)$ for another set of gate voltages using eq. (5.4). It enables to compute the potential for other gate voltages without the need of solving again the full self-consistent electrostatic problem. This efficient approach is based on the work of Liu who demonstrated that such graphene electrostatics problems could be solved equivalently via iterative resolution Poisson-Dirac problem or via determination of the local capacitances [228].

For our simulations, the self-consistent problem was solved using a modified version of MaxFEM (http://www.usc.es/en/proxectos/maxfem), an electromagnetic simulation software based on the finite-element method. It was calculated on a mesh grid extending over of 1 μm in vertical and 2 μm in horizontal that was computed using Gmsh (http://gmsh.info). The simulations were performed using the experimental values of h-BN thicknesses ($d_t = 22$ nm and $d_b = 18$ nm for the top and bottom h-BN), of the dielectric constant ($\epsilon_{BN} = 3$), and assuming that the graphite was behaving as a perfect metal. The back-gate voltage was fixed at $V_{bg} = 0.53$ V corresponding to the conditions of experiments displayed in Fig. 5.1.

The spatial variation of the potential energy $E(x) = -eV(x)$ in the graphene nearby the plunger gate that was computed for different plunger-gate voltages is plotted in Fig. 5.7.B. The intersects between the $E(x)$ plots and the zero-energy line give the positions x_{pn} of the pn interface for different V_{pg}. It moves away from the gate edge ($x = 0$) as V_{pg} is decreased (the potential energy beneath the gate increased). The corresponding evolution of x_{pn} with V_{pg} is plotted in Fig. 5.7.C. In this figure, the formation of the pn interface occurs at -0.65 V corresponding to the CNP below the plunger gate. This value is consistent with the experiments where oscillations appears at $V_{pg} \simeq -0.3$ V taking into account the hole doping of induced by the palladium electrodes ($V_{QPC}^{CNP} \simeq 0.38$ V). From these plots, the displacement rate of the pn interface $\frac{dx_{pn}}{dV_{pg}}$ can be computed and its evolution with V_{pg} is displayed in Fig. 5.7.D. It recovers all the features observed experimentally : the formation of the pn junction followed by its fast displacement when it is expelled outside the area covered by the plunger gate, and a decrease of the displacement rate of the pn interface as more and more negative V_{pg} are applied.

The displacement rate computed enables to calculate the non-linear lever arm $\alpha = L_{pg} \times \frac{dx_{pn}}{dV_{pg}}$ of the plunger gate where L_{pg} is the contour length. The quantity α/Φ_0 can be directly compared to the rescaled frequencies f_{pg2}/B. It is represented in Fig. 5.6 by the black line and it agrees quantitatively with the experimental points. This demonstrates that the evolution of the oscillations frequency f_{pg2} with V_{pg2} is only determined by the displacement of the pn interface. It confirms that the effect of the plunger gate in our to device is only to modulate the effective surface of the interferometer as one would expect in the AB regime.

Note that L_{pg} remains an adjustable parameter because the position of the graphene edges is known with an uncertainty of ± 150 nm. To reproduce the measurements a plunger-gate contour of $L_{\mathrm{pg}} = 1.8$ μm was used in good agreement with the expected lithographic length of 1.5 μm.

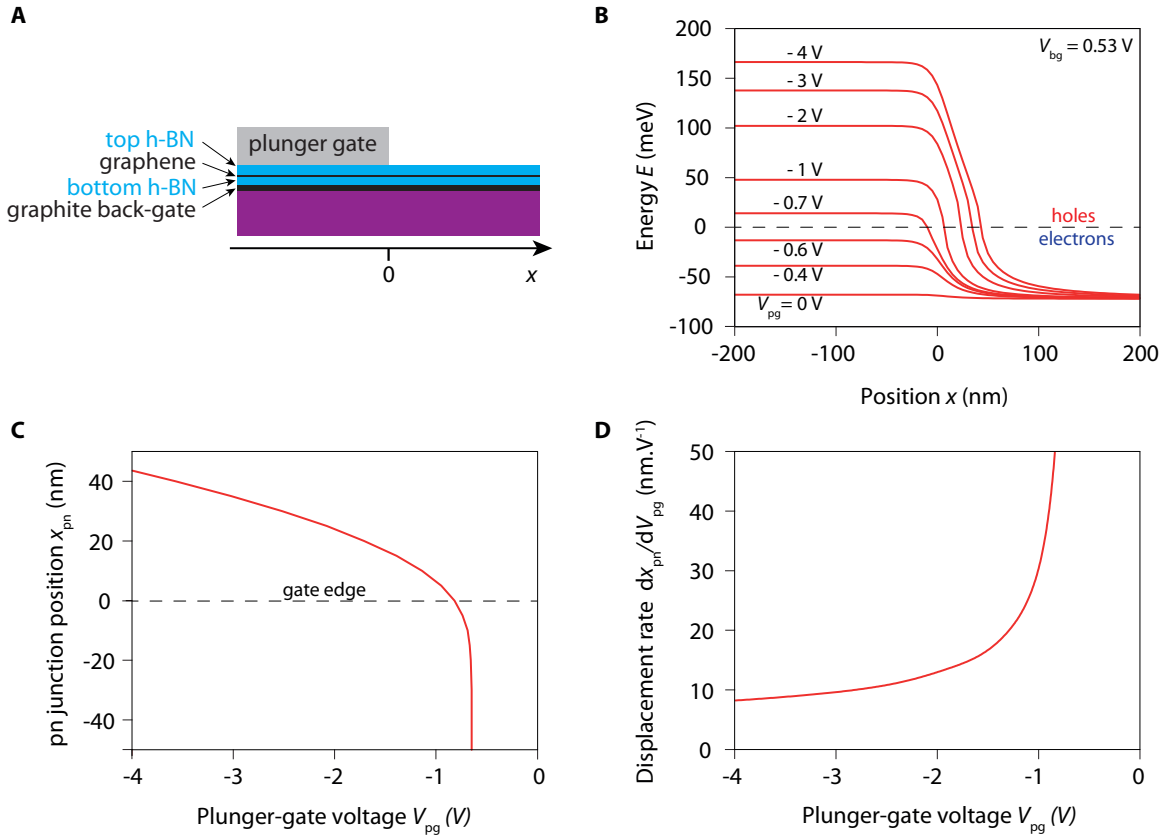

FIGURE 5.7: **Simulations of plunger-gate electrostatics. A**, Schematic of the electrostatics problem considered. **B**, Self-consistent electrostatic energy profiles $E = -eV$ in the graphene flake for a back-gate voltage $V_{\mathrm{bg}} = 0.53$ V and different plunger-gate voltages V_{pg}. **C**, Position of the pn interface with respect to the gate edge as a function of V_{pg}. **D**, Displacement rate of the pn interface $\frac{\mathrm{d}x_{\mathrm{pn}}}{\mathrm{d}V_{\mathrm{pg}}}$ with respect to V_{pg}.

5.1.2 Magnetic-field-induced oscillations

To demonstrate that the devices are operating as QH FP interferometers we must show that resistance oscillations can not only be generated by changing the plunger-gate voltage but also by changing the magnetic field. For this purpose, we performed interferometry experiments where the plunger-gate voltage was kept constant and the magnetic field was swept continuously at the minimum rate available with the magnet (0.18 mT/s) around 14 T. Fig. 5.8 presents the evolution of R_{D} measured in experiments with both outer or inner edge channel interfering.

Clear resistance oscillations appears when the magnetic field is varied except in Fig. 5.8.F where the oscillations are irregular and have a small amplitude. This is expected considering that this last experiment was performed in the largest and the least coherent device. Also this experiment was performed with the inner edge channel interfering resulting in a smaller oscillations amplitude compared to that measured with the outer edge channel interfering. In the medium and large interferometers, two sets of coexisting oscillations can be distinguished: the overall signal appears as rapid oscillations with small magnetic field period on top of an oscillating background with a much larger magnetic field period. The period of the fast resistance oscillations decreases with the size of the FP interferometer.

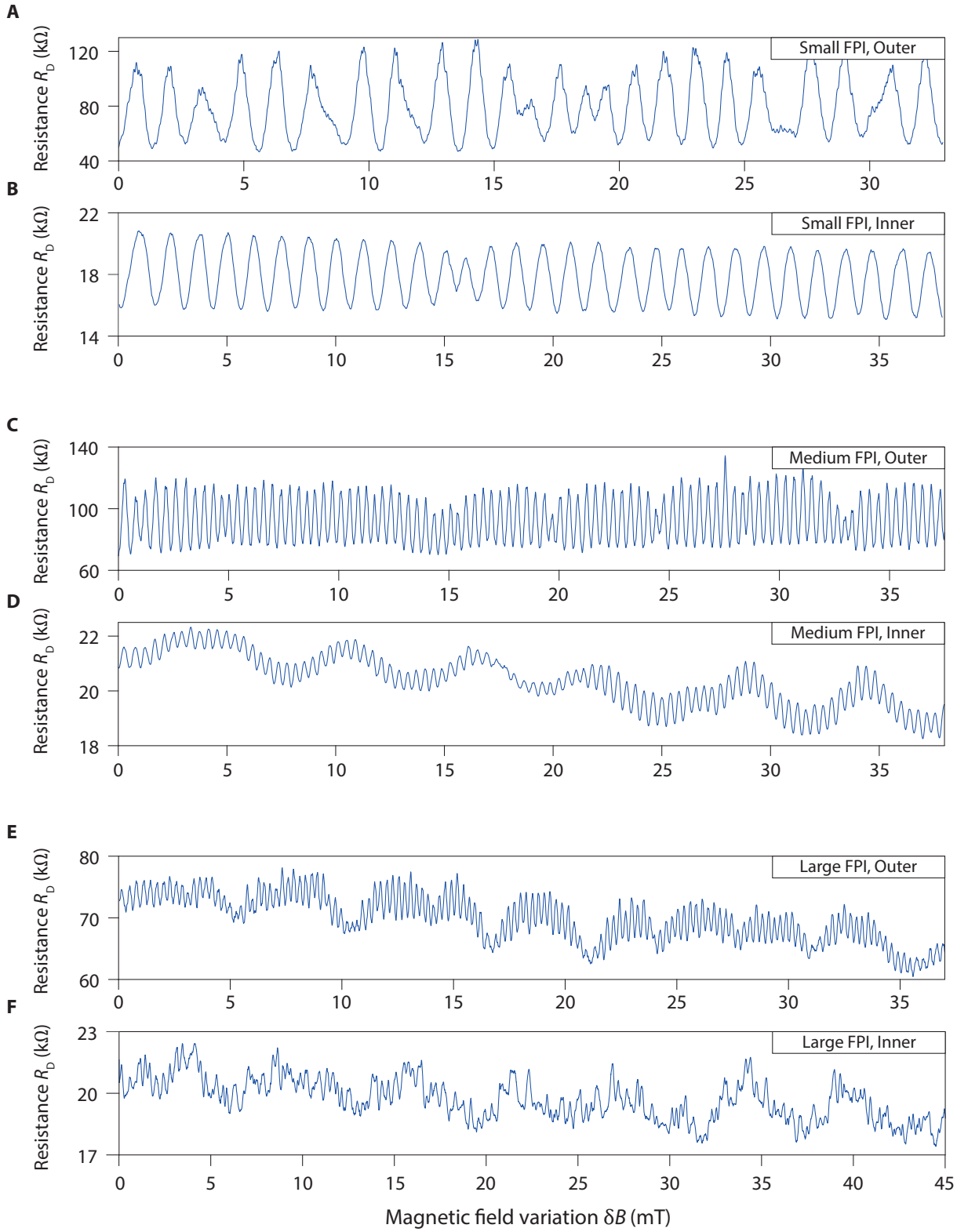

FIGURE 5.8: **Magnetic-field-induced oscillations at 14 T.** Diagonal resistance oscillations observed by sweeping the magnetic field around 14 T in the three QH FP interferometers for experiments performed **A**, **B**, **C**, with the outer edge channel and **D**, **E**, **F**, with the inner edge channel.

At this point, we already notice that oscillations are visible even in experiments with the outermost edge channel is interfering. It discards the possibility that the devices operate in the Coulomb-dominated regime. Indeed, in this regime, one should observe no magnetic field dependence of resistance oscillations when the outermost edge channel is interfering [148, 149, 164]. Thus, these measurements already show that the devices operate either in the AB or intermediate regime.

To identify the origin of each sets of oscillations, we computed the Fourier transform of each field sweep. They are displayed in Fig. 5.9 and they are typically composed of one or two peaks. We now focus on the main peaks marked by the red arrows and on the secondary features marked by the blue arrows. Their positions in the reciprocal space are respectively reported in Table 5.1 and Table 5.2 as well as the corresponding magnetic field periods and the equivalent Aharonov-Bohm surfaces.

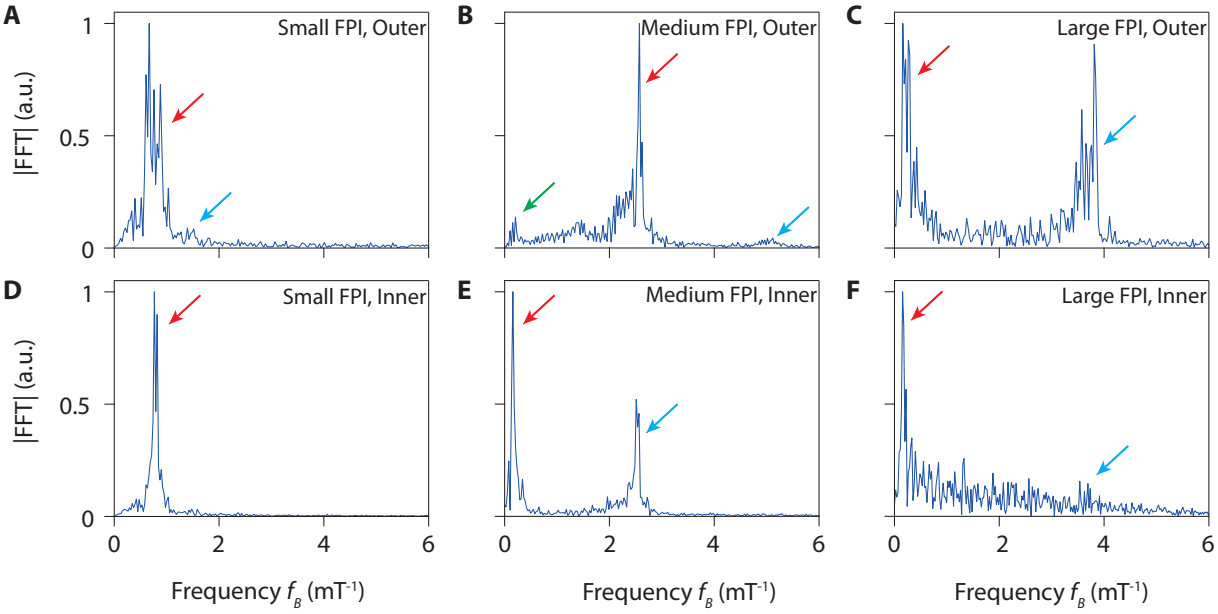

FIGURE 5.9: **Fourier amplitudes of the magnetic-field-induced oscillations at 14 T.** Fourier amplitudes of the resistance oscillations displayed in Fig. 5.8 versus magnetic-field frequency f_B.

For the experiments in the small interferometers, the main peak frequencies correspond to AB areas of 3.1 and 3.3 μm^2 which are close to the lithographic area of FP cavity $A_{\text{geo}} = 3.1$ μm^2. It shows that the resistance oscillations emerge from the winding of the electrons in the FP cavity as expected for AB oscillations. A small second harmonic peak is even distinguishable in the spectrum corresponding to the experiment with the outer edge channel. Likewise, for experiment with the outer edge channel in the medium interferometer, the frequencies of the main and second peaks correspond to areas of 10.6 and 21.1 μm^2 which can be readily attributed to interference processes corresponding to one and two loops inside the medium FP cavity.

For the experiment in the medium interferometer with the inner edge channel and the experiments in the large interferometer, the situation is different. The main Fourier peaks appear at low frequencies and correspond to oscillations with large magnetic field period ranging typically between 3 and 7 mT. They can be attributed to the background oscillations discussed above. The equivalent AB areas range between 0.5 and 1.3 μm^2. It roughly fits with once or twice the area covered by one split gate (1.8/2.7 μm$\times$0.3 μm$=$ 0.5/0.8 μm^2). Yet, the exact origin of such oscillations is unclear. It may arise from a periodic modulation of the transmission of the (non active) split gates with the magnetic field which would also explain the periodic visibility drop observed

in Fig. 5.8.E. We note that such low frequency modulation also exists in the experiment with the outer edge channel interfering in the medium interferometer (green peak in Fig. 5.9.B).

In these experiments, the second Fourier peaks are more easily understood as they appears at frequencies corresponding to AB areas of 10.5, 15.2 and 14.9 μm^2 in good agreement with the lithographic area of the devices used in each experiments. It shows that the fast magnetic field oscillations with the small periods emerge from interference processes corresponding to one lop inside either the medium or the large FP cavity. We nevertheless note that the blue peak in Fig. 5.9.E hardly emerges from the noisy background reflecting the irregular form of the oscillations in Fig. 5.8.F.

QH FP cavity	Interfering edge channel	Main peak frequency f_B (mT^{-1})	Corresponding period ΔB (mT)	AB area A_{AB} (μm^2)	Origin
Small	Outer	0.74 ± 0.17	1.35 ± 0.31	3.1 ± 0.7	Interferometer
Small	Inner	0.79 ± 0.03	1.27 ± 0.05	3.3 ± 0.1	Interferometer
Medium	Outer	2.57	0.39	10.6	Interferometer
Medium	Inner	0.16	6.25	0.7	Split gates ?
Large	Outer	0.23 ± 0.07	4.35 ± 1.32	1.0 ± 0.3	Split gates ?
Large	Inner	0.18 ± 0.04	5.56 ± 1.23	0.7 ± 0.2	Split gates ?

TABLE 5.1: **Fourier analysis of magnetic-field-induced oscillations: main peaks.** Frequencies f_B of the main peaks (red arrows) in the Fourier amplitudes of oscillations displayed in Fig. 5.8, corresponding periods ΔB and Aharonov-Bohm areas $A_{AB} = \Phi_0/\Delta B$. The uncertainties are given when there are two close-by peaks or when the peak is wide and when we can approximate its width.

QH FP cavity	Interfering edge channel	Second peak frequency f_B^* (mT^{-1})	Corresponding period ΔB^* (mT)	AB area A_{AB}^* (μm^2)	Origin (+ Comments)
Small	Outer	≈ 1.5	≈ 0.67	≈ 6.2	Second harmonic (hardly visible)
Small	Inner	X	X	X	X
Medium	Outer	≈ 5.1	≈ 0.20	21.1	Second harmonic
Medium	Inner	2.54 ± 0.03	0.39 ± 0.01	10.5 ± 0.1	Interferometer
Large	Outer	3.67 ± 0.25	0.27 ± 0.02	15.2 ± 1.0	Interferometer
Large	Inner	≈ 3.6	≈ 0.28	≈ 14.9	Interferometer (hardly visible)

TABLE 5.2: **Fourier analysis of magnetic-field-induced oscillations: second peaks.** Frequencies f_B^* of the second peaks (blue arrows) in the Fourier amplitudes of oscillations displayed in Fig. 5.8, corresponding periods ΔB^* and Aharonov-Bohm areas $A_{AB}^* = \Phi_0/\Delta B^*$. The uncertainties are given when there are two close-by peaks or when the peak is wide and when we can approximate its width.

5.1.3 Evidencing the origin of the oscillations

The nature of quantum interference observed, i.e AB or Coulomb dominated, can be straightforwardly determined by measuring the evolution of resistance oscillations with both the magnetic field and the plunger-gate voltage. Indeed, the pattern formed by the oscillations is directly related to the sensitivity of the device to charging effects [147–149, 164, 165] as discussed in chapter 3 section 3.3.1.

Thus we systematically investigated the magnetic-field dependence of the gate-induced oscillations. To do that we recorded the evolution of R_D oscillations generated by sweeping the

plunger-gate voltage regularly while letting the magnetic field decay spontaneously with the magnet in persistent mode (decay rate of 0.14 mT/hour at 14 T).

This approach was preferred over measurements performed by changing directly current supplied in the magnet between each sweep because the magnet resolution is about 0.2 mT. It is comparable to the AB period expected for the large interferometer which prevents the observation magnetic-field-induced oscillations generated when the field is changed discretely. Also, when the current is delivered inside the magnet it generates some noise which affects the visibility of the oscillations.

Fig. 5.10 presents the result of such measurements performed at 14 T in the three interferometers for both interference with the inner and the outer edge channel. In all these color-coded maps (sometimes referred as "pyjama" maps), extrema of R_D form diagonal lines with negative slopes in the $B - V_{pg}$ plane. It unambiguously demonstrates that the three different FP interferometers are operating in the AB regime. It is worth noting that the small FP interferometer is also operating in AB regime despite its small geometrical area $A_{geo} = 3.1\ \mu m^2$. In contrast, GaAs/AlGaAs devices with comparable sizes and similar designs, i.e. without central ohmic contact or other advanced screening architectures, usually operate in Coulomb-dominated regime [144, 147, 149, 164].

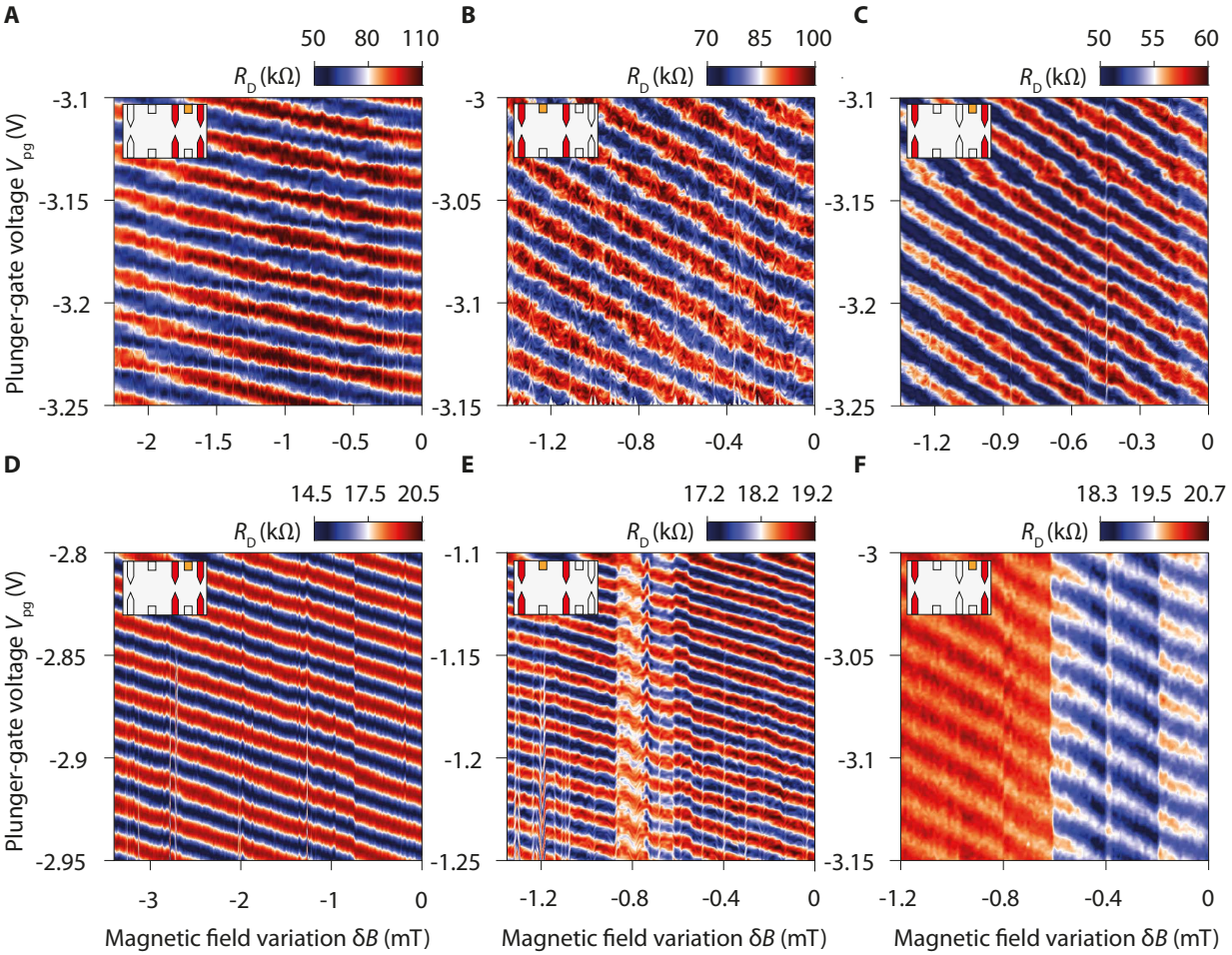

FIGURE 5.10: **Pyjama maps at 14 T.** Evolution of the diagonal resistance R_D with small changes of magnetic field δB and of plunger-gate voltage V_{pg} around 14 T. **A**, **B**, **C**, Experiments with the outer edge channel respectively for the small, medium and large FP interferometers. **D**, **E**, **F**, Experiments with the inner edge channel respectively for the small, medium and large FP interferometers. The extrema of R_D form lines with negative slopes characteristic of AB oscillations. Insets: Schematics of the device with active QPCs (red) and plunger gates (orange).

From these measurements (actually performed over longer plunger-gate voltage and field ranges than the ones displayed in Fig. 5.10), we can also estimate the field periods of AB oscillations that are gathered in Table 5.3. These periods are consistent with the ones estimated from field sweeps shown in the previous section and thus the corresponding AB areas are in good agreement with the surface of FP cavities.

QH FP cavity	Interfering edge channel	Period period ΔB (mT)	AB area A_{AB} μm^2
Small	Outer	1.32	3.1
Small	Inner	1.23	3.4
Medium	Outer	0.40	10.4
Medium	Inner	0.39	10.6
Large	Outer	0.27	15.3
Large	Inner	0.27	15.3

TABLE 5.3: **Aharonov-Bohm periods extracted from pyjama maps.** Period ΔB and Aharonov-Bohm areas $A_{AB} = \Phi_0/\Delta B$ extracted from the pyjama maps (same measurements than Fig. 5.10 over larger δB and V_{pg} scales). Magnetic field periods are estimated from the time evolution of the resistance and the field decay rate (0.14 mT/hour at 14 T).

5.1.4 AB oscillations in other devices

In addition to the sample (BNGr74) presented above, we performed similar interferometry experiments in three other graphene QH FP interferometers fabricated in different heterostructures. It allowed us to confirm the reproducibility of our results and that AB oscillations could also be observed in other devices. Fig. 5.11 and Fig. 5.12 presents respectively optical and SEM images of these devices and the characteristics of the heterostructures are summarized in Table 5.4.

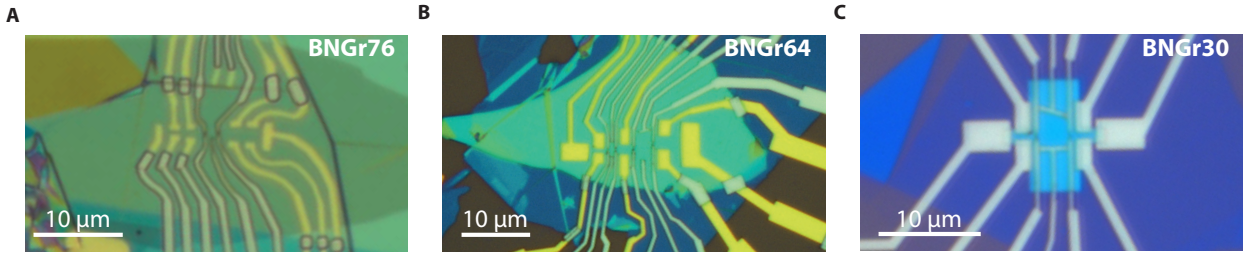

FIGURE 5.11: **Optical images of other graphene QH FP interferometers. A**, BNGr76 device and **B**, BNGr64 device and **C**, BNGr30 device. BNGr76 has a graphite back gate contrary to the other samples. Only the large interferometer of BNGr64 sample was investigated because the QPCs of the small device were not operating.

These devices are based on a common design (split-gated QPCs + plunger gate above graphene pristine edges) but each sample has some specificities. In particular, BNGr30 and BNGr64 are only composed of h-BN/graphene/h-BN flake and do not have a graphite back gate whereas the BNGr76 heterostructure has one. Also, contrary to other devices, the BNGr30 heterostructure was priorly etched before any metal deposition and the plunger-gate electrodes fully cover the graphene pristine edges.

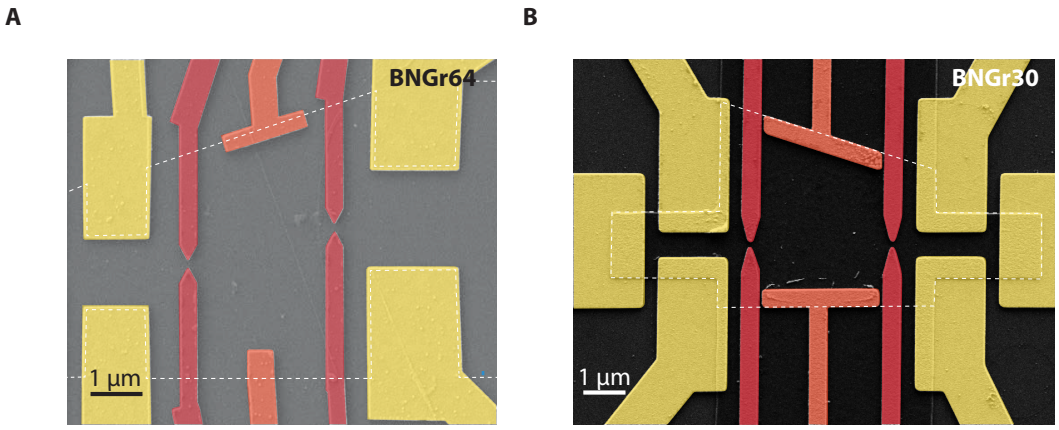

FIGURE 5.12: **SEM images of other graphene QH FP interferometers.** False-coloured scanning electron micrographs of **A**, BNGr64 and **B**, BNGr30 devices. The graphene edges are represented by the white dotted line. The contacts, QPCs and plunger gates are coloured in yellow, red and orange.

Sample	Top h-BN thickness (nm)	Bottom h-BN thickness (nm)	Graphite thickness (nm)	Split-gate gap (nm)	Geometric area A_{geo} (μm^2)
BNGr76	31	20	6	65/65 (design)	2.25
BNGr64	20	50		148 / 159	11.5
BNGr30	25	15		129 / 140	10.1

TABLE 5.4: **Characteristics of other samples.** The thicknesses of the h-BN and graphite layers are measured by atomic force microscopy. The gap size of the split-gate electrodes is measured by scanning electron microscopy except for BNGr76 sample where the values indicated correspond to the gap size in the lithography design. The geometric areas A_{geo} are based on the lithography design.

Results of interferometry measurements performed in each device are presented in Fig. 5.13, 5.14 and 5.15. In all devices, after suitable tuning of the QPCs, we observe gate-induced resistance oscillations which persist over long ranges of plunger-gate voltage as shown in Fig. 5.13.C, 5.14.C and 5.15.C. It appears that devices with silicon oxide back gate have a lower stability (background resistance drifts and spurious phase jumps in the oscillations) and display oscillations with smaller visibilities than the devices with graphite back gate.

The zooms on the oscillations over limited voltage range and the Fourier transforms of the resistance oscillations highlight, for each case, the decrease of the oscillations frequency with the lowering plunger-gate voltage similar to what we observed in BNGr74 sample. It gives a first indication that oscillations also arise from AB effect in the three other devices.

Pyjamas maps for the three devices, shown in Fig. 5.13.E, 5.14.E and 5.15.E, confirmed that the devices operate in the AB regime. Their magnetic field periods give AB surfaces which are consistent with the lithographic area of the FP cavities (see Table 5.5). The observation of such oscillations in devices with different designs and in different experimental conditions shows that the charging effects are intrinsically limited in graphene QH FP interferometer based on Van der Waals heterostructures.

Device	Bulk filling factor ν_b	Interfering edge channel	Number of bulk edge channel	Period ΔB (mT)	AB area A_{AB} (μm^2)
BNGr76	$\simeq 1.7$	Outer	2	2.1	2.0
BNGr64	$\simeq 1.1$	Outer	1	0.42	9.9
BNGr30	$\simeq 2.3$	Inner	2	0.37	11.2

TABLE 5.5: **Parameters for pyjama maps with other devices.** The periods ΔB and Aharonov-Bohm areas $A_{AB} = \Phi_0/\Delta B$ are extracted from the pyjama maps displayed in Fig. 5.13.E, Fig. 5.14.E and Fig. 5.15.E

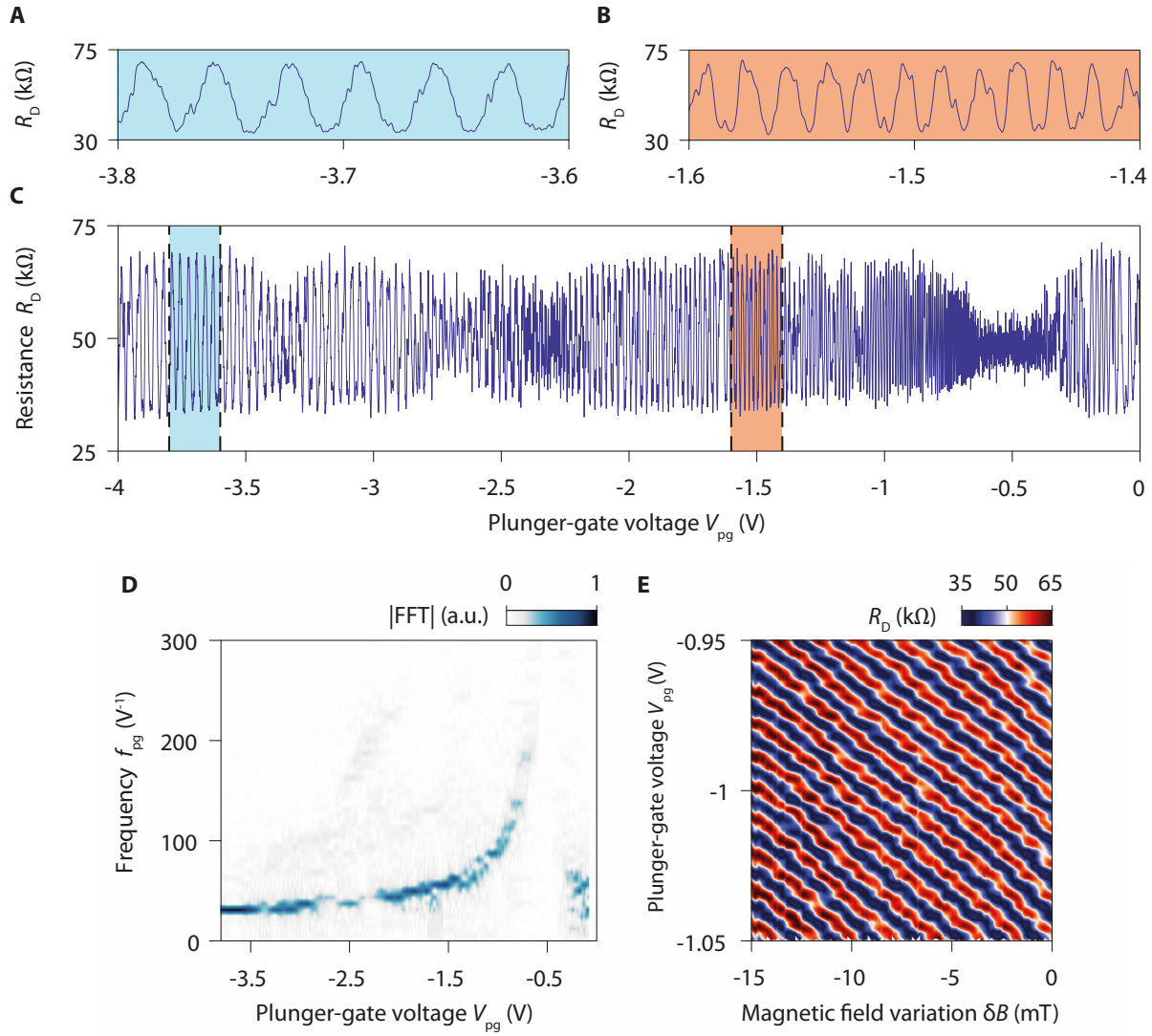

FIGURE 5.13: **Resistance oscillations in sample BNGr76. A**, **B**, **C**, Resistance oscillations induced by changing the plunger-gate voltage V_{pg} in interferometry experiments with the outer edge channel interfering at 14 T (two edge channels in the bulk). A and B show zooms on smaller V_{pg} ranges of the resistance oscillations. **D**, Amplitude of the Fourier transform of resistance oscillations presented in C with respect to the plunger-gate voltage V_{pg} and the frequency f_{pg}. A continuous decrease of the oscillations frequency is observed while decreasing V_{pg}. **E**, Evolution of the resistance oscillations as a function of the plunger-gate voltage V_{pg} and the magnetic field variation δB. The constant resistance lines have a negative slope characteristic of oscillations arising from Aharonov-Bohm effect. Contrary to similar measurements performed in other devices, the pyjama map in E is measured by changing the magnetic field by small increments between each plunger-gate voltage sweep.

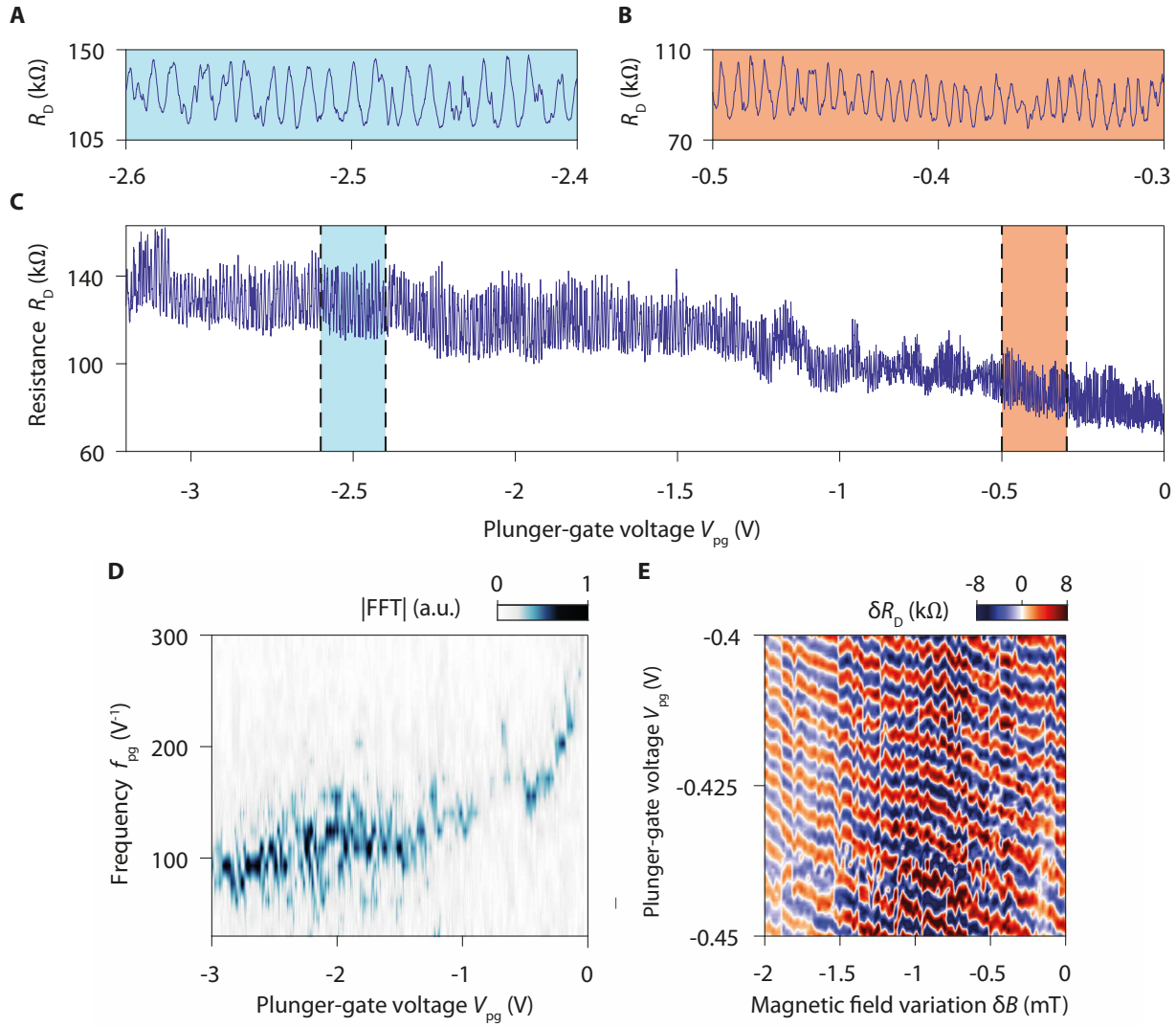

FIGURE 5.14: **Resistance oscillations in sample BNGr64. A**, **B**, **C**, Resistance oscillations induced by changing the plunger-gate voltage V_{pg} in interferometry experiments with the inner edge channel at 14 T. Clear resistance oscillations, on top of a continuous increase of the mean resistance of the device as shown in C. A and B show zooms on smaller V_{pg} ranges of the resistance oscillations. **D**, Amplitude of the Fourier transform of resistance oscillations presented in C with respect to the plunger-gate voltage V_{pg} and the frequency f_{pg}. A continuous decrease of the oscillations frequency is observed while decreasing V_{pg}. **E**, Evolution of the resistance oscillations as a function of the plunger-gate voltage V_{pg} and the magnetic field variation δB after subtraction of a resistance background for each plunger-gate voltage sweep. The constant δR_D lines have a negative slope characteristic of oscillations arising from Aharonov-Bohm effect. Note that for these experiments, there is only one edge channel in the bulk of the sample.

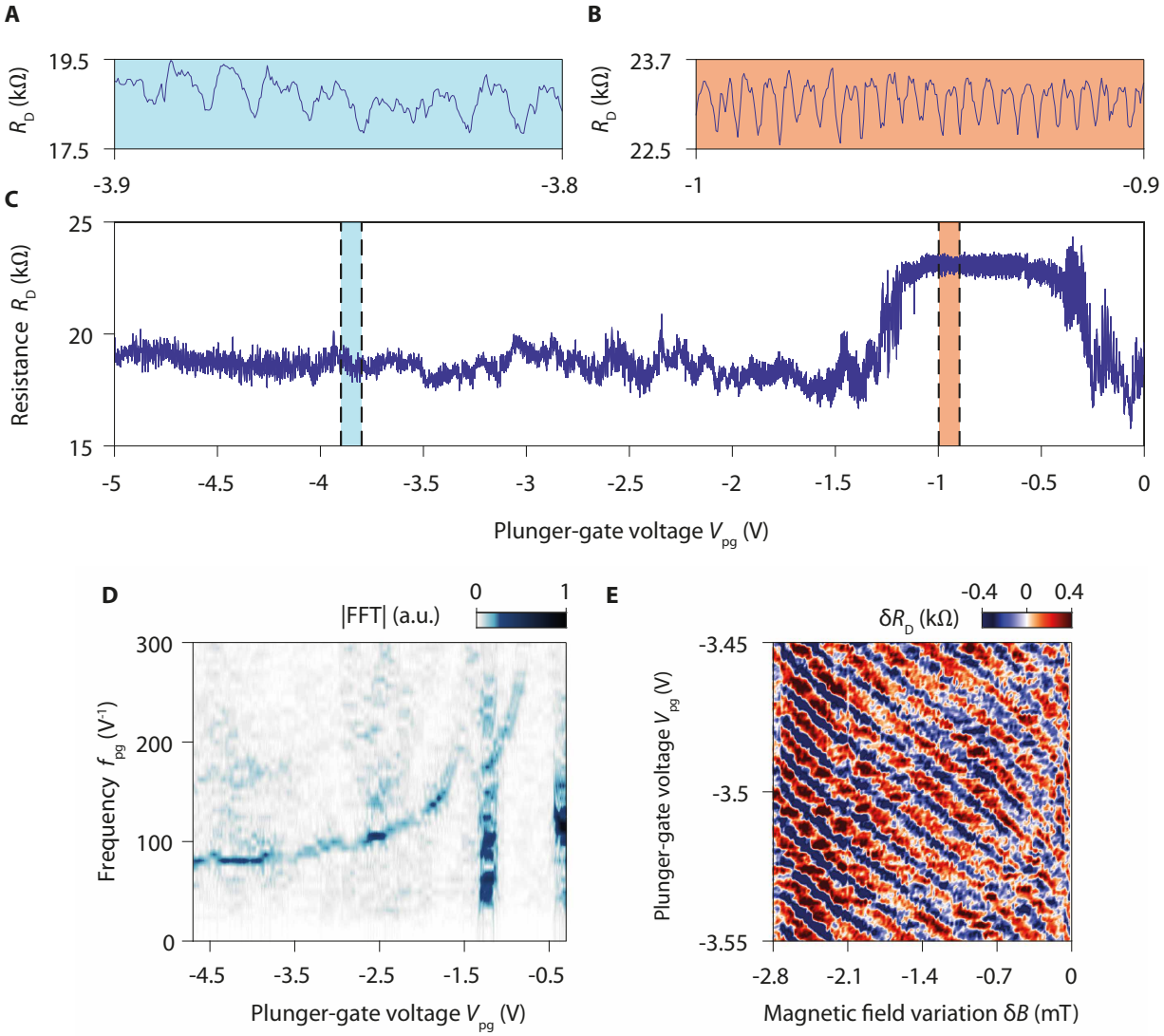

FIGURE 5.15: **Resistance oscillations in sample BNGr30. A**, **B**, **C**, Resistance oscillations induced by a change of the plunger-gate voltage V_{pg} in interferometry experiments with the inner edge state at 14 T. The abrupt change in C of the mean resistance value at $V_{pg} \approx -1.2$ V and $V_{pg} \approx -0.2$ V might originate from instabilities of the QPCs. A and B show zooms on smaller V_{pg} ranges of the resistance oscillations. **D**, Amplitude of the Fourier transform of resistance oscillations presented in C with respect to the plunger-gate voltage V_{pg} and the corresponding voltage frequency f_{pg}. A continuous decrease of the oscillations frequency is observed while decreasing V_{pg}. The divergence at $V_{pg} \approx -1.2$ V is an artefact arising from the rapid change of the mean resistance value at this plunger-gate voltage. **E**, Evolution of the resistance oscillations with both the plunger-gate voltage V_{pg} and the magnetic field variation δB after subtraction of a resistance background for each plunger-gate voltage sweep. The constant δR_D lines have a negative slope characteristic of oscillations induced by the Aharonov-Bohm effect.

5.1.5 Mitigation of charging effects in graphene Van der Waals heterostructures

To understand why we do not observe the Coulomb-dominated regime in our graphene FP interferometers, we follow the approach proposed by Halperin and cowokers and try to estimate the parameter $\xi = \frac{C_{eb}}{C_b + C_{eb}}$ determining in which regime the interferometers operate. We thus need to estimate the relevant capacitances describing the electrostatics of the FP interferometers.

Bulk capacitance C_b

The bulk capacitance C_b refers to the capacitance between the electrons in the central part of the FP cavity (the island in Rosenow and Halperin model) and the different gate electrodes.

For the device with graphite back gates, the bulk capacitance is mostly given by $C_b = C_{bg} A_{geo}$ where C_{bg} is the effective back-gate capacitance and A_{geo} is the geometrical area. For our small FP cavity in BNGr74 sample, we obtain $C_b = 4.5 \times 10^{-15}$ F (corresponding to a bulk charging energy of $E_C = \frac{e^2}{2C_b} = 18$ μeV) and similarly, for BNGr76 sample, where $C_{bg} = 1.36$ mF/m^2 , we obtain $C_b = 3.1 \times 10^{-15}$ F.

In devices without graphite back gate, the back-gate capacitance is composed of two capacitance in series corresponding respectively to the 285 nm thick SiO_2 layer ($\epsilon_{SiO_2} = 3.9$) and the bottom h-BN ($\epsilon_{BN} = 3$ here). It gives $C_{bg} = 99$ µF/m^2 and $C_{bg} = 0.11$ mF/m^2 respectively for BNGr64 and BNGr30 devices. Therefore, the C_{bg} is reduced by one order of magnitude in device without graphite back-gate. The corresponding bulk capacitance is $C_b = 1.1 \times 10^{-15}$ F in both BNGr64 and BNGr30 devices.

On top of this bulk-to-back-gate capacitance, one needs to add the contribution of the gate electrodes resting atop the 20-30 nm thick capping h-BN. It provides an additional parallel capacitive coupling leading to an increase of C_b and a reduction of the overall bulk charging energy. This contribution probably plays a significant role in devices on silicon substrate and may become the main contribution to the bulk capacitance. However it is difficult to evaluate it because these top gates are not located directly above the bulk island.

Edge-to-bulk capacitive coupling C_{eb}

The second relevant parameter to evaluate is C_{eb}, the capacitive coupling between the edge channel and the bulk. To estimate it, we use the theoretical analysis developed by Evans and coworkers. In ref. [229], they proposed a model describing the transport through a dot in the QH regime. The dot is supposed to be composed of a conducting island surrounded by to a conducting ring much like in the simplified model of FP interferometers where we have a compressible island surrounded by the interfering edge channel.

In ref. [229], Evans and coworkers suggest that the problem is equivalent to that of two parallel conducting stripes capacitively coupled. Thus, one can calculate C_{eb} by calculating the charge distribution induced by a potential difference between the two stripes. The latter depends on two parameters: a the distance separating the stripe and d the characteristic distance over which the influence of the potential difference is screened. In the real system, a is the typical width of the incompressible stripe separating the bulk from the edge channels, that can be assumed to be given by the magnetic length l_B (6.9 nm at 14 T) for simplicity. In the limit $2d \gg a$, Evans and coworkers assessed that the mutual capacitance is:

$$C_{eb} = \frac{2L\epsilon_{BN}\epsilon_0}{2\pi^2} \ln\left(\frac{4d}{a}\right). \tag{5.5}$$

For our devices with a graphite back-gate electrode, d is basically fixed by the thickness of the bottom h-BN, that is $d \simeq 20$ nm in both case. Thus, we can estimate that $C_{eb} = 2.8 \times 10^{-17}$ F for the small interferometer of BNGr74 sample and $C_{eb} = 2.3 \times 10^{-17}$ F for BNGr76 device ($L \simeq 3.5$ μm).

Likewise, we expect that C_{eb} remains of the same order of magnitude for the other devices because the gates above the FP cavity are also typically 20 nm away from the graphene. For our BNGr64 and BNGr30 devices, which respectively have perimeters $2L = 15.1$ and 13.3 μm, it gives $C_{eb} = 5.0 \times 10^{-17}$ and 4.4×10^{-17} F. Alternatively, in these device one may take, $d = d_{SiO_2} + d_b$, that is the sum of the thickness of the oxide layer d_{SiO_2} and the thickness of the bottom h-BN d_b. In this case, we get $C_{eb} = 10.7 \times 10^{-17}$ and 9.2×10^{-17} F.

Note that, this approximation relies on the value taken for a. One may expect a to be larger because of edge channel reconstructions according to the work of Chklovskii and coworkers [163]. Yet, this effect may still remain limited due to the proximity between the top gates and the graphene flake.

Discussion

From these calculations, we can estimate the parameter $\xi = \frac{C_{eb}}{C_b + C_{eb}}$. We obtain $\xi = 0.006$ for the small interferometer of BNGr74 sample and $\xi = 0.007$ for the device BNGr76 which both have a graphite back gate. On the other hand, for the devices with silicon back gate, we obtain $\xi = 0.04 - 0.09 \ll 1$. In all the cases, $\xi \ll 1$ consistent with the observation of oscillations in the AB dominated regime.

The above analysis reveals the important role of the back-gate electrodes in graphene QH interferometers. Their systematic presence provides efficient screening of charging effects and a large gate-to-bulk capacitance that enables to observe Aharonov-Bohm interference. It is obviously true in devices with graphite back gate because the latter is only a few tenths of nanometers from the graphene flake but it also remains valid in devices with silicon oxide back-gate despite a reduction by one order of magnitude of the effective back gate capacitance C_{bg}. Similarly, the close proximity of top-gate electrodes probably helps to screen the interactions between the interfering edge channel and the compressible bulk.

5.2 Aharonov-Bohm interference at positive plunger-gate voltages

We now consider experiments where positive voltages are applied on the plunger gates. This regime is rather unsual because one usually applies negative voltages on the plunger gates to repel the interfering edge channel, tune its trajectory and modulate the effective interferometer surface

5.2.1 Observations of resistance oscillations at positive plunger-gate voltages

In this unusual configuration, we also observe resistance oscillations. A typical example is shown in Fig. 5.16. It displays the extension of the measurements presented in Fig. 5.1. Similarly to the oscillations observed at negative plunger-gate voltages, these oscillations have large amplitude and persist over the full range of voltage spanned. However, they have a rather irregular shape and their frequency evolves non-monotonously with V_{pg2}. This observation is confirmed by looking at the oscillations on limited voltage ranges (Fig. 5.16.A. and Fig. 5.16.B) but also by looking at the evolution of the Fourier amplitude with the plunger-gate voltage V_{pg2} (Fig. 5.17). Similar oscillations can actually be observed in the three interferometers of BNGr74 sample, but also in BNGr76 sample, and for both outer or inner edge channel interfering.

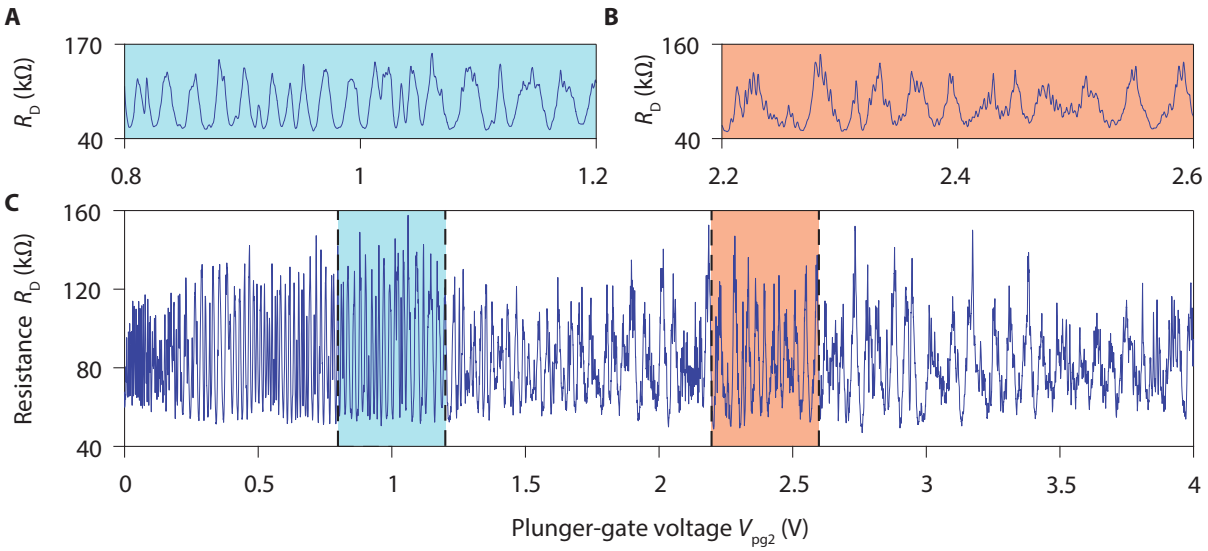

FIGURE 5.16: **Resistance oscillations at positive plunger-gate voltages.** Evolution of the resistance with the plunger-gate voltage V_{pg2} at positive voltages. Experiment performed at 14 T in the small FP cavity of BNGr74 sample with the outer edge channel interfering. **C**, Full voltage range spanned. **A**, **B**, Zooms on limited voltage ranges revealing the non-monotonic evolution of oscillation frequencies and their non-regular shape.

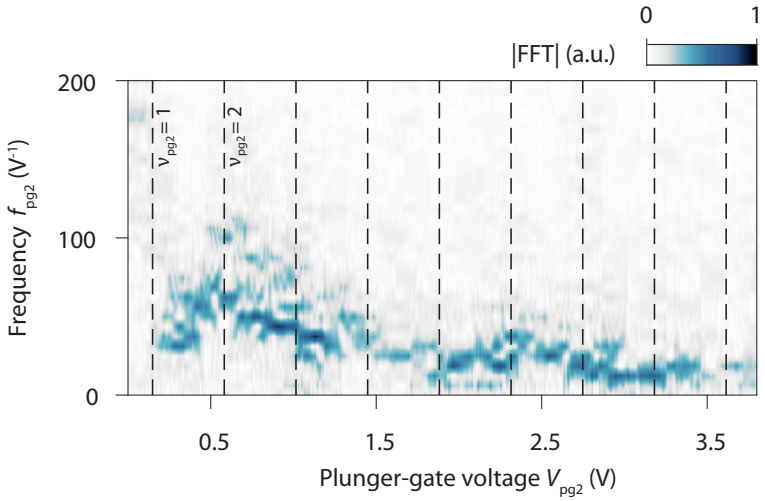

FIGURE 5.17: **Fourier amplitude of resistance oscillations at positive plunger-gate voltages.** Evolution of Fourier amplitude of resistance oscillations displayed in Fig. 5.16.A with plunger-gate voltage V_{pg2} and frequency f_{pg2}. Vertical dashed lines indicate constant integer filling factor below the plunger gate ν_{pg2}. A non-monotonic evolution of the frequency of the oscillations with V_{pg2} is observed contrary to the oscillations at negative V_{pg2}.

To know whether these oscillations arise from AB interference or from charging effects, we studied their magnetic field dependence. Fig. 5.18 displays a pyjama-map measured at positive plunger-gate voltages in an experiment where the inner edge channel is interfering. Like in the previous experiments, the resistance oscillations draw lines with negative slopes in the $\delta B - V_{pg2}$ plane. They are distorted because of the irregular shape and the irregular spacing between the oscillations. Thus, in this configuration, the interferometer also operates in the AB regime. It is further confirmed by estimating the magnetic field period of resistance oscillations: it is about 1.1 mT and it corresponds to an AB surface of 3.8 μm^2 in agreement with the dimensions of the small cavity.

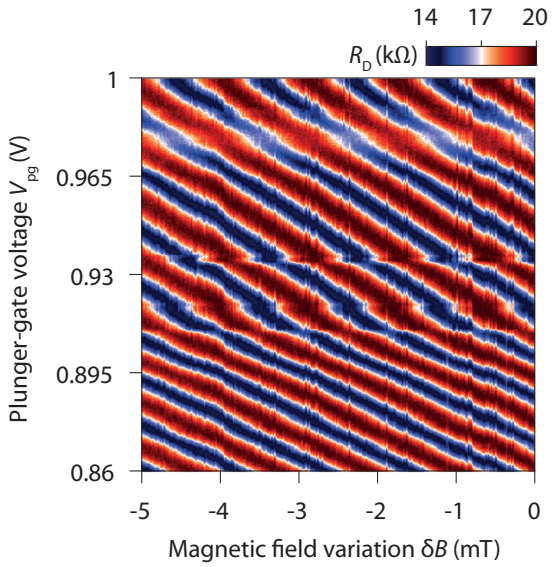

FIGURE 5.18: **Pyjama map at positive plunger-gate voltages.** Evolution of the diagonal resistance R_D in the small FP interferometer of BNGr74 sample versus magnetic field variation δB and plunger-gate voltage V_{pg2} at positive voltages. Experiment with inner edge channel interfering performed at 14 T.

5.2.2 Tuning of the AB phase at positive plunger-gate voltages

We can wander how the change of plunger-gate voltage allows to observed these AB oscillations in this situation. In this purpose, we should consider how the edge channel trajectories nearby the plunger-gate evolves at positive voltages. Such evolution is schematized in Fig. 5.19.

At small plunger-gate voltages V_{pg2}, the filling factor below the plunger gate is $\nu_{pg2} \approx 1$. Then, the outer edge channel propagates below the gated region whereas the inner edge channel is forced to circulate around the edges of the gate as shown in Fig 5.19.A. As V_{pg2} is increased, the inner edge channel trajectory evolves: it progressively goes more and more beneath the gate and, at $\nu_{pg2} \simeq 2$, it directly crosses the gated region. In the meantime, the potential experienced by the outer edge channel decreases and its trajectory also shifts: it progressively gets closer to the graphene edges.

Likewise, when V_{pg2} is further increased, such that $\nu_{pg2} > 2$, both edge channel trajectories shift towards the graphene edge as depicted in Fig. 5.19.B. Therefore, the increase of V_{pg2} leads to an increase of the area of the interfering loop and an increase of the AB phase exactly like in the negative plunger-gate voltage regime. This surface modulation is however less efficient because there is a sharp confining potential nearby pristine graphene edges. Nevertheless, it explains the emergence of AB oscillations at positive voltages.

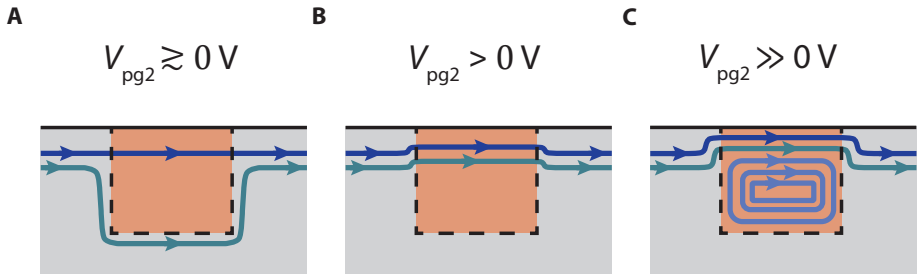

FIGURE 5.19: **Edge channel trajectories around the plunger gate at postive voltages. A**, At small positive voltages V_{pg2}, such that $\nu_{pg2} \approx 1$, only the outer edge channel (navy blue) can pass below the gated region (orange) while the inner one (green-blue) circulates following the gate edges (dotted line). **B**, Increasing V_{pg2}, we reach $\nu_{pg2} \gtrsim 2$ and the two edge channels can circulate below the gated region following the graphene edges (black thick line). In this regime, any increase of V_{pg2} results in a shift of edge channel trajectories towards the graphene edges. **C**, At even higher voltages, $\nu_{pg2} > 2$, the trajectories of the bulk edge channels are shifted further towards the graphene edges and localized electrons states (sky blue) appear beneath the gate.

Yet, others effects may also lead to a change of the phase of the interfering electrons:

- First, as the position of the interfering edge channel shifts towards the graphene edges, its velocity might also change because the confining potential evolves rapidly. Such change would lead to a variation the dynamic phase acquired by the electrons.

- On the other hand, at high V_{pg2} ($\nu_{pg2} > 2$), there are additional electrons edge channels localized below the plunger gate as depicted in Fig. 5.19.C. These localized states are close to the bulk edge channels and likely to interact with them. Thus, they may modify the trajectory of the interfering one depending on their exact locations and on their charging states that both evolve with the gate voltage.

Hence, the exact mechanism under the emergence of AB oscillations at positive gate voltage is probably quite complex and not only linked with the surface modulation. All the above phenomena may modify the phase of the interfering electrons and may compete leading to the non-monotonic evolution of the oscillations frequency observed. We also note that, in this regime, the potential disorder along the graphene edges may also have a significant impact.

5.3 Study of coherence and of dephasing effects

We now focus on the study of the coherence and the dephasing mechanisms affecting the visibility of quantum oscillations in BNGr74 FP interferometers. We begin by investigating the bias-induced oscillations and study how these oscillations evolve depending on the dimensions of the FP interferometer. We show that this evolution is consistent with the theory of Fabry-Pérot interferometers operating in the AB regime. We then focus on the temperature dependence of AB oscillations and evidence the key role of thermal broadening in the limitation of oscillations visibility. Finally, we show how we can estimate the phase coherence length taking advantage of the geometry of our device.

5.3.1 Study of bias-induced oscillations

As discussed in chapter 3 section 3.2.4, quantum interference can also emerge with the application of a dc-voltage bias. In the weak backscattering limit, the amplitude of differential resistance oscillations δR_D in presence of a dc-voltage bias can be written as:

$$\delta R_D = \delta R_0 \cos\left(2\pi \frac{\Phi}{\Phi_0}\right) \cos\left(2\pi \frac{eLV_{dc}}{hv}\right), \tag{5.6}$$

where δR_0 is the oscillations amplitude, L is the interfering path length i.e. the average distance between the two QPCs and v is the edge-excitation velocity. In this expression, the period of bias-induced oscillations $\Delta V_{dc} = hv/eL$ is fixed by the ballistic Thouless energy $E_{Th} = hv/L$ associated with the time of flight $\tau = L/v$ of the interfering electrons between the QPCs.

The observation of such checkerboard patterns was already reported in GaAs/AlGaAs FP interferometers [151, 167, 230, 231] and the study of these bias-induced oscillations has revealed to be a powerful tool to probe the properties of the edge channels [151, 167, 230] as well as the dephasing mechanisms appearing at finite bias [165, 231, 232].

Out-of-equilibrium transport measurements

We investigated this effect in the three FP interferometers of BNGr74 sample by studying how the differential diagonal resistance evolves with a dc-voltage bias V_{dc} applied in the source contact (see Fig. 4.5 in chapter 4). For these measurements, both ac and dc components of the diagonal voltage V_D were recorded. It allows to extract the evolution of R_D with V_D^{dc} the exact voltage difference generated between both sides of the interferometer after application of the dc-voltage bias V_{dc} at the source contact.

The results of out-of-equilibrium transport measurements performed at 14 T with both outer and inner edge channel interfering are shown respectively in Fig. 5.20.A-C and Fig. 5.21.A-C. They display the evolution of the diagonal resistance variations δR_D with both the plunger-gate voltage V_{pg} and the dc diagonal voltage V_D^{dc} (δR_D is the diagonal resistance after subtraction of a background $\delta R_D(V_{pg}, V_{dc}) = R_D(V_{pg}, V_{dc}) - \overline{R}_D(V_{dc})$ where $\overline{R}_D(V_{dc})$ is the mean value of R_D at a given bias V_{dc}).

In these figures, the color-coded maps present checkerboard-like patterns. It highlights the existence of the two sets of oscillations expected theoretically: the AB oscillations, which appear when V_{pg} is changed at fixed bias and the bias-induced oscillations that arise at fixed V_{pg}. The characteristic periods ΔV_{dc} (Table 5.6) of these second oscillations are similar to the ones reported for GaAs devices of comparable sizes. We note that the period of bias-induced oscillations decreases with the size of the interferometer and it actually scales as $1/L$ in agreement with eq. (5.6) (see Fig. 5.24).

The observation of such oscillations is another proof that our graphene devices behave as QH FP interferometers and follow the theory of Chamon and coworkers [143]. Nevertheless, contrary to eq. (5.6), we note that the oscillations rapidly fade at large V_D^{dc} values showing the existence energy relaxation processes at finite bias.

Effect of an asymmetric biasing

Still, there is another major difference between our experimental results and eq. (5.6): the checkerboards Fig. 5.20.A-B and Fig. 5.21.A-B are tilted especially for the small interferometer.

Such tilt had never been reported before in GaAs/AlGaAs FP interferometers although the literature provides few ideas about its potential origin. In ref. [230], McClure and coworkers briefly discuss the impact of the way to apply the voltage bias and they emphasize that eq. (5.6) is actually only valid when the voltage bias V_{dc} is applied on the sample symmetrically i.e. with $+V_{dc}/2$ voltage on the source contact and $-V_{dc}/2$ voltage on the drain contact. The situation is rather different in experiments: the bias is usually applied asymmetrically only at the source contact for convenience. In this condition, according to McClure and coworkers, we should ideally observe a diagonal stripe pattern. Such predictions were recovered by S. Ngo Dinh in ref. [230, 232] and he showed that, at first order, the differential diagonal resistance oscillations reads as:

$$\delta R = \delta R_0 \cos\left(2\pi\frac{\Phi}{\Phi_0} - 2\pi\frac{2L}{hv}eV_{dc}\right). \tag{5.7}$$

In practise, such pattern is not observed. Everything happens as if the potential drop at both QPCs was effectively symmetrized even when the bias is applied asymmetrically.

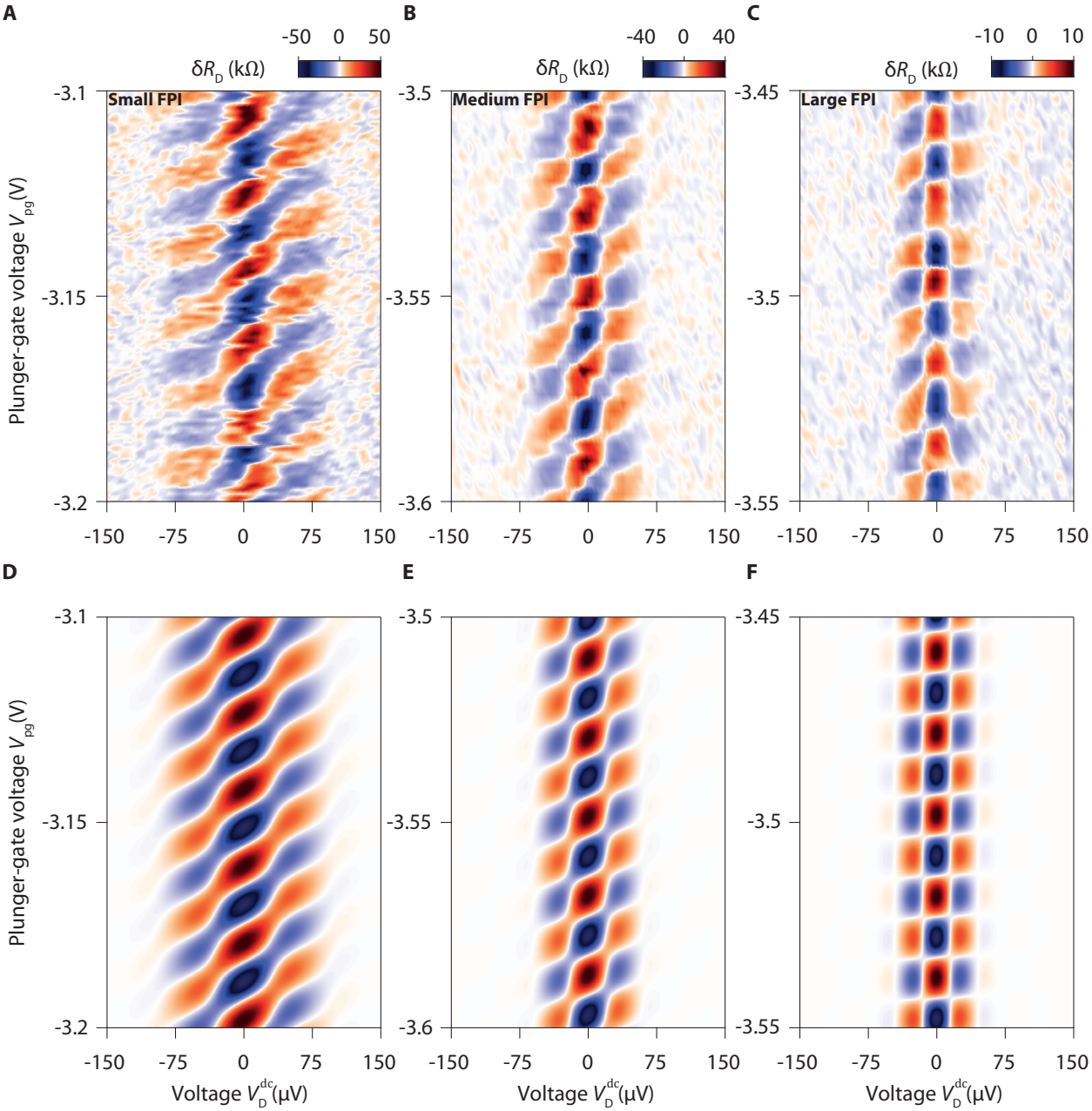

FIGURE 5.20: **Out-of-equilibrium transport in interferometry experiments with the outer edge channel. A**, **B**, **C**, Differential diagonal resistance variations δR_{D}, after background subtraction, versus plunger-gate voltage V_{pg} and dc component of the diagonal voltage $V_{\mathrm{D}}^{\mathrm{dc}}$ for interferometry experiments with the outer edge channel in the small, medium and large interferometers. Typical checkerboard patterns are observed with a significant tilt for the smallest interferometers revealing incomplete symmetrization of the potential drop. **D**, **E**, **F**, Numerical simulations of resistance oscillations induced by changes of voltage bias and plunger-gate voltage that reproduce the data presented in A, B and C, respectively. The simulation incorporates an asymmetric potential drop at the two QPCs and a Gaussian envelope used to reproduce out-of-equilibrium decoherence at high bias. Asymmetry factor $x = 0.2$, 0.1 and $x = 0.02$ are respectively used for D, E and F.

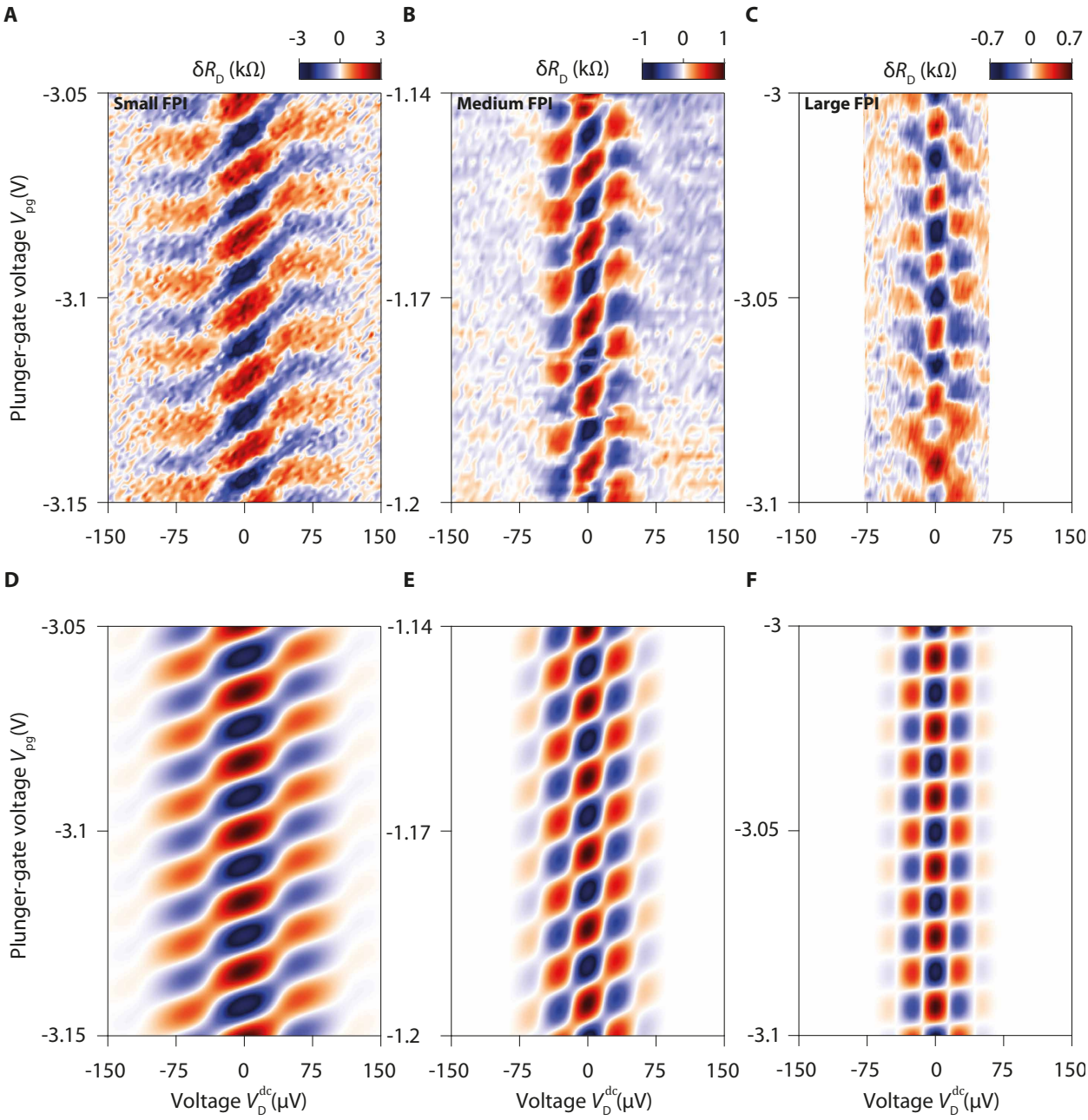

FIGURE 5.21: **Out-of-equilibrium transport in interferometry experiments with the inner edge channel.** **A**, **B**, **C**, Differential diagonal resistance variations δR_{D}, after background subtraction, versus plunger-gate voltage V_{pg} and dc component of the diagonal voltage $V_{\mathrm{D}}^{\mathrm{dc}}$ for interferometry experiments with the inner edge channel in the small, medium and large interferometers. Typical checkerboard patterns are observed with a significant tilt for the smallest interferometers revealing incomplete symmetrization of the potential drop. **D**, **E**, **F**, Numerical simulations of resistance oscillations induced by changes of voltage bias and plunger-gate voltage that reproduce the data presented in A, B and C, respectively. The simulation incorporates an asymmetric potential drop at the two QPCs and a Gaussian envelope used to reproduce out-of-equilibrium at high bias. Asymmetry factor $x = 0.16$, 0.1 and $x = 0.02$ are respectively used for D, E and F.

In experiments presented in Fig. 5.20.A-C and Fig. 5.21.A-C, the voltage bias is also applied only at the source contact. For the large interferometer, straight checkerboard patterns are observed. Contrastingly, for the medium and especially the small interferometers, the oscillations form a pattern which is an intermediate case between the checkerboard and the diagonal stripe patterns. It shows that the potential drop can indeed be effectively symmetrized in FP interferometers but also that this symmetrization effect can be reduced in small size interferometers.

To confirm that the asymmetry of the potential drop is at the origin of the tilts of the checkerboard patterns, we derived the theoretical expression giving the evolution of the amplitude of the differential resistance oscillations in presence an asymmetric potential drop at the two QPCs. In the weak backscattering limit, it reads as:

$$\delta R = \delta R_0 \left[\beta \cos\left(2\pi \frac{\Phi}{\Phi_0} - 2\pi \frac{2L}{hv} e\beta V_{\mathrm{dc}} \right) + \overline{\beta} \cos\left(2\pi \frac{\Phi}{\Phi_0} + 2\pi \frac{2L}{hv} e\overline{\beta} V_{\mathrm{dc}} \right) \right], \tag{5.8}$$

where $x \in [-\frac{1}{2}, \frac{1}{2}]$ is a factor describing the asymmetry of the potential drop, $\beta = \frac{1}{2} + x$ and $\overline{\beta} = \frac{1}{2} - x$. In this framework, the electrons coming from the source have an energy $-e\beta V_{\mathrm{dc}}$ whereas the electrons coming from the drain have an energy $e\overline{\beta} V_{\mathrm{dc}}$. The full derivation of eq. (5.8) is provided in Appendix 10. Note that it reduces to respectively eq. (5.6) and eq. (5.7) in the limit where $x = 0$ (symmetric potential drop) and $x = \frac{1}{2}$ (completely asymmetric potential drop).

Using this expression and adding a Gaussian envelope which takes into account the effect of dephasing at large bias (see next subsection), we can reproduce these out-of-equilibrium transport measurements with simulations as shown in Fig. 5.20.D-F and Fig. 5.21.D-F. These simulations recover all experimental features and in particular, they reproduce with a remarkable agreement the tilts of the checkerboard patterns we observed. It demonstrates that these tilts are a consequence of an asymmetric potential drop. It also confirms that the originally fully asymmetric biasing is at least partially symmetrized in the FP interferometers. This self-symmetrization of the potential drop appears to be less efficient when the dimensions of the interferometer are reduced as suggested by larger values of x (see Table 5.6).

The actual asymmetry of the potential drop at the two QPCs reflects how the electrochemical potential inside the FP cavity adjusts itself between the source and drain potentials. It mainly results from a balance between two competing effects. On one hand, like in quantum dots, it is affected by the capacitive couplings with the gates and the contacts such that the potential in the FP cell depends on the relative strengths of the electrostatic couplings. On the other hand, the FP potential also depends on energy relaxation processes which favour equilibration of FP chemical potential with the contact potentials. They are likely to symmetrize the potential drop because of Coulomb interactions within the dot [230, 232]. Therefore, the observation of tilted checkerboard pattern and thus of an incomplete symmetrization of the potential drop in our smallest devices may either reflect the large couplings to the gates or a less effective chemical potential equilibration in graphene.

Extraction of the Thouless energy

Considering how well our model reproduces the shape of the experimental data, we can use it to extract the corresponding Thouless energies $E_{\mathrm{Th}} = hv/L$. In this purpose, we studied the evolution of the amplitude of the Fourier amplitude of AB oscillations with the voltage bias and compared it with theoretical expectations derived from our generalized model. Indeed, the latter predicts that the amplitude of the flux-periodic oscillations should oscillates with V_{dc} with the following dependence:

$$\mathcal{A}\left(V_{\mathrm{dc}}\right) = \sqrt{\cos^2\left(2\pi \frac{eV_{\mathrm{dc}}}{E_{\mathrm{Th}}}\right) + 4x^2 \sin^2\left(2\pi \frac{eV_{\mathrm{dc}}}{E_{\mathrm{Th}}}\right)} \tag{5.9}$$

This expression is derived in Appendix 10 and it allows to evaluate E_{Th} by fitting the evolution of Fourier amplitude with V_{dc} with the above formula. In this purpose, one has to first calculate the Fourier amplitude of gate-induced oscillations at fixed bias, then to extract its values at the plunger-gate frequency corresponding to that of AB oscillations and to fit its evolution with V_{dc}. Note that for the analysis, we did not used the asymmetry factors as x fitting parameters but we rather fixed their values at the ones determined from simulations in previous subsection.

Fig. 5.22 shows such evolutions for out-of-equilibrium transport measurements corresponding to Fig. 5.20.A-C and Fig. 5.21.A-C (blue dots). The Fourier amplitudes display a lobe structure consistent with eq. (5.9) but the amplitude of the oscillations rapidly fades at large bias and vanishes typically after one voltage period. This decay, that is not predicted in an non-interacting model, must be taken into account to fit the data.

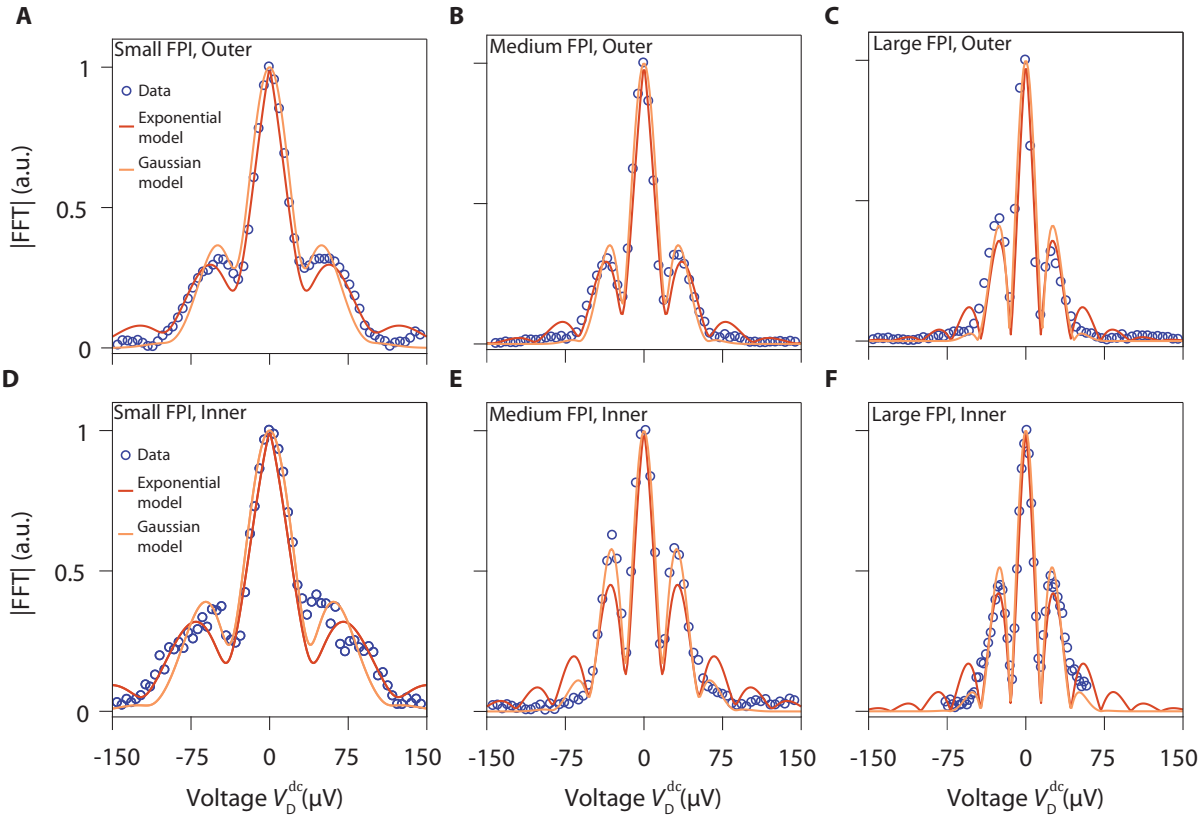

FIGURE 5.22: **Decay of bias-induced oscillations.** Fourier amplitudes of the AB oscillations displayed in Fig. 5.20.A-C and Fig. 5.21.A-C versus diagonal dc-voltage $V_{\mathrm{D}}^{\mathrm{dc}}$. The amplitudes display a lobe structure and rapidly decay at finite bias. Fits of the experimental data (blue dots) with eq. (5.10) (red line) and eq. (5.11) (orange line) allow to extract the period of bias-induced oscillations.

In GaAs FP interferometers, such a rapid fading of the bias-induced oscillations with the bias was already reported [230, 231]. In ref. [230], McClure and coworkers observed an exponential decay of the oscillation amplitude with the bias. This dependence was recovered few years after by S. Ngo Dinh in theroretical investigations and he found that it was likely to emerge from Coulomb interactions within the FP cavity [165]. We thus fitted our data with:

$$\mathcal{A}(V_{\mathrm{dc}}, \Delta V_{\mathrm{expo}}) \exp\left(-2\pi\chi \frac{|V_{\mathrm{dc}}|}{\Delta V_{\mathrm{expo}}}\right) \tag{5.10}$$

where χ is a phenomenological parameter that describes how fast the oscillations vanish with

voltage bias, and ΔV_{expo} is the period of the resistance oscillations for this exponential decay. In Fig. 5.22, the results of such fits are reported with the red lines. A good agreement between the model and the data is found for the three interferometers. This phenomenological model however does not capture the absence of secondary lobes in experiments which suggests that the decay of the oscillations is faster than exponential.

We also considered a second phenomenological model that assumes a Gaussian decay of the oscillations amplitude with bias. Such dependence was originally observed in Mach-Zehnder interferometers [233, 234] but was also reported in FP interferometers by Yamauchi and coworkers in ref. [231]. Investigations in Mach-Zehnder inferometers revealed that such Gaussian decay may arise from phase fluctuations of the interfering edge channel due to Coulomb interactions or the charge noise in the non-interfering edge channels [234–236]. Hence, we also fitted the data with:

$$\mathcal{A}(V_{\text{dc}}, \Delta V_{\text{gauss}}) \exp\left(-\frac{V_{\text{dc}}^2}{2{V_0}^2}\right) \tag{5.11}$$

where V_0 is the voltage scale characterizing the width of the Gaussian envelope, and ΔV_{gauss} is the period of the resistance oscillations for this Gaussian decay. The fits with this model are displayed in Fig. 5.22 with the orange lines. They also reproduce well the experimental data.

The parameters extracted from the fits with both models are summarized in Table 5.6. Voltage periods ΔV_{expo} and ΔV_{gauss} extracted in the two cases are really close and they provide a reliable estimate of the corresponding Thouless energies. As shown in Fig. 5.24, they scale as $1/L$ as expected theoretically and they do not change much for experiments performed with either inner or the outer edge channel. The damping rates χ extracted for the model with an exponential decay range from 0.2 to 0.45 evidencing a fast blurring of the oscillations at finite bias. Similarly, the V_0 values extracted for the model with a Gaussian decay scale as $1/L$ and are typically two/three times smaller than ΔV_{gauss} consistent with observation of Yamauchi and coworkers [231]. The qualitative difference between the two models is that the exponential decay fits slightly better the amplitude of the first lobe, especially for data obtained with the small interferometer, but fails to reproduce the vanishing of the second ones, whereas the Gaussian model is less accurate for the first lobe but shows a suppressed second lobe.

QH FP cavity	Interfering edge channel	ΔV_{expo} (μV)	χ	ΔV_{gauss} (μV)	V_0 (μV)	Asymmetry factor x
Small	Outer	134	0.42	128	40	0.2
Small	Inner	162	0.39	151	49	0.16
Medium	Outer	83	0.42	81	25	0.1
Medium	Inner	70	0.26	70	30	0.1
Large	Outer	57	0.35	61	21	0.02
Large	Inner	57	0.29	57	23	0.02

TABLE 5.6: **Fitting parameters for the different models of bias-induced oscillation decay.** Voltage period ΔV_{expo} for the exponential decay model, χ damping rate for the exponential decay model, voltage period ΔV_{gauss} for the Gaussian decay model, V_0 width of the Gaussian envelope, x asymmetry factor (parameter fixed for the fits and adjusted priorly to reproduce data with numerical simulations displayed in Fig. 5.20.A-C and Fig. 5.21.A-C).

5.3.2 Temperature-induced dephasing

Exponential decay of oscillations amplitude

The change of the temperature is also expected to affect significantly the coherent transport in the device. To investigate this effect, we studied systemically the evolution of the oscillations amplitude with the temperature in the three interferometers in experiments with the outer edge channel interfering.

Fig. 5.23.A shows a typical evolution for experiments performed in the small interferometer. It clearly appears that amplitude of the resistance oscillations decreases fastly as the temperature increases and no oscillations can actually be observed in this interferometer above 200 mK. We observed even faster decay in the medium (oscillations disappear above 100 mK) and large interferometer (oscillations disappear above 65 mK). The decay of the oscillations amplitude is actually exponential as revealed by Fig. 5.23.B where the evolutions of Fourier amplitudes of AB oscillations are plotted. A fit of the data with e^{-T/T_0} allows to extract the characteristic temperature scales T_0 associated with the decay and we remark that T_0 decreases when the dimensions of the interferometer increases.

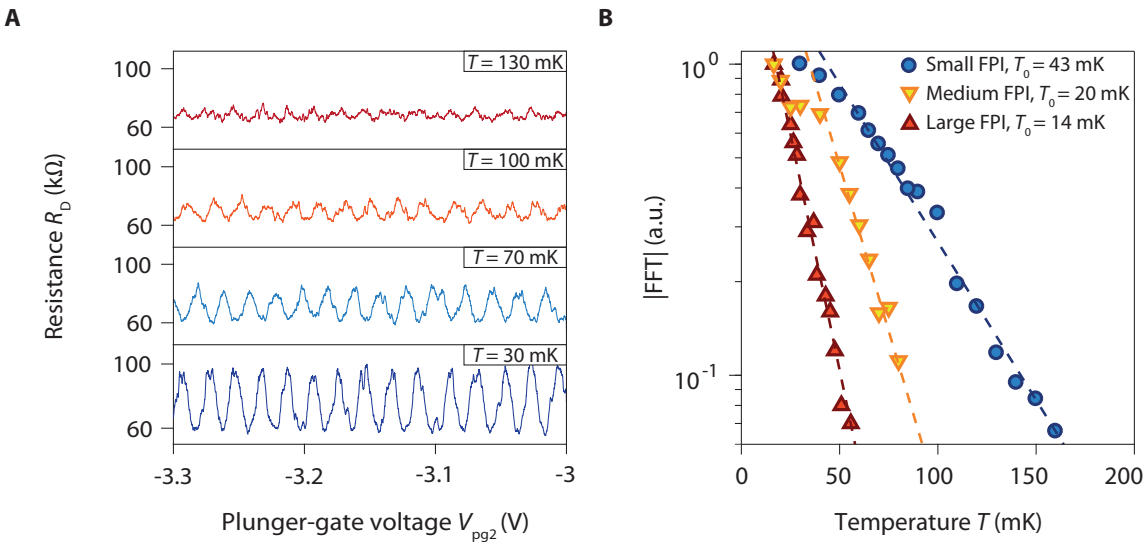

FIGURE 5.23: **Exponential decay of oscillations amplitude with temperature. A**, Temperature evolution of the resistance oscillations versus plunger-gate voltage V_{pg2} for the small interferometer. **B**, Exponential decays of the Fourier amplitudes of the resistance oscillations for the three interferometers.

Similar exponential decays of oscillations amplitude are commonly observed in GaAs QH FP interferometers in both AB and Coulomb-dominated regimes with integer [144, 166, 167, 231] and fractional edge channels [144, 151] as well as in Mach-Zehnder interferometers [146, 231, 237, 238]. In FP interferometers, different effects can lead to such dependence, e.g. thermal broadening [143], the dephasing induced by the noisy environment [231] or the electrostatics of the system [148].

Thermal broadening

In the non-interacting theory of Chamon and coworkers [143], the increase of the temperature is expected to lead to an exponential decrease of the oscillations amplitude due to thermal broadening (also called thermal averaging/smearing). At finite temperatures, wavepackets of interfering electrons have a $k_B T$ energy bandwidth. Thus, they are composed of different spectral components

that all generate their own set of quantum interference. The resistance oscillations measured experimentally then result from the sum of the contributions coming from each single component. While propagating inside the FP cavities, the different spectral components are progressively dephased with respect to each other which leads to a progressive blurring of the measured oscillations. This blurring is more and more significant as the perimeter of the interferometer or the temperature are increased and it ultimately results in a complete washout of the oscillations.

Chamon and coworkers calculated the effect of thermal broadening in their non-interacting theory of FP interferometers [143]. They found that it leads to a reduction of the amplitude of the oscillations by a factor:

$$\Lambda(T,L) = \frac{\pi k_B T 2L/\hbar v}{\sinh(\pi k_B T 2L/\hbar v)} = \frac{4\pi^2 k_B T/E_{Th}}{\sinh(4\pi^2 k_B T/E_{Th})}, \tag{5.12}$$

which indeed decreases when T or L increases. This relation, that remains valid even in presence of an asymmetric potential drop (see Appendix 11), confirms that thermal broadening is intrinsically linked with the time of flight of interfering electrons in the FP cavity as intuited above. At high temperature, the above expression leads to an approximate exponential dependence of the oscillations amplitude with the temperature given by:

$$e^{-\pi k_B T 2L/\hbar v} = e^{-4\pi^2 k_B T/E_{Th}} = e^{-T/T_0}, \tag{5.13}$$

where $T_0 = \frac{E_{Th}}{4\pi^2 k_B}$ is the characteristic temperature scale of the exponential decay. Eq. 5.13 allows to check whether the blurring of the interference signal with the temperature arises from thermal broadening or from another effect: one simply has to compare the Thouless energies $E_{Th} = e\Delta V_{dc}$ extracted from out-of-equilibrium transport measurements and the characteristic energy scales $4\pi^2 k_B T_0$ associated with the thermal decay of the oscillations amplitude.

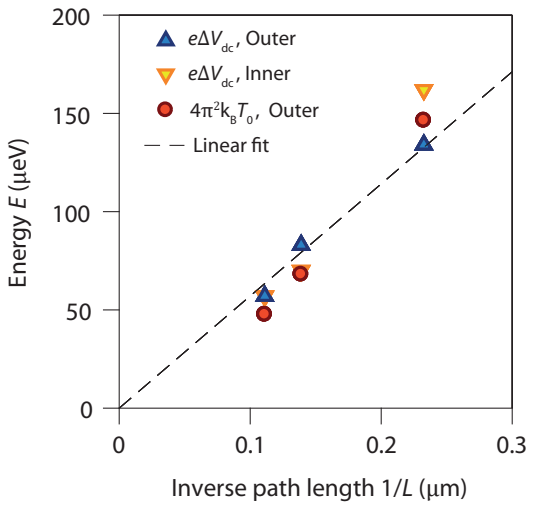

FIGURE 5.24: **Thouless energies and thermal broadening.** Evolution of the energy scales as a function of $1/L$. Thouless energies $E_{Th} = e\Delta V_{dc}$ are extracted from fits displayed in Fig. 5.22 and are compared to energy scales $4\pi^2 k_B T_0$ extracted from the temperature dependence of resistance oscillations. All energy scales follow a $1/L$ dependence as expected. For the outer edge channel, both E_{Th} and $4\pi^2 k_B T_0$ coincide evidencing that the decay of the oscillation amplitude with the temperature is limited by thermal broadening. The dashed line is a linear fit for the data obtained with the outer edge channel which allows to estimate an edge excitation velocity of 1.4×10^5 m/s.

Fig. 5.24 shows the evolution of these two energy scales extracted from separated measurements with the inverse path length $1/L$. It clearly evidences that E_{Th} and $4\pi^2 k_{\mathrm{B}} T_0$ scales as $1/L$ and also that two energy scales coincide for a given interferometer. It is in remarkable agreement with theoretical predictions and it demonstrates that the exponential decay of oscillations amplitude mainly arises from thermal broadening. Therefore, we can estimate the edge-excitation velocity v from a linear fit of the data points coming from the two types of measurements. We found $v \simeq 1.4 \times 10^5$ m/s for the experiments with the outer edge. It is of the same order of magnitude that the ones measured in GaAs QH interferometers [167, 230, 239] though somehow higher.

5.3.3 Estimation of the phase coherence length

Size-dependence analysis

Besides thermal broadening, other effects (the noise in the non interfering edge channel [235] or the electrostatic coupling with the compressible bulk [230] for example) can affect coherence. They lead to a limitation of the oscillations visibility even at zero temperature and thus to a finite phase coherence length. To estimate L_ϕ, the phase coherence length associated with extrinsic effects (i.e other mechanisms than thermal broadening), we followed an approach proposed by P. Roulleau and coworkers [238] and study the evolution of the visibility $\mathcal{V}$ of coherent oscillations with the dimensions of our graphene FP interferometers. In this framework, we assume that $\mathcal{V}$ is given by:

$$\mathcal{V} = \mathcal{V}_0 \frac{2L/L_T}{\sinh(2L/L_T)} \exp\left(-\frac{2L}{L_\phi(T)}\right), \tag{5.14}$$

where $L_T = \frac{hv}{2\pi^2 k_B T}$ is the thermal length i.e. the characteristic length associated with the decay of the visibility due to thermal broadening at temperature T (see eq. (5.12) in previous section), $L_\phi(T)$ is the phase coherence length associated with extrinsic effects, $2L$ is the the perimeter of the FP cavity and $\mathcal{V}_0$ is the asymptotic limit reached by the visibility when L tends to zero.

One can make a few comments about eq. (5.14). First, $L_\phi(T)$ actually depends on the temperature and is very likely to decrease when T increases because of the enhancement of inelastic dephasing effects. Also, in this expression, the thermal broadening and the other extrinsic dephasing mechanisms are purposely separated. Experimentally, they add up and it results in an effective decoherence length given by $1/L_\phi^*(T) = 1/L_T + 1/L_\phi$ for the limit of long interfering path lengths. Finally, we note that this expression is valid for $2L$ above L_ϕ. For smaller perimeters, the decrease of $\mathcal{V}$ with $L_\phi(T)$ is not exponential anymore and $\mathcal{V}$ should saturate to a particular visibility below unity. Eq. (5.14) nevertheless provides a way to estimate L_ϕ by fitting the evolution of $\mathcal{V}$ with $2L$ at fixed temperature.

Experimentally, the apparent oscillations visibility can be strongly affected by external parameters not related to dephasing mechanisms. In particular, the noise in the measurement set-up or charge noise in the gates can significantly affect it. We performed this length-dependence analysis by considering our best visibility data obtained for the three sizes of interferometers. We evaluate the electron temperature at our base temperature to be $T \simeq 20$ mK, which corresponds approximately to the temperature below which the T-dependence of the visibility saturates. For experiments with the inner edge channel, we extracted the visibility through $\frac{G_{\max}-G_{\min}}{(G_{\max}-e^2/h)+(G_{\min}-e^2/h)}$, which subtracts the conductance contribution of the fully transmitted outer edge channel.

Fig. 5.25 shows the evolution of these visibilities $\mathcal{V}$ with the perimeter of the interferometers $2L$. For comparison, the decrease of the visibility induced by the thermal broadening at 20 mK is shown with the solid red line (eq. (5.14) with $L_\phi(T)$ infinite and an edge state velocity $v \simeq 1.4 \times 10^5$ m/s giving $L_T = 17$ μm. For both experiments with the outer and experiments the inner edge channel, a fast decrease of $\mathcal{V}$ with $2L$ is observed which cannot be explained by the effect of thermal broadening. The best visibilities for both interfering edge channels are virtually the same except for the data in the large interferometer with the inner edge channel, which shows a

significant drop compared to the data with the outer one. It probably reflects that the tuning of the QPC could have been improved. We thus discard it for our semi-quantitative analysis.

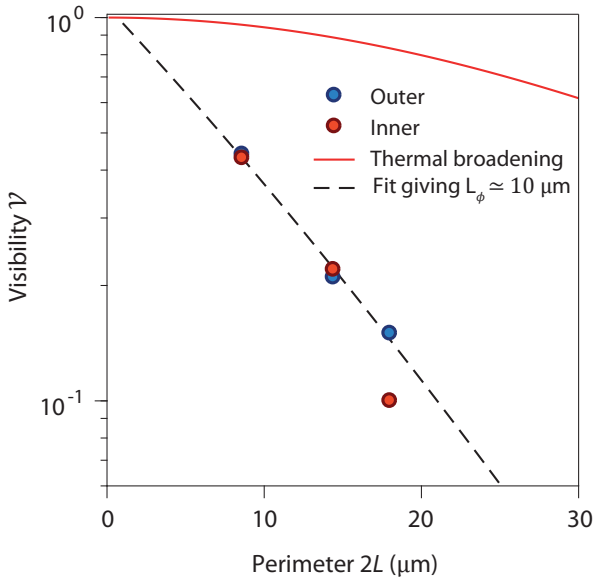

FIGURE 5.25: **Phase coherence length L_ϕ.** Evolution of the best visibilities $\mathcal{V}$ with the perimeter $2L$ of the interferometers obtained in experiments at base temperature with the outer (blue dots) and the inner (red dots) edge channel. The red solid line shows the thermal broadening contribution. Fitting the data (black dashed line) with eq. (5.14) and discarding the inner edge channel experiment for the large interferometer, we extract a coherence length of 10 μm at 20 mK.

By fitting the visibility decay, we extract a phase coherence length $L_\phi \simeq 10$ μm at 20 mK consistent with the observation of relatively high visibility oscillations in our large interferometers. It is smaller or comparable to the perimeter length, which justifies the exponential decrease used in eq. (5.14) (the saturation would appear for smaller perimeters as the ones studied here).

Comparison with other QH interferometers

It is instructive to compare our value of the phase coherence length with that measured in previous works on QH interferometers.

In GaAs/AlGas Mach-Zehnder interferometers, the phase coherence length are usually significantly larger. In 2008, Roulleau and coworkers measured a phase coherence length of 20 μm at 20 mK [238]. It was then shown that the coherence length could be increased by designing the device geometry such that the non-intefering edge channel make closed loops in the interferometer [240, 241]. With such a strategy, Duprez and coworkers measured a coherence length of 0.25 mm at 10 mK such that they managed to observe AB interference in devices with arm length of 0.1 mm [242].

Likewise, in graphene Mach-Zehnder interferometers, Wei and coworkers observed high visibility conductance oscillations in a device with a 22 μm long gate at 20 mK [212]. Hence, we can think that the phase coherence length in such samples exceeds tenths of microns. These predictions are somehow confirmed by the PhD work of Paul Brasseur [215]. Following the approach of Roulleau *et al.* [238], he studied the evolution of oscillations visibility in graphene pn junctions with both the temperature and the junction length and he extrapolated that the phase coherence

length was about 0.37 mm at 20 mK.[1] Thus, we can assume that the dephasing in our device is not due to the presence of pn junctions.

On the other hand, the phase coherence length is usually not estimated in FP devices. Yet, in ref. [166], Choi and coworkers evaluated it in a 12 μm^2 GaAs/AlGaAs device with a central ohmic contact. They found a 35 μm coherence length at 30 mK, that is, three times larger than in our device.

Therefore, we believe that the coherence in our graphene FP devices can still be enhanced by improving the device design and its quality. In particular, fully gate-defined devices with graphite gate electrodes seem promising as discussed below.

5.4 Conclusion

In this chapter, we have demonstrated that high mobility graphene encapsulated heterostructures equipped with a series of split-gates allows to fabricate QH Fabry-Pérot interferometers. Operating the device with the edge channels of the zeroth Landau levels, we observed widely gate-tunable quantum interference which arise from Aharonov-Bohm effects and have a high visibility. We have shown that the systematic presence of a back gate in graphene QH FP interferometers intrinsically mitigates charging effects, especially when they are equipped with graphite back gate. It allows to fabricate small size interferometers operating in the AB regime without the need of complex interferometer design. The investigations of out-equilibrium transport measurements and of the dephasing mechanisms comply with most theoretical predictions of Chamon and coworkers regarding non-interacting FP interferometers.

In the meantime, Y. Ronen and coworkers from Philip Kim's group also fabricated and studied a fully gate-defined graphene QH FP interferometer [243]. Their device shown in (see Fig 5.26.A) was fabricated from a h-BN/graphene/h-BN heterostructure encapsulated between two graphite flakes. The bottom graphite flake was used as a back gate. The top flake was selectively etched to make the different gates of the samples: the QPCs, the plunger-gate but also a central gate defining a 3 μm^2 FP cavity (see Fig 5.26.B). Ronen and coworkers measured both high visibility AB and bias-induced oscillations with $\nu = 1,\ 2$ and 3 edge channels interfering (Fig 5.26.C and Fig 5.26.D) and they observed several of the experimental features discussed in this chapter (for instance the tilted checkerboard patterns).

Y. Ronen and coworkers also estimated the phase coherence length in their device and they found that it was about 8 μm at 60 mK. It is similar to that measured in our device though at higher temperatures. It reflects the higher level coherence in their device reached thanks to the graphite gates. They provide a strong screening isolating the interfering channels from its environment (they basically act as the screening wells of devices fabricated by the Purdue group [151, 167]). The higher coherence may also arise from the use of graphite top gates which were shown to generate a lower amount of disorder than metal electrodes [186].

Our work, together with the parallel study of Ronen *et al.*, clearly show that graphene Van der Waals heterostructures are suitable platforms for QH FP interferometry. They offer new opportunities to confirm and complete the results obtained in GaAs devices and potentially to unveil new phenomena. In particular, they provide a new system to investigate the physics of anyons.

[1] Yet, one has to be cautious about this result considering that the longest junctions studied was 1.5 μm long. The estimation of the phase coherence length has to be confirmed by making similar studies with junctions at least one order of magnitude longer.

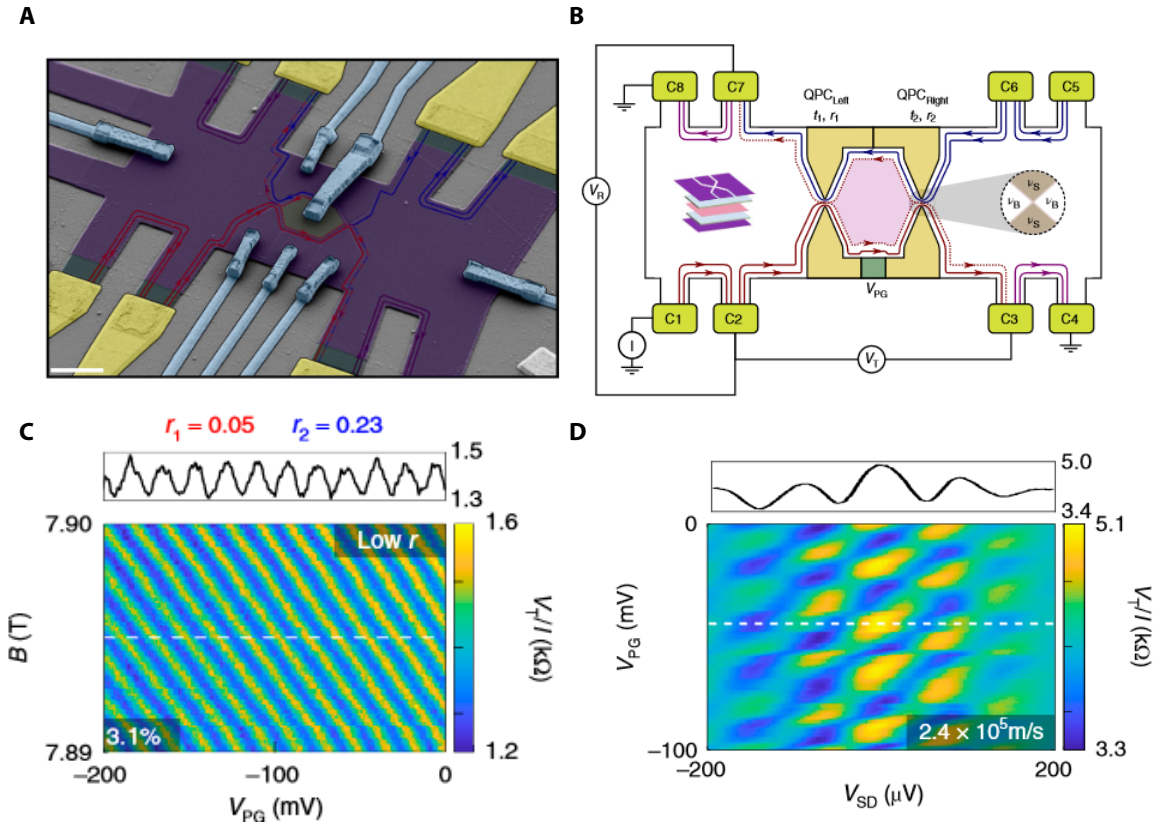

FIGURE 5.26: **Fully-gate defined graphene QH FP interferometers fabricated in Philip Kim's group. A**, Scanning electron micrograph of the device. The device is fabricated from a h-BN/graphene/h-BN heterostructure encapsulated between two graphite flakes. The top graphite flake is etched to define the QPCs, the plunger gate and the FP cavity. The contacts are coloured in yellow and the air bridges contacting the graphite top gates are coloured in blue. Scale bare is 2 microns. **B**, Schematics of the edge channels and of the contact configurations in the device. **C**, Pyjama map measured at 8 T with inner edge channel interfering at bulk filling factor $\nu_b = 2$. **D**, Corresponding out-of-equilibrium transport measurements. Note that the checkerboard pattern is tilted like in our interferometers. Adapted from ref. [243].

Chapter 6

Period halving of Aharonov-Bohm oscillations

Contents

In this short chapter, we focus on a specific interference regime characterised by the emergence of AB oscillations with a halved periodicity. After an introduction about previous work on the subject, we show that this regime of oscillations also appears in graphene FP interferometers under certain conditions and we discuss some of its specificities.

6.1 Period halving of AB oscillations in GaAs QH FP interferometers

In ref. [166], the Weizmann group reported the observation of a new interference regime in GaAs FP interferometers where AB oscillations had a $\Phi_0^* = \frac{h}{2e}$ periodicity. They observed this regime in several devices with different designs and they found that it appeared in experiments with the outermost edge channel interfering and at sufficient large filling factors ($\nu_b \geqslant 2.5$ in their experiments). At high filling factors $\nu_b \geqslant 4.5$, they recovered the standard AB regime. Similar features were observed few years after by the group of Purdue university also in experiments with the outermost edge channel interfering and at filling factors $\nu_b > 1.8$ [167].

To investigate the origin of this specific oscillation regime, Choi, Sivan and coworkers performed several elaborated interferometry experiments and shot noise measurements [166, 244]. It allowed them to make important observations:

- they found that, in the new oscillation regime, the effective charge of the interfering quasiparticle was $-e^* = -2e$

- they observed that these peculiar oscillations had a similar visibility and a similar resilience against temperature-induced dephasing than the standard AB oscillations,

- they noticed that the $\frac{h}{2e}$ periodic oscillations were washed out when the non-interfering $\nu = 2$ edge channel was dephased in stark contrast with what happens with standard AB interference.

- they reported a surprising dependence of the periodicity of the $\frac{h}{2e}$ periodic oscillations with the flux enclosed by the $\nu = 2$ edge channel.

Thanks to these experiments, Sivan, Choi and coworkers were able to show that the unusual AB oscillations were arising from electron-electron interactions between the $\nu = 1$ and the $\nu = 2$ edge channels.

Some of these experimental findings were recovered later on in a theoretical work by Frigeri, Scherer and Rosenow in ref. [245]. They confirmed that such unusual regime could exist and they found that it is favoured when the electrostatic coupling between the $\nu = 1$ and the $\nu = 2$ edge channels is strong. Yet, their model was only derived for filling factors $2 < \nu_b < 3$ thus it did not capture the disappearance of the interaction-induced oscillations at filling factors $\nu_b \geqslant 4.5$. Also, their model did not explain the charge $-2e$ measured in the shot noise experiments.

Therefore, the exact underlying mechanism giving rise to this regime still remains elusive up to now.

6.2 AB interference with halved periods in graphene FP interferometers

6.2.1 Signatures of AB oscillations with halved periodicities in graphene FP interferometers

In graphene FP interferometers, such peculiar AB oscillations can also be observed.

They appear more distinctly in the largest devices. Fig. 6.1.A and Fig. 6.1.B display pyjama maps measured in the large FP cavity in experiments with the outer edge channel interfering and at bulk filling factors of $\nu_b \simeq 1.6$ and $\nu_b \simeq 2.5$ respectively. These two maps show resistance oscillations that arise from AB interference and which clearly have different periodicities: both the gate and the magnetic field periods in Fig. 6.1.B are approximately halved compared to that in Fig. 6.1.A. Fig. 6.1.A, that was already presented in last chapter, corresponds to the standard AB regime whereas Fig. 6.1.B corresponds to the unusual regime observed in ref. [166].

It is further confirmed by the magnetic field period in Fig. 6.1.B which is about 0.13 mT. It gives an AB surface of 15.9 μm^2, consistent with the dimensions of the device, if we assume that the oscillations have a $\Phi_0^* = \frac{h}{2e}$ periodicity. It clearly evidences the existence of such $\frac{h}{2e}$ periodic AB oscillations in graphene FP interferometers.

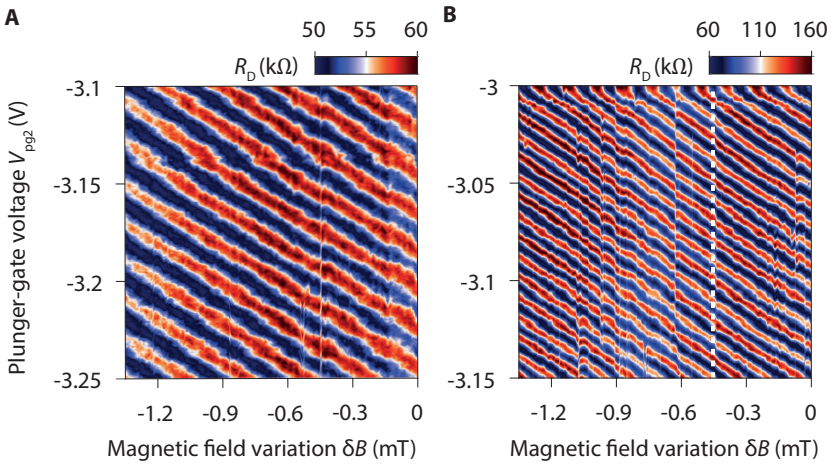

FIGURE 6.1: **Halving of the period of Aharonov-Bohm interference in the large FP cavity of BNGr74 sample.** Evolution of the diagonal resistance R_D versus magnetic field variation δB and plunger-gate voltage V_{pg2} in experiments with the outer edge channel interfering. **A**, At bulk filling factor $\nu_b \simeq 1.6$ and **B**, $\nu_b \simeq 2.5$. Measurements performed at 14 T.

Fig. 6.2 shows a linecut of Fig. 6.1.B along the white dotted line. We observe that the amplitude of the resistance oscillations is periodically modulated: one oscillation out of two has a slightly lower amplitude. It reveals that $\frac{h}{2e}$ periodic AB oscillations coexist with very weak standard AB oscillations which slightly modulate the amplitude of the former. Such coexistence

between the two regimes was already reported by Choi and coworkers in Supplementary information of ref. [166] but at much larger filling factor $\nu_b \simeq 4.5$.

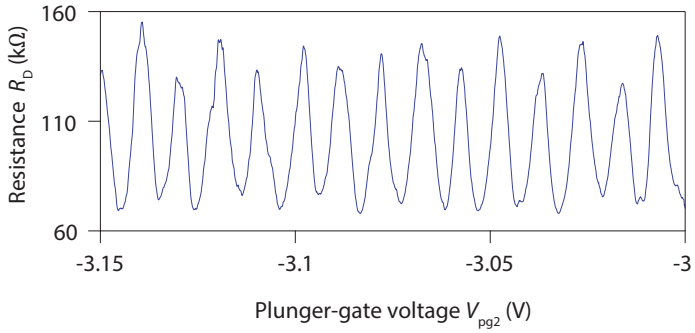

FIGURE 6.2: **Coexistence of two sets of AB oscillations in the large FP cavity of BNGr74 sample.** Linecut of Fig. 6.1.B along whit dotted line. $\frac{h}{2e}$ periodic AB oscillations display a weak amplitude modulation highlighting the weak contribution of standard AB interference to the coherent transport.

In the small graphene FP interferometers, these interaction-induced AB oscillations, and their coexistence with standard AB oscillations, manifest in a different way. Fig. 6.3 displays gate-induced oscillations measured in the small FP cavity with the outer edge channel interfering and at $\nu_b = 2.3$. Contrary to the previous measurements, the oscillations have an irregular shape. Looking at the oscillations on a limited plunger-gate voltage range (Fig. 6.3.B), we see that this shape actually results from a beating between two sets of oscillations with different frequencies.

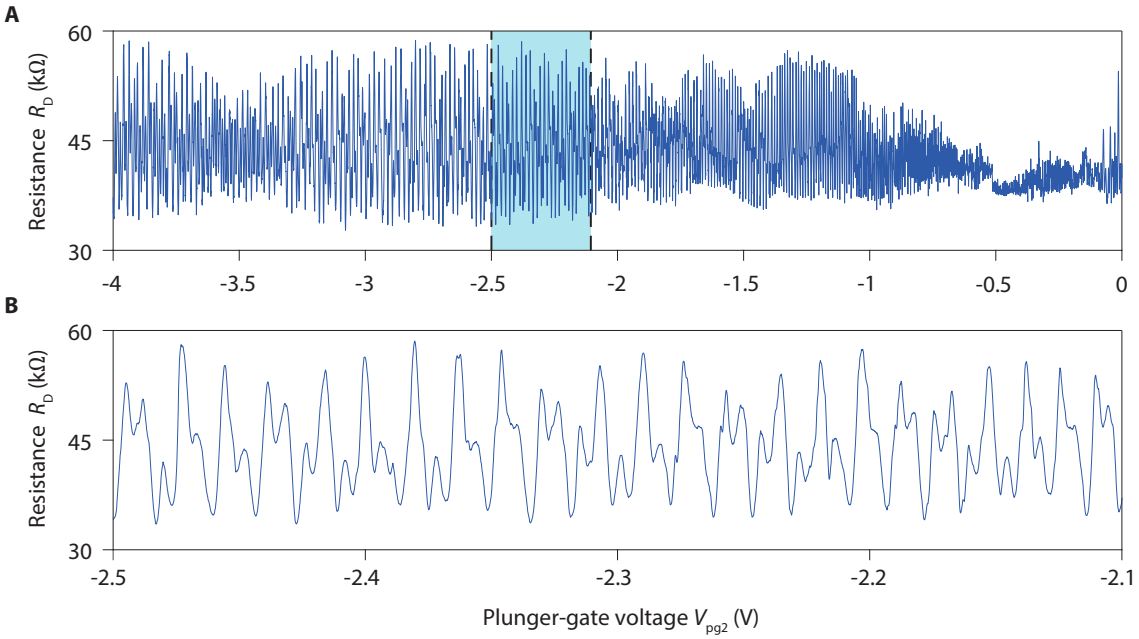

FIGURE 6.3: **Coexistence of two sets of AB oscillations in the small FP cavity of BNGr74 sample.** Evolution of the resistance with the plunger-gate voltage V_{pg2} in an experiment with the outer edge channel interfering at $\nu_b \simeq 2.3$. **A**, Full voltage range spanned. **B**, Zoom on a limited range. Measurement performed at 14 T.

The evolution of the Fourier amplitude of these resistance oscillations with the plunger-gate voltage is displayed in Fig. 6.4.A. It confirms the coexistence of the two oscillating components with different frequencies and it shows that both have the same V_{pg2} dispersion.

We notice that one oscillating component has a frequency approximately twice larger than the other one. From the experiments presented in previous chapter, we can easily identify the low frequency component has being the standard AB oscillations.

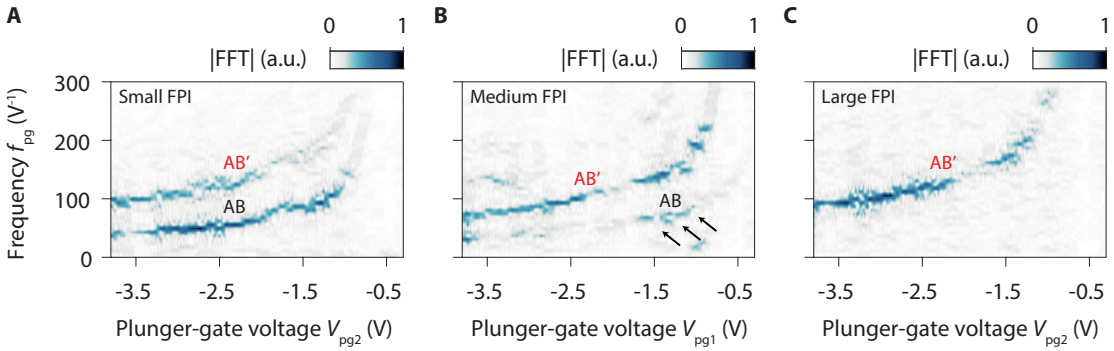

FIGURE 6.4: **Size dependence of *h*/2*e* periodic AB-like oscillations.** Evolution of Fourier amplitude of resistance oscillations with plunger-gate voltage V_{pg} and frequency f_{pg} in interferometry experiments with the outermost edge channel interfering in BNGr74 sample. **A**, In the small FP cavity, $\nu_b \simeq 2.3$, **B**, in the medium FP cavity, $\nu_b \simeq 2.3$ and **C**, in the large FP cavity, $\nu_b \simeq 2.5$. AB and AB' labeled the two types of Aharonov-Bohm oscillations which are respectively $\frac{h}{e}$ and approximately $\frac{h}{2e}$ periodic. In A, the AB and the AB' oscillations coexist resulting in a beating in the oscillations (see Fig. 6.3). In B, the resistance oscillations mostly arise from AB' interference except around $V_{pg1} = -1.3$ V where the contribution of AB interference leads to a beating in the resistance oscillations. In C, only the AB' oscillations are observed. Note that the plunger gate used in A and C is different from that used in B.

One then may believe that the high frequency component corresponds to the second harmonic. Yet, this is inconsistent with its large Fourier amplitude especially if we consider the relatively high transmission of the device in this experiment ($T \simeq 55 - 60$ %). Therefore, this high frequency component can only be interpreted as the signature of AB oscillations approximately $\frac{h}{2e}$ periodic coexisting with standard AB oscillations. Contrary to the previous case, the contribution of the two types of interference to the coherent transport are similar.

To evaluate more quantitatively the ratio of the frequencies, we fitted the V_{pg2}-dispersions of the frequencies in the two traces (Fig. 6.5.A) with two rational fractions of the form $\frac{p_1 V_{pg2} + p_2}{V_{pg2}^2 + q_1 V_{pg2} + q_2}$. The results of these fits are shown in form of the solid lines in Fig. 6.5.A. Fig. 6.5.B shows the ratio of the frequencies calculated using these fits. It is displayed on a voltage range which is far from the plunger-gate voltage where the frequencies diverge. This ratio is virtually constant and it is about 2.1 to 2.2. It demonstrates unambiguously that the periodicity of the second set of oscillations is approximately halved compared to that of standard AB oscillations. Importantly, we remark that the two frequencies are not perfectly commensurate in this case. It explains the beating and the amplitude modulation observed in Fig. 6.3.

These two examples evidence that the regime where the AB oscillations have a halved or approximately halved periodicity is not specific to GaAs/AlGaAs FP interferometers. For the rest of this section, we note AB' this new regime of oscillations.

6.2.2 Specificities of halved-period AB oscillations in graphene FP interferometers

We now discuss different aspects and properties of the AB' oscillations that we observed in our graphene devices.

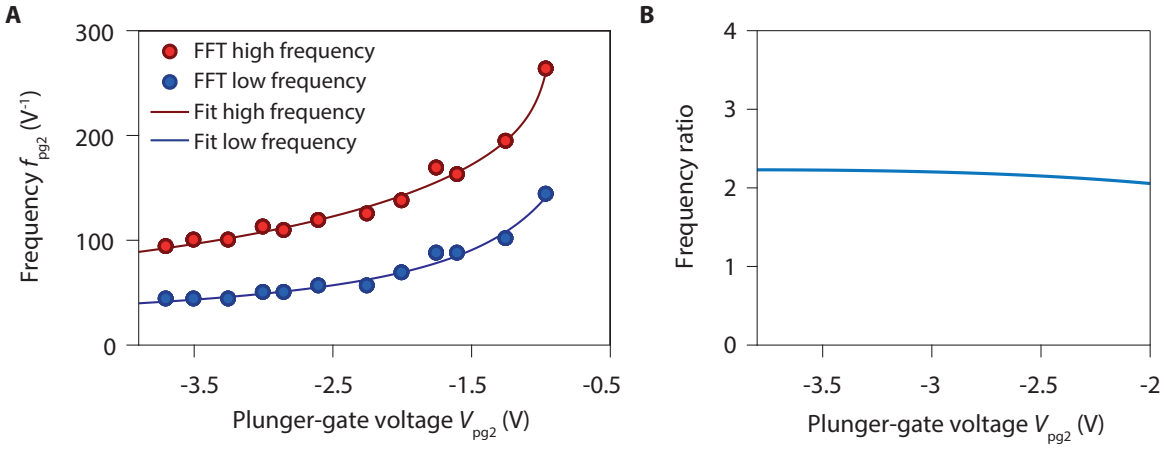

FIGURE 6.5: **Frequencies of two types of AB oscillations in the small FP interferometer at 14 T. A**, Evolution of the frequencies f_{pg2} of the two sets of oscillations in the experiment displayed in Fig. 6.3 with the plunger-gate voltage V_{pg2}. The frequencies, which are extracted from the Fourier transform in Fig. 6.4.A, are fitted with rational fractions to extract the average frequency ratio. **B**, Ratio of the frequencies calculated from the fits in A. The ratio is constant and its value varies typically between 2.1 and 2.2 far from the plunger-gate voltage where the frequencies diverge.

Dependence with the dimensions of the interferometer

The above experiments revealed that the dimensions of the FP interferometers may affect the manifestation of the AB' oscillations and their coexistence with AB oscillations. In the small interferometers, they manifest in a beating in the resistance oscillations as the AB' oscillations coexist with the AB oscillations that still have a significant contribution to the quantum transport. In contrast, in the large interferometers the resistance oscillations mostly arise from the AB' regime and the signatures of the AB regime are hardly visible. These observations are supported by additional experiments.

On the one hand, in experiments performed in the medium interferometer, the contribution of AB oscillations in the resistance oscillations is significantly smaller than that of AB' oscillations. Fig. 6.4.B shows the Fourier amplitude of resistance oscillations measured in the medium FP cavity in a configuration similar to that of Fig. 6.3 and Fig. 6.1.B. A careful look at this figure reveals the existence of two sets of oscillations drawing two traces in the color coded-map: a clear one and a weaker one, which mostly appears around $V_{pg} = -1.3$ V, at approximately halved frequency (see black arrows). The weak trace actually corresponds to the standard AB oscillations.

In this experiment, the contribution of the standard AB oscillations mostly appears on a small range of plunger-gate voltage. In this voltage range, we observe a beating in the oscillations similar to that observed in the small interferometer (Fig. 6.6.A). Outside this voltage range, the oscillations are regular (Fig. 6.6.B) although we distinguish an amplitude modulation reminiscent of that observed in Fig. 6.2.

Thus, the results of the experiments in the medium FP interferometer are somehow an intermediate case between what we observe in the small FP interferometer, where both the AB and the AB' oscillations have significant contributions over the full range of voltage spanned (Fig. 6.4.A), and what happens in the large interferometer, where we hardly or do not distinguish the contribution of AB oscillations (Fig. 6.4.C).

The coexistence of the two regimes in the small interferometers is also observed in BNGr76 device (2.25 μm^2). It readily appears in the form of a beating in the resistance oscillations measured and in the appearance of two clear traces in their Fourier transform as shown respectively in Fig. 6.7 and in Fig. 6.8.A.

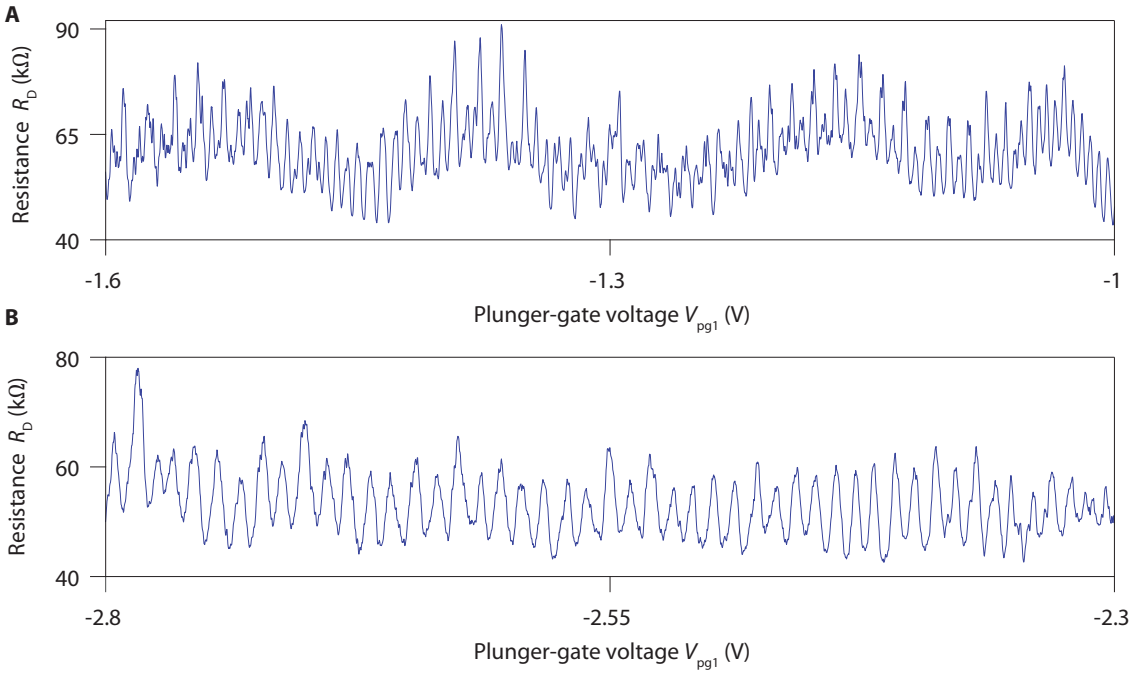

FIGURE 6.6: **Coexistence of two sets of AB oscillations in the medium FP cavity of BNGr74 sample.** Evolution of the resistance with the plunger-gate voltage V_{pg1} in an experiment with the outer edge channel interfering at $\nu_b \simeq 2.3$. **A**, Around $V_{pg1} = -1.3$ V, both AB and AB' interference coexist and both contribute significantly to the transport leading to a beating in the resistance oscillations. **B**, Around $V_{pg1} = -2.55$ V, the resistance oscillations mostly arise from AB' oscillations.

The ratio of the frequencies extracted from fits of the data is displayed in Fig. 6.8.B. Like in the small interferometer of BNGr74 sample, we see that this ratio is almost constant, about 2.1 to 2.3, explaining the beating pattern observed. It further confirms the size dependence observed in BNGr74 sample.

Influence of the tuning of the QPCs

The coexistence between the two regimes is also affected by the tuning of the QPCs. We performed seven experiments with different transmissions of the QPCs in the small FP device. In six out of seven configurations, we clearly observed a coexistence of AB and AB' oscillations leading to some beatings in the resistance oscillations.

Yet, we also found one particular set of split-gate voltages, where the contribution of AB interference was very weak compared to that of AB' interference such that the oscillations measured in the small interferometer did not display a beating pattern (see Fig. 6.9). There was no obvious reason explaining the differences between both cases: the coexistence between AB and AB' oscillations was observed at similar, higher and lower transmissions than that used for the experiment displayed in Fig. 6.9.

Anyway, the coexistence of the two sets of oscillations may not only depend on the size of the interferometer but also on the tuning of the QPCs.

Enhanced visibility of *h*/2*e* periodic oscillations

Otherwise, it is interesting to note that, in the large FP cavity, the AB' oscillations have a high visibility which varies typically between 30 % and 40 %. This is significantly higher than the visibilities usually obtained for standard AB oscillations in this device. It points towards a different

origin of these peculiar oscillations in agreement with the previous investigations in GaAs FP interferometers.

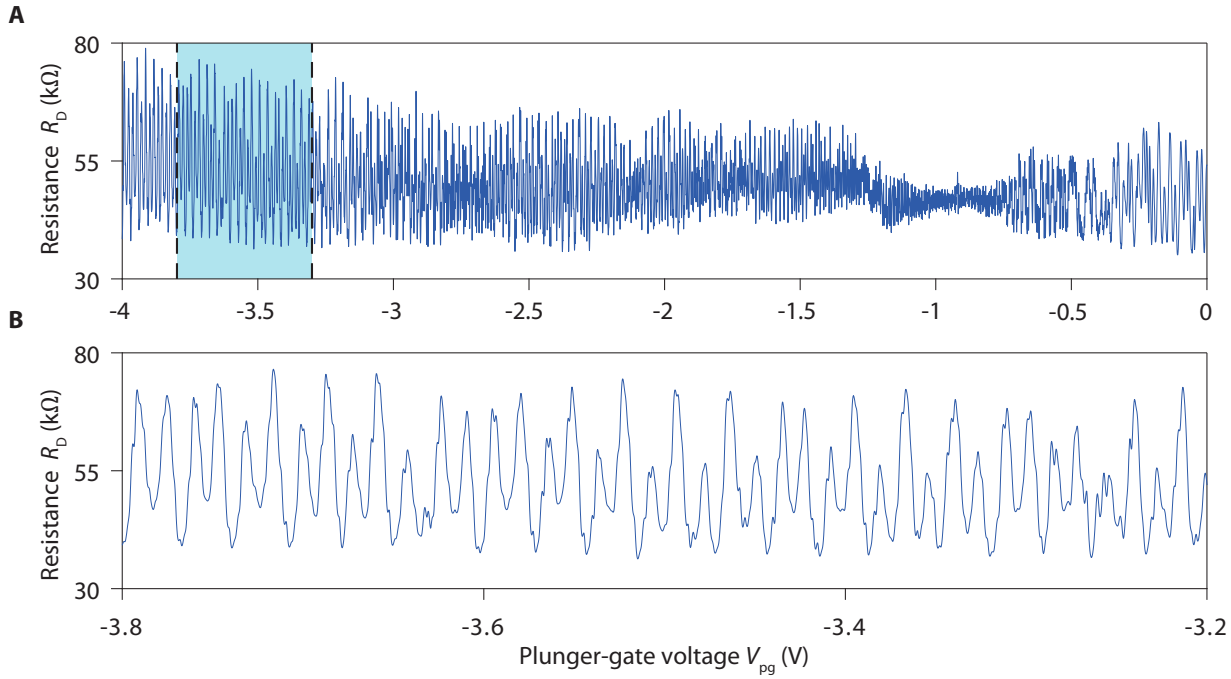

FIGURE 6.7: **Interaction-induced oscillations in BNGr76 sample.** Evolution of the resistance with the plunger-gate voltage V_{pg} in an experiment with the outer edge channel interfering at $\nu_b \simeq 2.4$. **A**, Full voltage range spanned. **B**, Zoom on a limited range.

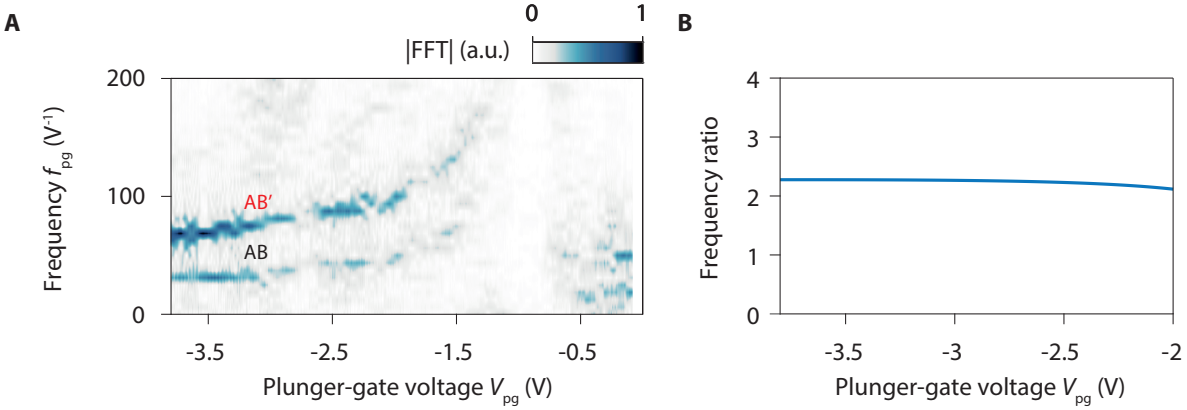

FIGURE 6.8: **Fourier amplitude of AB-like interaction-induced oscillations in BNGr76 FP interferometer.** **A,** Evolution of Fourier amplitude of resistance oscillations displayed in Fig. 6.7 with plunger-gate voltage V_{pg} and frequency f_{pg}. Signatures of both standard AB and AB′ oscillations are observed. **B**, Ratio of the frequencies calculated from the fits of the frequencies. The ratio is virtually constant and its value is about 2.1 to 2.3 far from the plunger-gate voltage where the frequencies diverge.

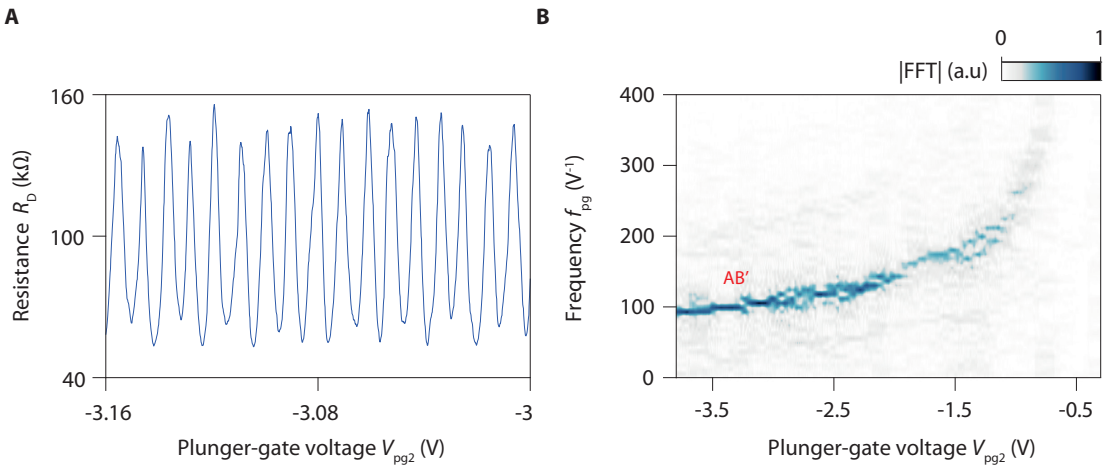

FIGURE 6.9: **Suppression of standard AB oscillations in the small FP cavity of BNGr74 sample.** For one specific tuning of the split-gate voltages, we measured resistance resistance oscillations arising mainly from AB′ interference with virtually no contribution of standard AB interference. **A**, Resistance oscillations measured over a limited voltage range. The oscillations have a regular periodic shape. **B**, Fourier transform of resistance oscillations over the full voltage range spanned. Only the trace characteristic of AB′ oscillations is observed. Experiments at $\nu_b \simeq 2.3$ with the outer edge channel interfering.

Conditions of emergence of the *h*/2*e* periodic oscillations

Finally, we can have an idea of the conditions necessary to observe AB′ oscillations because we performed several interferometry experiments in both oscillations regimes.

In this purpose, it is instructive to reconsider Fig. 5.5 of chapter 5 that we discussed previously. It displays the Fourier amplitudes of resistance oscillations measured at different magnetic fields and with different edge channel interfering in the small FP cavity of BNGr74 sample. In all the Fourier maps except Fig. 5.5.D, there is only a single trace and we previously showed that it corresponds to the standard AB oscillations. These measurements were performed at bulk filling factors $2.5 \leqslant \nu_b \leqslant 2.7$ for the experiments with the inner edge channel and at $1.5 \leqslant \nu_b \leqslant 1.8$ for the experiments with the outer edge channel.

In contrast, in Fig. 5.5.D (which is also presented in Fig. 6.10.B), two traces can be observed showing the coexistence of two sets of oscillations with one having a frequency about twice to three times (see below) larger than the other. We previously identified the low frequency oscillations as the standard AB oscillations and we can assumed that the high frequency oscillations are the manifestations of AB′ oscillations. This experiment was performed with the outer edge interfering at bulk filling factor $\nu_b \simeq 2$.

Hence, in our experiments, the AB′ regime seems to appear only in experiments where the outer edge channel interferes and at bulk filling factors $\nu_b \geq 2$. This is in good agreement with the experimental findings made in GaAs FP interferometers [166, 167, 244].

Frequency tripling ?

We finally report an unexpected feature observed in the experiment at 8 T and $\nu_b \simeq 2$ in the small interferometer of BNGr74 sample. Fig. 6.10.A presents the gate-induced oscillations measured in this case. Like in the other experiments, we observe a clear beating in the resistance oscillations resulting from the coexistence of the two types of AB oscillations with non-commensurate frequencies. Yet, here we notice that there are approximately three AB′ oscillations for each AB oscillation.

This is confirmed by the Fourier transform of the oscillations in Fig. 6.10.B and the frequency ratio (Fig. 6.10.C) calculated from fits of the dispersions of the frequencies. Far from the divergence

of the oscillation frequencies, it is approximately constant and its values ranges from 2.6 to 2.8. Therefore, the intriguing AB' oscillations manifest rather as oscillations with a triple frequency in this experiment.

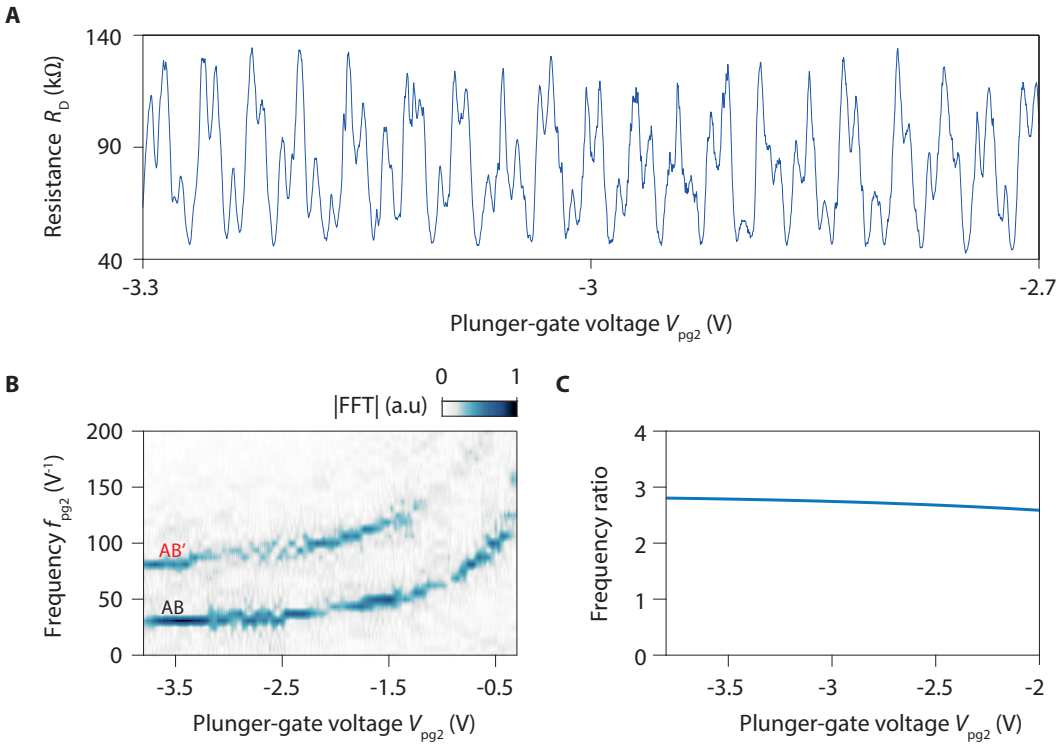

FIGURE 6.10: **Tripling of the frequency of AB oscillations at 8 T in the small interferometer of BNGr74 sample. A**, Gate-induced oscillations measured at 8 T with the outer edge interfering at $\nu_b \simeq 2$. The coexistence of two sets of oscillations, one having a frequency three times larger then the other, appears in the form of a beating in the oscillations. **B**, Fourier transform of resistance oscillations over the full voltage range spanned. The two traces correspond to the AB and AB' oscillations. **C**, Ratios of the frequencies extracted from fits of the data. Far from the plunger-gate voltage where the frequencies diverge, the frequency ratio is approximately constant and its values varies between 2.6 to 2.8.

6.3 Conclusion

In this chapter, we discussed about a peculiar oscillation regime in FP interferometer where AB oscillations have halved or approximately halved periodicities. These oscillations, that were first observed in GaAs/AlGaAs devices, can also be observed in graphene QH FP interferometers under similar experimental conditions.

Yet, in graphene FP devices, they manifest in a different ways depending on the size of the interferometer. In large interferometers, the resistance oscillations virtually only arise from these period-halved interference. In small devices, both types of oscillations coexist, have similar contributions to the quantum transport but they do not have commensurate frequencies resulting in a beating in the oscillations. The size dependence observed in our experiments may help to determine the exact mechanism giving rise to such oscillations.

Likewise, it would be particularly interesting to perform shot noise measurements in the small interferometers: it would allow to determine what is the effective charge of the quasiparticles interfering in the regime where the frequencies are incommensurate. It may also help to identify the origin of these peculiar oscillations.

Chapter 7

Double quantum Hall Fabry-Pérot interferometry

Contents

In ref. [246], Das Samar and coworkers proposed a FP device specifically designed to manipulate non-Abelian anyons at filling factor $\nu = 5/2$ and to use them to perform topological quantum computation. The device originally proposed was composed of three QPCs in series with a dot between the split-gate electrodes of the central QPC. In the prospect of implementing such a device, it is necessary to investigate what are the signatures of coherent transport in FP interferometers with three QPCs in series. To our knowledge, such study has never been reported so far.

In this section, we present the results of both our theoretical and experimental investigations of the coherent transport in such double FP configuration. The experiments presented here were performed in BNGr74 sample which has the suitable geometry with three QPCs in series.

7.1 Theory of coherent transport in a double QH FP interferometer

In this section, we derive the theoretical expression giving the transmission of a double FP interferometer composed of two FP cavities in series which are coherently coupled. We then discuss how the Fourier analysis of resistance oscillations in the device allows to distinguish whether the transport remains coherent or not in such interferometer.

We consider a QH FP interferometer composed of three QPCs in series similar to that depicted in Fig. 7.1.A. Following, the approach of Chamon and coworkers [143], we derive the transmission of such device using the scattering matrix formalism. We do not consider the contribution of the dynamic phase shift here and we only work at zero dc-voltage bias.

The transmission and reflection amplitudes of a single Fabry-Pérot interferometer with two QPCs reads:

$$t_{\mathrm{FP}}(\varphi_{\mathrm{AB}}) = \frac{t_1 t_2 e^{i\varphi_{\mathrm{AB}}}}{1 - r_1^{'} r_2 e^{i2\varphi_{\mathrm{AB}}}}, \tag{7.1}$$

$$t'_{\mathrm{FP}}(\varphi_{\mathrm{AB}}) = \frac{t'_1 t'_2 e^{i\varphi_{\mathrm{AB}}}}{1 - r_1^{'} r_2 e^{i2\varphi_{\mathrm{AB}}}}, \tag{7.2}$$

$$r_{\mathrm{FP}}(\varphi_{\mathrm{AB}}) = r_1 + \frac{r_2 t_1 t'_1 e^{i2\varphi_{\mathrm{AB}}}}{1 - r_1^{'} r_2 e^{i2\varphi_{\mathrm{AB}}}}, \tag{7.3}$$

$$r'_{\mathrm{FP}}(\varphi_{\mathrm{AB}}) = r'_2 + \frac{r'_1 t'_2 t_2 e^{i2\varphi_{\mathrm{AB}}}}{1 - r'_1 r_2 e^{i2\varphi_{\mathrm{AB}}}}, \tag{7.4}$$

with $2\varphi_{\mathrm{AB}}$ the Aharonov-Bohm phase accumulated by electrons after one loop in the cavity, t_i (t'_i) the transmission amplitude, and r_i (r'_i) the reflection amplitude of $\mathrm{QPC_i}$ for the right (left) moving particles.

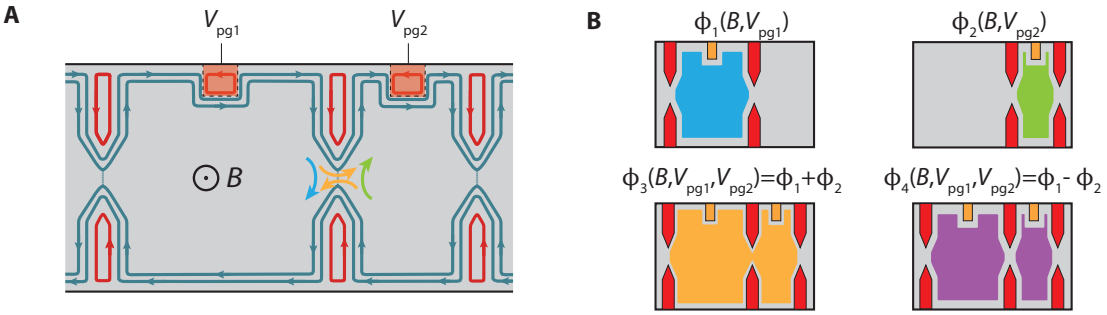

FIGURE 7.1: **Double QH FP interferometry. A**, Schematic of a graphene double FP interferometer in a configuration of partial backscattering of the inner edge channel. The central QPC can either reflect an incoming electron from the left cavity (blue arrow) or the right cavity (green arrow), or transmit coherently an electron from one cavity to the other (yellow arrows). In the latter case, the electrons pick up the Aharonov-Bohm phase given by the combined areas of the small and medium interferometers. In higher order processes, the electrons make multiple loops in the two cavities. **B**, Schematics of the cavities involved in the different interference processes in a double FP cavity. $\phi_{1,2,3,4}$ are the corresponding Aharonov-Bohm phases, indicated with the magnetic field and plunger-gate voltages that modulate them.

The total transmission amplitude t_{tot} of two coupled FP cavities can be calculated using the transmission and reflection amplitudes of one FP cavity and the transmission and reflection amplitudes of a third QPC. Thus, using the previous expressions, we have:

$$t_{\mathrm{tot}}(\varphi_1, \varphi_2) = \frac{t_{\mathrm{FP}}(\varphi_1) t_3 e^{i\varphi_2}}{1 - r'_{\mathrm{FP}}(\varphi_1) r_3 e^{i2\varphi_2}}, \tag{7.5}$$

where $2\varphi_1$ and $2\varphi_2$ are the Aharonov-Bohm phases accumulated by the electrons after one loop in the cavity between $\mathrm{QPC_1}$ and $\mathrm{QPC_2}$ and between $\mathrm{QPC_2}$ and $\mathrm{QPC_3}$, respectively.

Using $|t_i|^2 = |t'_i|^2 = T_i$, $|r_i|^2 = |r'_i|^2 = R_i$ and the relation $r'_i = -\bar{r}_i t'_i / \bar{t}_i$ (the overline indicates complex conjugate), we can express the transmission as:

$$T_{\mathrm{tot}}(\phi_1, \phi_2) = \frac{T_1 T_2 T_3}{|1 - \sqrt{R_1 R_2} e^{i\phi_1} - \sqrt{R_2 R_3} e^{i\phi_2} + \sqrt{R_1 R_3} e^{i(\phi_1 + \phi_2)}|^2} = \frac{T_1 T_2 T_3}{D}, \tag{7.6}$$

where ϕ_1 and ϕ_2 are the Aharonov-Bohm phases acquired when the electrons make a loop into the medium and small cavities respectively (including the phase factor from the reflection amplitudes of the QPCs). In absence of voltage bias, the transmission T_{tot} gives directly the oscillating part of the diagonal conductance $G_{\mathrm{D}}^{\mathrm{osc}} = \frac{e^2}{h} \frac{T_1 T_2 T_3}{D}$. Likewise, the oscillating part of the diagonal resistance oscillations is given by:

$$R_{\mathrm{D}}^{\mathrm{osc}} = \frac{h}{e^2} \frac{D}{T_1 T_2 T_3}. \tag{7.7}$$

The oscillating factor D can be written as:

$$D = 1 + R_1R_2 + R_3R_2 + R_1R_3 - 2(1+R_3)\sqrt{R_1R_2}\cos(\phi_1) - 2(1+R_1)\sqrt{R_2R_3}\cos(\phi_2) + 2\sqrt{R_1R_3}\cos(\phi_1+\phi_2) + 2R_2\sqrt{R_1R_3}\cos(\phi_1-\phi_2), \tag{7.8}$$

or equivalently as :

$$D = 1 + R_1R_2 + R_3R_2 + R_1R_3 - 2(1+R_3)\sqrt{R_1R_2}\cos(\phi_1) - 2(1+R_1)\sqrt{R_2R_3}\cos(\phi_2) + 2T_2\sqrt{R_1R_3}\cos(\phi_1+\phi_2) + 4R_2\sqrt{R_1R_3}\cos(\phi_1)\cos(\phi_2). \tag{7.9}$$

In these expressions, four oscillation frequencies appear, namely, ϕ_1, ϕ_2, $\phi_3 = \phi_1 + \phi_2$ and $\phi_4 = \phi_1 - \phi_2$. The terms in ϕ_3 and ϕ_4 in eq. (7.8) result from coherent interference through the two interferometers. In particular, the ϕ_3 term includes the contribution of the trajectory where the electrons make a loop inside the coupled cavities without being reflected by the central QPC.

Importantly, these two components do not have the same prefactors: the amplitude of the ϕ_3 oscillations is larger than the amplitude of the ϕ_4 oscillations. The latter is even negligible in the weak backscattering limit. In contrast, in a situation where the transport through the double cavity would be incoherent, one would expect the appearance of term in the form of $\cos(\phi_1)\times\cos(\phi_2) = \frac{1}{2}\left[\cos(\phi_3)+\cos(\phi_4)\right]$ which would lead to equal amplitudes of ϕ_3 and ϕ_4 oscillating components.

Therefore, the comparison between the amplitudes of each component allows to distinguish both scenarios.

Fourier transform analysis

Relating this model to the geometry of our device (see Fig. 7.1.A), we can ascribe to each of these four Aharonov-Bohm phases a coupling to the relevant plunger gates:

$$\phi_1 \simeq \frac{2\pi}{\Phi_0}(\delta A_1 B + A_1\delta B) = \frac{2\pi}{\Phi_0}(\alpha_1 V_{\mathrm{pg1}} B + A_1\delta B), \tag{7.10}$$

$$\phi_2 \simeq \frac{2\pi}{\Phi_0}(\delta A_2 B + A_2\delta B) = \frac{2\pi}{\Phi_0}(\alpha_2 V_{\mathrm{pg2}} B + A_2\delta B), \tag{7.11}$$

$$\phi_3 \simeq \frac{2\pi}{\Phi_0}\left[(\delta A_1 + \delta A_2)B + (A_1+A_2)\delta B\right] = \frac{2\pi}{\Phi_0}\left[(\alpha_1 V_{\mathrm{pg1}} + \alpha_2 V_{\mathrm{pg2}})B + (A_1+A_2)\delta B\right], \tag{7.12}$$

$$\phi_4 \simeq \frac{2\pi}{\Phi_0}\left[(\delta A_1 - \delta A_2)B + (A_1-A_2)\delta B\right] = \frac{2\pi}{\Phi_0}\left[(\alpha_1 V_{\mathrm{pg1}} - \alpha_2 V_{\mathrm{pg2}})B + (A_1-A_2)\delta B\right], \tag{7.13}$$

where A_1 and A_2 are the areas of the medium and small cavities respectively, V_{pg1} and V_{pg2} the plunger-gate voltages that tune these areas and α_1 and α_2 their lever arms. In these expressions, there are three parameters which can be tuned experimentally to generate resistance oscillations: V_{pg1}, V_{pg2} and B (or equivalently δB). The parameters affecting the values of each AB phases are summarized in Fig. 7.1.B.

The four phases depend differently on the three tuning parameters. Thus, it is possible to evaluate the amplitude of each oscillating component by making the Fourier transform of resistance oscillations arising when we tune two of the three parameters. Figure 7.2 displays the positions of peaks appearing in the Fourier space for oscillations induced by changes of either both plunger-gate voltages (Fig. 7.2.A), or of one plunger-gate voltage and of the magnetic field (Fig. 7.2.B-C). In the three situations, the Fourier maps display four distinct peaks that correspond to each oscillating component.[1]

[1] The Fourier maps are centrosymmetric.

In all the configurations, the peaks corresponding to the four different components are separated in the Fourier space (in particular in the situations corresponding to Fig. 7.2.A and Fig. 7.2.B). It allows to compare the amplitudes of the ϕ_3 and ϕ_4 components in experiments and to assess whether the transport through the double FP cavity remains coherent or not.

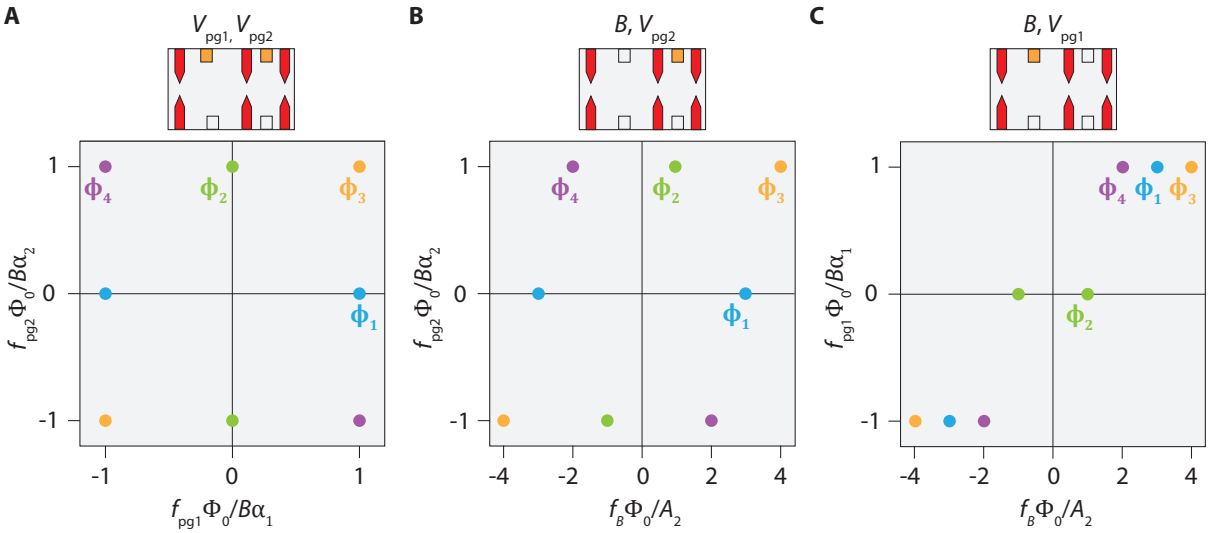

FIGURE 7.2: **Fourier analysis of double QH FP interferometry experiments. A**, **B**, **C**, Positions in reciprocal space of the normalized oscillation frequencies for the three different configurations of interferometry experiments (assuming $A_1 = 3A_2$). Each peak is labelled with its Aharonov-Bohm phase. Top schematics depict the active QPCs (red) and plunger gates (orange) in each experiment. The parameters used to tune the Aharonov-Bohm phases in each case are indicated above the corresponding schematic.

7.2 Experimental evidence of coherent transport in a double FP cavity

Having derived a theoretical model for a double QH FP interferometer, we can now focus on the experiments and compare them with this theory. In this section, we present experimental results obtained by studying BNGr74 sample in double FP configuration where the three QPCs were set at partial reflection of a given edge channel. We show typical resistance oscillations observed in such configuration, perform their Fourrier analysis and discuss it.

7.2.1 Resistance oscillations in double FP geometry

Operating BNGr74 device in a double FP configuration, we performed systematic studies of the evolution of resistance oscillations with the different tunable parameters. The most relevant results are shown in Fig. 7.3 that displays 2D color-coded maps of the diagonal resistance R_D versus plunger-gate voltages and/or magnetic field in the three possible configurations.

Fig. 7.3.A shows the evolution of R_D with V_{pg1} and V_{pg2} in an experiment where the three QPCs are tuned at partial transmission of the outer edge channel. We see that R_D oscillates with both voltages and that the resistance oscillations draw a regular 2D pattern. It highlights the flux modulations in both the small and medium cavities and it confirms that the three QPCs are partially reflecting the same edge channel.

Similarly, Fig. 7.3.B displays a pyjama map obtained by measuring the evolution of R_D with V_{pg2} and δB (experiment with the inner edge channel). It shows a diagonal stripe pattern, characteristic of AB oscillations in the small cavity, with an additional wiggling. The magnetic field period, associated with this wiggling, is about 0.4 mT and corresponds to the AB period expected

for the medium cavity. It shows that the wiggling originates from AB oscillations in the medium interferometer which is in series with the small one.

Finally, Fig. 7.3.C displays the last configuration where the evolution of R_D with V_{pg1} and δB is measured (experiments with the outer edge channel). This color-coded map shows a diagonal stripe pattern, reminiscent of the AB oscillations in the medium cavity, on top of large resistance oscillations (vertical bands). These last oscillations do not depend on V_{pg1} and are periodic with δB. Their magnetic field period is about 1.1 mT and corresponds to the AB period expected for oscillations in the small FP cavity. Again, it shows the coupling between the two FP cavities.

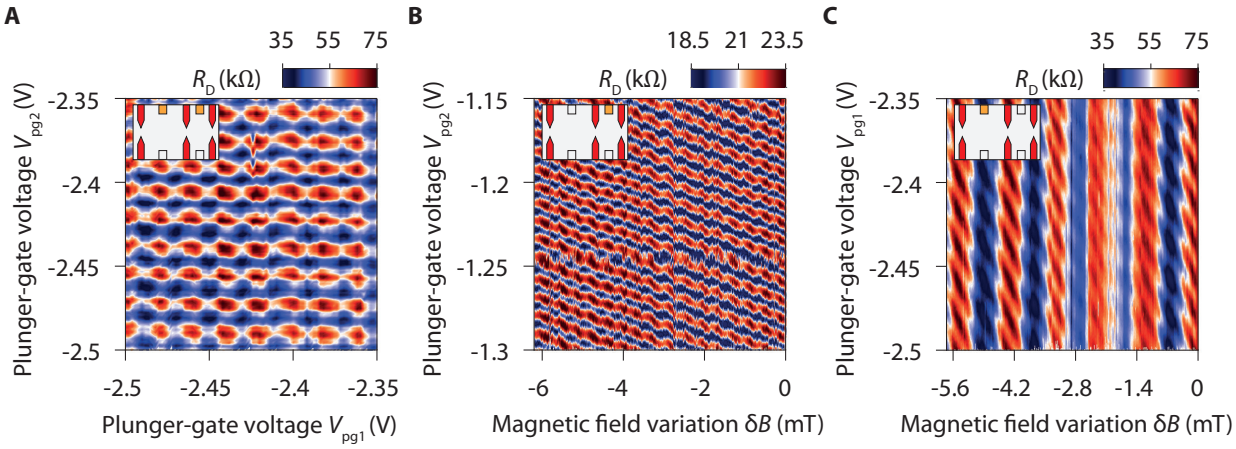

FIGURE 7.3: **Aharonov-Bohm interference in a double FP cavity.** **A**, Diagonal resistance R_D versus plunger-gate voltages V_{pg1} and V_{pg2} (outer edge channel interfering). **B**, Diagonal resistance R_D versus magnetic field variation δB and plunger-gate voltage V_{pg2} (inner edge channel interfering). **C**, Diagonal resistance R_D versus magnetic field variation δB and plunger-gate voltage V_{pg1} (outer edge channel interfering). Resistance oscillations in the three pyjama-maps display features characteristic of Aharonov-Bohm interference in both the small and the medium cavities showing that the device operate as a double QH FP interferometer. Schematics : Active QPCs (red) and plunger-gates (orange). Measurements performed at $B = 14$ T.

7.2.2 Fourier analysis

In all these experiments, features characteristic of AB oscillations in both the medium and the small cavities are observed. To investigate the coherence of the transport through the couple cavities, we computed and analysed 2D Fourier transforms of the resistance oscillations measured according to the previous discussion. Fig. 7.4 shows the color-coded maps of the Fourier amplitudes for the measurements of Fig. 7.3. They all display three or four distinct Fourier peaks whose positions are reported in Table 7.1. The presence of these peaks, and their respective positions in each measurement configuration, are consistent with our theoretical expectations. We now detail their different origins.

In Fig. 7.4.A, the two main peaks with the largest amplitudes (in the positive quadrant) are located at frequencies (f_{pg1}, f_{pg2}) = (53 V^{-1}, 0 V^{-1}) and (0 V^{-1}, 60 V^{-1}) and thus correspond to oscillations which are only affected by the change of one of the two plunger-gate voltage. Hence, they can be directly attributed to the AB interference respectively in the medium and the small cavities (component oscillating with ϕ_1 and ϕ_2). These peaks have the largest amplitudes as they are associated with first order processes. Similarly, the main peaks in Fig. 7.4.B-C can be readily attributed to the AB oscillations respectively in the medium and small interferometers. In this two cases, the magnetic field frequencies f_B of the oscillations fit with the AB surfaces of the corresponding cavities (see Table 7.2).

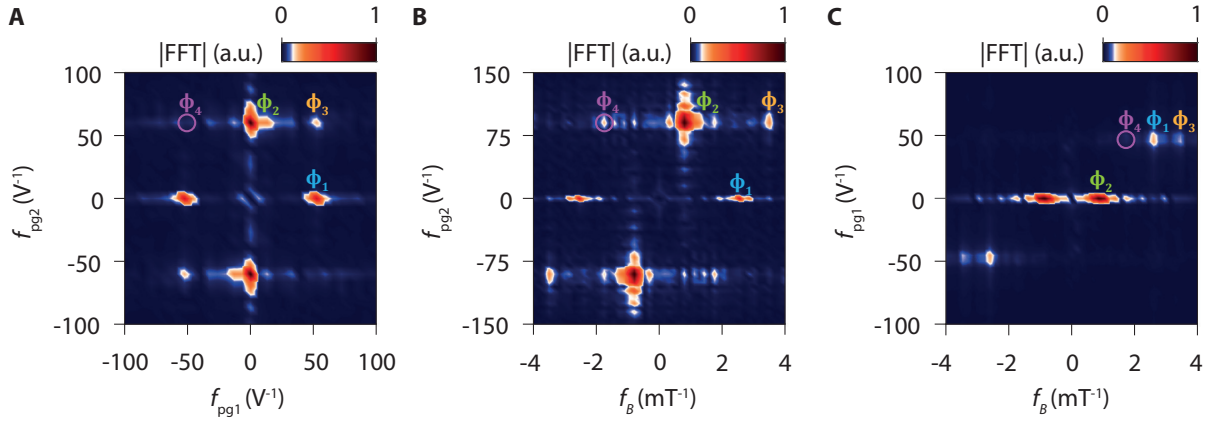

FIGURE 7.4: **Fourier analysis of resistance oscillations in the double FP cavity. A, B, C**, Four-quadrant Fourier amplitudes of the resistance oscillations displayed respectively in Fig. 7.3.A-C in their reciprocal space. The peaks corresponding to the different Aharonov-Bohm phases are identified in each case and their coordinates are gathered in Table 7.1. In the three cases, the ϕ_3 peak has a larger amplitude than the ϕ_4 one (which is even hardly visible in A and C) demonstrating the coherent coupling of the two FP cavities. The violet circles highlight the expected positions of ϕ_4 peaks.

Experiments	Frequencies of ϕ_1 peak	Frequencies of of ϕ_2 peak	Frequencies of ϕ_3 peak	Frequencies of ϕ_4 peak
Fig. 7.3.A	53 V^{-1}, 0 V^{-1}	0 V^{-1}, 60 V^{-1}	53 V^{-1}, 60 V^{-1}	hardly visible
Fig. 7.3.B	2.54 mT^{-1}, 0 V^{-1}	0.79 mT^{-1}, 90 V^{-1}	3.49 mT^{-1}, 90 V^{-1}	-1.75 mT^{-1}, 90 V^{-1}
Fig. 7.3.C	2.60 mT^{-1}, 45 V^{-1}	0.87 mT^{-1}, 0 V^{-1}	3.47 mT^{-1}, 45 V^{-1}	hardly visible

TABLE 7.1: **Coordinates of the peaks in the reciprocal spaces in double FP experiments.**

Experiments	AB area for ϕ_1 peak (μm^2)	AB area for of ϕ_2 peak (μm^2)	AB area for ϕ_3 peak (μm^2)	AB area for ϕ_4 peak (μm^2)
Fig. 7.3.B	10.5	3.3	14.4	7.2
Fig. 7.3.C	10.8	3.6	14.4	x

TABLE 7.2: **AB areas associated with the peaks in the reciprocal spaces.**

A third peak, corresponding to the component oscillating with ϕ_3, is also visible in the three Fourier spaces. It appears at finite plunger-gate-voltage frequencies which are equal to that of the ϕ_1 or ϕ_2 peak as expected considering that $\phi_3 = \phi_1 + \phi_2$. Likewise, its magnetic field frequency corresponds approximately to the sum of that of the main peaks. This is expected as this peak is associated with interference processes that involve a loop inside the double cavity formed by the addition of the small and the medium ones in series.

This peak should come with a fourth one associated with the AB phase $\phi_4 = \phi_1 - \phi_2$. It can be observed in Fig. 7.4.B but it can hardly be seen in Fig. 7.4.A and Fig. 7.4.C. In all the configurations, the Fourier amplitude of this last peak is smaller than the amplitude of the ϕ_3 peak as expected from eq.(7.8).

This actually shows that the ϕ_3 peak is mainly the result of the interference process for which the electron wavefunctions interfere coherently after passing twice (back and forth) through the partially-transmitting middle QPC. It demonstrates the coherent coupling of the two FP cavities and it is consistent with the 10 μm coherence length estimated for our device.

7.3 Conclusion

In this chapter, we focused on double QH FP interferometers composed of three QPCs in series. We derived a theoretical model to describe the coherent transport in such device. We found a remarkable agreement between our predictions and our experiments allowing us to demonstrate, with a Fourier analysis of the oscillations, that the transport remains coherent in the double FP configuration.

This study provides a first step towards the experimental study of devices with multiple FP cavities in series. It might be extended to the FQH regime for the probing of quasiparticles properties with novel device geometries.

Chapter 8

Investigations of the fractional regime in graphene FP interferometers

Contents

The ultimate purpose of QH FP interferometry is to evidence the existence of anyonic quasiparticles by studying AB interference in FQH regime. During this thesis, we managed to fabricate a sample, BNGr76, where we observed clearly the formation of fractional states. In this chapter, we present our attempts to make interference with fractional edge channels in this device. We begin by presenting the transport signatures observed in this sample, which demonstrate the formation of fractional edge states both in the bulk and in the QPCs. We shortly show results obtained in the integer regime before presenting unexpected features that we observed trying to make interference at fractional transmissions of the QPCs but at integer bulk filling factors. We finally present interferometry experiments performed at fractional bulk filling factor.

8.1 Signatures of fractional QH states in graphene QH FP interferometers.

8.1.1 Characteristics of BNGr76 sample

The device studied in this section is BNGr76 device, which was already presented in section 5.1.4. It is shown in Fig. 8.1. It is a single QH FP interferometer equipped with a graphite back gate. The mobility of the bulk graphene in this sample is about 120.000 $cm^2.V^{-1}.s^{-1}$ at a density $n = 10^{12}$ cm^{-2}. It corresponds to a mean free path about 1.4 μm. The geometric characteristics and the different gate capacitances are gathered respectively in Table 8.1 and Table 8.2.

The geometric characteristics and the different gate capacitances are gathered respectively in Table 8.1 and Table 8.2.

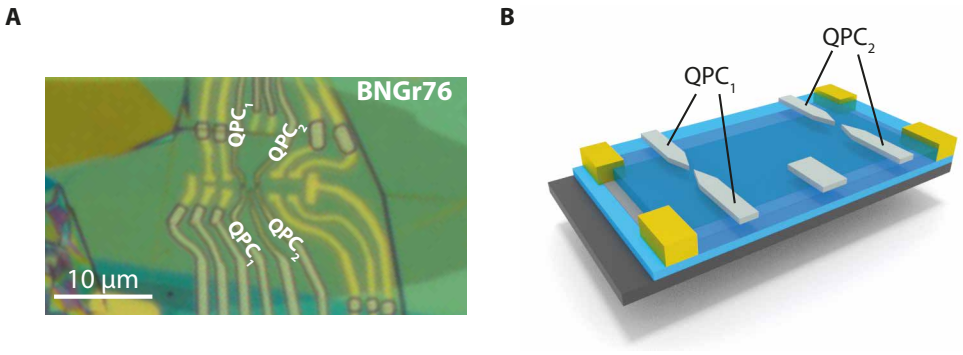

FIGURE 8.1: **BNGr76 QH FP interferometer. A**, Optical image of the device. **B**, 3D schematic of the device.

Top h-BN thickness (nm)	Bottom h-BN thickness (nm)	Graphite thickness (nm)	Split-gate gap (nm)	Geometric area A_{geo} (μm^2)	Path length L (μm)
31	20	6	65/65 (design)	2.25 ± 0.25	3.5 ± 0.4

TABLE 8.1: **Geometric characteristics of BNGr76 device.** The thicknesses of the h-BN and graphite layers are measured by atomic force microscopy. The geometric area A_{geo} and the QPC gap sizes are extracted from the lithographic design (no SEM image available at the time of the writing).

Back-gate capacitance (mF/m^2)	Charge neutral point in the whole sample	Capacitance ratios at 0 T $C_{sg1,2}/C_{bg}$	Capacitance ratios at 14 T $C_{QPC1,2}/C_{bg}$
1.36	$(V_{bg}, V_{QPC}) = (-0.04\,V, 0.48\,V)$	0.65, 0.65	0.29, 0.43

TABLE 8.2: **Split-gate characteristics in BNGr76 sample.** The doping induced by the palladium gate electrodes can be compensated by application of a $+0.48$ V voltage on the split-gate electrodes.

8.1.2 Formation of fractional QH states in the bulk

We now focus on the QH transport in this device. We begin by discussing Fig. 8.2 which shows the evolution of the longitudinal resistance R_{xx} of the sample with both back-gate voltage V_{bg} and magnetic field B in the form of Landau fan diagram. For this measurement, R_{xx} was measured between two contacts located on each side of the FP cavity and a positive voltage was applied on each QPC to compensate the doping induced by the palladium gate electrodes.

In this sample, signatures of QH effect appear above 0.5 T and the $\nu = 1$ broken symmetry state emerges starting from 3 T. The full degeneracy lifting of the $N = 1$ LL occurs approximately around 10 T (although $\nu = 5$ is not well-defined). At higher fields, above 12 T, R_{xx} shows minima in the transitions between two successive integer QH states. For instance, in Fig. 8.2.B, these minima (red arrows) clearly appear between $\nu = 2, 3, 4$ and 5 states. These features disperse linearly in the V_{bg}-B plane as highlighted by the red arrows in Fig. 8.2.A and become more pronounced as the magnetic field is increased. They are the signatures of gap openings associated with the formation of fractional QH states in the bulk.

The emergence of these states also clearly appears in Fig. 8.3. It displays the diagonal conductance G_D of the sample as a function of the back-gate voltage at 14 T. During this measurement a voltage of $+0.48$ V was applied on the QPCs to compensate the hole-doping induced by the palladium gate electrodes. In Fig. 8.3.B, we observe all the integer filling factor plateaus appearing successively as we increase the back-gate voltage. Yet, in the transitions between integer plateaus, G_D shows fractional plateaus appearing approximately at $G_D = \frac{e^2}{h}(M + \frac{1}{3})$ and $G_D = \frac{e^2}{h}(M + \frac{2}{3})$

where M is an integer. These additional plateaus mark the formation of fractional states of the $\nu = \frac{k}{3}$ family.

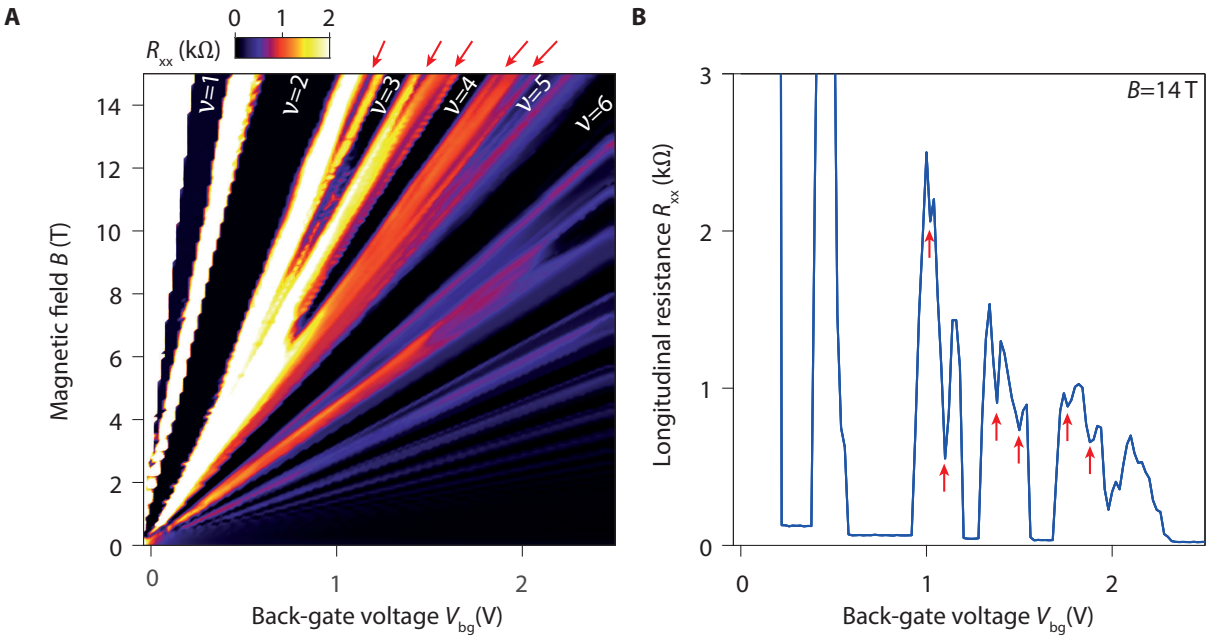

FIGURE 8.2: **Landau fan diagram of BNGr76 sample.** **A**, Evolution of the longitudinal resistance R_{xx} measured between both sides of the interferometer with respect to the magnetic field B and the back-gate voltage V_{bg}. **B**, Linecut at 14 T. The resistance minima (red arrows) in the transitions between the integer plateaus mark the opening of gaps and the formation of fractional QH states in the bulk.

From these two measurements, we see that in our sample there are clear signatures of $\nu = \frac{8}{3}, \frac{10}{3}, \frac{11}{3}, \frac{14}{3}$ and $\frac{15}{3}$ states forming in the bulk as well as weaker signatures of states forming at $\nu = \frac{1}{3}, \frac{2}{3}, \frac{4}{3}$ and $\nu = \frac{7}{3}$.

8.1.3 Signatures of fractional edge channels in the QPCs

The formation of fractional QH edge channels can also be observed by studying the evolution of the QPCs transmission with the split-gate voltages. Fig. 8.4 displays the evolution of the diagonal conductance G_D with the voltage applied on one QPC. For these measurements, a positive voltage of $V_{QPC} = 0.48$ V was applied on the other QPC such that it does not induce any backscattering. Thus, in this map, the value of G_D directly indicates the transmission of the QPC considered.

The color-coded maps are similar to that discussed section 4.4: they display quantized G_D stripes with a slope lower than that of the split gates at zero field (dotted lines). It proves that the split gates indeed act as QPCs. Yet, we observe a few differences compared to the QPC transmission maps discussed previously.

First, contrary to the maps of Fig 4.4, the positions of the horizontal G_D bands match rather well with the bulk integer fillings determined from capacitance measurements. It shows that indeed the second QPCs does not induce backscattering. Likewise the conductance is well quantized on the diagonal stripe even in the $N = 1$ LL.

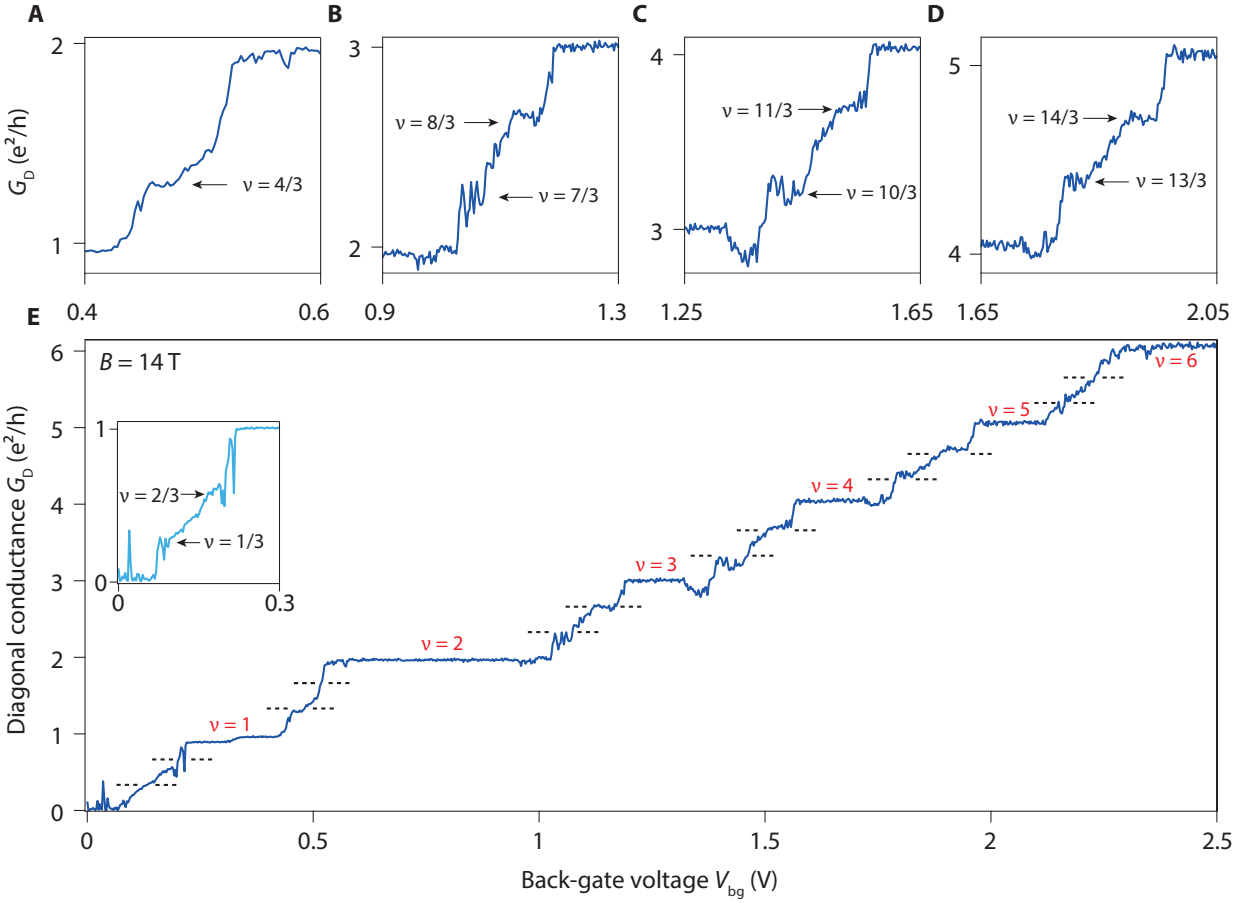

FIGURE 8.3: **Fractional quantum Hall plateaus.** Evolution of the diagonal conductance G_D with the back-gate voltage V_{bg}. **E**, Full gate voltage range spanned and **A**, **B**, **C**, **D**, zooms on limited voltage ranges. Between integer QH plateaus, additional plateaus appear marking the formation of FQH states at filling factors $\nu = \frac{k}{3}$. Black dotted lines indicates when $G_D = \frac{k}{3}\frac{e^2}{h}$. For these measurements, a voltage of 0.48 V is applied on the QPCs such that the whole graphene flake is at isodensity. Inset in E: Zoom at low back-gate voltages after corrections. At low back-gate voltages, the signal has a large out-of-phase component. We take it into account by plotting the modulus of the impedance. It allows to unveiled the formation of a $\frac{e^2}{3h}$ plateaus which could not be seen otherwise.

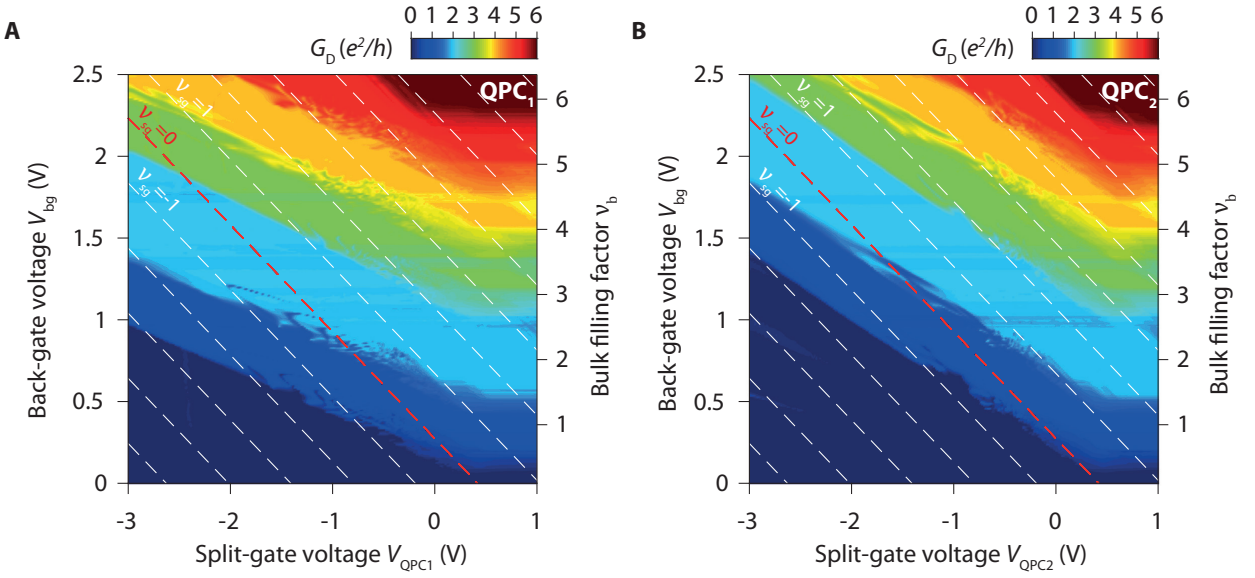

FIGURE 8.4: **BNGr76 QPC characteristics at 14 T.** Evolution of the diagonal conductance G_D with the back-gate voltage and the voltage V_{QPC} applied on the split-gate electrodes of one QPC. During these measurements, a positive voltage of 0.48 V is applied on the other QPC such that it does not induce any backscattering. The two maps show all the typical features characteristic of split gates operating as QPC in the QH regime. G_D diagonal bands are well quantized even in the $N = 1$ LL. The transitions between quantized G_D diagonal stripes are noisy at small voltages (typically $-0.5\ \text{V} \leq V_{QPC} \leq 0.5\ \text{V}$) whereas they are smooth at more negative voltages. These noisy transitions are due to the reconstruction of fractional QH states in the QPCs.

Another important feature in these maps is that the transitions between quantized G_D stripes have different shape depending on the split-gate voltage. It can be readily seen in Fig. 8.5 which shows linecuts of Fig. 8.4 at fixed back-gate voltages. At large negative voltages, typically for $V_{QPC1} < -1$ V and $V_{QPC2} < -0.5$ V, the transitions are rather smooth and continuous although we observe a few resonances or reentrances in the QPCs (see for instance sky blue plots around $V_{QPC1} \simeq -1.8$ V and $V_{QPC2} \simeq -1.1$ V). These features are commonly observed in our split-gated QPCs [16, 211] and they were already present in the QPCs of BNGr74 sample (see QPC$_2$ map in Fig. 4.16).

In contrast, at low voltages, for $-1\ \text{V} < V_{QPC1} < 1\ \text{V}$ and $-0.5 < V_{QPC2} < 1$ V, additional features appear. Indeed, when we start to pinch the innermost edge channel, we observe the presence of kinks or small plateaus in the transition between integer plateaus. These features appear on smaller voltage ranges than the previous resonances and approximately at $G_D = \frac{e^2}{h}(M + \frac{1}{3})$ and $G_D = \frac{e^2}{h}(M + \frac{2}{3})$ (black dotted lines). They mark the voltage ranges where fractional states form in the QPC constrictions. These plateaus are noisy compared to the integer plateaus and there are actually composed of several sharp peaks and dips as we can see for instance in Fig 8.6.A for QPC$_1$. Such features are the signatures of the (resonant) tunnelling between counterpropagating fractional QH edge channels in the QPCs. They reflect the chiral Luttinger liquid nature of this fractional edge states [247–252] (the resonances associated with the tunnelling of the $\nu = \frac{7}{3}$ state were studied by K. Zimmermann in her PhD thesis [211]). These resonances tend to disappear when we apply a dc-voltage bias in addition to the ac-voltage excitation as we can see in Fig. 8.6.B. At large voltage bias, they vanish and the $\nu = \frac{4}{3}$ and $\frac{5}{3}$ fractional plateaus appear in both QPC$_1$ and QPC$_2$, although they are not clearly marked in the latter, corroborating our interpretation.

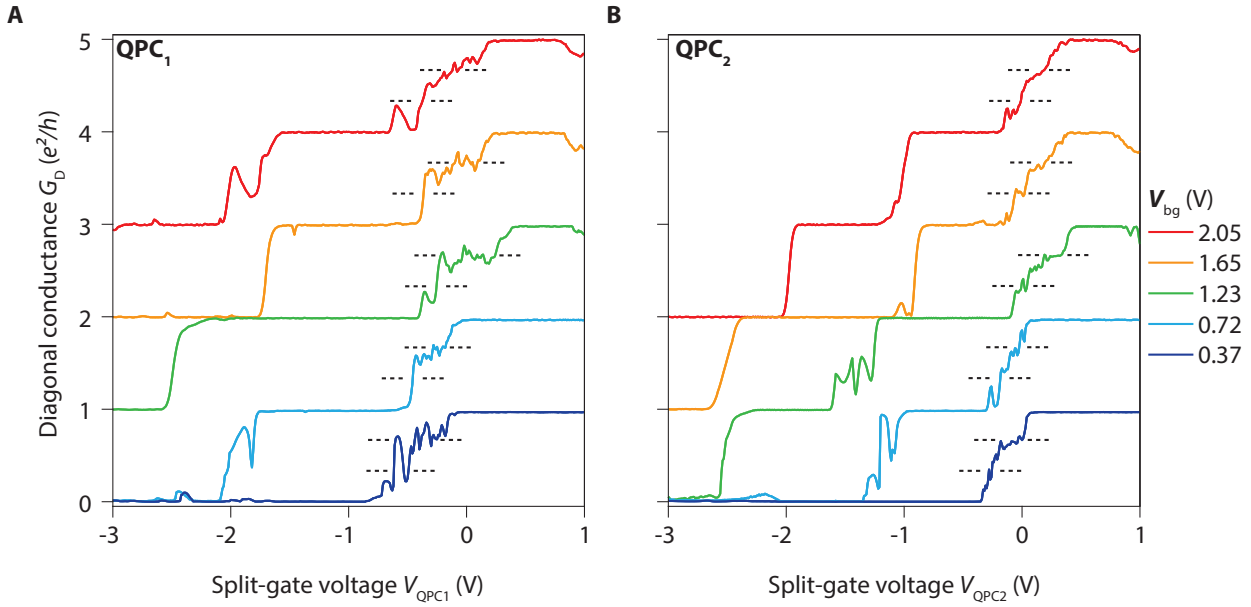

FIGURE 8.5: **QPC transmission plots.** Linecuts of Fig. 8.4 at fixed back-gate voltages for **A**, QPC_1 and, **B**, for QPC_2. The black dotted lines indicate when $G_D = \frac{k}{3}\frac{e^2}{h}$. Noisy fractional plateaus appear in the QPCs transmission. These plateaus are composed of several resonances appearing when we start to pinch the QPCs and backscatter the innermost edge channel. When the QPCs are more pinched, the transitions between the integer plateaus become smooth and do not show any plateaus.

We note that the $\nu = \frac{5}{3}$ state was not visible in Fig. 8.2 and Fig. 8.3. It suggests that the smooth electrostatic potential in the QPC favours the reconstruction of this fractional state that does not form in the bulk. A recent paper by Khanna and cowokers indeed suggests that reconstructed fractionnal edge modes may appear at the boundaries of integer QH states in presence of a smooth potential [253]. We also stress that fractional QH plateaus mainly appear in the transition between the first integer plateaus i.e. only when the innermost integer edge channel is reflected and when the other integer edge modes pass below the split gates.

Fig. 8.5 and Fig. 8.6 show that we can control the transmissions of fractional edge channels when the bulk is at integer filling factor. Likewise, we can also selectively backscatter some fractional edge channels with our QPCs when the bulk is at fractional filling factors. Fig. 8.7 shows transmissions plots measured at back-gate voltages of $V_{bg} = 0.47$ V and $V_{bg} = 1.15$ V where we observed plateaus $G_D = \frac{4}{3}\frac{e^2}{h}$ and $G_D = \frac{8}{3}\frac{e^2}{h}$ in Fig. 8.3. In Fig. 8.7, we indeed notice that G_D displays the corresponding fractional plateau around $V_{QPC} = 0.48$ V which is the voltage where the doping of palladium electrode is fully compensated. When V_{QPC} is lowered the conductance continuously drops down to $\frac{e^2}{h}$ or $\frac{2e^2}{h}$ showing that we can tune the transmission of the corresponding fractional QH edge channels. Note that the transitions present some resonances as discussed above. In Fig. 8.7.B, some of them may arise from the tunnelling between counterpropagating $\nu = \frac{7}{3}$ edge channels.

Thus, in our interferometer, we can make two types of interferometry experiments with fractional edge channel: either at fractional or at integer bulk filling factors.

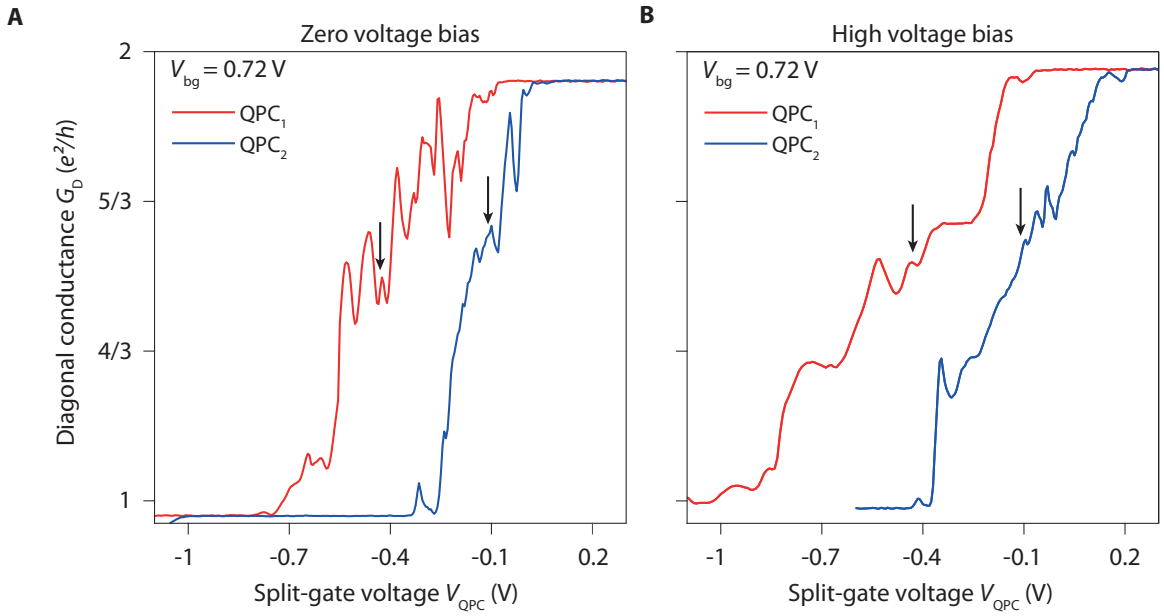

FIGURE 8.6: **Effect of a dc-voltage bias on the QPC transmissions.** Evolution of the diagonal conductance G_D with the voltage V_{QPC} applied on the split-gate electrodes of one QPC. Measurements performed, **A**, without a dc-voltage bias and, **B**, with a 800 μV voltage bias. The resonances associated with the tunnelling of fractional QH edge channels disappear at high voltage bias and $\frac{4}{3}\frac{e^2}{h}$ and $\frac{5}{3}\frac{e^2}{h}$ conductance plateaus appear. The black arrows indicate the QPC set points for the experiments discussed in section 8.3.1. Measurements performed at 14 T.

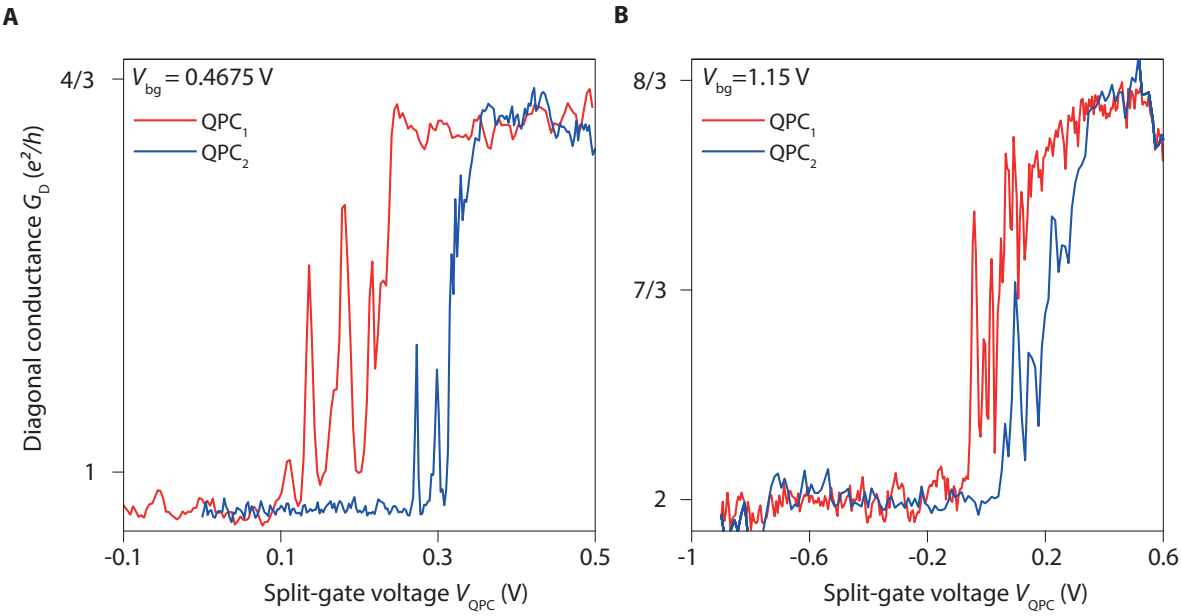

FIGURE 8.7: **QPC transmission plots at bulk fractional filling factors.** Evolution of the diagonal conductance G_D with V_{QPC} the voltage applied on the split-gate electrodes of one QPC (zero dc-voltage bias). **A**, $V_{bg} = 0.47$ V. **B**, $V_{bg} = 1.15$ V. At these voltages, the bulk graphene is respectively at filling factors $\nu_b \simeq \frac{4}{3}$ and $\nu_b \simeq \frac{8}{3}$ as indicated by the presence of the corresponding G_D plateaus at $\frac{4}{3}\frac{e^2}{h}$ and $\frac{8}{3}\frac{e^2}{h}$ when the QPCs are open. The conductance lowers down to $\frac{e^2}{h}$ and $\frac{2e^2}{h}$ when V_{QPC} is decreased showing that one can tune the transmissions of the $\nu = \frac{4}{3}$ and $\nu = \frac{8}{3}$ edge channels in each QPCs exactly like in the integer case. Measurements performed at 14 T.

8.2 Experiments with integer edge channels

Before presenting the results of our investigations of the fractional regime, we begin by showing some results obtained with the integer edge channels of the $N = 0$ LL and with a compressible bulk. They will be compared to the results obtained with fractional edge channels interfering in the next sections.

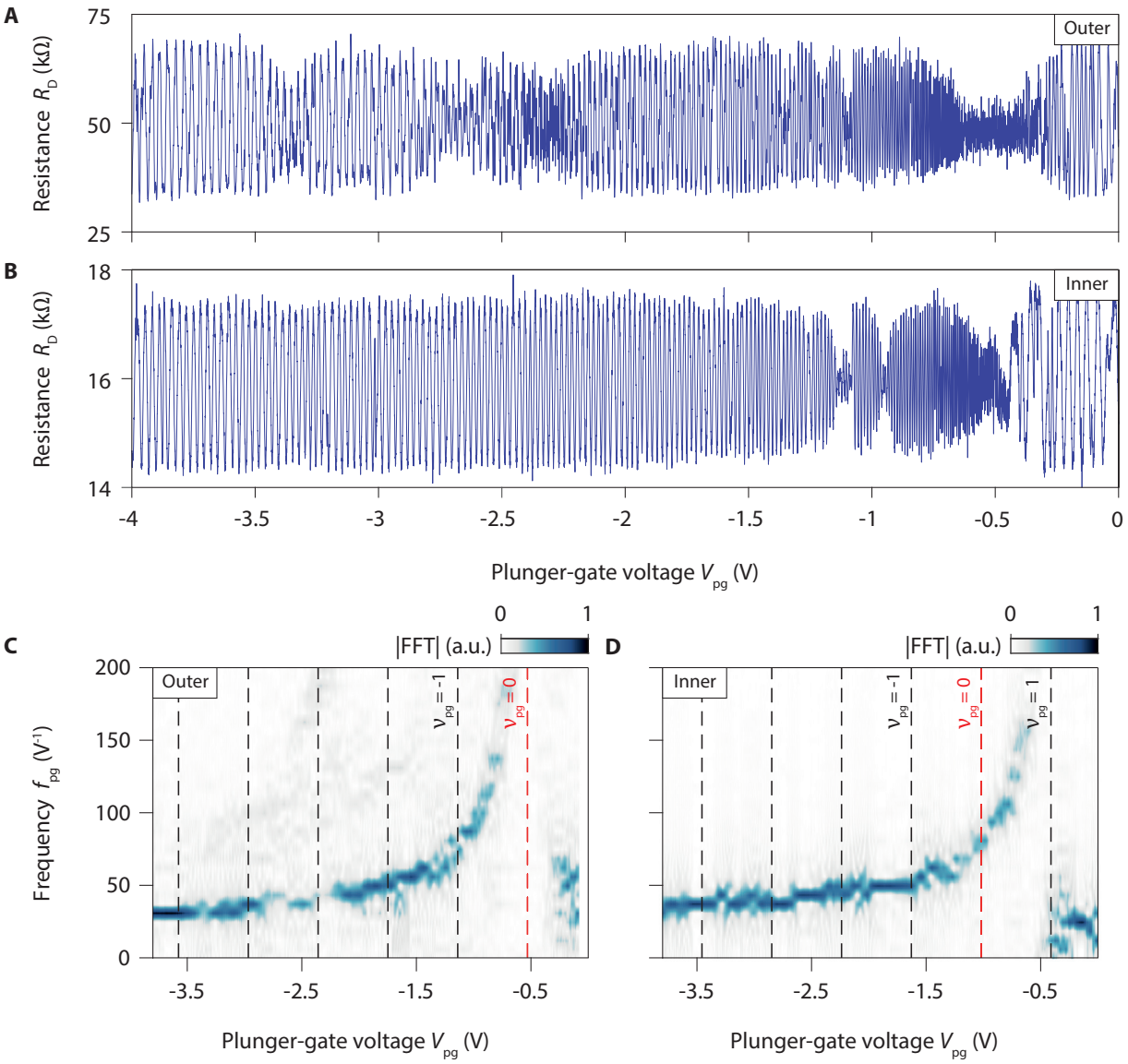

FIGURE 8.8: **Gate-induced oscillations with integer edge channels interfering.** Diagonal resistances oscillations measured in BNGr76 device while sweeping the plunger-gate voltage V_{pg} in experiments with, **A**, the outer edge channel interfering and, **B**, inner edge channel interfering. The measurements are performed at 14 T respectively at filling factors $\nu_b \simeq 1.7$ and $\nu_b \simeq 2.5$. **C** and **D**, Corresponding Fourier transforms.

Fig. 8.8.A and Fig. 8.8.B present gate-induced oscillations measured with respectively the outer and the inner edge channel interfering at 14 T. Clear and stable oscillations are observed over the full range of voltage spanned in the two cases. They display the same features than the gate-induced oscillations observed in BNGr74 devices. We notice that the average resistance is nearly constant over the whole range of plunger-gate voltage.

The Fourier transforms of theses resistance oscillations are displayed in Fig. 8.8.C and Fig. 8.8.D. They are really similar to the ones computed for the experiments performed in the multiple QH FP interferometer (chapter 5). We recover the decrease of the frequency of the oscillations with the lowering of the plunger-gate voltage starting from the voltage where the interfering edge channel is expelled away from the gated region.

The pyjamas maps corresponding to the two sets of experiments are shown on Fig. 8.9. In the two cases, the resistance oscillations form lines with negative slopes demonstrating that the device operates in the AB regime. The magnetic field periods extracted from these pyjama maps are respectively $\Delta B = 2.1$ mT for the experiment with the outer edge channel interfering and $\Delta B = 2.7$ mT for the experiment with the inner edge interfering. The corresponding AB areas are respectively of 2 μm^2 and 1.5 μm^2. This is consistent with the expected lithographic size of the device (2.25 ± 0.25 μm^2) thought somehow smaller.

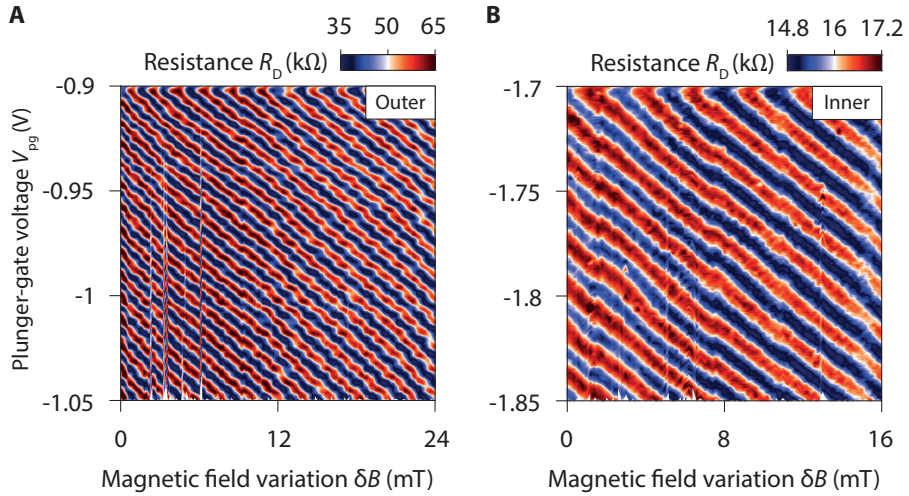

FIGURE 8.9: **Pyjama maps with integer edge channels interfering.** Evolution of the diagonal resistance R_D in BNGr76 device with the magnetic-field variation δB and the plunger-gate voltage V_{pg} in experiments with, **A**, the outer edge channel interfering and, **B**, inner edge channel interfering. The resistance oscillations form lines with a negative slope characteristic of AB regime.

8.3 Experiments with fractional edge channels at integer bulk filling factors

In this section, we present the results of experiments where we tried to make interference with fractional edge channels at integer bulk filling factors. This configuration is unusual because, as far as we know, the experiments in GaAs/AlGaAs heterostructures explored the fractional QH regime mostly at fractional bulk filling factors. In graphene devices, we can access this unusual regime easily thanks to the back gate which allows to tune precisely the electron density in the interferometer at any magnetic field. We investigated this regime at different back-gate voltages corresponding to integer bulk filling factors $\nu_b \simeq 1$ and 2, with the QPCs tuned in the fractional transmission plateaus $\frac{5}{3}$ and $\frac{2}{3}$.

We begin by discussing the results obtained at $\nu_b \simeq 1.9$ ($V_{bg} = 0.72$ V at 14 T) with the QPCs tuned to partially reflect the $\nu = \frac{5}{3}$ state (blue stars in Fig. 8.10). We demonstrate that AB oscillations appear in this regime and that they display unexpected phase jumps. We then show that similar phase jumps can also be observed at $\nu_b \simeq 1.0$ ($V_{bg} = 0.37$ V at 14 T) with the QPCs tuned to partially reflect the $\nu = \frac{2}{3}$ state (yellow stars in Fig. 8.10). We also demonstrate that this new

oscillation regime comes with other specific features and we finally discuss its possible origins as well as the implications of our experiments.

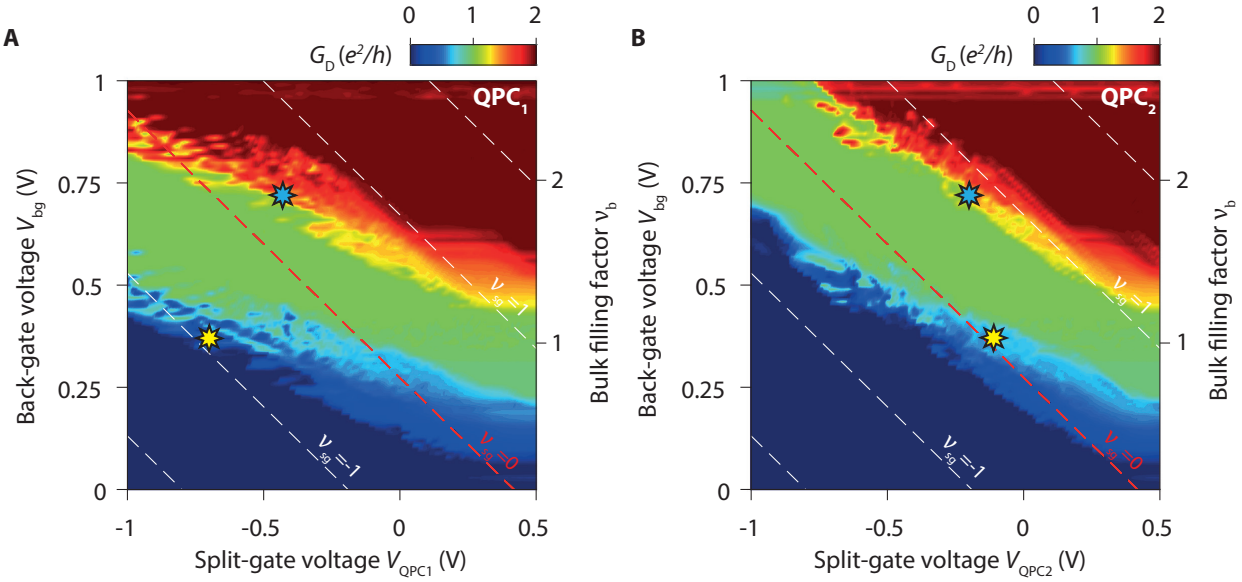

FIGURE 8.10: **QPC setting points for the experiments with fractional edge channels at integer bulk filling factors.** Zoom of Fig. 8.4 on limited voltage ranges. The yellow and blue stars mark the setting points for the pyjama maps presented Fig. 8.25 and Fig. 8.15.

8.3.1 Experiments at bulk filling factor $\nu_b \simeq 2$ with $\nu_{QPC} \simeq \frac{5}{3}$

Gate-induced oscillations at $\nu_b \simeq 2$

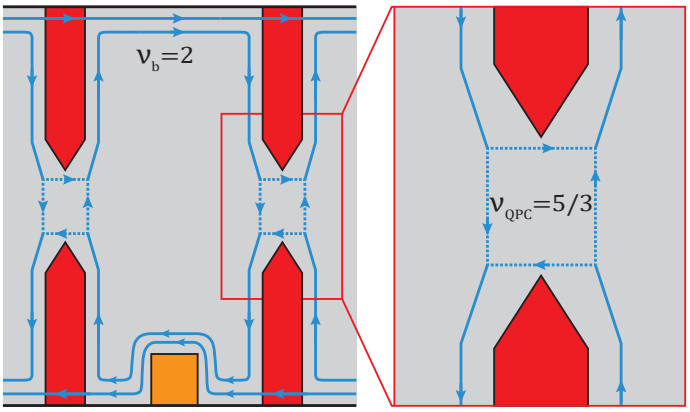

FIGURE 8.11: **Edge channel configuration for the experiments at $\nu_b \simeq 2$ and $\nu_{QPC} \simeq \frac{5}{3}$.** The QPCs are set in the voltage ranges where the transmission plots show sharp resonances that we attributed to the tunnelling of the reconstructed $\nu = \frac{5}{3}$ state. Considering the split-gate voltages used, we can assume that the $\nu = 1$ edge channel pass beneath the QPCs.

We first discuss a series of experiments performed at back-gate voltage $V_{bg} = 0.72$ V and at 14 T. This back-gate voltage corresponds to the central part of the $\frac{2e^2}{h}$ plateaus in Fig. 8.3.E and to a bulk filling factor $\nu_b \simeq 1.9$ such that the bulk of the FP is incompressible. For these experiments,

we also tuned the voltages applied on the split-gates around $V_{\mathrm{QPC1}} \simeq -0.43$ V and $V_{\mathrm{QPC2}} \simeq -0.11$ V such that they lie in the voltage ranges where the QPCs show resonances or kinks in the transmissions plots of Fig. 8.6 (black arrows). These resonances seem to arise from the pinching of the reconstructed $\nu = \frac{5}{3}$ state in the QPCs.

At these split-gate and back-gate voltages, the $\nu = 1$ integer edge channel circulates beneath the split-gate electrodes of QPC_2 and potentially also beneath those of QPC_1 as one can see in Fig. 8.10 (blue stars). Indeed, the filling factors beneath the split gates are respectively of $\nu_{\mathrm{sg1}} = 0.44$ and $\nu_{\mathrm{sg2}} = 0.94$ for QPC_1 and QPC_2. Therefore, we conjecture that the system is in the configuration depicted in Fig. 8.11.

Fig. 8.12 and Fig. 8.13 show resistance oscillations measured in such configuration. Like in the previous cases, the resistance oscillations are observed over the full range of plunger-gate voltage spanned. Likewise, their period increases when V_{pg} is decreased in agreement with all our previous measurements

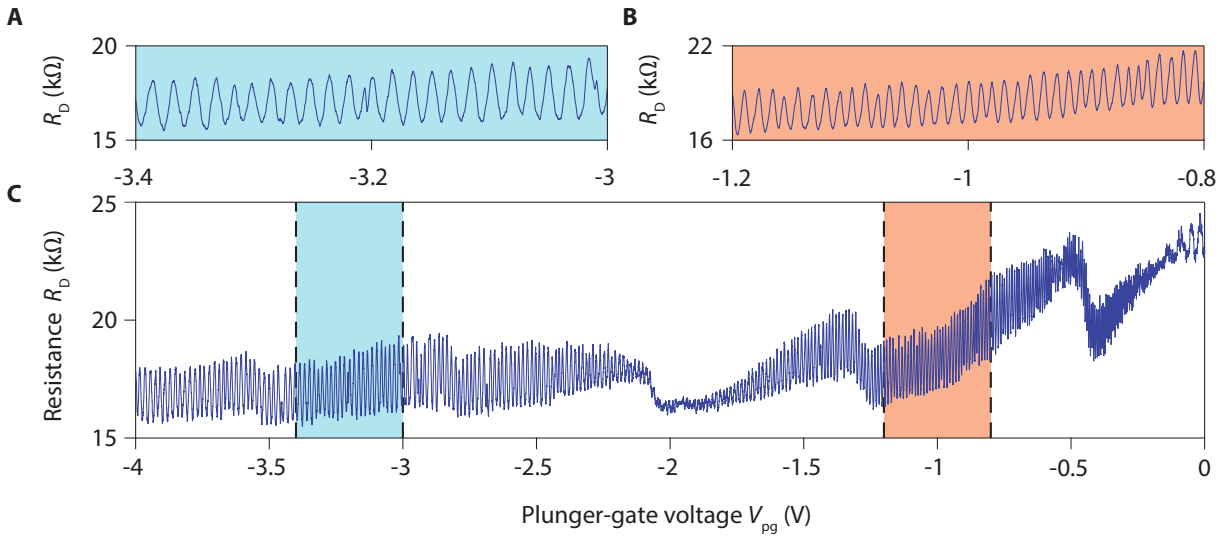

FIGURE 8.12: **Resistance oscillations measured at $\nu_b \simeq 1.9$ with $\nu_{\mathrm{QPC}} \simeq \frac{5}{3}$.** Evolution of the resistance with the plunger-gate voltage V_{pg}. **C**, Full voltage range spanned. Clear resistance oscillations appear on top of variations of the resistance background with the plunger-gate voltage. **A** and **B**, Zooms on limited voltage ranges. The back-gate voltage is set to $V_{\mathrm{bg}} = 0.72$ V such that the bulk is incompressible and the QPC voltages are set to $V_{\mathrm{QPC1}} = -0.43$ V and $V_{\mathrm{QPC2}} = -0.11$ V in the voltages ranges where the transmission plots show resonances attributed to the tunnelling of the $\nu = \frac{5}{3}$ state in the QPCs. Experiments performed at 14 T.

Yet, contrary to previous experiments, we note that the mean resistance value varies significantly when the plunger-gate voltage is changed. These variations of the resistance background are not reproducible as we can see by comparing measurements shown Fig. 8.12 and Fig. 8.13 that were performed exactly under the same conditions and in a few hours time lapse. This is somehow expected. We conjecture that a large variation of the plunger-gate voltage is likely to affect the electrostatic potential and the charge offset nearby the QPCs even with limited cross-talk between the gate. Such change then leads to large variations of the transmission because the QPCs are tuned in the voltage ranges where they display sharp resonances. These variations of the resistance are not reproducible as they depend on the past charging state of the gates and on charge relaxation.

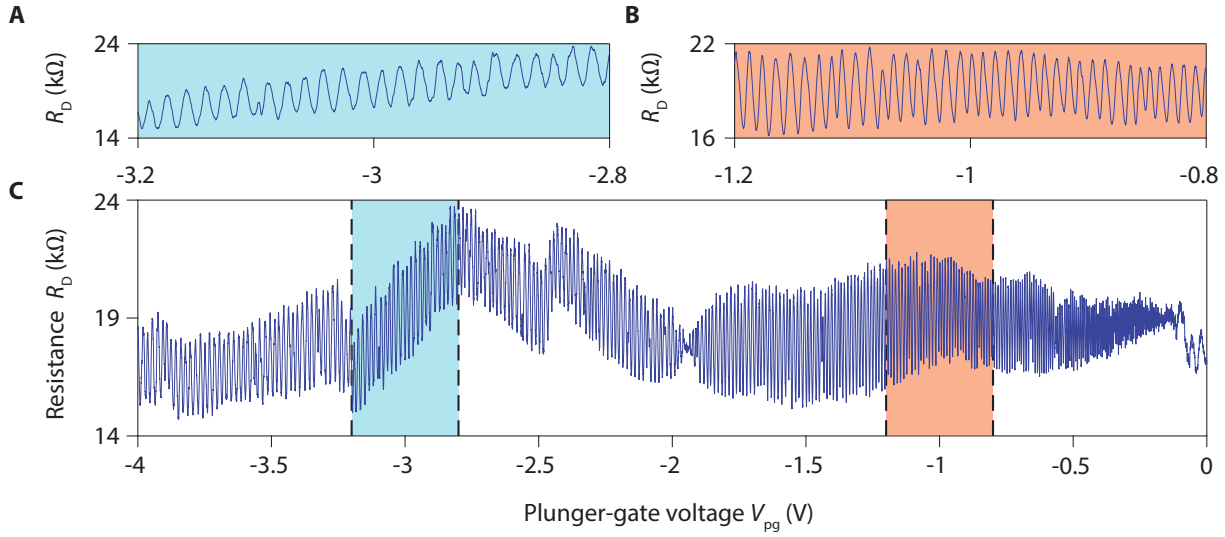

FIGURE 8.13: **Resistance oscillations measured at $\nu_b \simeq 1.9$ with $\nu_{QPC} \simeq \frac{5}{3}$ (second sweep).** Evolution of the resistance with the plunger-gate voltage V_{pg}. **C**, Full voltage ranged spanned. Clear resistance oscillations appear on top of variations of the resistance background with the plunger-gate voltage. **A** and **B**, Zooms on limited voltage ranges. The measurements are performed a few hours after the ones displayed in Fig. 8.12. We note that the resistance background is different from that of Fig. 8.12.C although the QPCs were not detuned.

The Fourier transforms of these two sets of resistance oscillations are shown in Fig. 8.14.A and Fig. 8.14.B. Both are very similar to that displayed in Fig. 8.8.C and Fig. 8.8.D for the integer case.

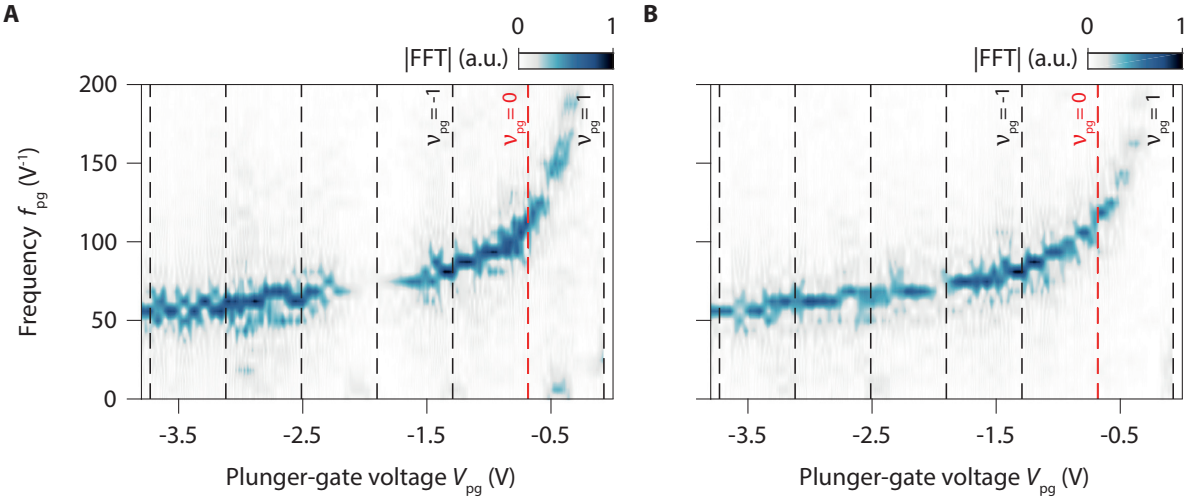

FIGURE 8.14: **Fourier amplitudes of resistance oscillations measured at $\nu_b \simeq 1.9$ with $\nu_{QPC} \simeq \frac{5}{3}$.** **A** and **B**, Evolution of Fourier amplitudes of resistance oscillations respectively displayed in Fig. 8.12.C and Fig. 8.13.C with plunger-gate voltage V_{pg} and frequency f_{pg}. The vertical dashed lines indicate constant integer filling factors below the plunger gate ν_{pg}.

We notice that the frequency of the oscillations increases fastly approaching the voltage where the filling factor below the plunger gate reaches $\nu_{pg} = 1$. This is consistent with either the $\nu = \frac{5}{3}$ or $\nu = 2$ edge channel interfering. Comparing carefully the Fourier transforms in Fig. 8.8.D and in Fig. 8.14, we note that the frequency of the oscillations is higher in the latter case. It can be seen, for example, by looking at the frequencies for plunger-gate voltages corresponding to $\nu_{pg} = -4$:

in Fig. 8.8.D, $f_{pg} \simeq 40\ V^{-1}$ when $\nu_{pg} = -4$ whereas $f_{pg} \simeq 60\ V^{-1}$ when $\nu_{pg} = -4$ in Fig. 8.14.A and Fig. 8.14.B.

Phase jumps in AB oscillations at $\nu_b \simeq 2$

We now present the corresponding pyjama map in Fig. 8.15. Fig. 8.15.B displays the raw data and shows that, during the measurements, there are large variations of the transmission of the FP interferometer with the magnetic field which are reminiscent of the variations of resistance background with the plunger-gate voltage observed in Fig. 8.12.C and Fig. 8.13.C.

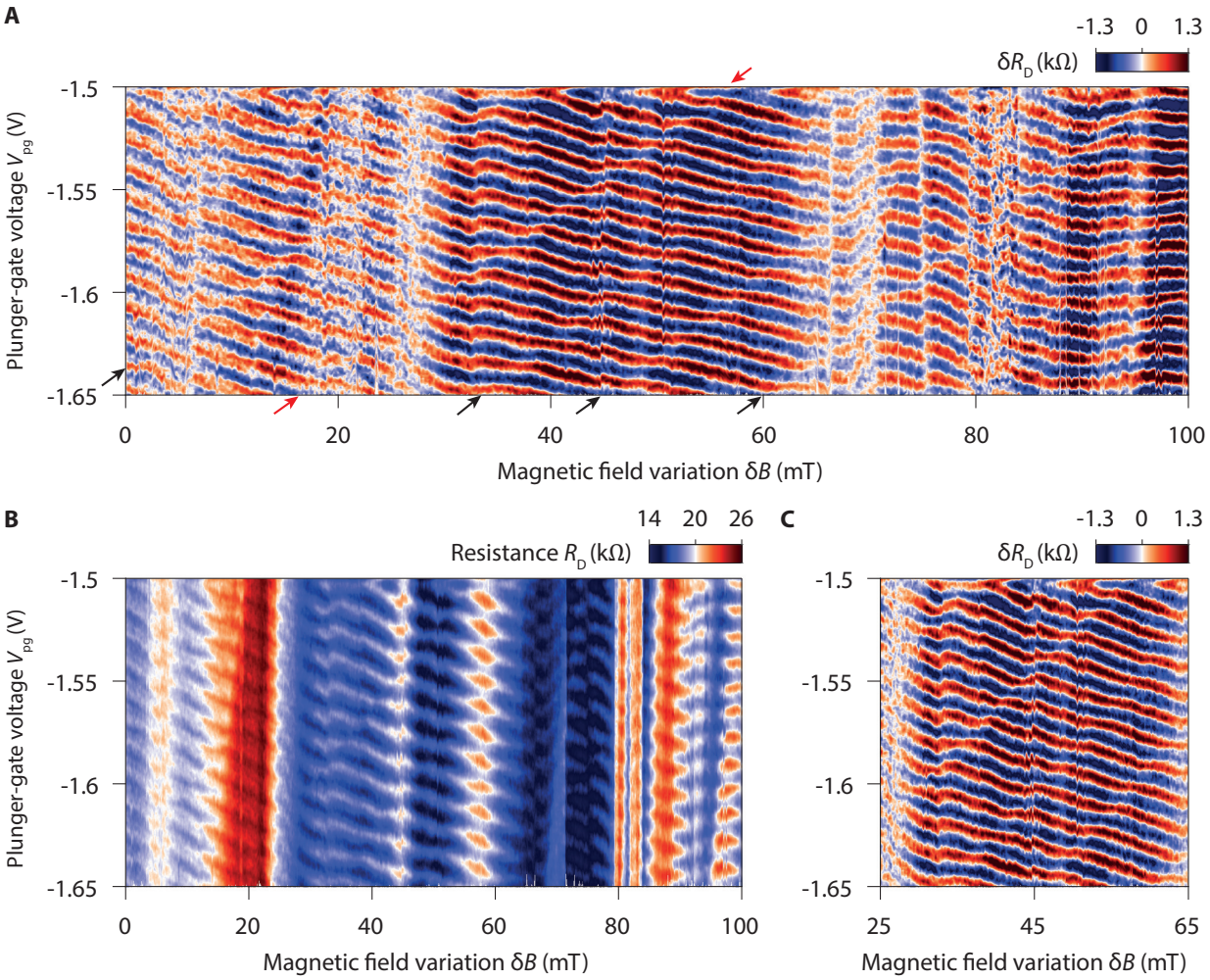

FIGURE 8.15: **Pyjama map measured at $\nu_b \simeq 1.9$ with $\nu_{QPC} \simeq \frac{5}{3}$ (n°1).** Evolution of the diagonal resistance with the magnetic field variation δB and the plunger-gate voltage V_{pg}. **A**, With and, **B**, without subtraction of a resistance background for each gate-voltage sweep. The AB oscillations present an anomalously large magnetic field period (≈ 14 mT). **C**, Zoom on limited field and gate-voltage ranges. In A, some lines with positive slopes (arrows) crossed the AB oscillations. Along these lines, the AB oscillations present some phase shifts. Measurement performed starting from $B = 13.95$ T and at $V_{bg} = 0.72$ V.

Fig. 8.15.A shows the same data after subtraction of a resistance background for each plunger-gate voltage sweep. It highlights the dispersion of the resistance oscillations with the magnetic field. Like in Fig. 8.9, the constant resistance lines have a negative slope characteristic of oscillations arising from AB effect.

Yet, we observe important differences compared to the previous measurements. First, the magnetic-field period of AB oscillations is anomalously large: it is approximately of 14 mT corresponding to an area of 0.3 μm^2 about one order of magnitude smaller than the real size of the device. For $\delta B \geq 70$ mT, the oscillations even have no dependence with the magnetic field.

Likewise, in the pyjama map, we also see that there are lines with positive slopes. They are marked by arrows in Fig. 8.15.A. Along these lines, we distinguish slight phase shifts in the AB oscillations leading to apparent drops of the oscillations amplitude. The existence of such phase shifts is not expected here and cannot be attributed to the localization of anyonic quasiparticles since we work at integer bulk filling and since the cyclotron gap at 14 T is about 135 meV$=$ 1565 K.

These phase shifts are not some measurement artefacts. First, we performed a few measurements without detuning the QPC. We observed that the most visible line (red arrow in Fig. 8.15.A) appears reproducibly at the same position in the different experiments, independently of range of magnetic field spanned and of the direction of the field variation (see Fig. 8.16).

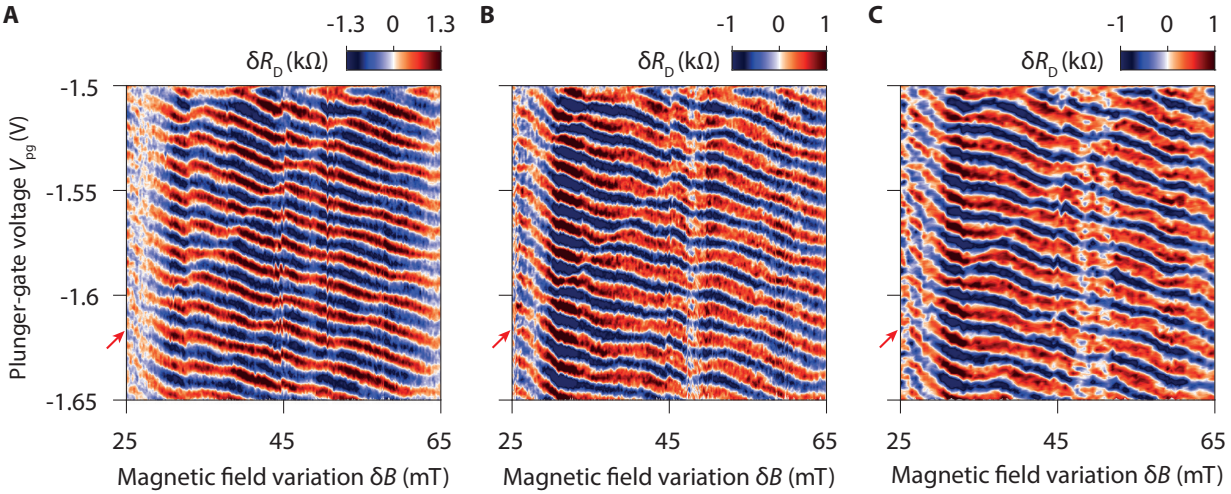

FIGURE 8.16: **Reproducibility of the line with phase shifts.** Pyjama maps measured repetitively for different ranges of field spanned. **A**, Data displayed in Fig. 8.15.A. B is varied from 13.95 T to 14.05 T. **B,** B is varied from 14.03 T to 13.97 T. **C**, B is varied from 14.15 T to 13.85 T. All axis are shifted such that $\delta B = 0$ mT corresponds to a field of 13.95 T. The line along which the phase shifts occur can be distinguished in each case. It appears virtually at the same position in the three color-coded maps.

On the other hand, these phase shifts also appear in other experiments. We performed additional measurements with similar QPCs settings and at the same back-gate voltage after detuning of the gate voltages. The results of these measurements are presented in Fig. 8.17 and Fig. 8.18. They display the same features than Fig. 8.15. Indeed, the pyjama maps show resistance oscillations that seem to form lines with slightly negative slopes and thus to originate from Aharonov-Bohm effect. However, their magnetic field period is very large and can hardly be determined.

Furthermore, in these color-coded maps, we readily notice the presence of lines with positive slopes along which the oscillations display phase jumps like in previous measurements. In Fig. 8.17 and Fig. 8.18, these phase jumps are much more pronounced than in Fig. 8.15. The lines along which the phase jumps occur are irregular: they do not appear periodically, they have different slopes and their slopes can even vary depending on the plunger-gate voltage and the magnetic field.

Moreover, we observe that during these measurements there were also large changes of resistance background as the magnetic field was varied. It appears that the position of the lines with phase jumps are not correlated with the values of the average resistance (see for instance in Fig. 8.17).

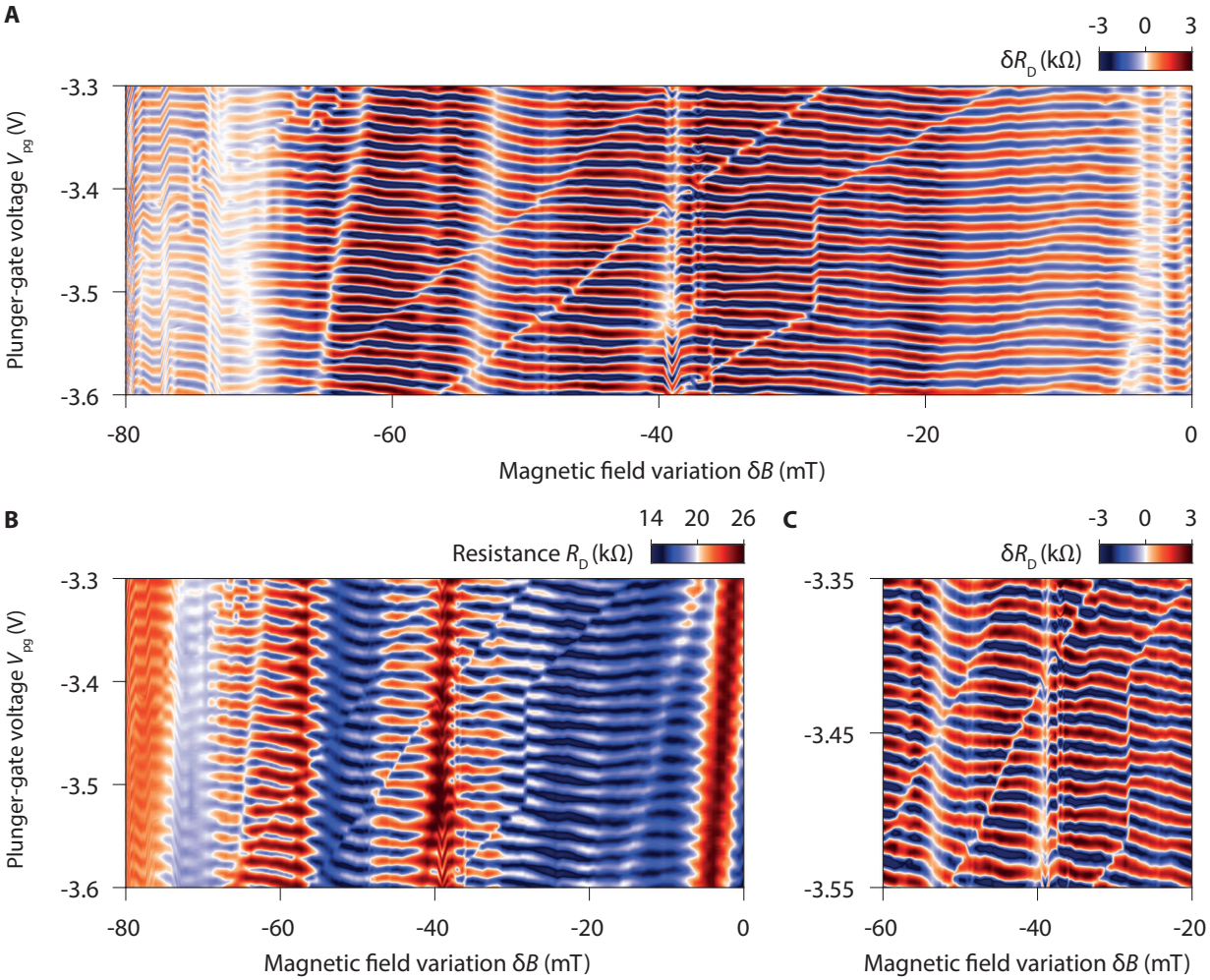

FIGURE 8.17: **Pyjama map measured at $\nu_b \simeq 1.9$ with $\nu_{QPC} \simeq \frac{5}{3}$ (n°2).** Evolution of the diagonal resistance with the magnetic field variation δB and the plunger-gate voltage V_{pg}. **A**, With and, **B**, without subtraction of a resistance background for each gate-voltage sweep. The oscillations have nearly no magnetic field dependence. **C**, Zoom on limited field and gate-voltage ranges. Some lines crossing the AB oscillations can be distinguished. Along these lines, the AB oscillations present clear phase shifts. Measurements performed starting from $B = 14.03$ T and at $V_{bg} = 0.72$ V.

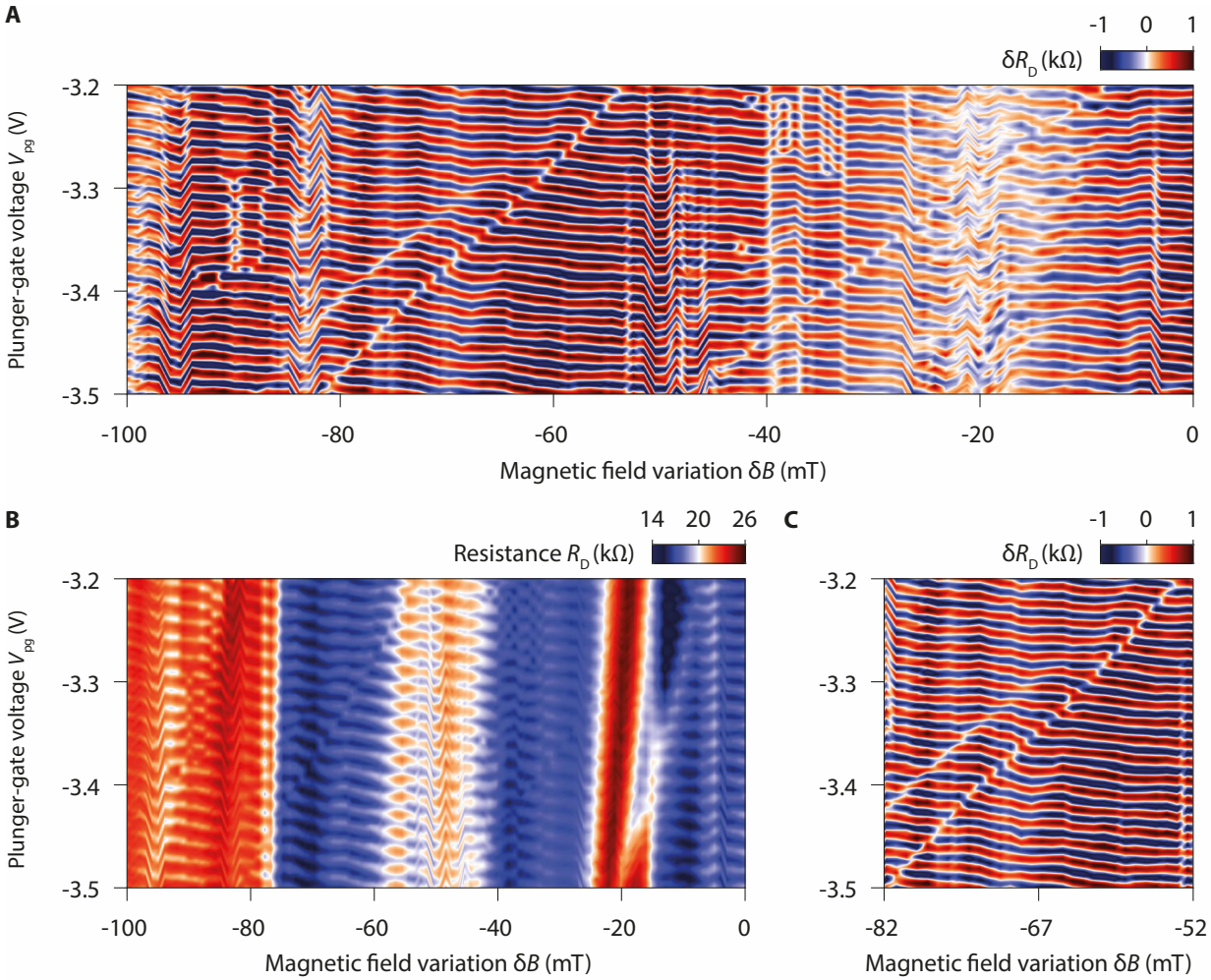

FIGURE 8.18: **Pyjama map measured at $\nu_b \simeq 1.9$ with $\nu_{QPC} \simeq \frac{5}{3}$ (n°3).** Evolution of the diagonal resistance with the magnetic field variation δB and the plunger-gate voltage V_{pg}. **A**, With and, **B**, without subtraction of a resistance background for each gate-voltage sweep. The AB oscillations have an anomalously large magnetic field period ($\approx$ 20 mT). **C**, Zoom on limited field and gate-voltage ranges. Some lines crossing the AB oscillations can be distinguished in three color-coded maps. Along these lines, the AB oscillations present clear phase shifts. Measurements performed starting from $B = 14.05$ T and at $V_{bg} = 0.72$ V.

We also performed similar experiments at back-gate voltage of 0.74 V, corresponding to a bulk filling factor of $\nu \simeq 2$ at 14 T, slightly above that of previous measurements and with the QPCs tuned in the voltage ranges where the transmission plots display resonances (see Fig. 8.19). The pyjama map measured in this case is shown in Fig. 8.20. It displays clear AB oscillations having a period of 5.6 mT, which is more than twice larger than the periods measured with integer edge channel interfering (the corresponding AB area is about 0.74 μm^2). This pyjama map also exhibits a line where the AB oscillations display clear phase jumps.

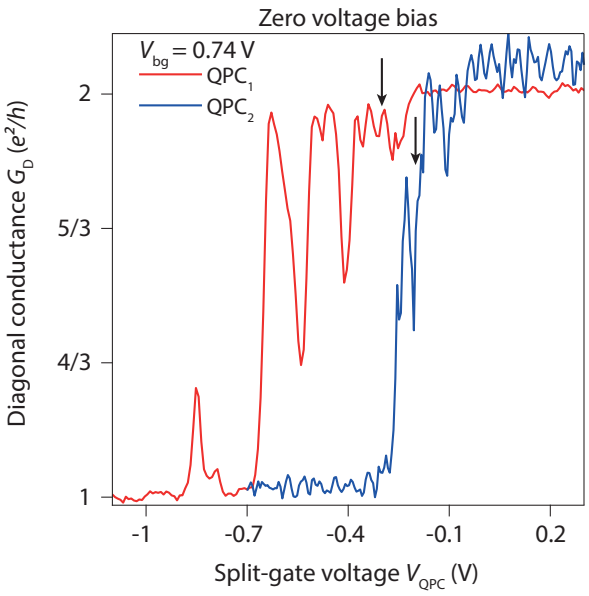

FIGURE 8.19: **QPC transmissions at $V_{bg} = 0.74$ V.** Evolution of the diagonal conductance G_D with the voltage applied on the split-gate electrodes V_{QPC}. Although the quantization is imperfect, the integer plateaus can clearly be distinguished. Several resonances can be observed in QPC$_1$ after the flat $\frac{2e^2}{h}$ plateau. Likewise a resonance around $G_D = \frac{5}{3}\frac{e^2}{h}$ in QPC$_2$ is observed. The black arrows mark the voltages applied on the QPCs for the experiment displayed in Fig. 8.20. Measurements performed at 14.1 T.

Therefore, these peculiar AB oscillations with large magnetic field periods and phase jumps are a robust feature of experiments performed at $\nu_b \approx 2$ with the QPCs set in the resonances corresponding to the tunnelling of $\nu = \frac{5}{3}$ state.

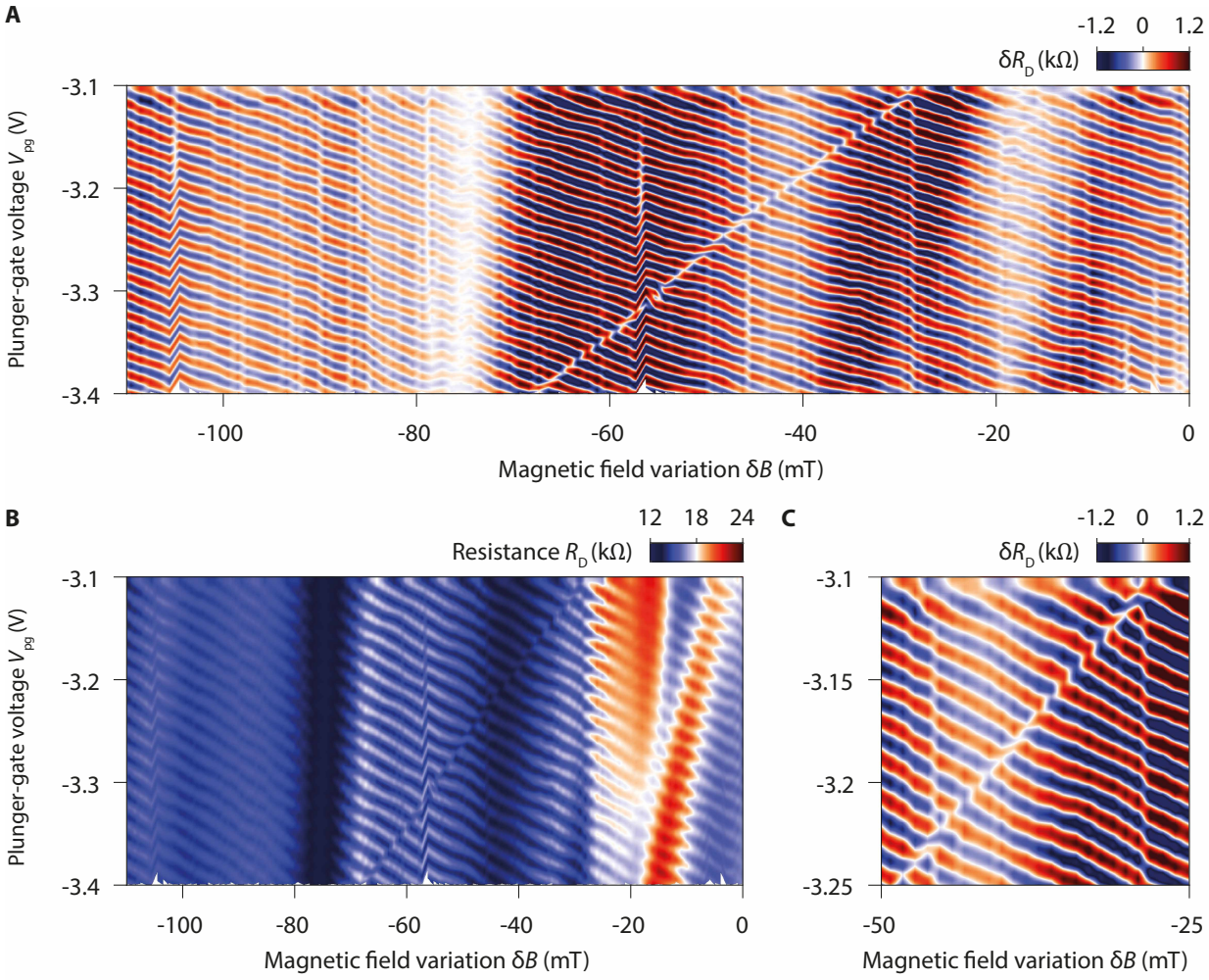

FIGURE 8.20: **Pyjama map with measured at $\nu_b \simeq 2.0$ with $\nu_{QPC} \simeq \frac{5}{3}$ (n°3).** Evolution of the diagonal resistance with the magnetic field variation δB and the plunger-gate voltage V_{pg}. **A**, With and, **B**, without subtraction of a resistance background for each gate-voltage sweep. The AB oscillations have an anomalously large magnetic field period (5.6 mT). **C**, Zoom on limited field and gate-voltage ranges. In the color-coded map, we observe a line with a positive slope that crosses the AB oscillations. Along this line, the AB oscillations present clear phase shifts. Measurements performed starting from $B = 14.1$ T and at $V_{bg} = 0.74$ V.

8.3.2 Experiments at bulk filling factor $\nu_b \simeq 1$ with $\nu_{QPC} \simeq \frac{2}{3}$

Gate-induced oscillations at $\nu_b \simeq 1$

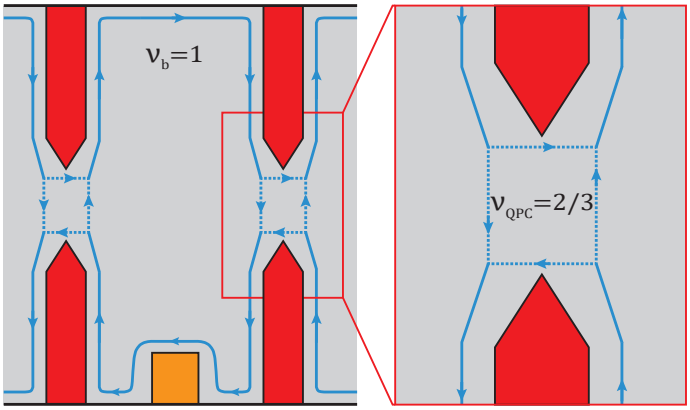

FIGURE 8.21: **Edge channel configuration for the experiments at $\nu_b \simeq 1$ and $\nu_{QPC} \simeq \frac{2}{3}$.** The QPCs are set in the voltage ranges where the transmission plots show sharp resonances that we attributed to the tunnelling of the $\nu = \frac{2}{3}$ state.

We performed similar experiments at back-gate voltage of $V_{bg} = 0.37$ V corresponding to a bulk filling factor of $\nu_b \simeq 1$ at 14 T. Fig. 8.22.A and Fig. 8.22.B display the evolution of the transmission of the QPCs with the split-gate voltages respectively at zero and high dc-voltage bias.

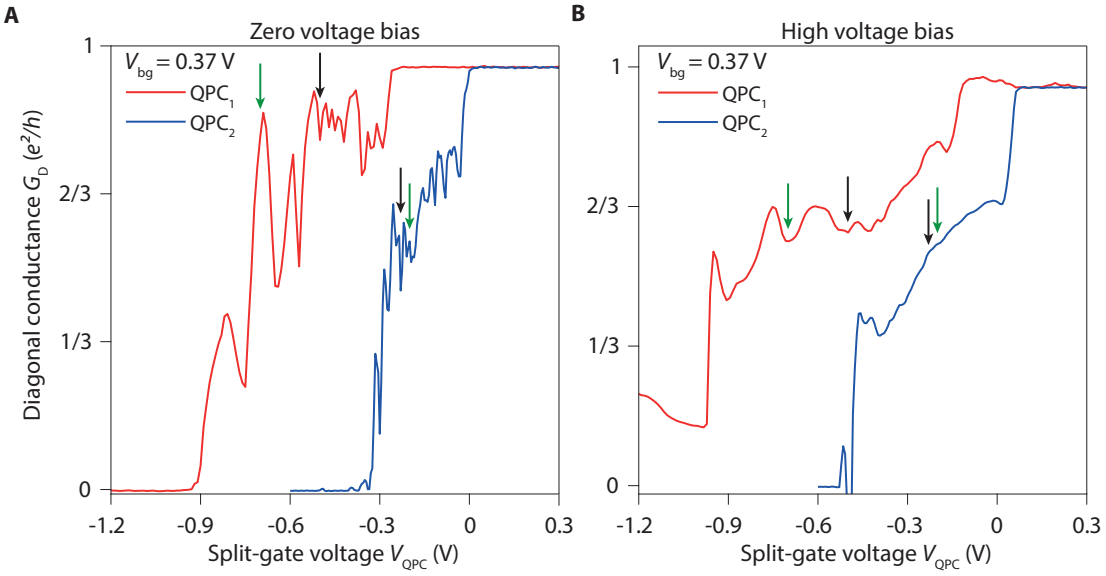

FIGURE 8.22: **QPC transmissions at $V_{bg} = 0.37$ V.** Evolution of the diagonal conductance G_D with the voltage applied on the split-gate electrodes of one QPC V_{QPC}. Measurements performed, **A**, without a dc-voltage bias and, **B**, with a 800 μV voltage bias. The resonances associated with the tunnelling of fractional QH edge channel disappear at high voltage bias and $\frac{2}{3}\frac{e^2}{h}$ and $\frac{1}{3}\frac{e^2}{h}$ conductance plateaus appear. The green and black arrows mark the voltages applied on the QPCs for the experiments displayed respectively in Fig. 8.25 and Fig. 8.26. Experiments performed at 14 T.

Again, at zero bias, we observe that the transmission plots display several resonances after the $\frac{e^2}{h}$ plateaus. These resonances most probably arise from the tunnelling of the $\nu = \frac{2}{3}$ state as

suggested by the corresponding transmission plateaus at high voltage bias. We performed two series of experiments at this back voltage and with the QPCs tuned in the voltage ranges where we observe resonances. The setting points for the QPCs in each case are indicated in Fig 8.22.A by the black and green arrows. With this setting, we can assume that the $\nu = \frac{2}{3}$ edge channel is interfering and that the edge channel configuration in the interferometer corresponds to the one depicted in Fig. 8.21.

In Fig. 8.23, we display the gate-induced oscillations measured in the configuration corresponding to the green arrows and we show their Fourier transform in Fig. 8.24.

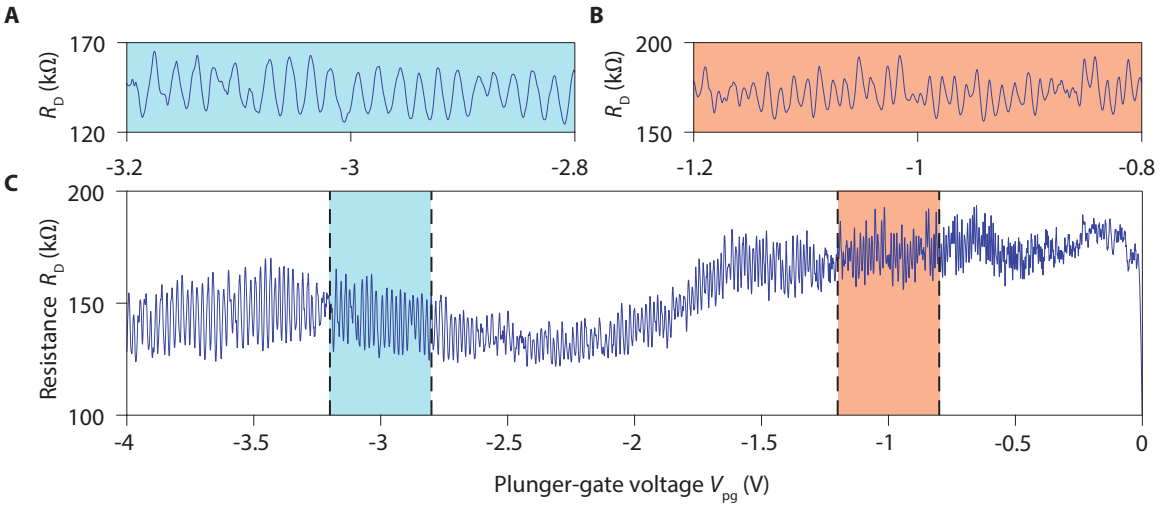

FIGURE 8.23: **Resistance oscillations measured at $\nu_b \simeq 1.0$ with $\nu_{QPC} \simeq \frac{2}{3}$.** Evolution of the resistance with the plunger-gate voltage V_{pg}. **C**, Full voltage range spanned. Clear resistances oscillations appear on top of variations of the resistance background with the plunger-gate voltage. **A** and **B**, Zooms on limited voltage ranges. The back-gate voltage is set to $V_{bg} = 0.37$ V such that the bulk is incompressible. The split-gate voltages are set to $V_{QPC1} = -0.7$ V and $V_{QPC2} = -0.2$ V in the voltage ranges where resonances associated with tunnelling of $\nu = \frac{2}{3}$ state appear in the transmission plots. Experiments performed at 14 T.

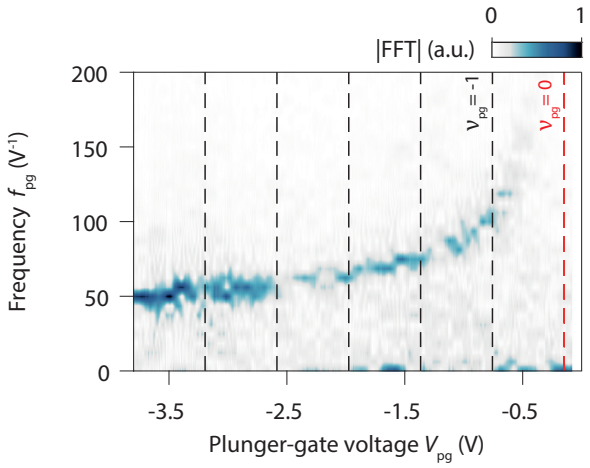

FIGURE 8.24: **Fourier amplitude of resistance oscillations measured at $\nu_b \simeq 1.0$ with $\nu_{QPC} \simeq \frac{2}{3}$.** **A** and **B**, Evolution of Fourier amplitude of resistance oscillations displayed in Fig. 8.23.C with plunger-gate voltage V_{pg} and frequency f_{pg}. Vertical dashed lines indicate constant integer filling factors below the plunger gate ν_{pg}.

The resistance oscillations are also observed over the full range of voltage spanned and the evolution of the frequency with the plunger-gate voltage is similar to that of other experiments.

The oscillations frequency drops rapidly nearby the voltage corresponding $\nu_{\mathrm{pg}} = 0$ as we would expect for either $\nu = 1$ or $\nu = \frac{2}{3}$ edge channel interfering. We also note that the frequency of the oscillations is similar to what we measured in Fig. 8.14.

Phase jumps in AB oscillations at $\nu_{\mathrm{b}} \simeq 1$

The corresponding pyjama map is displayed in Fig. 8.25. It shows AB oscillations crossed by two lines along which phase jumps occur. Contrary to the previous experiments, in Fig. 8.25 the magnetic field period of AB oscillation is 2.6 mT similar to that measured in Fig. 8.9.B with integer edge channels. During these experiments, there were also large variations of the transmission of the device as we can see in Fig. 8.25.B. Yet, these variations do not seem to affect the lines along which the phase jumps occur.

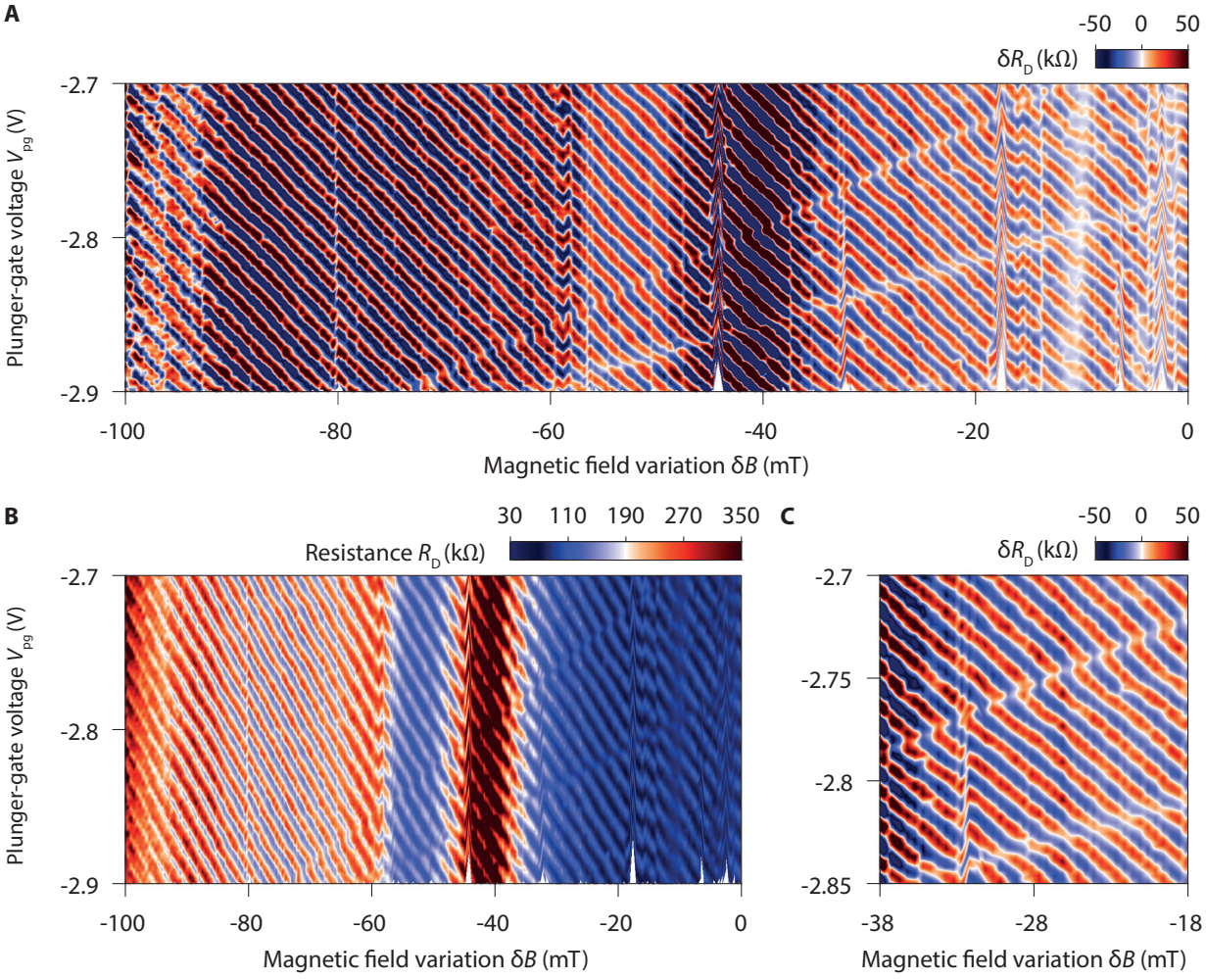

FIGURE 8.25: **Pyjama map measured at $\nu_{\mathrm{b}} \simeq 1.0$ with $\nu_{\mathrm{QPC}} \simeq \frac{2}{3}$.** Evolution of the diagonal resistance with the magnetic field variation δB and the plunger-gate voltage V_{pg}. **A,** With and, **B,** without subtraction of a resistance background for each gate-voltage sweep. The AB oscillations have the same magnetic field period than in the integer regime (2.6 mT). **C**, Zoom on limited field and gate-voltage ranges. In the color-coded map, we observe lines with positive slopes that cross the AB oscillations. Along these lines, the AB oscillations present clear phase shifts. Measurements performed starting from $B = 14.05$ T and at $V_{\mathrm{bg}} = 0.37$ V.

Likewise, in the configuration corresponding to the black arrows in Fig. 8.22, we also observe AB oscillations with a 2.6 mT period as shown in the pyjama map in Fig. 8.26. These oscillations are also crossed by two lines with positive slope marked by a decrease of the amplitude of the oscillations. It also seems that some phase jumps occur along these lines although we can not assess it firmly because of the lack of resolution of these measurements.

Therefore, the observation of phase jumps in the AB oscillations, in configurations where the bulk is at integer filling factors and where the QPCs are tuned in the resonances of the fractional QH states, is robust.

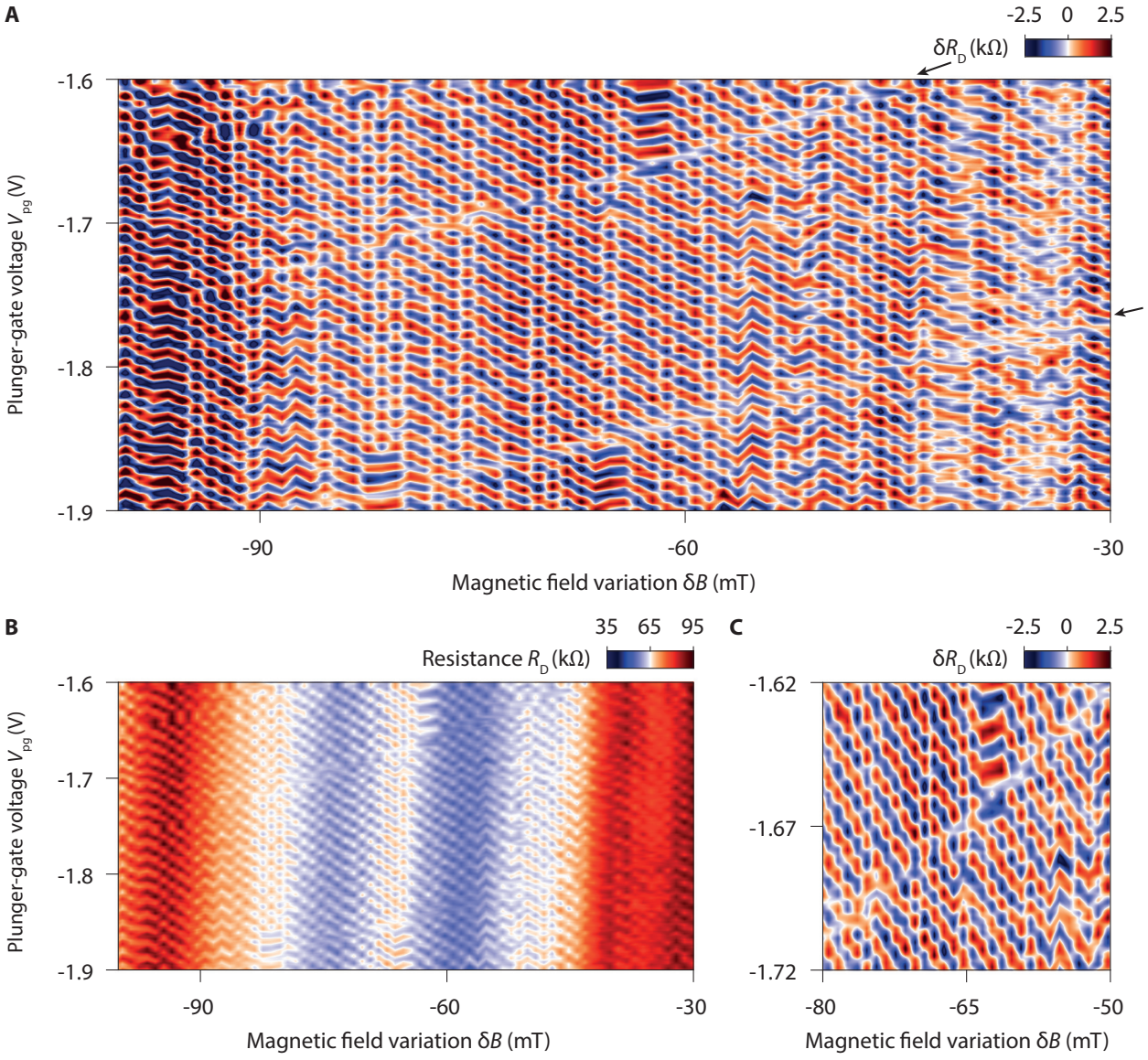

FIGURE 8.26: **Pyjama map measured at $\nu_b \simeq 1.0$ with $\nu_{QPC} \simeq \frac{2}{3}$ (n°2).** Evolution of the diagonal resistance with the magnetic field variation δB and the plunger-gate voltage V_{pg}. **A,** With and, **B,** without subtraction of a resistance background for each gate-voltage sweep. The AB oscillations have the same magnetic field period than in the integer regime (2.6 mT). **C,** Zoom on limited field and gate-voltage ranges. In the color-coded map, we observe two lines with positive slopes that cross the AB oscillations and along which the amplitude of the oscillations decreases. Measurements performed starting from $B = 14.1$ T and at $V_{bg} = 0.37$ V.

8.3.3 Comparison with experiments with integer edge channels

To get further information about this regime with phase jumps, we performed additional experiments and compared the results obtained for integer edge channel interfering at non-integer filling factors with the results obtained at integer filling factors and with the QPCs tuned at fractional transmissions.

Comparison of the frequencies of gate-induced oscillations

First, we compared more systematically the frequency of gate-induced oscillations in the two regimes to confirm our observations. In this purpose, we performed the same analysis than in section 5.1.1 and compared the evolution of the rescaled frequency with the plunger-gate voltage after suitable voltage shifts depending on the interfering edge channel. The result of this analysis is displayed in Fig. 8.27. For the experiments with the QPCs are tuned such that $\nu_{\mathrm{QPC}} = \frac{5}{3}$ and $\nu_{\mathrm{QPC}} = \frac{2}{3}$, we assume that the interfering edge channel is expelled outside from the gated-region when the filling factor below the plunger gate reaches respectively $\nu_{\mathrm{pg}} = 1$ and $\nu_{\mathrm{pg}} = 0$.

Fig. 8.27 shows that the rescaled frequencies collapse into two distinct curves depending on the type of experiment. The data points corresponding to the experiments performed with integer edge channel interfering form a single plot, as expected according to section 5.1.1, whereas the data points corresponding to the experiments performed at fractional QPCs fillings formed virtually the same curve shifted towards higher frequencies. It confirms our previous observations.

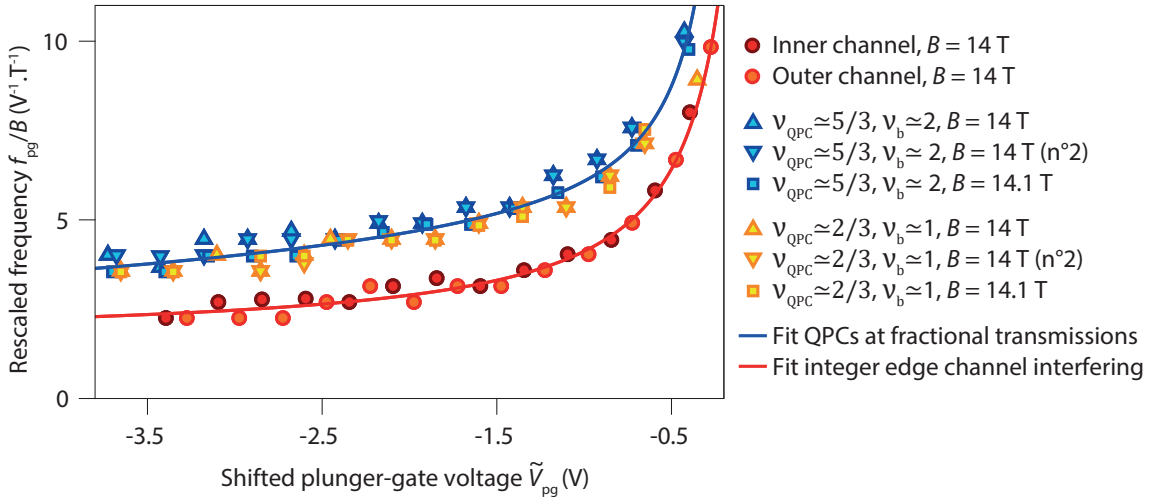

FIGURE 8.27: **Comparison of oscillations frequency.** Evolution of the rescaled oscillation frequencies f_{pg}/B with the shifted plunger-gate voltages $\tilde{V}_{\mathrm{pg}}$ for the two types of interferometry experiments. The data for the two types of measurements collapse on two very similar curves. The curves draw by each set of data points are fitted with rational fractions to extract the average frequencies at fixed plunger-gate voltage.

We emphasize that the different sets of points reported for the experiments at integer bulk filling factors and fractional QPCs fillings were obtained for different QPCs tunings or magnetic fields. It shows that the frequencies measured in the two cases are robust and we actually see that these frequencies all rescale on the same plot. It suggests a common origin of the peculiar features observed in both the experiments with $\nu_{\mathrm{QPC}} \simeq \frac{5}{3}$ and with $\nu_{\mathrm{QPC}} \simeq \frac{2}{3}$.

To evaluate the ratio of the average frequencies, we fitted the experimental points with two rational fractions of the form $\frac{p_1 V_{\mathrm{pg}} + p_2}{V_{\mathrm{pg}}^2 + q_1 V_{\mathrm{pg}} + q_2}$. It allows to get rid of the individual variations in each measurement. Fig. 8.28 displays the evolution of the frequency ratio η with the plunger-gate voltage calculated using the two fits in Fig. 8.27. η increases when V_{pg} is lowered and it saturates to

1.6 at large negative voltages. Yet, we note that the variations of the frequency ratio at $V_{pg} \geqslant -2$ V may be artefacts resulting from the fluctuations between different experiments together with the fast variation of the oscillations frequency at low plunger-gate voltages.

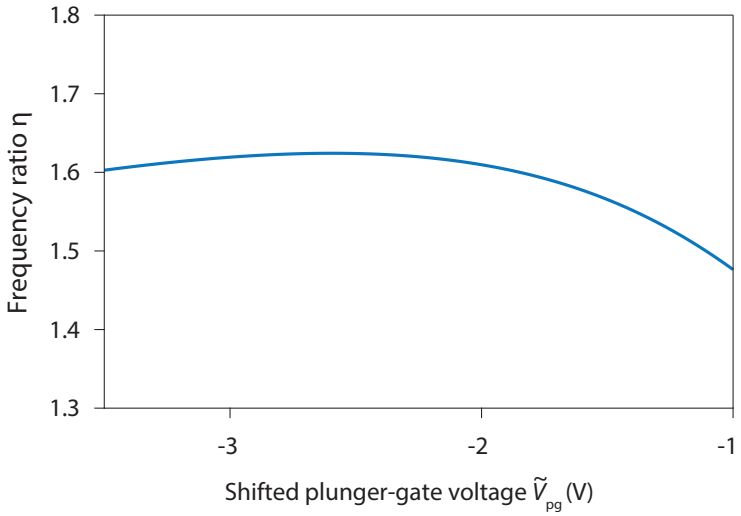

FIGURE 8.28: **Ratio of the frequencies.** Evolution of the ratio η of the frequencies measured in the two types of experiments with plunger-gate voltage V_{pg}. η is calculated from the fits in Fig. 8.27 (blue and red lines). At large negative plunger-gate voltages, η saturates to 1.6.

In the pure AB regime, the frequency of the oscillations f_{pg} is given by:

$$\frac{f_{pg}}{B} = \frac{\alpha}{\Phi_0^*} = \frac{e^*}{e}\frac{\alpha}{\Phi_0}, \tag{8.1}$$

where α is the plunger-gate lever arm (see section 5.1.1 for the integer case and ref. [99, 167] for the fractional case). Thus, the variation of the frequencies between the two types of experiments can have different origins : it can either reflect a change of gate-lever arm or a change in the effective charge of the interfering quasiparticles.

If we assume that the gate-lever arm α is constant then the increase of frequency would reflect a change in the effective charge of the interfering quasiparticles which would be $-e^* \simeq -1.6\,e$. It would imply that interference would not arise from simple electrons but either from fractionally charged quasiparticles or complex edge excitations although no theory predicts such an effective charge to our knowledge. We remark that this $-e^* \simeq -1.6\,e$ effective charge somehow coincides with the QPCs filling factors in the experiments where $\nu_{QPC} \simeq \frac{5}{3}$.

Alternatively, if the interfering quasiparticles are electrons then the increase of the frequency implies that α would be increased by a factor 1.6. It would mean that the electrostatics associated with the displacement of the pn junction nearby the plunger gate would be somehow modified when the bulk is incompressible. This seems unlikely.

Comparison between out-of-equilibrium transport measurements

We also performed out-of-equilibrium transport measurements in both regimes. Fig. 8.29.A-C show the results of these experiments with either the outer or inner integer edge channel interfering and a compressible bulk or at bulk filling factor $\nu_b \simeq 1.9$ and with $\nu_{QPC} \simeq \frac{5}{3}$.

We first note that the checkerboard patterns of Fig. 8.29.B and Fig. 8.29.C are very similar to that described in section 5.3.1. They present a tilt that is due to the limited syummetrization of the

potential drop in the small graphene FP interferometer. Yet, we notice that the secondary lobes in Fig. 8.29.B are weakly defined and can hardly be distinguished especially on the negative bias side. On the other hand, the checkerboard pattern of Fig. 8.29.A measured with the inner edge interfering at $\nu_b \simeq 1.7$ is distorted and its shape cannot be described by the non-interacting theory (eq. (5.8)) even taking into account the effect of an asymmetric potential drop.

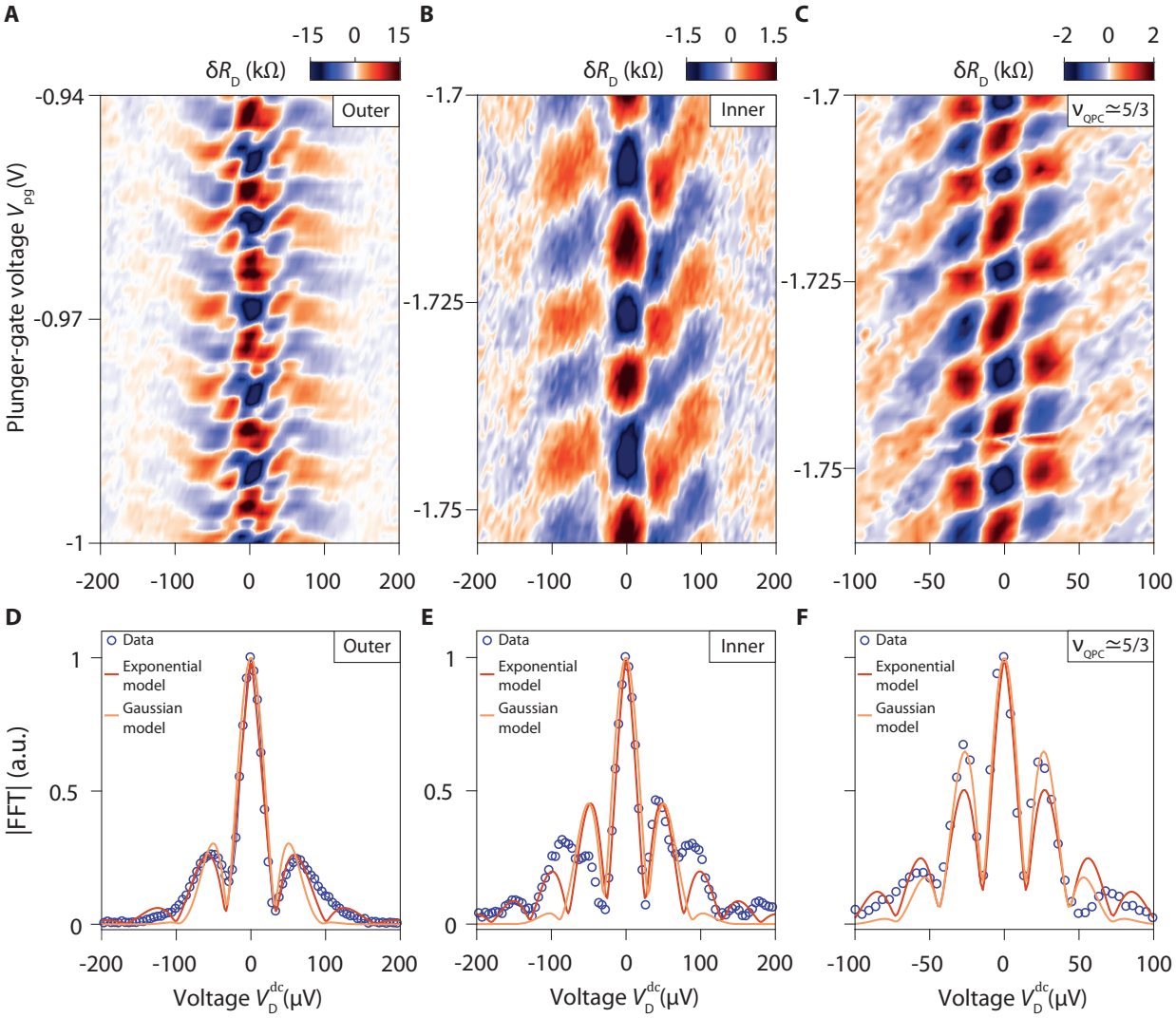

FIGURE 8.29: **Out-of-equilibrium transport measurements for the two types of interferometry experiments.** Differential diagonal resistance variations δR_D, after background subtraction, versus plunger-gate voltage V_{pg} and measured dc diagonal voltage V_D^{dc}. Experiments with **A**, the outer edge channel interfering at $\nu_b \simeq 1.7$, **B**, the inner edge channel interfering at $\nu_b \simeq 2.5$, and **C**, $\nu_{QPC} \simeq \frac{5}{3}$ and $\nu_b \simeq 1.9$. **D**, **E**, **F**, Evolution of the Fourier amplitudes of AB oscillations with the dc diagonal voltage V_D^{dc}. The fits of the data with eq. (5.8) with exponential and Gaussian envelopes are respectively displayed in red and orange.

Fig. 8.29.A	Fig. 8.29.B	Fig. 8.29.C
$\Delta V_{dc} \simeq 130\ \mu V$	$\Delta V_{dc} \simeq 100\ \mu V$	$\Delta V_{dc} = 58\ \mu V$

TABLE 8.3: **Voltage periods of bias-induced oscillations for the experiments displayed in Fig. 8.29.**

Fig. 8.29.D-F displays the evolution of the Fourier amplitudes of AB oscillations with the dc-voltage bias for the three measurements. We notice that the lobe structure in Fig. 8.29.F is close to that discussed in chapter 5. It allows us to extract the corresponding voltage period by fitting the data with the non-interacting theoretical model. The results of the fits with both a Gaussian and an exponential envelopes and an asymmetry factor $x = 0.09$ are shown respectively in orange and red. They both give a period $\Delta V_{\mathrm{dc}} = 58\ \mu$V.

In Fig. 8.29.E, the minima between the second and the third lobes are not pronounced and thus the evolution of the Fourier transform amplitude cannot be well fitted. Yet, the period of bias-induced oscillations can still be estimated from the positions of the lobes/nodes and we find $\Delta V_{\mathrm{dc}} \simeq 100\ \mu$V. Similarly, we can extract a voltage period $\Delta V_{\mathrm{dc}} \simeq 130\ \mu$V from Fig. 8.29.D. In this case, the fits of lobe structure are better although the checkerboard pattern observed cannot be described by the non-interacting theory.

Thus, we note that the period of bias-induced oscillations measured for the experiment where $\nu_{\mathrm{QPC}} \simeq \frac{5}{3}$ is reduced compared to the ones measured with integer edge channels and a compressible bulk: it is divided by a factor 1.7 compared to the experiment with the inner edge interfering and by a factor 2.2 compared to the experiment with the outer edge interfering. In the AB regime, this reduction translates either a change of the edge-excitation velocity, a change of interfering path length (or combination of both effects) or a change of the effective charge of interfering quasiparticles.

In the first case, the edge channel velocity would vary from $v = 1.1 \times 10^5$ m.s^{-1} and $v = 8.4 \times 10^4$ m.s^{-1} for experiments shown in Fig. 8.29.A-B to $v = 4.9 \times 10^4$ m.s^{-1} for the experiment shown in Fig. 8.29.C (taking $L = 3.5\ \mu$m). Such large variations of the edge-excitation velocity may arise from the change of filling factor. Indeed, in ref. [167], Nakamura and coworkers performed similar out-of-equilibrium transport measurements with the edge channels of $N = 0$ LL. They observed large and non-monotonic variations of the velocity with the bulk filling factor. Similar variations were also reported in GaAs Mach-Zehnder interferometers in ref. [239]. Yet, we stress that in these experiments the filling factor is varied through changes of magnetic field contrary to our experiments: it can also influence the strength of electron-electron interactions modifying the edge velocity.

Besides, a reduction of the interfering path length by a factor 2 seems unlikely: it would likely result in a distancing of the interfering edge channel with the plunger gate inconsistent with the increase of oscillations frequency observed. Thus, if it exists, the reduction of the path is most probably accompanied by a reduction of the velocity. A reduction of the path length would also be consistent with the anomalously large AB periods measured.

8.3.4 Discussion

To summarize, when we operate the FP interferometer at integer filling factors (incompressible bulk) and with the QPCs tuned at fractional transmissions, we observe several unexpected features in the AB oscillations. First, the pyjama maps display clear phase jumps and they have an anomalously large magnetic field period at filling factor 2. Second, the frequency of gate-induced oscillations is significantly increased compared to that measured in experiments at non-integer filling factor with integer edge channel. Finally, the period of bias-induced oscillations is reduced by a similar factor.

Origin of the oscillations

The exact origin of such unexpected features remains unclear. Different scenarios might be at the origin of the features observed.

We remark that there are two major differences between the experiments of section 8.2 and the experiments section 8.3. In the first case, we work with integer edge channel and the bulk

is compressible i.e ν_b is close to half integer values. In the second case, we presumably make interference with fractional edge channels although the bulk is incompressible and an integer filling factor. Therefore, the differences observed between the two types of experiments can either reflect a change in the nature of the quasiparticles interfering or they can reflect the existence of unexpected effects appearing when the bulk is incompressible.

To disentangle both effects, it would be necessary to make further studies over large ranges of bulk filling factor and for different edge channel configurations. Alternatively, it would be particularly relevant to perform shot noise experiments in both configurations. It would allow to unveil whether interference arise from quasiparticles with an anomalous charge($-1.6e$) or from electrons or even from complex edge channel excitations (as suggested for example to explain the halving of AB oscillations [166, 244]).

If the oscillations indeed originate from interference of fractional quasiparticles, our experiments raise fundamental questions. One may indeed wonder how such interference can appear when the fractional edge channel only reconstruct in the QPCs and not in the bulk of the interferometer. One may also wonder what are the edge structures of $\nu = \frac{5}{3}$ and $\nu = \frac{2}{3}$ states and how they can explain the differences (magnetic field periods) and the similarities (plunger-gate-voltage frequencies) observed in our different experiments.

On the other hand, we cannot discard that the features observed here are sample dependent. Thus, it would be important to repeat our experiments in other devices with different sizes and different designs to see whether these phenomena are robust and universal or not.

Finally, another possibility is that these features emerge from Coulomb interactions even if the device apparently operates in the AB regime. In the experiments with integer edge channels, we observed some variations of the field periods. It suggest that the charging effects may still have an appreciable effect although they are weak. According to Feldman and Halperin in ref. [99], the existence of residual charging effects can explain why we observe anomalously large AB periods. They argue that, when the FP bulk is incompressible, the magnetic field period of AB oscillations is given by:

$$\Delta B = \frac{e\Phi_0}{e^* A}\left(1 - \xi \frac{\nu_{in}}{\nu_{in} - \nu_{out}}\right)^{-1}, \tag{8.2}$$

where e^* is the effective charge of the interfering quasiparticle (assumed here to be particle-like), ξ is the parameter presented in section 3.3.1 characterising the origin of oscillations and where ν_{in} and $\nu_{out}(< \nu_{in})$ are respectively the filling factors corresponding to the interfering edge channel and the filling factor corresponding to the fully transmitted edge channels. Therefore, any weak Coulomb interactions can lead to an increase of the magnetic field period at integer filling factors similar to what we observed experimentally.

We can use this formula to evaluate ξ in the configurations where we observed anomalously large magnetic field periods. For the experiments with $\nu_{QPC} = \frac{5}{3}$, we can assume that we have $\nu_{in} = \frac{5}{3}$ and $\nu_{out} = \frac{4}{3}$ or potentially $\nu_{in} = \frac{5}{3}$ and $\nu_{out} = 1$. Taking $e^*/e = 1.6$, $A = 2.25\ \mu m^2$ and $\Delta B = 5.6$ mT (Fig. 8.20), we get $\xi \simeq 0.16$ in the first case and $\xi \simeq 0.32$ in the second case. Likewise, if we take $e^*/e = 1$, we get $\xi \simeq 0.13$ in the first case and $\xi \simeq 0.27$ in the second case. These values are rather large and seem incompatible with the AB regime observed with integer edge channels.[1]

Consequences of our experiments

The most important observation is that discrete phase jumps can also appear in AB oscillations at integer bulk filling factors. These phase jumps are very similar to that expected at fractional bulk filling factors but they cannot be attributed to the localization of anyonic quasiparticles in the bulk of the FP cell. It suggests that different phenomena can lead to the emergence of such features and

[1] If we take larger values of ΔB, we obtain larger values of ξ and ξ saturates to $\frac{\nu_{in}-\nu_{out}}{\nu_{in}}$ in the limit where $\Delta B = 0$ mT.

they cannot be directly interpreted as signatures of anyonic statistics even at fractional bulk filling factors.

This has important consequences in the prospect of probing anyonic statistic with FP interferometers and clearly complicates the analysis of the experiments at fractional fillings. In particular, our experiments raise questions about the interpretations of the results of Nakamura and coworkers [151, 167] especially considering that our data look very similar to theirs (pyjama maps with anomalously large magnetic field periods and phase jumps).

Further investigations must be thus conducted to understand how such non-anyonic phase jumps can appear and to determine a way that allows to discriminate the different types of phase jumps.

8.4 Experiments at fractional bulk filling factors

We now present some measurements performed at fractional bulk filling factors. Despite several attempts, we most of time failed to observe oscillations in this case. In the $N = 0$ LL, we did not succeed in making interference. In the $N = 1$ LL, our effort were partially spoilt by the existence of a cross-talk between the QPCs preventing to have a control on which edge channel was interfering.

Nevertheless, we still managed to observe some resistance oscillations working at bulk filling factor $\nu_b \simeq \frac{7}{3}$ that we now discuss.

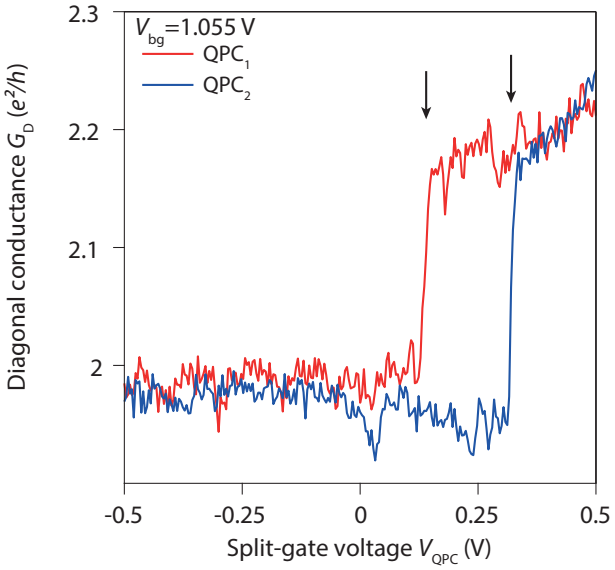

FIGURE 8.30: **QPC transmissions at $\nu_b \simeq \frac{7}{3}$.** Evolution of diagonal conductance G_D with the split-gate voltages at back-gate voltage $V_{bg} = 1.055$ V corresponding to a bulk filling factor $\nu_b \simeq \frac{7}{3}$. When the QPCs are fully open ($V_{QPC} = 0.48$ V) a fractional conductance plateaus $G_D \simeq 2.2\frac{e^2}{h}$ appears marking the formation of the $\nu = \frac{7}{3}$ QH state in the bulk. The black arrows indicate the QPCs tuning for the experiments discussed of Fig. 8.31. Measurements performed at 14 T.

Fig. 8.30 displays the QPC transmission plots measured at back-gate voltage $V_{bg} = 1.055$ V where the $\nu = \frac{7}{3}$ state develops at 14 T. The formation of this state is marked by the emergence of a $G_D \simeq 2.2\frac{e^2}{h}$ plateaus when the QPCs are open.

At this filling factor, the tuning of the QPCs is particularly difficult. Indeed, as we can see in Fig 8.30, the transitions between the $G_D \simeq 2.2\frac{e^2}{h}$ and $G_D \simeq \frac{2e^2}{h}$ plateaus are particularly abrupt in both QPCs and the pinching of $\nu = \frac{7}{3}$ state occurs in a voltage range of about 25 mV. This enhances

the sensitivity of the QPCs to the electrostatic environment and to the charge noise. Likewise, the transmission of the whole FP device is thus very hard to tune.

Despite these difficulties, we managed to observe some resistance oscillations at this filling factor. Fig. 8.31.C presents the evolution of R_D with the plunger-gate voltage V_{pg} measured after tuning of the QPCs. Contrary to the experiments with integer edge channels, the background resistance is not flat but it shows several resistance peaks on top of a 13 kΩ resistance background.

These peaks seem to appear by series of a few peaks approximately regularly spaced but the average spacing changes with the plunger-gate voltage. For instance, it is about 150-200 mV for $-1\ \text{V} < V_{pg} < 0\ \text{V}$ whereas it is about 350 mV for $-4\ \text{V} < V_{pg} < -2.5\ \text{V}$. These peaks do not originate from modifications of the QPC potential induced by the change of plunger-gate voltage: we indeed checked that there was no significant cross-talk between the QPCs and the plunger gate at this specific back-gate voltage.

When the resistance increases above the 13 kΩ background, for example on a resistance peak, oscillations appear as highlighted by Fig. 8.31.A and Fig. 8.31.B. These oscillations vanish or become undistinguishable from the noise when the average resistance decreases and this behaviour was consistently observed for different experiments with similar QPCs tunings.

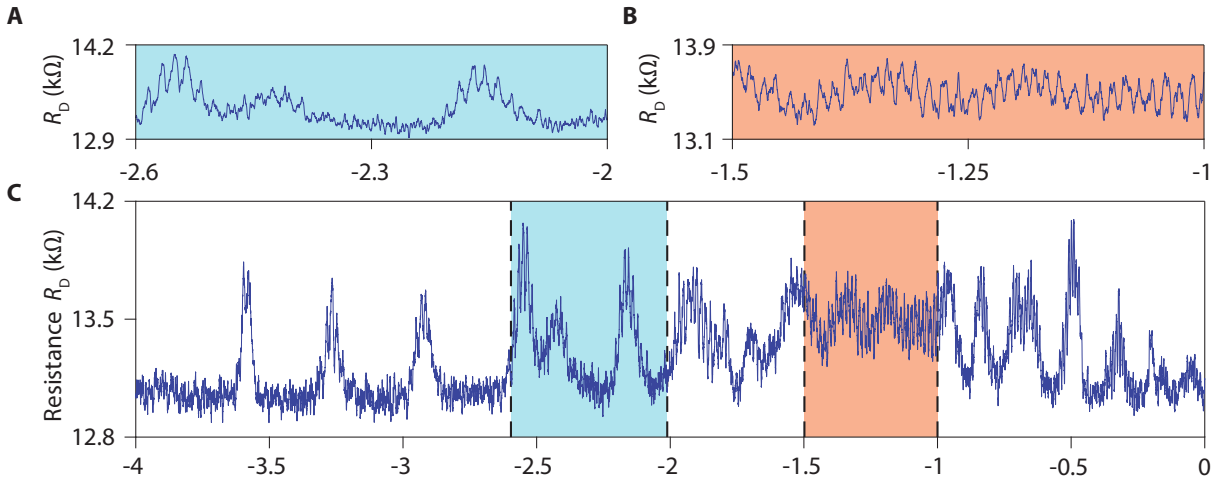

FIGURE 8.31: **Resistance oscillations at $\nu_b \simeq \frac{7}{3}$.** Evolution of the diagonal resistance R_D with the plunger-gate voltage V_{pg}. **C,** Full voltage range spanned. Resistance peaks appear on top of a 13 kΩ background. Some oscillations emerge when the resistance increases on a peak. **A** and **B,** Zooms on limited voltage ranges. Experiment performed at 14 T and at $V_{bg} = 1.055$ V.

The Fourier transform of the resistance oscillations, obtained after subtraction of the background including the peaks, is shown in Fig. 8.32. It confirms that oscillations appear on small voltage ranges and that they emerge when the resistance increases on a peak. The evolution of the frequency of the oscillations seems similar to that we observed previously: it decreases with V_{pg}.

We now discuss the origin of these oscillations. We first remark that the resistance background is always larger than 13 kΩ and that the resistance peaks go up to 14.1 kΩ. Such values correspond to conductances $G_D < \frac{2e^2}{h}$ that are apparently inconsistent with interference emerging from the partial backscattering of the $\nu = \frac{7}{3}$ state. It seems that the latter is completely backscattered by the QPCs and thus that the oscillations arise from a residual backscattering of inner integer edge channel. This apparent inconsistency can be a measurement artefact coming from the existence

of an out-of-phase signal and the imprecisions we have on the exact value of the resistance.[2] It would also explain why the conductance drops below $\frac{2e^2}{h}$ when the QPCs are closed (see Fig. 8.30).

This scenario where the oscillations arise from a residual backscattering of $\nu = 2$ edge channel is also inconsistent with the Fourier transform in Fig. 8.32: the oscillations frequency does not diverge when $\nu_{pg} > 1$. It contrasts with what we observed for AB interference with the inner edge channel interfering where the resistance oscillations appear when $\nu_{pg} = 1$. On the contrary, if we assume that interference arise from the $\nu = \frac{7}{3}$ state, we expect the oscillations to appear when $\nu_{pg} \approx 2$ in agreement with what we observe experimentally.

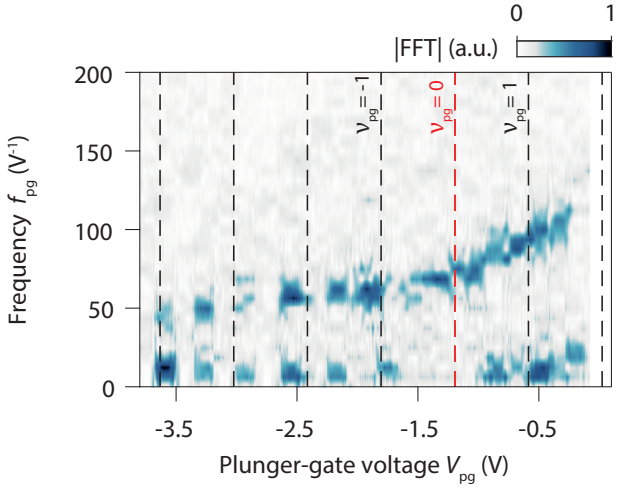

FIGURE 8.32: **Fourier transform of resistance oscillations at $\nu_b \simeq \frac{7}{3}$.** Evolution of Fourier amplitude of resistance oscillations displayed in Fig. 8.31.C after subtraction of a background which includes the resistance peaks. The large Fourier amplitudes at low frequencies are due to the imperfect subtraction of the background and mark the plunger-gate voltages where resistance peak occur.

It is also instructive to compare the frequency of the oscillations in Fig. 8.31 to the dispersions measured in the different experiments of this chapter. Fig. 8.33 shows the evolution of the rescaled frequencies with the shifted plunger-gate voltages for the different types of edge channel configurations studied with the data discussed in this section. For the experiments with $\nu_b = \frac{7}{3}$, the plunger-gate voltages were shifted assuming that the interfering edge channel is expelled outside from the plunger gate when $\nu_{pg} = 2$.

We observe that the data for the experiment at $\nu_b = \frac{7}{3}$ collapse on the plot drawn by the experiments where the QPCs were tuned at fractional filling factors and the bulk was at integer filling factor. It shows that the two types of measurements have common characteristics and somehow supports the hypothesis that interference arise from the partial backscattering of the $\nu = \frac{7}{3}$ state.

[2] When we take that the real part of the complex impedance, we obtain a background of 11.5 kΩ with peaks going up to 12.4 kΩ. Alternatively, when we take the modulus of the impedance, the resistance background is about 12.5 kΩ and the peaks reach 13.6 kΩ. Thus, there is an ambiguity on the exact value of the resistance and on the edge channel configuration.

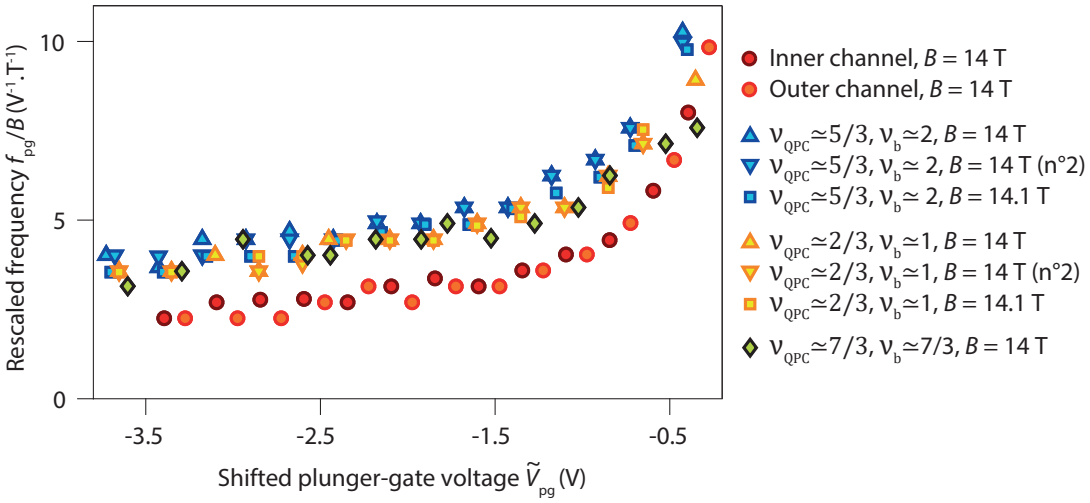

FIGURE 8.33: **Comparison of oscillations frequency.** Evolution of the rescaled oscillations frequencies f_{pg}/B with the shifted plunger-gate voltages $\tilde{V}_{pg}$ for the different types of interferometry experiments. The data points obtained in the experiment where $\nu_b = \frac{7}{3}$ rescale with the data points corresponding to experiments where the bulk is at integer filling factor and the QPCs at fractional fillings.

Unfortunately, we did not manage to measure a pyjama map for these oscillations. It prevents us to assess whether these oscillations arise from AB interference or charging effects.

8.5 Conclusion and perspectives

In this chapter, we investigated FP interferometry with fractional QH edge channels in our graphene devices. We discussed what are the typical signatures of FQH in graphene FP interferometers and how they manifest in split-gated devices. We presented our attempts to make interferometry with fractional edge channels both at integer and fractional filling factors.

In the first case, we tuned the QPCs at fractional fillings $\nu_{QPC} = \frac{5}{3}$ and $\nu_{QPC} = \frac{2}{3}$ states and we unveiled a robust oscillation regime where AB interference present non-anyonic phase jumps accompanied with an anomalously large magnetic field period. We investigated the characteristics of gate induced oscillations in such regime and out-of-equilibrium transport in this regime and found major differences with the results obtained with integer channels interfering at non-integer bulk filling factor. The existence of such non-anyonic phase jumps has deep consequences for the interpretation of interferometry experiments with fractional edge channels: it implies that anyonic signatures in AB oscillations can be mimicked by other phenomena. They must be identified and studied in the prospects of evidencing braiding statistics with QH FP interferometers.

We also presented our attempts to set interferometry experiments at fractional bulk factor $\nu_b = \frac{7}{3}$ where we observed a few resistance oscillations when trying to pinch the fractional edge modes. Our study of the plunger-gate-voltage dispersion of the oscillation frequency provided indications that interference observed indeed were arising from the pinching of the fractional edge modes.

FP interferometry in the fractional regime in graphene devices was also investigated in ref. [243] by Y. Ronen and coworkers. In their high quality device, they observed the formation of fractional QH states down to 3 T. Likewise at 8 T, they had robust fractional QH states developing in their sample, with large gaps, and they managed to observe AB interference arising from integer edge modes at $\nu_b = \frac{8}{3}$ and $\nu_b = \frac{10}{3}$. Yet, they did not succeed in making interference with fractional edge modes despite the superior quality of their device. The absence of interference with fractional edge modes was attributed to an insufficient radio frequency filtering and to the relatively high electron temperature at which their measurements were performed (60 mK).

We nevertheless believe that their double graphite-gated devices are extremely promising in the prospect of probing fractional statistics because of the very low level of disorder in this sample and of the high screening environment provided by the graphite gates. Such a screening has proven to be very important to access AB interference with fractional edge channels [151, 167].

We finally stress that the investigations of the FQH effect in graphene and of FP interferometry would greatly benefit from shot noise measurements. It would allow to determine the effective charge of quasiparticles at different filling factors and to determine the edge structures. Such experiments in graphene are now accessible with gate-tunable QPCs.

Conclusion and perspectives

In this PhD work, we successfully fabricated and investigated two new types of high mobility encapsulated graphene devices aiming at probing and harvesting the topological properties of quantum Hall phases: graphene devices on $SrTiO_3$ where a helical quantum Hall phase appears at charge neutrality and graphene devices with multiple split gates in series operated as quantum Hall Fabry-Pérot interferometers.

Helical edge transport in graphene devices on $SrTiO_3$

We developed a new strategy based on subtrate engineering to induce the formation of a quantum Hall phase exhibiting helical edge transport at charge neutrality. For this purpose, we fabricated encapsulated graphene devices with few nanometers thick bottom h-BN that we deposited on top of high-*k* dielectric $SrTiO_3$ substrates.

We evidenced that a robust helical edge transport appears in such devices at charge neutrality and at intermediate magnetic fields. We demonstrated that this helical quantum Hall phase emerges thanks to the screening provided by the substrate which allows to restore the predominance of the spin splitting terms over the valley splitting terms. We showed that the helical edge transport survives over micron long distances and up to 110 K. We finally discussed its breakdown with magnetic field and temperature.

Our work provides a new platform for the investigation of topological superconductivity and the physics of Majorana modes in graphene heterostructures [98]. Alternatively, our substrate engineering strategy also offers new perspectives to investigate the physics of highly correlated electronic phases developing thanks to Coulomb interactions like, for instance, in twisted multilayer graphene devices.

Graphene quantum Hall Fabry-Pérot interferometers

We also fabricated encapsulated graphene devices equipped with a series of split gates used as quantum point contacts and we demonstrated that these devices operate as quantum Hall Fabry-Pérot interferometers.

In the integer regime, we investigated several aspects of the quantum coherent transport in this device. On the first hand, we observed gate-tunable resistance oscillations in these devices. We evidenced that they arise from Aharonov-Bohm effect and studied how the electrostatics of the plunger-gate affect these oscillations. On the other hand, we probed the oscillations emerging with the application of the dc-voltage bias, together with the coherence of the Aharonov-Bohm oscillations in our devices, and we studied how both are affected by the dimensions of the interferometers. We showed that our experimental results are in remarkable agreement with the theory of non-interacting theory of quantum Hall Fabry-Pérot interferometers.

We also investigated the existence of a peculiar regime transport, that was previously evidenced in GaAs/AlGaAs devices, where Aharonov-Bohm oscillations have a halved periodicity. We demonstrated that such regime also exists in graphene devices. We showed that it appears under similar conditions and that it can coexist with the standard Aharonov-Bohm regime in graphene devices. We also evidenced that, in our small graphene interferometers, the frequencies of the two types of oscillations are not commensurate.

Besides, we derived a theoretical model describing the quantum transport in an interferometer with three quantum point contacts in series and we applied it to unveil the coherence of the transport in a double interferometer.

We finally discussed our attempts to make interference with fractional edge channels at fractional filling factor and in an unusual configuration with the quantum point contacts at fractional transmissions and the bulk at integer filling. In the latter case, we discovered an intriguing oscillation regime where Aharonov-Bohm oscillations display phase jumps mimicking the signatures of braiding statistics. The existence of such unexpected phase jumps has important consequences in the prospect of probing anyons physics with quantum Hall Fabry-Pérot interferometers.

Our work demonstrates that graphene is a suitable and promising platform for the study of quantum Hall Fabry-Pérot interferometers. It also shows the high tunability offered by graphene split-gate devices which allows to investigate unusual experimental configurations and unveil new phenomena. These advanced devices open up new opportunities to investigate the rich physics of anyons in the fractional quantum Hall effect and exploit their topological properties.

Our investigations also open the path towards the development of a new generation of hybrid mesoscopic devices where the coupling between quantum Hall effect and superconductivity is probed via coherent transport measurements [254]. In particular, graphene Fabry-Pérot interferometers may be useful to investigate the superconducting correlations induced in quantum Hall edge channels [194] or the coherence in chiral Andreev edge states [195]. They may also be used to probe the topological excitations emerging in such hybrid devices [196, 197]. Efforts are under way to develop new graphene quantum Hall interferometers with superconducting contacts in our group.

Part III

Appendices

Chapter 9

Quantized resistance values for helical edge transport

In this section, we focus on the helical edge transport regime and we derive the expressions giving the values of resistance expected depending on the contact configuration.

Modelling by an electric circuit.

Along a free sample edge, the backscattering between the counterpropagating edge channels of a single helical pair is fully suppressed because the two edge channels have opposite spin polarization. The transmission of helical edge states is thus supposedly perfect along a free edge. In contrast, in a metallic contact, the carriers lose their spin coherence and thus the two helical edge channels are equilibrated. Therefore an helical edge section between two contacts can be seen as single resistor of quantized resistance $R_{\mathrm{Q}} = \frac{h}{e^2}$ as represented in Fig. 9.1.A.

Remembering that in real devices, there are two edges connecting the source and drain contacts, we can calculate the resistance values expected in helical edge transport regime by modelling the device by an equivalent electric circuit. This circuit is composed of two parallel branches of R_{Q} resistors in series symbolizing the two graphene edges between the source and drain contacts. Each branch is composed of N resistors in series which represent the N helical edge sections between the source and drain contacts along the edge considered. An example of such modelling is shown in Fig. 9.1.B.

Two-terminal resistance.

We now derive the formula giving the values of the two terminal resistance expected in the helical edge transport regime depending on the contact configuration. We consider the general circuit schematized in Fig. 9.2 which modelled any graphene Hall-bar device operating in the helical edge transport regime. We first compute the two-terminal resistance $R_{2\mathrm{t}} = U/I$. The application of Kirchhoff circuit laws gives:

$$I_1 = \frac{U}{\mathrm{N}_1 R_{\mathrm{Q}}} \text{ and } I_2 = \frac{U}{\mathrm{N}_2 R_{\mathrm{Q}}}, \tag{9.1}$$

thus we have:

$$I = \frac{U}{R_{\mathrm{Q}}}\left(\frac{1}{\mathrm{N}_1} + \frac{1}{\mathrm{N}_2}\right), \tag{9.2}$$

and finally:

$$R_{2t} = \frac{U}{I} = \frac{h}{e^2}\left(\frac{1}{\mathrm{N}_1} + \frac{1}{\mathrm{N}_2}\right)^{-1}, \tag{9.3}$$

which is the formula giving the R_{2t} depending on the contact configuration i.e. depending on the number of helical edge sections between source and drain contacts along both edges.

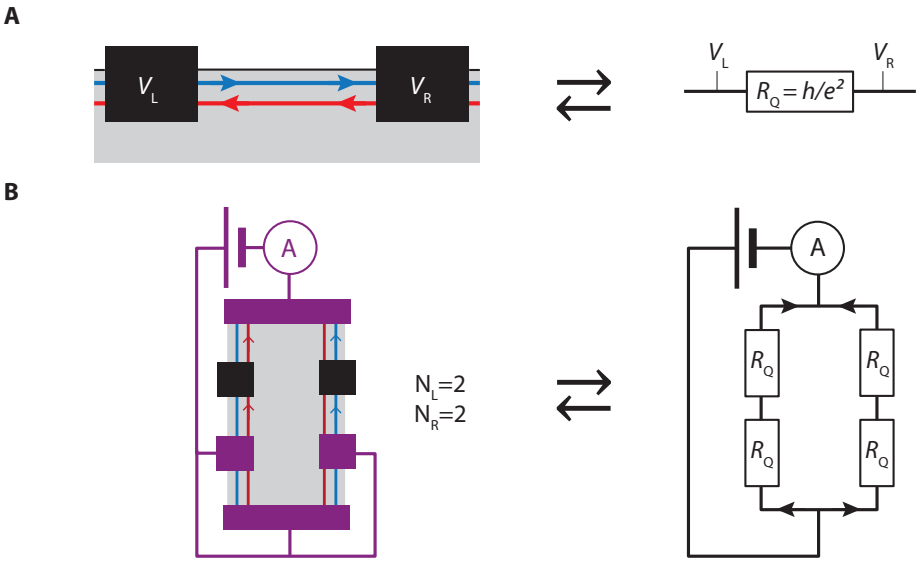

FIGURE 9.1: **Equivalence between a contact configuration and an electric circuit in the helical edge transport regime. A**, A helical edge section between adjacent contacts, respectively at electric potential V_L and V_R, can be modelled by a resistor $R_Q = \frac{h}{e^2}$. **B**, A given contact configuration can then be modelled by an electric circuit composed of two branches of $R_Q = \frac{h}{e^2}$ resistors in series. Each branch represents an edge of the device between the source and drain contact. The numbers of resistor in each branch, N_L and N_R, are respectively given by the numbers of helical edge sections on the left (L) edge and on the right (R) edge of the device.

Four-terminal/Non-local resistance.

Using the same model electric circuit, we can also derive the values of resistance expected for any non-local or four terminal configurations (which are equivalent in helical edge transport regime). In Fig. 9.2, it corresponds to $R_{4t} = V/I$. V can be easily expressed considering the voltage division in the second circuit branch:

$$V = U\frac{N_V}{N_2} = U\frac{N_V}{N_I}, \tag{9.4}$$

where N_I is the number of helical edge sections between source and drain contacts along the edge where the voltage probes are placed. Using this expression, we easily recover:

$$R_{4t} = \frac{V}{I} = \frac{U}{I}\frac{N_V}{N_I} = R_{2t}\frac{N_V}{N_I}. \tag{9.5}$$

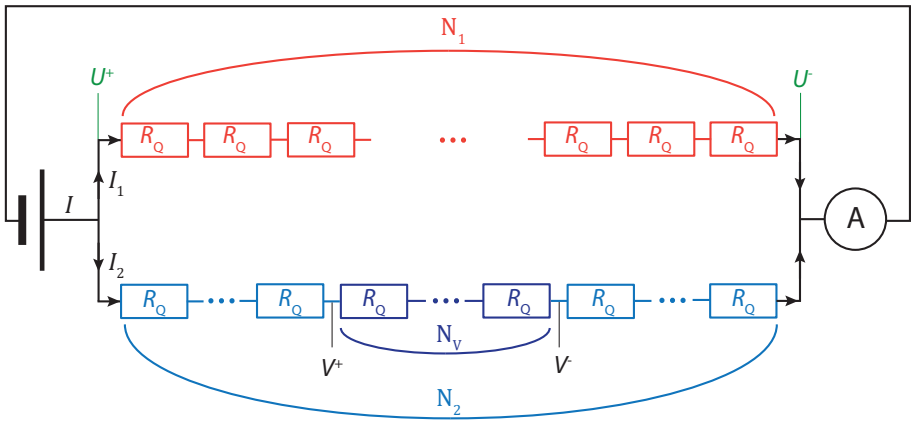

FIGURE 9.2: **Generalized equivalent electric circuit .**

Chapter 10

Bias-induced oscillations with asymmetric potential drop

Here, we derive the formula for the transmission of a QH-FP interferometer as a function of magnetic field and voltage bias using the scattering matrix formalism as in ref. [143], but taking into account a possible asymmetric potential drop at the two QPCs.

The transmission of a non-interacting QH Fabry-Pérot interferometer reads:

$$t(\epsilon,\Phi) = \frac{t_1 t_2 e^{i\pi\frac{\Phi}{\Phi_0}+i\frac{L\epsilon}{\hbar v}}}{1-r_1' r_2 e^{2i\pi\frac{\Phi}{\Phi_0}+i\frac{2L\epsilon}{\hbar v}}}, \tag{10.1}$$

where $2\pi\frac{\Phi}{\Phi_0}$ is the Aharonov-Bohm phase, $\frac{2L\epsilon}{\hbar v}$ the dynamic phase accumulated by electrons after one winding in the cavity of length $2L$, t_1 and t_2 the transmission amplitudes of QPC_1 and QPC_2 for right moving particles, r_1' the reflection amplitude for left-movers at QPC_1 and r_2 the reflection amplitude for right-movers at QPC_2.

The transmission probability is:

$$T(\epsilon,\Phi) = \frac{\mid t_1 \mid^2 \mid t_2 \mid^2}{1+\mid r_1' r_2 \mid^2 -2 \mid r_1' r_2 \mid \cos(2\pi\frac{\Phi}{\Phi_0}+\frac{2L\epsilon}{\hbar v}+\varphi)}, \tag{10.2}$$

where φ is a constant phase factor which depends on the scattering phase of the QPCs. Given that $\mid r_{1,2} \mid^2 = \mid r'_{1,2} \mid^2 = R_{1,2}$ and $\mid t_{1,2} \mid^2 = T_{1,2}$, we can rewrite (10.2) as

$$T(\epsilon,\Phi) = \frac{T_1 T_2}{1+R_1 R_2 - 2\sqrt{R_1 R_2}\cos(2\pi\frac{\Phi}{\Phi_0}+\frac{2L\epsilon}{\hbar v}+\varphi)}, \tag{10.3}$$

In the weak backscattering limit, $R_i \ll 1$, and omitting the constant phase term φ, we obtain at first order:

$$T(\epsilon,\Phi) = 1 - R_1 - R_2 + 2\sqrt{R_1 R_2}\cos\left(2\pi\frac{\Phi}{\Phi_0}+\frac{2L\epsilon}{\hbar v}\right). \tag{10.4}$$

We then consider a finite dc-voltage bias V applied between source and drain contacts. We note $q = -e < 0$ the electron charge. Depending on the energy relaxation processes consecutive to the current flow, and on the electrostatic coupling between the cavity, the back gate, the source and the drain, the electrochemical potential in the cavity will adjust itself at a value intermediate between that of the source and that of the drain. The right-movers coming from the source contact have an energy $qV^+ = qV(\frac{1}{2}+x) = qV\beta$ with respect to the chemical potential within FP cavity and the left-movers coming from the drain have an energy $qV^- = -qV(\frac{1}{2}-x) = -qV\overline{\beta}$. In these expressions, $x \in [-\frac{1}{2},\frac{1}{2}]$ is the voltage bias asymmetry factor. $x = 0$ corresponds to a symmetric biasing with $V^+ = \frac{V}{2}$ and $V^- = -\frac{V}{2}$, meaning that the potential drop is the same across both QPCs. When $x = \frac{1}{2}$ (or equivalently $x = -\frac{1}{2}$) the bias is completely asymmetric, $V^+ = V$ and

$V^- = 0$ (or equivalently $V^+ = 0$ and $V^- = -V$), the potential drop only occurs at one QPC while the FP cavity is at the potential of one of the two contacts.

At zero temperature, the current through the device is given by $I = \frac{q}{h}\int_{qV^-}^{qV^+} T(\epsilon,\Phi)\mathrm{d}\epsilon$. In the weak backscattering limit, it writes:

$$I = \frac{q}{h}\int_{qV^-}^{qV^+}\left[1 - R_1 - R_2 + 2\sqrt{R_1R_2}\cos\left(2\pi\frac{\Phi}{\Phi_0} + \frac{2L\epsilon}{\hbar v}\right)\right]d\epsilon = I_0 + I_{\mathrm{osc}}, \tag{10.5}$$

where $I_0 = \frac{e^2}{h}(1 - R_1 - R_2)V$ is the constant part of the current and I_{osc} is the oscillating part of the current which writes:

$$I_{\mathrm{osc}} = \frac{e^2}{h}2\sqrt{R_1R_2}\frac{\hbar v}{2Lq}\left[\sin\left(2\pi\frac{\Phi}{\Phi_0} + \frac{2L}{\hbar v}qV\beta\right) - \sin\left(2\pi\frac{\Phi}{\Phi_0} - \frac{2L}{\hbar v}qV\overline{\beta}\right)\right]. \tag{10.6}$$

The corresponding differential conductance is then:

$$\frac{dI_{\mathrm{osc}}}{dV} = g_{\mathrm{osc}}\left[\beta\cos\left(2\pi\frac{\Phi}{\Phi_0} - \frac{2L}{\hbar v}eV\beta\right) + \overline{\beta}\cos\left(2\pi\frac{\Phi}{\Phi_0} + \frac{2L}{\hbar v}eV\overline{\beta}\right)\right], \tag{10.7}$$

with $g_{\mathrm{osc}} = \frac{e^2}{h}2\sqrt{R_1R_2}$ and restoring $q = -e$.

When the potential drop at the constrictions is symmetrical, that is, $V^+ = V/2$ and $V^- = -V/2$, we have $\beta = \overline{\beta} = \frac{1}{2}$ ($x = 0$) and then:

$$\frac{dI_{\mathrm{osc}}}{dV} = g_{\mathrm{osc}}\cos\left(2\pi\frac{\Phi}{\Phi_0}\right)\cos\left(2\pi\frac{L}{hv}eV\right), \tag{10.8}$$

leading to a checkerboard pattern with a period versus bias voltage which is equal to the ballistic Thouless energy : $e\Delta V = hv/L = E_{\mathrm{Th}}$.

If the bias is completely asymmetrical, for example when $V^+ = V$ and $V^- = 0$ with $\beta = 1$ and $\overline{\beta} = 0$ ($x = \frac{1}{2}$), we obtain:

$$\frac{dI_{\mathrm{osc}}}{dV} = g_{\mathrm{osc}}\cos\left(2\pi\frac{\Phi}{\Phi_0} - 2\pi\frac{2L}{hv}eV\right), \tag{10.9}$$

that draws a diagonal strip pattern with a period versus bias voltage (at fixed magnetic field) which is equal to half the Thouless energy. Any intermediate value of x leads to a mixed pattern, that is, a tilted checkerboard as observed in our experiment.

Note that the measured diagonal resistance $\delta R_{\mathrm{D}} = -\frac{\mathrm{d}I_{\mathrm{osc}}}{\mathrm{d}V}(\frac{h}{e^2})^2$ shows exactly the same oscillatory features as the conductance in the weak backscattering limit. This latter expression is used for simulations displayed in Fig. 5.20.A-C and Fig. 5.21.A-C that reproduce with a good agreement the tilting of the checkerboard pattern observed experimentally.

We now derive the evolution of the Fourier transform amplitude of AB oscillations with the bias. For this calculation, we note $\varphi_{\mathrm{AB}} = 2\pi\frac{\Phi}{\Phi_0}$ and $\varphi_V = 2\pi\frac{LeV}{hv}$. Eq. (10.7) can then be written as:

$$\frac{dI_{\mathrm{osc}}}{dV} = g_{\mathrm{osc}}\left[\beta\cos\left(\varphi_{\mathrm{AB}} - 2\beta\varphi_V\right) + \overline{\beta}\cos\left(\varphi_{\mathrm{AB}} + 2\overline{\beta}\varphi_V\right)\right], \tag{10.10}$$

Using Euler formulas, one can write previous expression as:

$$\frac{dI_{\mathrm{osc}}}{dV} = \frac{g_{\mathrm{osc}}}{2}\left(e^{i\varphi_{\mathrm{AB}}}(\beta e^{-2i\beta\varphi_V} + \overline{\beta}e^{2i\overline{\beta}\varphi_V}) + \mathrm{c.c.}\right), \tag{10.11}$$

where c.c. denotes the complex conjugate term. Therefore, the Fourier transform of AB oscillations reads as:

$$\mathrm{FFT}(\varphi_{\mathrm{AB}}) = \frac{g_{\mathrm{osc}}}{2}\left(\beta e^{-2i\beta\varphi_V} + \overline{\beta} e^{2i\overline{\beta}\varphi_V}\right), \tag{10.12}$$

and its amplitude can be written as:

$$|\mathrm{FFT}(\varphi_{\mathrm{AB}})|^2 = \frac{g_{\mathrm{osc}^2}}{4}\left[\beta^2 + \overline{\beta}^2 + 2\beta\overline{\beta}\cos\left(2(\overline{\beta}+\beta)\varphi_V\right)\right], \tag{10.13}$$

$$|\mathrm{FFT}(\varphi_{\mathrm{AB}})|^2 = \frac{g_{\mathrm{osc}}^2}{4}\left[\frac{1}{2} + 2x^2 + 2(\frac{1}{4} - x^2)\cos(2\varphi_V)\right], \tag{10.14}$$

$$|\mathrm{FFT}(\varphi_{\mathrm{AB}})|^2 = \frac{g_{\mathrm{osc}}^2}{4}\left[\frac{1}{2} + 2x^2 + 2(\frac{1}{4} - x^2)(2\cos^2(\varphi_V) - 1)\right], \tag{10.15}$$

$$|\mathrm{FFT}(\varphi_{\mathrm{AB}})|^2 = \frac{g_{\mathrm{osc}}^2}{4}\left[4x^2\sin^2(\varphi_V) + \cos^2(\varphi_V)\right]. \tag{10.16}$$

Restoring $\varphi_V = 2\pi\frac{LeV}{h\upsilon} = 2\pi\frac{eV}{E_{\mathrm{Th}}}$, we finally get :

$$|\mathrm{FFT}(\varphi_{\mathrm{AB}})| = \frac{g_{\mathrm{osc}}}{2}\sqrt{\cos^2(2\pi\frac{eV}{E_{\mathrm{Th}}}) + 4x^2\sin^2(2\pi\frac{eV}{E_{\mathrm{Th}}})} = \frac{g_{\mathrm{osc}}}{2}\mathcal{A}(\frac{eV}{E_{\mathrm{Th}}}). \tag{10.17}$$

Thus the amplitude of AB interference oscillates with V with a period given by E_{Th}.

Chapter 11

Thermal averaging of oscillations amplitude

The effect of temperature on the visibility of the Aharonov-Bohm oscillations has been calculated by Chamon and coworkers [143] in the limit of weak backscattering and at finite bias voltage for a symmetric potential drop at the two constrictions. This calculation considers only the thermal averaging of the interference and does not introduce decoherence by inelastic scattering or energy relaxation at finite bias.

Here we explain in details the calculation in the symmetric case and then extend the result to the case of an asymmetric potential drop as observed in our device. In the following, we use the expression of the transmission coefficient obtained in the previous section in the limit of weak backscattering:

$$T(\epsilon,\Phi) = 1 - R_1 - R_2 + \sqrt{R_1 R_2}\left(e^{i2\pi\Phi/\Phi_0}e^{i2L\epsilon/\hbar v} + e^{-i2\pi\Phi/\Phi_0}e^{-i2L\epsilon/\hbar v}\right). \tag{11.1}$$

Symmetric potential drop

Assuming a symmetric potential drop at the two constrictions as in ref. [143], the current at finite temperature T and finite voltage V is given by:

$$I(\Phi,V,T) = \frac{q}{h}\int_{-\infty}^{+\infty} T(\epsilon,\Phi)\left(\frac{1}{1+e^{(\epsilon-\frac{qV}{2})/k_BT}} - \frac{1}{1+e^{(\epsilon+\frac{qV}{2})/k_BT}}\right)\mathrm{d}\epsilon, \tag{11.2}$$

where $q = -e < 0$ is the electron charge. Using the expression of the transmission coefficient in the limit of weak back-scattering, the current writes:

$$I(\Phi,V,T) = \frac{q^2}{h}(1-R_1-R_2)V - \frac{q}{h}\sqrt{R_1R_2}\left(e^{i2\pi\Phi/\Phi_0}H(V,T) + e^{-i2\pi\Phi/\Phi_0}H(V,T)^*\right), \tag{11.3}$$

where we introduce the function:

$$H(V,T) = \int_{-\infty}^{+\infty} e^{i2L\epsilon/\hbar v}\left(\frac{1}{1+e^{(\epsilon-\frac{qV}{2})/k_BT}} - \frac{1}{1+e^{(\epsilon+\frac{qV}{2})/k_BT}}\right)\mathrm{d}\epsilon. \tag{11.4}$$

By changing the variable in the integral, it becomes:

$$H(V,T) = \left(e^{i\frac{qV}{2}2L/\hbar v} - e^{-i\frac{qV}{2}2L/\hbar v}\right)\int_{-\infty}^{+\infty} e^{i2L\epsilon/\hbar v}\,\frac{1}{1+e^{\epsilon/k_BT}}\,\mathrm{d}\epsilon, \tag{11.5}$$

where the choice of a symmetric potential drop influences only the term in the parenthesis. The calculation of the integral gives:

$$\int_{-\infty}^{+\infty} e^{i2L\epsilon/\hbar v}\,\frac{1}{1+e^{\epsilon/k_BT}}\,\mathrm{d}\epsilon = -i2\pi k_BT\sum_{n=0}^{+\infty} e^{-\omega_n 2L/\hbar v} = \frac{-i2\pi k_BT}{2\sinh(\pi k_BT2L/\hbar v)}, \tag{11.6}$$

where $\omega_n = (2n+1)\pi k_BT$ are the Matsubara frequencies, with $n \in \mathbb{Z}$. In this case of a symmetric potential drop, the function $H(V,T)$ is real and writes:

$$H(V,T) = \sin(\frac{qVL}{\hbar v})\,\frac{2\pi k_BT}{\sinh(\pi k_BT2L/\hbar v)}. \tag{11.7}$$

The current finally writes:

$$I(\Phi,V,T) = G_0V - \frac{q}{h}\sqrt{R_1R_2}\;2\cos(2\pi\frac{\Phi}{\Phi_0})\,\sin(\frac{qVL}{\hbar v})\,\frac{2\pi k_BT}{\sinh(\pi k_BT2L/\hbar v)}, \tag{11.8}$$

which is equivalent to equations (16) and (18) in ref. [143]. The differential conductance writes:

$$G(\Phi,V,T) = G_0 - \frac{q^2}{h}\sqrt{R_1R_2}\;2\cos(2\pi\frac{\Phi}{\Phi_0})\,\cos(\frac{qVL}{\hbar v})\,\frac{\pi k_BT2L/\hbar v}{\sinh(\pi k_BT2L/\hbar v)}, \tag{11.9}$$

which forms a checkerboard pattern as a function of field and voltage. At high temperature, the amplitude of these oscillations decreases exponentially with a dependence of the form:

$$e^{-\pi k_BT2L/\hbar v} = e^{-4\pi^2k_BT/E_{\mathrm{Th}}} = e^{-T/T_0}, \tag{11.10}$$

where $E_{\mathrm{Th}} = hv/L$ is the ballistic Thouless energy which corresponds to the oscillation period $q\Delta V$ versus bias voltage, and T_0 is the fitting parameter of the exponential temperature dependence which is related to the Thouless energy by:

$$4\pi^2k_BT_0 = E_{\mathrm{Th}} = q\Delta V. \tag{11.11}$$

Asymmetric potential drop

In case of an asymmetric potential drop at the two constrictions, the potential energy is $qV^+ = \beta qV$ at the source contact and $qV^- = -\bar{\beta}qV$ at the drain contact, with $\beta = \frac{1}{2}+x$ and $\bar{\beta} = \frac{1}{2}-x$ with the parameter $x \in [-\frac{1}{2},\frac{1}{2}]$ characterizing the asymmetry of the potential drop. The current at finite temperature T and finite voltage V is then given by:

$$I(\Phi,V,T) = \frac{q}{h}\int_{-\infty}^{+\infty} T(\epsilon,\Phi)\left(\frac{1}{1+e^{(\epsilon-\beta qV)/k_BT}} - \frac{1}{1+e^{(\epsilon+\bar{\beta}qV)/k_BT}}\right)\mathrm{d}\epsilon. \tag{11.12}$$

Following the same calculations as above now gives the function:

$$H(V,T) = e^{ixqV2L/\hbar v}\sin(\frac{qVL}{\hbar v})\,\frac{2\pi k_BT}{\sinh(\pi k_BT2L/\hbar v)}, \tag{11.13}$$

which contains a complex phase factor. The current writes:

$$I(\Phi,V,T) = G_0V - \frac{q}{h}\sqrt{R_1R_2}\;2\cos(2\pi\frac{\Phi}{\Phi_0}+x\frac{qV2L}{\hbar v})\,\sin(\frac{qVL}{\hbar v})\,\frac{2\pi k_BT}{\sinh(\pi k_BT2L/\hbar v)}, \tag{11.14}$$

which is modified only by the term $xqV2L/\hbar v$ in the cosine function. The differential conductance writes:

$$G(\Phi, V, T) = G_0 - \frac{q^2}{h}\sqrt{R_1 R_2}\ \ 2\, g(\Phi, V)\, \frac{\pi k_B T 2L/\hbar v}{\sinh(\pi k_B T 2L/\hbar v)}, \tag{11.15}$$

where the oscillation term:

$$g(\Phi, V) = \cos(2\pi\frac{\Phi}{\Phi_0} + x\frac{qV2L}{\hbar v})\cos(\frac{qVL}{\hbar v}) - 2x\sin(2\pi\frac{\Phi}{\Phi_0} + x\frac{qV2L}{\hbar v})\sin(\frac{qVL}{\hbar v}), \tag{11.16}$$

gives a titled checkerboard pattern as a function of field and voltage for $x \neq 0$. Indeed, restoring $q = -e$ we have:

$$\begin{aligned} g(\Phi, V) = \frac{1}{2}\cos(2\pi\frac{\Phi}{\Phi_0} + (1-2x)\frac{LeV}{\hbar v}) + \frac{1}{2}\cos(2\pi\frac{\Phi}{\Phi_0} - (1+2x)\frac{LeV}{\hbar v}) \\ + x\cos(2\pi\frac{\Phi}{\Phi_0} - (1+2x)\frac{LeV}{\hbar v}) - x\cos(2\pi\frac{\Phi}{\Phi_0} + (1-2x)\frac{LeV}{\hbar v}), \end{aligned} \tag{11.17}$$

such that:

$$g(\Phi, V) = \beta\cos(2\pi\frac{\Phi}{\Phi_0} - 2\pi\beta\frac{2LeV}{hv}) + \overline{\beta}\cos(2\pi\frac{\Phi}{\Phi_0} + 2\pi\overline{\beta}\frac{2LeV}{hv}). \tag{11.18}$$

Comparing eq. (11.9) and eq. (11.16), we note that the temperature dependence is not affected by the asymmetry of the potential drop at the constrictions. The fitting parameter T_0 of the exponential temperature dependence is still related to the ballistic Thouless energy by $4\pi^2 k_B T_0 = E_{Th}$.

Chapter 12

Fabrication of high mobility graphene devices

Contents

From the past fifteen years, the quality of the graphene devices has been improving. Major breakthroughs, especially the use of h-BN flakes as substrates for graphene and the development of Van der Waals heterostructures, have allowed to significantly lower the level of disorder in the samples and have enabled the study of a wealth of mesoscopic phenomena. New fabrication processes are still being proposed nowadays. In this chapter, we present the fabrication of high mobility graphene heterostructures used to study coherent transport in the QH regime. We start by briefly reviewing the major improvements in the fabrication processes and we emphasize the role of the underlying substrate. We then describe how we fabricate high mobility Van der Waals heterostructures in our group and how we make QH FP interferometers based on these heterostructures.

12.1 Review of the major breakthroughs in the fabrication of graphene heterostructures

In the beginning, the graphene devices were fabricated by contacting directly graphene flakes exfoliated on silicon substrate [8, 9]. The mobility of these devices was limited by the substrate roughness, that favoured the appearance of corrugations in graphene [255], but also by the scattering induced by the charged impurities trapped in silicon substrates [256, 257].

To get rid of these effects, suspended graphene samples were developed. They enabled the first studies of FQH effect in graphene [258, 259] at the cost of some limitations on the device geometries and functionalities.

The first major breakthrough which led to an improvement the mobility was the use of h-BN as a substrate for graphene [32]. h-BN has several physical and chemical properties making it the best substrate for the study of electrons transport in graphene. First, it is a layered material which can be mechanically exfoliated to obtain atomically flat flakes and it has a honeycomb crystallographic structure very similar to that of graphene. There is only a 1.7 % lattice mismatch between the two materials and thus, graphene on h-BN has a reduced amount of mechanical strains and corrugations compared to graphene deposited directly on silicon substrates. Second, h-BN is an insulator with a large bandgap ($\simeq$ 5.97 eV), a moderate dielectric constant (ϵ_{BN} ranging

from 2 to 4 [227]) and a rather large breakdown electric field ($\simeq$ 0.7 V.nm^{-1}) making it a good gate dielectric for graphene devices. Finally, h-BN is inert, free of dangling bonds and of charge traps such that it does not affect the electronic transport properties of a graphene flake which is deposited atop it.

Therefore, one can significantly improve the mobility of graphene devices by transferring the graphene flakes on top of h-BN using polymer films. It was first demonstrated by C. Dean and coworkers in 2010 who showed that the mobility of graphene devices could be improved by one order of magnitude using h-BN flakes [32]. It allowed the investigation of the QHF [13] and the FQHE [12] in details.

The transfer techniques were rapidly improved and adapted to deposit the h-BN/graphene heterostructures on top of exfoliated graphite flakes used as back gates. It further improves the mobility of graphene devices because the graphite flakes screen the charged impurities trapped in the underlying substrate without generating additional corrugations in the h-BN/graphene heterostructure (contrary to others metallic gates). This strategy was used to investigate delicate phenomena associated with QH effect in h-BN/graphene heterostructures such as the physics of the Hofstadter's butterfly [14] and the physics of the composite fermions [76].

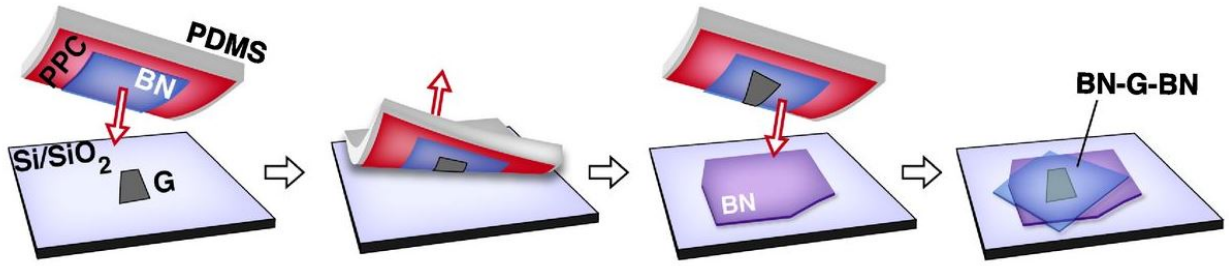

FIGURE 12.1: **Schematics of the fabrication of a high mobility h-BN/graphene/h-BN heterostructures.** A PDMS (polydimethylsiloxane) stamp coated with a sticky PPC (polypropylene carbonate) layer is preliminary used to detach a first h-BN flake from a silicon substrate. The stamp with the capping h-BN is then approached to the graphene flake and brought into contact with it such that the h-BN flake covers fully the graphene flake. Van der Waals interactions developed between h-BN and graphene allowing to detach it from silicon substrate by removing the stamp. The overall h-BN/graphene heterostructure is finally deposited on a second h-BN layer by repeating the process and melting the polymers before removing the stamp. Taken from ref. [33].

The second critical breakthrough was the development of encapsulated graphene devices i.e h-BN/graphene/h-BN heterostructures (refered as **stacks**) in 2013 by Wang and coworkers [33]. The method consists in taking advantage of the strong Van der Waals interactions that developed between 2D layered materials to encapsulate graphene between two h-BN flakes. It allows to protect it against any external contaminations.

The fabrication of the heterostructure is depicted in Fig. 12.1. It begins by picking up a first h-BN flake from the silicon substrate using a stamp with a sticky polymer. The stamp with the h-BN flake is then approached to a graphene flake and the two flakes are brought in contact. Thanks to the Van der Waals interactions developing between the flakes, the graphene binds to the h-BN which allows to detach the graphene flake from its substrate. This operation is repeated to pick-up a second h-BN flake. Once the h-BN/graphene/h-BN heterostructure is formed, it is released either on a virgin substrate or on another flake (like a graphite one) by simply melting the polymer on the stamp. During the fabrication of the heterostructures, the graphene flake is not exposed to any polymer residues. It remains clean and only very few impurities are trapped in the stack reducing significantly the amount of disorder in the sample.

Since the h-BN/graphene interfaces are atomically flat, the encapsulation of graphene allows to isolate it fully from its external environment [33]. Yet, it must be contacted to perform transport measurements. That's why, Wang and cowokers developed a specific process to connect graphene to metallic leads without exposing it. This process is sketched in Fig. 12.2.

After the encapsulation, the stack is selectively plasma-etched to uncover the edges of graphene at given places where a suitable metal combination is then deposited. It enables to make good one dimensional electrical contacts without uncovering the whole graphene flake as demonstrated by Wang *et al.* [33]. Thus, all along the lithographic processing, the graphene remains protected against any organic contamination (polymers, solvents, resist residues, etc.) thanks to the capping h-BN. It prevents the deterioration of its mobility.

This fabrication method is now the standard process followed to fabricate clean and high mobility samples where the transport can be ballistic over tenths of microns [260]. Recent studies nevertheless suggested that the mobility in this type of devices might still be intrinsically limited by random strain fluctuations [261–263].

The capping h-BN has another advantage: it can also be used as a gate dielectric for local metallic top gates. Therefore, graphene encapsulation also enables to define clean pn interfaces with limited equilibration in the QH regime and which are suitable for QH interferometry [16, 210, 212].

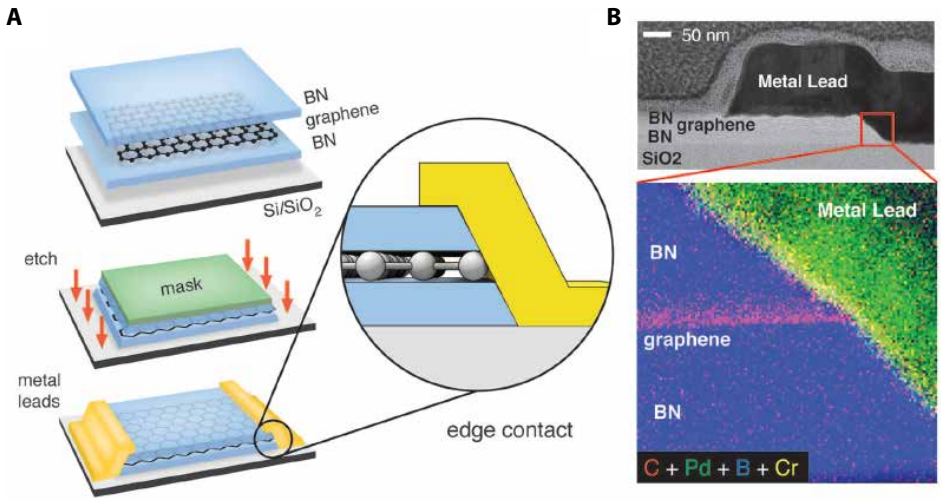

FIGURE 12.2: **Edge contacts in encapsulated graphene heterostructures. A**, Schematics of the fabrication of edge contacts in high mobility encapsulated graphene devices. A h-BN/graphene/h-BN heterostructure is fabricated, deposited on a substrate. Then, it is plasma-etched selectively to uncover graphene edges at specific places defined with a lithography step (for example using a resist mask). The metal is deposited on the edges of the heterostructure to make one dimensional contacts with the graphene along the exposed edges. **B**, Scanning transmission electron micrograph of an edge contact in an encapsulated graphene heterostructure and corresponding false-coloured electron energy-loss image showing the one dimensional interface between graphene and the metallic lead. Adapted from ref. [33].

Finally, more recent studies focused on the use of graphite flakes as top gates. It was demonstrated that the use of such top gates significantly facilitates the formation of FQH states in graphene [93, 187]. It also appeared that the devices with graphite top gates have a lower amount of disorder than the devices with metal-evaporated top gates and that a pre-patterning of the graphite gates (using plasma-etching) even enhances the quality of the devices [186]. Likewise, Ronen and coworkers demonstrated that the QPCs made from graphite flakes are particularly suitable for FP interferometry [243]. It opens up new perspectives for the fabrication of very high mobility devices dedicated to interferometry experiments with fractional edge states.

12.2 Fabrication of graphene QH FP interferometers

We now detail how we make Van der Waals heterostructures in our group and how we process them to fabricate graphene QH FP interferometers. All the processes presented in this section can be directly used or adapted to fabricate other types of devices for transport measurements in graphene. Especially, we use similar processes to make devices on $SrTiO_3$ substrates (the specificities related to the fabrication of these devices are given in chapter 2).

12.2.1 Fabrication of high mobility encapsulated graphene heterostructures

Exfoliation of graphite and h-BN crystals

The graphene, graphite and h-BN flakes, which are the basic materials composing our devices, are all fabricated via mechanical exfoliation [7, 264]. Macroscopic crystals (natural for the graphite and synthesised for the h-BN [265]) are placed on an adhesive tape which is repeatedly folded and unfolded on itself. It cleaves the crystals into thinner and thinner flakes homogeneously spread on a small area of the tape as shown in Fig. 12.4.A. The latter is then put into contact with a clean substrate, gently rubbed on it during a few minutes, and peeled off slowly such that cleaved crystals remain stuck on the substrate (see Fig. 12.4.B). This method allows to obtain flakes with various heights varying from monolayer flake to few microns thick crystals. We use doped silicon substrate with a typical oxide layer of 285 nm for the exfoliations because the monolayer graphene flakes have a sufficient contrast on such substrate [266].

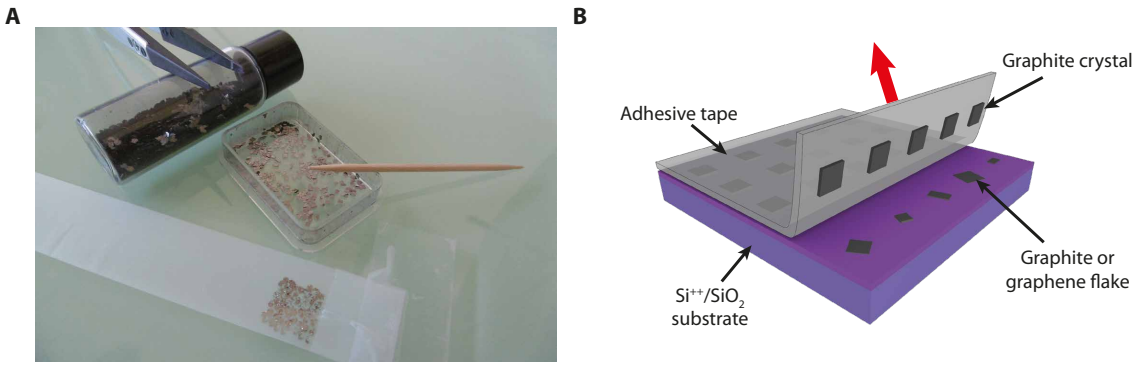

FIGURE 12.3: **Graphene exfoliation. A**, Exfoliation of graphene flakes from natural graphite crystals. The adhesive tape is repeatedly folded on itself to cleave the crystals into thinner and thinner layers spread on an uniform area of the tape. The latter is then put in contact with a clean substrate. **B**, After a gentle rubbing, the adhesive tape is peeled off slowly from the substrate (red arrow) and some of the graphite/graphene flakes remain stuck on it. Adapted from ref. [20].

Identifying suitable flakes

Once the exfoliated flakes are deposited on the substrate, they have to be sorted to identify which ones are suitable to fabricate high mobility heterostructures. Indeed, the flakes must fulfil different criteria.

The h-BN flakes have to be perfectly flat i.e. free from atomic terraces, wrinkles or cracks on large areas (minimum $10 \times 20\,\mu m^2$). They should also be clean and free from any glue residue coming from the exfoliation process. Finally, their heights should typically range from 15 to 40 nm to fit with the technical constrains imposed by the nanofabrication process.

For the graphene flakes, they must be perfectly clean, not folded on their edges and they should not show any sign of mechanical defects (holes, cracks, etc.). Crucially, we must check

that the flakes are indeed monolayer graphene and not few layer graphene which have different electronic properties [65]. The graphite flakes, used as back gates must also be clean, flat and relatively thin with a thickness varying typically from 3 to 15 nm.

A first sorting is done by looking carefully at the flakes with a high quality optical microscope equipped with an image processing software. The h-BN and graphite flakes which have the good thicknesses can be easily recognised because they appear with a characteristic blue, respectively violet, color on the substrate. The careful processing of the images of the flakes (by changing the contrast, color balance, etc.) allows to distinguish most of the defects or of the contaminations on the flakes and to see whether they are flat or not. The monolayer graphene flakes can be segregated from few layers graphene flakes because the contrast of the flakes on the substrate is proportional to the number of layers.

Once, the suitable flakes are selected, their cleanliness and flatness can be checked using atomic force microscopy. It sometimes leads us to discard some flakes which looked clean and flat on optical images. Ideally, this check has to be done for every flakes to make very high quality samples.

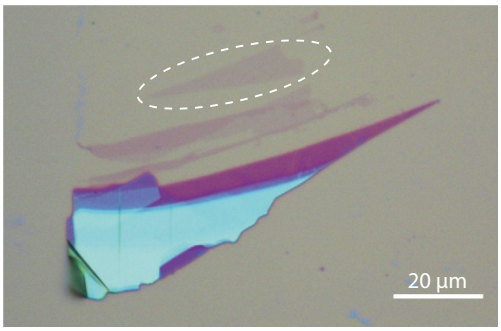

FIGURE 12.4: **Graphene flakes.** Optical image of graphite flakes. A graphene flake is encircled in white dashed line. The contrast of the flakes increases with the number of layers enabling to distinguish monolayer graphene from few layer graphene or thin graphite flakes. Note that the color of graphite flakes on the substrate turns from violet to blue above a certain number of layers.

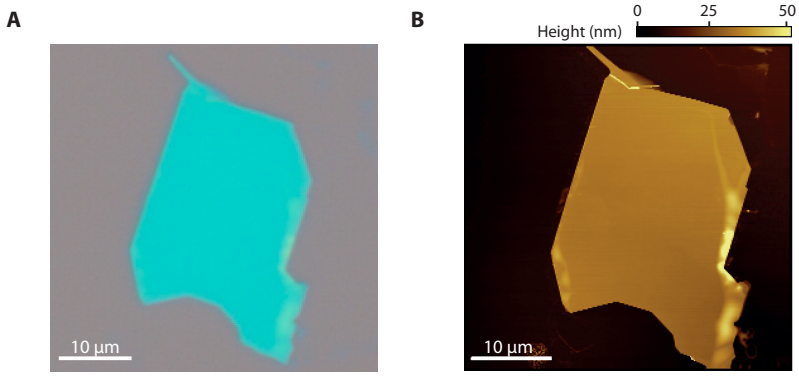

FIGURE 12.5: **h-BN flake. A**, Optical image and **B**, atomic force microscope topographic image of a clean h-BN flake. The h-BN flakes of suitable thickness appear a characteristic blue color on silicon substrates.

Assembling the heterostructures

Once suitable flakes have been found, they can be stacked using Van der Waals pick-up technique. Here we present briefly the set up used and discuss how we proceed in our group.

Transfer set-up used :

To detach the flakes from a substrate, we must place the stamp above the substrate and bring them into contact very precisely precisely at the position of the flake. To perform this operation, we use a set-up, shown in Fig. 12.6, specially designed to make stacks. It is composed of three main elements: an optical microscope, a mobile stage placed below the microscope and on which the substrate can be fixed and, finally, a micro manipulator which holds the stamp and which is installed on a separate platform.

The 3D position of the stage is controlled by piezoelectric motors. It allows to adjust the substrate's position with a precision in the micron range and to align precisely a flake under the microscope objective. Likewise, the micro manipulator allows to adjust the 3D position of the stamp - a glass slide with a solid PDMS dome covered by a sacrificial sticky PPC layer - above a specific part of the substrate with a precision of few microns. Taking advantages of the control we have on both the stamp and the stage positions, we can make a controlled contact between the apex of the stamp and a chosen part of the substrate.

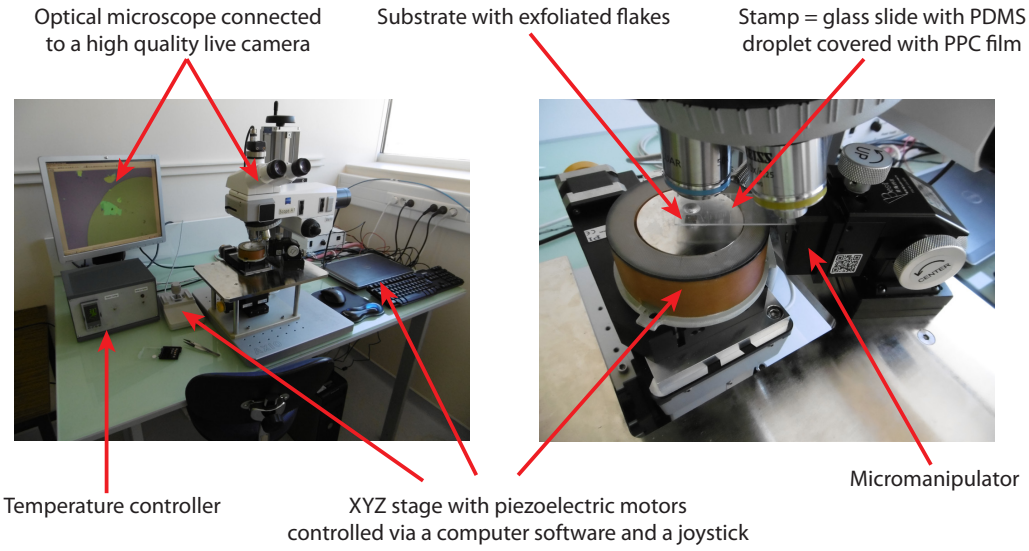

FIGURE 12.6: **Transfer microscope.** Photos of the transfer set-up used to assemble Van der Waals heterostructures. The set up is composed of a high quality optical microscope, a XYZ stage controlled by piezoelectric motors and a micromanipulator where the stamp is placed. It enables to pick-up and stack flakes with a precision of about one micron on the alignment of the flakes.

Pick-up method and assembling:

The contact between the stamp and the substrate is not directly done on the flake to pick-up itself but rather in its close vicinity. Once it is established, the stamp is approached and pressed on the substrate to expand progressively the contact area. When the limit of the contact area is only few microns away from the flake, the temperature of the substrate is increased by heating the stage. It results in an expansion of the PPC on the substrate which gradually covers the flake with a limited risk of damaging it. An example is shown in Fig. 12.7. Once the flake is fully covered by the sticky

polymer, we stop the heating and let the system cool down which tightens the PPC. It generates a strong strain on the polymer film which allows to pick-up the flake when the contact is broken.

The process is repeated to pick-up the other flakes. Before each contact, the flake on the substrate is carefully aligned with the heterostructure on the stamp to make sure that the latter is exactly above the former. After the first contact and the temperature increase, the partial stack covers the flake on the substrate and Van der Waals interactions develop between the two allowing the pick-up. An example of an assembling of a h-BN/graphene/h-BN stack is shown in Fig 12.8

When, all the flakes are stacked on the stamp, the heterostructure is released either on a virgin substrate or on top of another flake by repeating the previous process and increasing the temperature up to the melting point of the PPC.

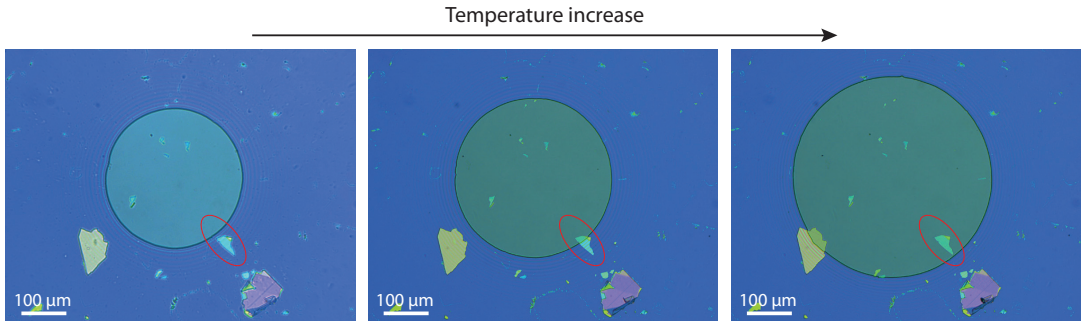

FIGURE 12.7: **Expansion of the PPC with the temperature**. Evolution of the PPC front with the temperature when the stamp is in contact with the substrate. Initially, the contact zone (blue-yellow circle) does not cover the flake to pick-up (encircled in red). By increasing the temperature, the PPC expands on the substrate and it smoothly covers the flake.

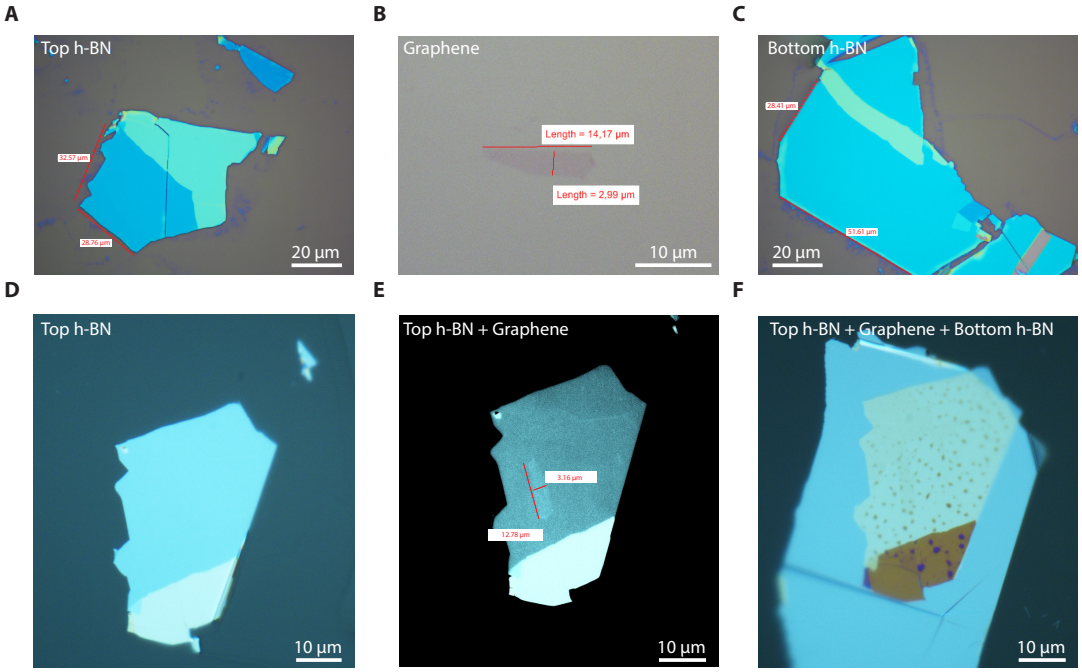

FIGURE 12.8: **Assembling of a h-BN/graphene/h-BN stack. A, B, C**, Optical images of the flakes used to make the heterostructure. **D, E, F**, Optical images of the heterostructure on the stamp after the successive pick-ups. The final heterostructure released on the substrate is shown in Fig 12.10

Annealing

During the fabrication of the heterostructure, bubbles can be trapped between the flakes or between the stack and the substrate. If they are located above or below the graphene, they can affect the electronic transport in the final device. Thus, the device should be placed in a region of the heterostructure which is large enough and (nearly) completely free of bubbles. To increase the chances of finding such an area, the stack is annealed by heating it to a few hundreds of degrees with a lamp in a vacuum chamber shown in Fig. 12.9.

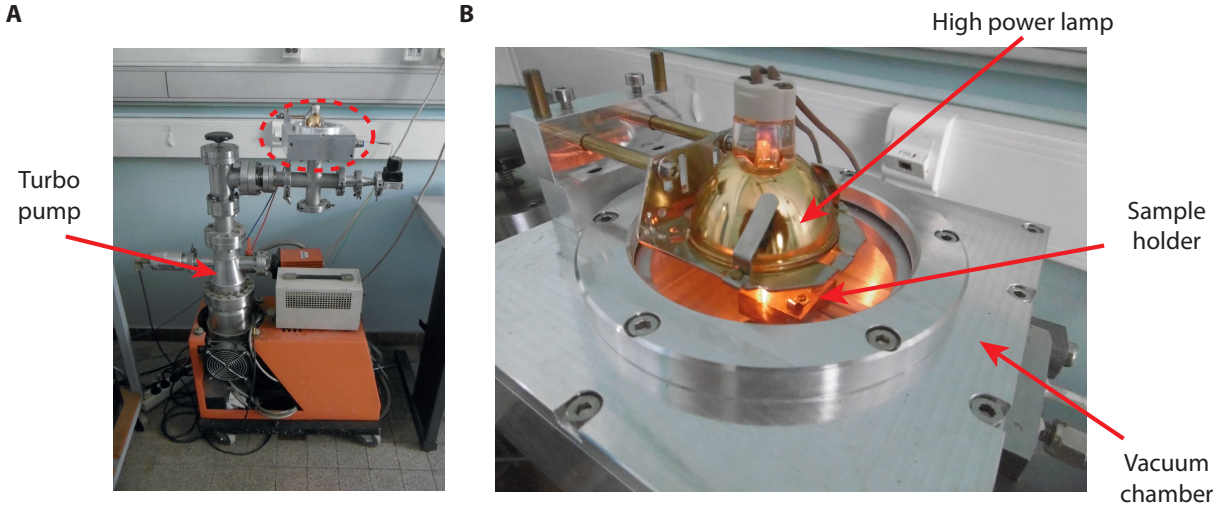

FIGURE 12.9: **Annealing set-up. A**, Overall set-up. The vacuum chamber is encircled in red. **B**, Zoom on the vacuum chamber. The sample is fixed on a cooper plate in the chamber and placed under a high power lamp for the annealing. The vacuum chamber is pumped with a turbo pump. The position of the lamp above the chamber can be changed to heat either directly the sample or the underlying cooper plate depending on the annealing conditions we want to achieve.

This annealing gives some mobility to the bubbles which can be expelled outside the stack or which can coalesce at some given points of the heterostructure. Therefore, the annealing can widen the bubble free regions in the stack as shown in Fig. 12.10. The results are unfortunately uncertain because of the random motion of the bubbles. The annealing can have simply no effect or sometimes it can even damage the heterostructure. Consequently, this step might be repeated several times with different conditions (final temperature of the substrate, time of heating, time of prior pumping, transient regime, etc.) before obtaining a suitable result. In our set-up, these conditions are tuned using a homemade computer software which allows to change the instantaneous power applied on the lamp at a given time of the process.

12.2.2 Lithographic processing and fabrication of the QH FP interferometers

After annealing, the stack can be processed and transformed into a graphene QH FP interferometer. The nanofabrication process involves several electron beam lithography steps that are discussed in next paragraphs. They are performed using a dedicated and commercial apparatus working with a beam voltage of 80 kV and with an interferometric platform. It allows to design features with a spatial resolution below a few tenths of nanometers and to align the structures made during different steps with a precision better than a hundred of nanometers. Such performances allow us to have a good reliability in the fabrication of the interferometers.

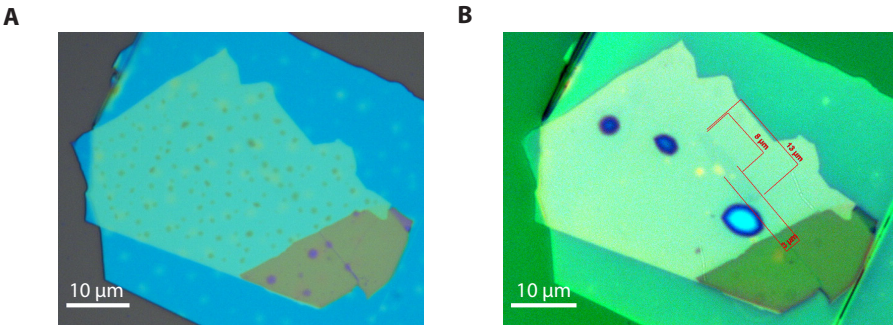

FIGURE 12.10: **Annealing of Van der Waals heterostructures.** Images of a heterostructure before and after annealing. **A**, Before annealing, many bubbles are trapped between the different flakes or between the flakes and the substrate preventing from finding a bubble free area. **B**, After annealing, some of bubbles have been released outside the stack and others have merged into larger bubbles leaving nearly bubble free areas (the substrate is covered with PMMA resist to facilitate to localization of the graphene in the heterostructure).

Markerfield and pads

To place precisely the gates and the contacts of the interferometer, the exact position of the graphene in the substrate must be known very accurately. Thus, we make a first lithography step which consists in metallizing a fields of square markers in the overall sample. They form an array and define a set of Cartesian coordinates on the substrate which can be used to locate structures or flakes on its surface. These marks are used to align the electron beam during the exposure. They are also use to incorporate precisely optical images of the substrate and of the stack in the lithography design software. It allows to place accurately the different structures in the interferometer design and to insolate the resist at the good positions in other lithography steps. The precision in the positioning of the structures is about two hundred nanometers and is mainly limited by the resolution of the images.

In the same step, we usually define and deposit also metallic pads, with typical dimensions of a few hundred of microns, which will be use for the wire bonding of the sample.

Contacts fabrication

The electrical contacts are made in a second lithography step. We begin by taking optical images of heterostructure that are processed to enhance the visibility of the graphene and we integrate them to the lithographic design. Thanks to them, we can place precisely the contacts above the graphene edges in the lithography design. These contacts are separated in two sets and we purposely leave a free area between both sets where the gates of the interferometers will be deposited on a later step. We designed the lines connecting the contacts to the pads in the same time. The lithography is performed and after the development, we etch the heterostructure directly in the PMMA lines using a reactive ion etching machine with CHF_3/O_2 mixture. The etching time is adapted to etch fully the capping h-BN and uncover the graphene edges without etching completely the bottom h-BN (a prior AFM imaging of the individual flakes or the overall stack is required to know their thickness). Immediately after the etching, a Cr/Au bilayer is deposited using high vacuum ebeam evaporation to make good one dimensional electrical contacts [33].

Note that contrary to the original process proposed by Wang *et al.* [33], our contacts are made in a single lithographic step and without the use of a hardened HSQ resist mask. It drastically limits the risk to contaminate of the graphene edges which are exposed after etching and it allows

to improve the reliability of the contact process. An example of such contact fabrication is shown in Fig. 12.11.

On the other hand, the regularity and the reproducibly of the etching process are critical. The etching rate must be known precisely to adapt the etching time finely for each heterostructure. Any under-etching would result in absence of electrical contact while any over-etching would lead to gate leakages in devices with a graphite back gate. Consequently, during this thesis, the parameters of the etching program (gas flow, pressure, applied RF power, etc.) were carefully optimized to improve the reliability of the contact processing.

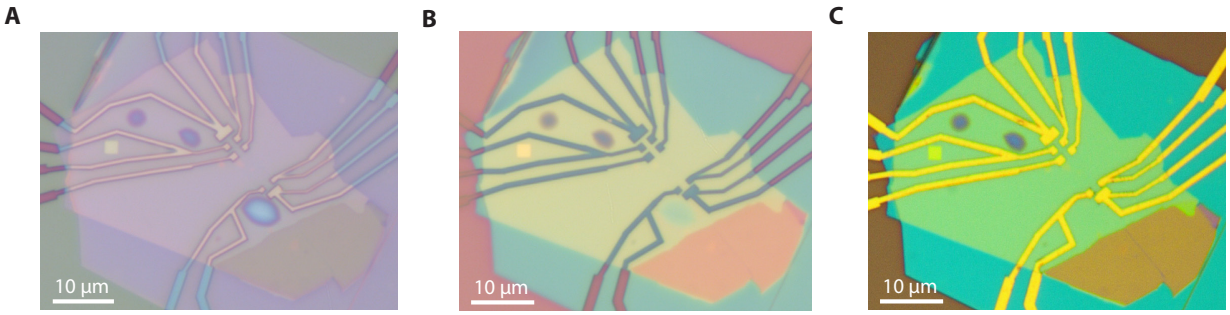

FIGURE 12.11: **Contact lithography.** **A**, Optical image of a device after development of the lithography performed to define the contacts. **B**, Optical image of the device after plasma etching of the heterostructure in the resist lines. Note the color difference between the lines passing only on capping h-BN (pink) and lines passing on top of the complete stack (blue). It shows the fine tuning of the etching time which is sufficient to uncover the graphene edges without etching the entire heterostructure. **C**, Optical image of the device after deposition of a Cr/Au bilayer in the resist lines after etching.

QPCs and gates fabrication

The final step consists in depositing the different gates of the interferometer. The procedure is similar to the one described in previous paragraph although there is no etching of the stack at this step. Using images of the heterostructure, we place the QPCs in the lithography design in the free space between the two sets of contacts.

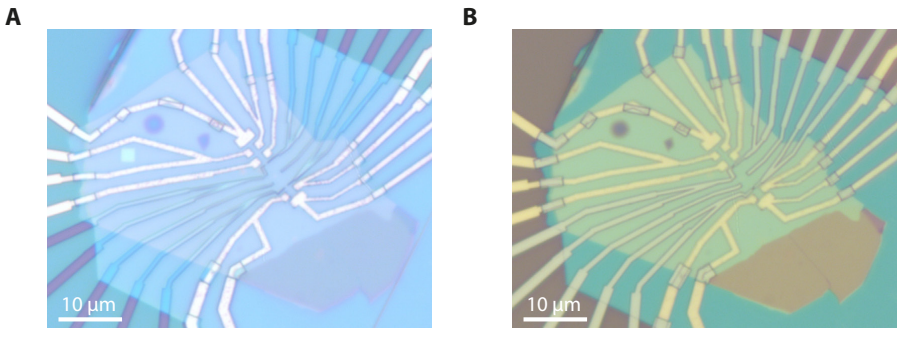

FIGURE 12.12: **Gate lithography.** **A**, Optical image of a device after development of the lithography performed to define the gates. **B**, Optical image of the device after deposition of the palladium gates in the resist lines.

The size of the gap is chosen depending on the type of device : typically 100 to 200 nm for the devices with a SiO_2 back gate and 20 to 60 nm for the devices with a graphite back gate. The position of the plunger gates is more carefully adjusted above the edges of the graphene flake: we

make sure that their extremity goes only a few hundreds of nanometers beyond the edges. The shape and the position of the gate electrodes can be changed to cover bubbles trapped nearby the graphene edges and to limit their effect on the electron transport in the graphene. After exposure and development, the gates are directly deposited atop the capping h-BN by ebeam evaporation in the resist lines. An example of such gate fabrication is shown in Fig. 12.12.

The choice of the metal used to make the gates is crucial: it determines the resolution of the gaps we can achieve and the reproducibility we have on it. After different tests, we decided to use palladium rather than gold to make our electrostatic gates. This metal has different advantages. It sticks well to h-BN flakes, even without an adhesion layer, and it does not oxidise. Importantly, the palladium grains formed during the ebeam evaporation are small compared to that of other metal like gold. They have a typical diameter of 10-20 nm, and they form a continuous film which allows to have clean and well-defined gate edges as shown in Fig. 12.13. This helps limiting equilibration at the pn junctions. This reduced granularity also allows to obtain QPC gaps below 60 nm with a limited risk of having a metal particle at the apex of one electrode. The latter would spoil the operation of the QPC.

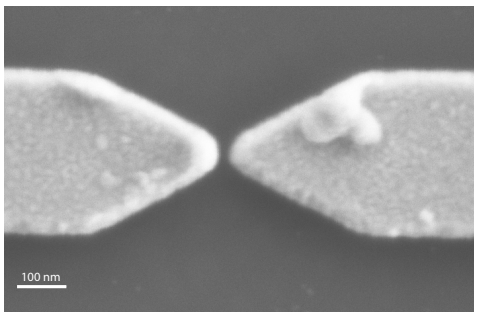

FIGURE 12.13: **Palladium QPC.** Scanning electron micrograph of a palladium QPC. The gap between the electrodes is 20 nm. The metal has a reduced granularity and forms a nearly continuous film. The edges of the electrodes are clean and clearly defined limiting equilibration.

Bibliography

1. Von Klitzing K., Dorda, G. & Pepper, M. New Method for High-Accuracy Determination of the Fine-Structure Constant Based on Quantized Hall Resistance. *Phys. Rev. Lett.* **45,** 494–497 (1980).
2. Tsui, D. C., Stormer, H. L. & Gossard, A. C. Two-Dimensional Magnetotransport in the Extreme Quantum Limit. *Phys. Rev. Lett.* **48,** 1559–1562 (1982).
3. Laughlin, R. B. Anomalous Quantum Hall Effect: An Incompressible Quantum Fluid with Fractionally Charged Excitations. *Phys. Rev. Lett.* **50,** 1395 (1983).
4. Halperin, B. I. Statistics of quasiparticles and the hierarchy of fractional quantized hall states. *Phys. Rev. Lett.* **52,** 1583–1586 (1984).
5. Arovas, D., Schrieffer, J. R. & Wilczek, F. Fractional statistics and the quantum Hall effect. *Phys. Rev. Lett.,* 722–723 (1984).
6. Sondh, S. L., Karlhede, A., Kivelson, S. A. & Rezayi, E. H. Skyrmions and the crossover from the integer to fractional quantum Hall effect at small Zeeman energies. *Phys. Rev. B* **47,** 16419 (1993).
7. Novoselov, K. S. *et al.* Electric Field Effect in Atomically Thin Carbon Films. *Science* **306,** 666–669 (2004).
8. Novoselov, K. S. *et al.* Two-dimensional gas of massless Dirac fermions in graphene. *Nature* **438,** 197–200 (2005).
9. Zhang, Y., Tan, Y. W., Stormer, H. L. & Kim, P. Experimental observation of the quantum Hall effect and Berry's phase in graphene. *Nature* **438,** 201–204 (2005).
10. Du, X., Skachko, I., Duerr, F., Luican, A. & Andrei, E. Y. Fractional quantum Hall effect and insulating phase of Dirac electrons in graphene. *Nature* **462,** 192–195 (2009).
11. Bolotin, K. I., Ghahari, F., Shulman, M. D., Stormer, H. L. & Kim, P. Observation of the fractional quantum Hall effect in graphene. *Nature* **462,** 196–199 (2009).
12. Dean, C. R. *et al.* Multicomponent fractional quantum Hall effect in graphene. *Nature Physics* **7,** 693–696 (2011).
13. Young, A. F. *et al.* Spin and valley quantum Hall ferromagnetism in graphene. *Nature Physics* **8,** 550–556 (2012).
14. Hunt, B. *et al.* Massive Dirac Fermions and Hofstadter Butterfly in a van der Waals Heterostructure. *Science* **340,** 1427–1430 (2013).
15. Amet, F. *et al.* Supercurrent in the quantum Hall regime. *Science* **352,** 966–969 (2016).
16. Zimmermann, K. *et al.* Tunable transmission of quantum Hall edge channels with full degeneracy lifting in split-gated graphene devices. *Nature Communications* **8,** 14983 (2017).
17. Castro Neto, A. H., Guinea, F., Peres, N. M. R., Novoselov, K. S. & Geim, A. K. The electronic properties of graphene. *Rev. Mod. Phys.* **81,** 109–162 (2009).
18. Goerbig, M. O. Electronic properties of graphene in a strong magnetic field. *Rev. Mod. Phys.* **83,** 1193–1243 (2011).

19. Goerbig, M. O. The quantum Hall effect in graphene – a theoretical perspective. *Comptes Rendus Physique* **12,** 369–378 (2011).
20. Coissard, A. The many-body ground states of the graphene quantum Hall effect and their edge channels. *PhD thesis, Université Grenoble Alpes* (2021).
21. Laughlin, R. B. Quantized Hall conductivity in two dimensions. *Phys. Rev. B* **23,** 5632 (1981).
22. Halperin, B. I. Quantized Hall conductance, current-carrying edge states, and the existence of extended states in a two-dimensional disordered potential. *Phys. Rev. B* **25,** 2185 (1982).
23. Brey, L. & Fertig, H. A. Edge states and the quantized Hall effect in graphene. *Phys. Rev. B* **73,** 195408 (2006).
24. Abanin, D. A., Lee, P. A. & Levitov, L. S. Spin-Filtered Edge States and Quantum Hall Effect in Graphene. *Phys. Rev. Lett.* **96,** 176803 (2006).
25. Abanin, D. A., Lee, P. A. & Levitov, L. S. Charge and spin transport at the quantum Hall edge of graphene. *Solid State Communications* **143,** 77–85 (2007).
26. Abanin, D. A. *et al.* Dissipative Quantum Hall Effect in Graphene near the Dirac Point. *Phys. Rev. Lett.* **98,** 196806 (2007).
27. Fertig, H. A. & Brey, L. Luttinger Liquid at the Edge of Undoped Graphene in a Strong Magnetic Field. *Phys. Rev. Lett.* **97,** 116805 (2006).
28. Delplace, P. & Montambaux, G. WKB analysis of edge states in graphene in a strong magnetic field. *Phys. Rev. B* **82,** 205412 (2010).
29. Büttiker, M. Absence of backscattering in the quantum Hall effect in multiprobe conductors. *Phys. Rev. B* **38,** 9375–9389 (1988).
30. Gusynin, V. P. & Sharapov, S. Unconventional Integer Quantum Hall Effect in Graphene. *Phys. Rev. Lett.* **95,** 146801 (2005).
31. Novoselov, K. S. *et al.* Room-Temperature Quantum Hall Effect in Graphene. *Science* **315,** 1379 (2007).
32. Dean, C. R. *et al.* Boron nitride substrates for high-quality graphene electronics. *Nature Nanotechnology* **5,** 722–726 (2010).
33. Wang, L. *et al.* One-Dimensional Electrical Contact to a Two-Dimensional Material. *Science* **342,** 614–617 (2013).
34. Girvin, S. M. *Les Houches Lecture Notes : Topological Aspects of Low Dimensional Systems* (eds A., C., T., J., S., O. & F., D.) chap. The Quantum Hall Effect : novel excitations and broken symmetries (Springer, 2000).
35. Alicea, J. & Fisher, M. P. A. Graphene integer quantum Hall effect in the ferromagnetic and paramagnetic regimes. *Phys. Rev. B* **74,** 075422 (2006).
36. Kharitonov, M. Phase diagram for the $\nu = 0$ quantum Hall state in monolayer graphene. *Phys. Rev. B* **85,** 155439 (2012).
37. Nomura, K. & MacDonald, A. H. Quantum Hall Ferromagnetism in Graphene. *Phys. Rev. Lett.* **96,** 256602 (2006).
38. Zhang, Y. *et al.* Landau-Level Splitting in Graphene in High Magnetic Fields. *Phys. Rev. Lett.* **96,** 136806 (2006).
39. Jiang, Z., Zhang, Y., Stormer, H. L. & Kim, P. Quantum Hall States near the Charge-Neutral Dirac Point in Graphene. *Phys. Rev. Lett.* **99,** 106802 (2007).
40. Alicea, J. & Fisher, M. P. A. Interplay between lattice-scale physics and the quantum Hall effect in graphene. *Solid State Communications* **143,** 504–509 (2007).

41. Jung, J. & MacDonald, A. H. Theory of the magnetic-field-induced insulator in neutral graphene sheets. *Phys. Rev. B* **80,** 235417 (2009).
42. Herbut, I. F. Theory of integer quantum Hall effect in graphene. *Phys. Rev. B* **75,** 165411 (2007).
43. Goerbig, M. O., Moessner, R. & Douçot, B. Electron interactions in graphene in a strong magnetic field. *Phys. Rev. B* **74,** 161407 (2006).
44. Ajiki, H. & Ando, T. Lattice Distorsion of Metallic Carbon Nanotubes Induced by Magnetic Fields. *Journal of the Physical Society of Japan* **64,** 260–267 (1995).
45. Hou, C. Y., Chamon, C. & Mudry, C. Electron Fractionalization in Two-Dimensional Graphene-like Structures. *Phys. Rev. Lett.* **98,** 186809 (2007).
46. Nomura, K., Ryu, S. & Lee, D. H. Field-Induced Kosterlitz-Thouless Transition in the $N = 0$ Landau Level of Graphene. *Phys. Rev. Lett.* **103,** 216801 (2009).
47. Hou, C. Y., Chamon, C. & Mudry, C. Deconfined fractional electric charges in graphene at high magnetic fields. *Phys. Rev. B* **81,** 075427 (2010).
48. Basko, D. M. & Aleiner, I. L. Interplay of Coulomb and electron-phonon interactions in graphene. *Phys. Rev. B* **77,** 041409 (2008).
49. Fuchs, J. N. & Lederer, P. Spontaneous Parity Breaking of Graphene in the Quantum Hall Regime. *Phys. Rev. Lett.* **98,** 016803 (2007).
50. Yang, K., Das Sarma, S. & MacDonald, A. H. Collective modes and skyrmion excitations in graphene $SU(4)$ quantum Hall ferromagnets. *Phys. Rev. B* **74,** 075423 (2006).
51. Kane, C. L. & Mele, E. J. Quantum Spin Hall Effect in Graphene. *Phys. Rev. Lett.* **95,** 226801 (2005).
52. Kane, C. L. & Mele, E. J. $\mathbb{Z}_2$ Topological Order and the Quantum Spin Hall Effect. *Phys. Rev. Lett.* **95,** 146802 (2005).
53. Bernevig, B. A., Hughes, T. L. & Zhang, S.-C. Quantum Spin Hall Effect and Topological Phase Transition in HgTe Quantum Wells. *Science* **314,** 1757–1761 (2006).
54. Hasan, M. Z. & Kane, C. L. Colloquium: Topological insulators. *Rev. Mod. Phys.* **82,** 3045–3067 (2010).
55. Qi, X. L. & Zhang, S. C. The quantum spin Hall effect and topological insulators. *Physics Today.* **63,** 33–38 (2010).
56. König, M. *et al.* Quantum Spin Hall Insulator State in HgTe Quantum Wells. *Science* **318,** 766–770 (2007).
57. Knez, I., Du, R.-R. & Sullivan, G. Evidence for Helical Edge Modes in Inverted InAs/GaSb Quantum Wells. *Phys. Rev. Lett.* **107,** 136603 (2011).
58. Wu, S. *et al.* Observation of the quantum spin Hall effect up to 100 kelvin in a monolayer crystal. *Science* **359,** 76–79 (2018).
59. Hatsuda, K. *et al.* Evidence for a quantum spin Hall phase in graphene decorated with Bi2Te3 nanoparticles. *Science Advances* **4,** eaau6915 (2018).
60. Roth, A. *et al.* Nonlocal Transport in the Quantum Spin Hall State. *Science* **325,** 294–297 (2009).
61. Young, A. F. *et al.* Tunable symmetry breaking and helical edge transport in a graphene quantum spin Hall state. *Nature* **505,** 528–532 (2014).
62. Pesin, D. & MacDonald, A. H. Spintronics and pseudospintronics in graphene and topological insulators. *Nature Materials* **11,** 409–416 (2012).

63. Qi, X.-L. & Zhang, S.-C. Topological insulators and superconductors. *Rev. Mod. Phys.* **83,** 1057–1110 (2011).
64. Mi, S., Pikulin, D. I., Wimmer, M. & Beenakker, C. W. J. Proposal for the detection and braiding of Majorana fermions in a quantum spin Hall insulator. *Phys. Rev. B* **87,** 241405 (2013).
65. Barlas, Y., Yang, K. & MacDonald, A. H. Quantum Hall effects in graphene-based two-dimensional electron systems. *Nanotechnology* **23,** 052001 (2012).
66. Herbut, I. F. SO(3) symmetry between Néel and ferromagnetic order parameters for graphene in a magnetic field. *Phys. Rev. B* **76,** 085432 (2007).
67. Kharitonov, M. Edge excitations of the canted antiferromagnetic phase of the $\nu = 0$ quantum Hall state in graphene: A simplified analysis. *Phys. Rev. B* **86,** 075450 (2012).
68. Gusynin, V. P., Miransky, V. A. M., Sharapov, S., Shovkovy, A. & Wyenberg, C. M. Edge states on graphene ribbons in magnetic field: Interplay between Dirac and ferromagnetic-like gaps. *Phys. Rev. B* **79,** 115431 (2009).
69. Wu, F., Sodemann, I., Araki, Y., MacDonald, A. H. & Jolicoeur, T. SO(5) symmetry in the quantum Hall effect in graphene. *Phys. Rev. B* **90,** 235432 (2014).
70. Atteia, J., Lian, Y. & Goerbig, M. O. Skyrmion zoo in graphene at charge neutrality in a strong magnetic field. *Phys. Rev. B,* 035403 (2021).
71. Tikhonov, P., Shimshoni, E., Fertig, H. A. & Murthy, G. Emergence of helical edge conduction in graphene at the $\nu = 0$ quantum Hall state. *Phys. Rev. B* **93,** 115137 (2016).
72. Murthy, G., Shimshoni, E. & Fertig, H. A. Collective edge modes near the onset of a graphene quantum spin Hall state. *Phys. Rev. B* **90,** 241410 (2014).
73. Knothe, A. & Jolicoeur, T. Edge structure of graphene monolayers in the $\nu = 0$ quantum Hall state. *Phys. Rev. B* **92,** 165110 (2015).
74. Kharitonov, M., Juergens, S. & Trauzettel, B. Interplay of topology and interactions in quantum Hall topological insulators: U(1) symmetry, tunable Luttinger liquid, and interaction-induced phase transitions. *Phys. Rev. B* **94,** 035146 (2016).
75. Knothe, A. Quantum Hall Ferromagnetism in Multicomponent Systems. *PhD thesis, Université Paris-Saclay* (2017).
76. Amet, F. *et al.* Composite fermions and broken symmetries in graphene. *Nature Communications* **6,** 5838 (2015).
77. Wei, D. S. *et al.* Electrical generation and detection of spin waves in a quantum Hall ferromagnet. *Science* **362,** 229–233 (2018).
78. Li, S. Y., Yin, L. J. & He, L. Scanning tunneling microscope study of quantum Hall isospin ferromagnetic states in the zero Landau level in a graphene monolayer. *Phys. Rev. B* **100,** 085437 (2019).
79. Barcellona, P., Bennett, R. & Buhmann, S. Y. Manipulating the Coulomb interaction: a Green's function perspective. *Journal of Physics Communications* **2,** 035027 (2018).
80. Hemberger, J. *et al.* Quantum paraelectric and induced ferroelectric states in $SrTiO_3$. *J. Phys. Condens. Matter* **8,** 4673–4690 (1996).
81. Müller, K. A. & Burkard, H. $SrTiO_3$: An intrinsic quantum paraelectric below 4 K. *Phys. Rev. B* **19,** 3593–3602 (1979).
82. Sakudo, T. & Unoki, H. Dielectric Properties of $SrTiO_3$ at Low Temperatures. *Phys. Rev. Lett.* **26,** 851–853 (1971).
83. Kawasaki, M. *et al.* Atomic Control of the $SrTiO_3$ Crystal Surface. *Science* **266,** 1540–1542 (1994).

84. Scott, J. F., Salje, E. K. H. & Carpenter, M. A. Domain Wall Damping and Elastic Softening in $SrTiO_3$: Evidence for Polar Twin Walls. *Phys. Rev. Lett.* **109,** 187601 (2012).
85. Salje, E. K. H., Aktas, O., Carpenter, M. A., Laguta, V. V. & Scott, J. F. Domains within Domains and Walls within Walls: Evidence for Polar Domains in Cryogenic $SrTiO_3$. *Phys. Rev. Lett.* **111,** 247603 (2013).
86. Honig, M. *et al.* Local electrostatic imaging of striped domain order in $LaAlO_3/SrTiO_3$. *Nature Materials* **12,** 1112–1118 (2013).
87. Harsan Ma, H. J. *et al.* Local Electrical Imaging of Tetragonal Domains and Field-Induced Ferroelectric Twin Walls in Conducting $SrTiO_3$. *Phys. Rev. Lett.* **116,** 257601 (2016).
88. Frenkel, Y. *et al.* Imaging and tuning polarity at $SrTiO_3$ domain walls. *Nature Materials* **16,** 1203–1208 (2017).
89. Sachs, R., Lin, Z. & Shi, J. Ferroelectric-like $SrTiO_3$ surface dipoles probed by graphene. *Scientific Reports* **4,** 3657 (2014).
90. Hemberger, J., Lunkenheimer, P., Viana, R., Böhmer, R. & Loidl, A. Electric-field-dependent dielectric constant and nonlinear susceptibility in $SrTiO_3$. *Phys. Rev. B* **52,** 13159 (1995).
91. Protogenov, A. P., Verbus, V. A. & Chulkov, E. V. Nonlocal edge state transport in topological insulators. *Phys. Rev. B* **88,** 195431 (2013).
92. Abanin, D. A. *et al.* Giant Nonlocality Near the Dirac Point in Graphene. *Science* **332,** 328–330 (2011).
93. Polshyn, H. *et al.* Quantitative Transport Measurements of Fractional Quantum Hall Energy Gaps in Edgeless Graphene Devices. *Phys. Rev. Lett.* **121,** 226801 (2018).
94. Zeng, Y. *et al.* High-Quality Magnetotransport in Graphene Using the Edge-Free Corbino Geometry. *Phys. Rev. Lett.* **122,** 137701 (2019).
95. Lado, J. L. & Fernández-Rossier, J. Noncollinear magnetic phases and edge states in graphene quantum Hall bars. *Phys. Rev. B* **90,** 165429 (2014).
96. Huang, C. & Cazalilla, A. Disorder effects on helical edge transport in graphene under strong titlted magnetic field. *Phys. Rev. B* **92,** 155124 (2015).
97. Wu, C., Bernevig, B. A. & Zhang, S.-C. Helical Liquid and the Edge of Quantum Spin Hall Systems. *Phys. Rev. Lett.* **96,** 106401 (2006).
98. San-Jose, P., Lado, J. L., Aguado, R., Guinea, F. & Fernández-Rossier, J. Majorana Zero Modes in Graphene. *Phys. Rev. X* **5,** 041042 (2015).
99. Feldman, D. E. & Halperin, B. I. Fractional Charge and Fractional Statistics in the Quantum Hall Effects. *arXiv,* 2102.08998 (2021).
100. Leinaas, J. M. & Myrheim, J. On the theory of identical particles. *Il Nuovo Cimento B* **37 B,** 1–23 (1977).
101. Wilczek, F. Quantum Mechanics of Fractional-Spin Particless. *Phys. Rev. Lett.* **49,** 957–959 (1982).
102. Stern, A. Anyons and the quantum Hall effect - A pedagogical review. *Annals of Physics* **323,** 204–249 (2008).
103. Nayak, C., Simon, S., Stern, A., Freedman, M. & Das Sarma, S. Non-Abelian anyons and topological quantum computation. *Rev. Mod. Phys.* **80,** 1083–1159 (2008).
104. Kitaev, A. Y. Fault-Tolerant Quantum Computation by Anyons. *Ann. Phys.* **303,** 2 (2003).
105. Su, W. P. Statistics of the fractionally charged excitations in the quantum Hall effect. *Phys. Rev. B* **34,** 1031–1033 (1986).

106. Blok, B. & Wen, X. G. Effective theories of the fractional quantum Hall effect: Hierarchy construction. *Phys. Rev. B* **42,** 8145 (1990).

107. Blok, B. & Wen, X. G. Effective theories of the fractional quantum Hall effect at generic filling fractions. *Phys. Rev. B* **42,** 8133 (1990).

108. Wen, X. G. & Zee, A. Classification of Abelian quantum Hall states and matrix formulation of topological fiuids. *Phys. Rev. Lett.* **46,** 2290–2301 (1992).

109. Jeon, G. S., Graham, K. L. & Jain, J. K. Fractional Statistics in the Fractional Quantum Hall Effect. *Phys. Rev. Lett.* **91,** 036801 (2003).

110. Haldane, F. D. M. Fractional quantization of the Hall effect : A hierarchy of incompressible quantum fluid states. *Phys. Rev. Lett.* **51,** 605–608 (1983).

111. Jain, J. K. Composite-fermion approach for the fractional quantum Hall effect. *Phys. Rev. Lett.* **63,** 199–202 (1989).

112. Jain, J. K. Theory of the fractional Quantum Hall effect. *Phys. Rev. B* **41,** 7653–7665 (1990).

113. Ezawa, Z. F. *Quantum Hall Effects Recent Theoretical and Experimental Developments* (World Scientific, 2013).

114. Tong, D. Lectures on the Quantum Hall Effect. https://arxiv.org/abs/1606.06687.

115. Hansson, T. H., Hermanns, M., Simon, S. H. & Viefers, S. F. Quantum Hall physics: Hierarchies and conformal field theory techniques. *Reviews of Modern Physics* **89,** 025005 (2017).

116. Stormer, H. L. *et al.* Fractional Quantization of the Hall Effect. *Phys. Rev. Lett.* **24,** 1953–1956 (1983).

117. Willett, R. L. *et al.* Observation of an even-denominator quantum number in the fractional quantum Hall effect. *Phys. Rev. Lett.* **59,** 1776–1779 (2013).

118. Moore, G. & Read, N. Nonabelions in the fractional quantum hall effect. *Nuclear Physics B* **360,** 362–396 (1991).

119. Freedman, M., Nayak, C. & Walker, K. Towards universal topological quantum computation in the $\nu = \frac{5}{2}$ fractional quantum Hall state. *Phys. Rev. B* **73,** 245307 (2006).

120. Bravyi., S. Universal quantum computation with the $\nu = \frac{5}{2}$ fractional quantum Hall state. *Phys. Rev. A* **73,** 042313 (2006).

121. Eisenstein, J. P., Cooper, K. B., Pfeiffer, L. N. & W., W. K. Insulating and Fractional Quantum Hall States in the First Excited Landau Level. *Phys. Rev. Lett.* **88,** 076801 (2002).

122. Stormer, H. L. Two-dimensional electron correlation in high magnetic fields. *Physica B* **177,** 401–408 (1992).

123. Pan, W. *et al.* Exact Quantization of the Even-Denominator Fractional Quantum Hall State at $\nu = 5/2$ Landau Level Filling Factor. *Phys. Rev. Lett.* **83,** 3530 (1999).

124. Wen, X. G. Chiral Luttinger liquid and the edge excitations in the fractional quantum Hall states. *Phys. Rev. B* **41,** 12838–12844 (1990).

125. MacDonald, A. H. Edge states in the fractional-quantum-Hall-effect regime. *Phys. Rev. Lett.* **64,** 220–223 (1990).

126. Beenakker, C. W. J. Edge channels for the fractional quantum Hall effect. *Phys. Rev. Lett.* **64,** 216–219 (1990).

127. Kane, C. L. & Fisher, M. P. A. *Perspectives in Quantum Hall Effects: Novel Quantum Liquids in Low-Dimensional Semiconductor Structures* chap. Chapter 4: Edge-state transport (Wiley, New York, 1975).

128. Kane, C. L. & Fisher, M. P. A. Contacts and edge-state equilibration in the fractional quantum Hall effect. *Phys. Rev. B* **52,** 17393–17405 (1995).

129. Büttiker, M. Quantized transmission of a saddle-point constriction. *Phys. Rev. B* **41,** 7906–7909 (1990).

130. Kane, C. L. & Fisher, M. P. A. Nonequilibrium noise and fractional charge in the quantum Hall effect. *Phys. Rev. Lett.* **72,** 724 (1994).

131. Chamon, C., Freed, D. E. & Wen, X. G. Tunneling and quantum noise in one-dimensional Luttinger liquids. *Phys. Rev. B* **51,** 2363–2380 (1995).

132. de-Picciotto, R. *et al.* Direct observation of a fractional charge. *Nature* **389,** 162–164 (1997).

133. Saminadayar, L., Glattli, D. C., Jin, Y. & Etienne, B. Observation of the $e/3$ Fractionally Charged Laughlin Quasiparticle. *Phys. Rev. Lett.* **79,** 2526–2529 (1997).

134. Bid, A., Ofek, N., Heiblum, M., Umansky, V. & Mahalu, D. Shot Noise and Charge at the $2/3$ Composite Fractional Quantum Hall State. *Phys. Rev. Lett.* **103,** 236802 (2009).

135. Heiblum, M. *Perspectives of Mesoscopic Physics: Dedicated to Yoseph Imry's 70th Birthday* 115–135 (Wiley, New York, 2010).

136. Dolev, M., Heiblum, M., Umansky, V., Stern, A. & Mahalu, D. Observation of a quarter of an electron charge at the $nu = 5/2$ quantum Hall state. *Nature* **452,** 829–834 (2008).

137. Safi, I., Devillard, P. & Martin, T. Partition Noise and Statistics in the Fractional Quantum Hall Effect. *Phys. Rev. Lett.* **86,** 4628–4631 (2001).

138. Kim, E., Lawler, M., Vishveshwara, S. & Fradkin, E. Signatures of Fractional Statistics in Noise Experiments in Quantum Hall Fluids. *Phys. Rev. Lett.* **95,** 176402 (2005).

139. Rosenow, B., Levkivskyi, I. P. & Halperin, B. I. Current Correlations from a Mesoscopic Anyon Collider. *Phys. Rev. Lett.* **116,** 156802 (2016).

140. Bartolomei, H. *et al.* Fractional statistics in anyon collisions. *Science* **368,** 173–177 (2020).

141. Banerjee, M. *et al.* Observation of half-integer thermal Hall conductance. *Nature* **559,** 205–210 (2018).

142. Mills, S. M., Averin, D. V. & Du, X. Localizing Fractional Quasiparticles on Graphene Quantum Hall Antidots. *Phys. Rev. Lett.* **125,** 227701 (2020).

143. Chamon, C., Freed, D. E., Kivelson, S. A., Sondhi, S. L. & Wen, X. G. Two point-contact interferometer for quantum Hall systems. *Phys. Rev. B* **55,** 2331–2343 (1997).

144. McClure, D. T., Chang, W., Marcus, C. M., Pfeiffer, L. N. & West, K. Fabry-Perot Interferometry with Fractional Charges. *Phys. Rev. Lett.* **108,** 256804 (2012).

145. Van Wees, B. J. *et al.* Anomalous integer quantum Hall effect in the ballistic regime with quantum point contacts. *Phys. Rev. Lett.* **62,** 1181–1184 (1989).

146. Ji, Y. *et al.* An electronic Mach-Zehnder interferometer. *Nature* **422,** 415–418 (2003).

147. Zhang, Y. *et al.* Distinct signatures for Coulomb blockade and Aharonov-Bohm interference in electronic Fabry-Perot interferometers. *Phys. Rev. B* **79,** 241304 (2009).

148. Halperin, B., Stern, A., Neder, I. & Rosenow, B. Theory of the Fabry-Pérot quantum Hall interferometer. *Phys. Rev. B* **83,** 155440 (2011).

149. Sivan, I. *et al.* Observation of interaction-induced modulations of a quantum Hall liquid's area. *Nature Communications* **7,** 12184 (2016).

150. Stern, A. & Halperin, B. Proposed Experiments to Probe the Non-Abelian $\nu = 5/2$ Quantum Hall State. *Phys. Rev. Lett.* **96,** 016802 (2006).

151. Nakamura, J., Liang, S., Gardner, G. & Manfra, M. Direct observation of anyonic braiding statistics. *Nature Physics* **16,** 931–936 (2020).

152. Bonderson, P., Kitaev, A. & Shtengel, K. Detecting Non-Abelian Statistics in the $\nu = 5/2$ Fractional Quantum Hall State. *Phys. Rev. Lett.* **96,** 016803 (2006).

153. Bonderson, P., Shtengel, K. & Slingerland, J. K. Probing Non-Abelian Statistics with Quasiparticle Interferometry. *Phys. Rev. Lett.* **97,** 016401 (2006).

154. Bishara, W. & Nayak, C. Odd-even crossover in a non-Abelian ν=5/2 interferometer. *Phys. Rev. B* **80,** 155304 (2009).

155. Bishara, W., Bonderson, P., Nayak, C., Shtengel, K. & Slingerland, J. K. Interferometric signature of non-Abelian anyons. *Phys. Rev. B* **80,** 155303 (2009).

156. Van Wees, B. J. *et al.* Observation of zero-dimensional states in a one-dimensional electron interferometer. *Phys. Rev. Lett.* **62,** 2523–2526 (1989).

157. Taylor, R. P., Sachrajda, A. S., Zawadzki, P., Coleridge, P. T. & Adams, J. A. Aharonov-Bohm Oscillations in the Coulomb Blockade Regime. *Phys. Rev. Lett.* **69,** 1989–1993 (1992).

158. Bird, J. P., Ishibashi, K., Aoyagi, Y. & Sugano, T. Precise period doubling of the Aharonov-Bohm effect in a quantum dot at high magnetic fields. *Phys. Rev. B* **53,** 3642–3645 (1996).

159. Camino, F. E., Zhou, W. & Goldman, V. J. Aharonov-Bohm Superperiod in a Laughlin Quasiparticle Interferometer. *Phys. Rev. Lett.* **95,** 246802 (2005).

160. Camino, F. E., Zhou, W. & Goldman, V. J. Aharonov-Bohm electron interferometer in the integer quantum Hall regime. *Phys. Rev. B* **72,** 155313 (2005).

161. Camino, F. E., Zhou, W. & Goldman, V. J. Quantum transport in electron Fabry-Perot interferometers. *Phys. Rev. B* **76,** 155305 (2007).

162. Rosenow, B. & Halperin, B. I. Influence of Interactions on Flux and Back-Gate Period of Quantum Hall Interferometers. *Phys. Rev. Lett.* **98,** 106801 (2007).

163. Chklovskii, D. B., Shklovskii, B. I. & Glazman, L. I. Electrostatics of edge channels. *Phys. Rev. B* **46,** 4026–4034 (1992).

164. Ofek, N. *et al.* Role of interactions in an electronic Fabry-Perot interferometer operating in the quantum Hall effect regime. *PNAS* **107,** 5276–5281 (2010).

165. Ngo Dinh, S. & Bagrets, D. A. Influence of Coulomb interaction on the Aharonov-Bohm effect in an electronic Fabry-Pérot interferometer. *Phys. Rev. B* **85,** 073403 (2012).

166. Choi, H. K. *et al.* Robust electron pairing in the integer quantum hall effect regime. *Nature Communications* **6,** 7435 (2015).

167. Nakamura, J. *et al.* Aharonov-Bohm interference of fractional quantum Hall edge modes. *Nature Physics* **15,** 563–569 (2019).

168. Camino, F. E., Zhou, W. & Goldman, V. J. $e/3$ Laughlin Quasiparticle Primary-Filling $\nu = 1/3$ Interferometer. *Phys. Rev. Lett.* **98,** 076805 (2007).

169. Camino, F. E., Zhou, W. & Goldman, V. J. Transport in the Laughlin quasiparticle interferometer: Evidence for topological protection in an anyonic qubit. *Phys. Rev. B* **74,** 115301 (2006).

170. Röösli, M. P. *et al.* Fractional Coulomb blockade for quasiparticle tunneling between edge channels. *arXiv,* 2005.12723 (2020).

171. Rosenow, B. & Stern, A. Flux Superperiods and Periodicity Transitions in Quantum Hall Interferometers. *Phys. Rev. Lett.* **124,** 106805 (2020).

172. Kane, C. L., Fisher, M. P. A. & Polchinski, J. Randomness at the edge: theory of quantum Hall transport at filling $\nu = 2/3$. *Phys. Rev. Lett.* **72,** 4129–4132 (1994).

173. Sabo, R. *et al.* Edge reconstruction in fractional quantum Hall states. *Nature Physics* **13,** 491–496 (2017).

174. Willett, R. L., Pfeiffer, L. N. & West, K. W. Measurement of filling factor 5/2 quasiparticle interference with observation of charge e/4 and e/2 period oscillations. *PNAS* **106,** 8853–8858 (2009).

175. Willett, R. L., Pfeiffer, L. N. & West, K. W. Alternation and interchange of e/4 and e/2 period interference oscillations consistent with filling factor 5/2 non-Abelian quasiparticles. *Phys. Rev. B* **82,** 205301 (2010).

176. Willett, R. L., Nayak, C., Shtengel, K., Pfeiffer, L. N. & West, K. W. Magnetic-Field-Tuned Aharonov-Bohm Oscillations and Evidence for Non-Abelian Anyons at $\nu = 5/2$. *Phys. Rev. Lett.* **111,** 186401 (2013).

177. Chamon, C. & Wen, X. G. Sharp and smooth boundaries of quantum Hall liquids. *Phys. Rev. B* **49,** 8227–8241 (1994).

178. Wan, X. & Yang K. anf Rezayi, E. Reconstruction of Fractional Quantum Hall Edges. *Phys. Rev. Lett.* **88,** 056802 (2002).

179. Joglekar, Y. N., Nguyen, H. K. & Murthy, G. Edge reconstructions in fractional quantum Hall systems. *Phys. Rev. B* **68,** 035332 (2003).

180. Bid, A. *et al.* Observation of neutral modes in the fractional quantum Hall regime. *Nature* **466,** 585–590 (2010).

181. Wang, J., Meir, Y. & Gefen, Y. Edge Reconstruction in the $\nu = 2/3$ Fractional Quantum Hall State. *Phys. Rev. Lett.* **111,** 246803 (2013).

182. Inoue, H. *et al.* Proliferation of neutral modes in fractional quantum Hall states. *Nature Communications* **5,** 4067 (2014).

183. Bhattacharyya, R., Banerjee, M., Heiblum, M., Mahalu, D. & Umansky, V. Melting of Interference in the Fractional Quantum Hall Effect: Appearance of Neutral Modes. *Phys. Rev. Lett.* **122,** 246801 (2019).

184. Park, J., Gefen, Y. & Sim, H.-S. Topological dephasing in the $\nu = 2/3$ fractional quantum Hall regime. *Phys. Rev. B* **92,** 245437 (2015).

185. Kim, Y. *et al.* Even denominator fractional quantum Hall states in higher Landau levels of graphene. *Nature Physics* **15,** 154–158 (2019).

186. Ribeiro-Palau, R. and Chen, S. and Zeng,Y. and Watanabe, K. and Taniguchi, T. and Hone, J. and Dean, C. R. High-Quality Electrostatically Defined Hall Bars in Monolayer Graphene. *Nano. Lett.* **19,** 2583–2587 (2019).

187. Zibrov, A. A. *et al.* Even-denominator fractional quantum Hall states at an isospin transition in monolayer graphene. *Nature Physics* **14,** 930–935 (2018).

188. Tőke, C., Lammert, P., Crespi, V. & Jain, J. K. Fractional quantum Hall effect in graphene. *Phys. Rev. B* **74,** 235417 (2006).

189. Goerbig, M. O. & Regnault, N. Theoretical Aspects of the Fractional Quantum Hall Effect in Graphene. *Physica Scripta* (2012).

190. Tőke, C. & Jain, J. K. SU(4) composite fermions in graphene: Fractional quantum Hall states without analog in GaAs. *Phys. Rev. B* **75,** 245440 (2007).

191. Papić Z. O. Goerbig, M. O. & N. Regnault, N. Atypical Fractional Quantum Hall Effect in Graphene at Filling Factor 1/3. *Phys. Rev. Lett.* **105,** 176802 (2010).

192. Li, G., Luican-Mayer, A., Abanin, D., Levitov, L. & Andrei, E. Y. Evolution of Landau levels into edge states in graphene. *Nature Communications,* 1744 (2013).

193. Seredinski, A. *et al.* Quantum Hall based superconducting interference device. *Sciences Advances* **5** (2019).

194. Lee, G. *et al.* Inducing superconducting correlation in quantum Hall edge states. *Nature Physics.* **13,** 693–698 (2017).

195. Zhao, L. *et al.* Interference of chiral Andreev edge states. *Nature Physics* **16,** 862–867 (2020).

196. Mong, R. *et al.* Universal Topological Quantum Computation from a Superconductor-Abelian Quantum Hall Heterostructure. *Phys. Rev. X* **4,** 011036 (2014).

197. Zocher, B. & Rosenow, B. Topological superconductivity in quantum Hall-superconductor hybrid systems. *Phys. Rev. B* **93,** 214504 (2016).

198. Tworzydlo, J., Snyman, I., Akhmerov, A. R. & Beenakker, C. W. J. Valley-isospin dependence of the quantum Hall effect in a graphene p-n junction. *Phys. Rev. B* **76,** 035411 (2007).

199. Williams, J. R., DiCarlo, L. & Marcus, C. M. Quantum Hall Effect in a Gate-Controlled p-n Junction of Graphene. *Science* **317,** 638–641 (2007).

200. Özyilmaz, B. *et al.* Electronic Transport and Quantum Hall Effect in Bipolar Graphene *p-n-p* Junctions. *Phys. Rev. Lett.* **99,** 166804 (2007).

201. Ki, D.-K. & Lee, H.-J. Quantum Hall resistances of a multiterminal top-gated graphene device. *Phys. Rev. B* **79,** 195327 (2009).

202. Nam, S. *et al.* Ballistic transport of graphene pnp junctions with embedded local gates. *Nanotechnology* **22,** 415203 (2011).

203. Nakaharai, S., Williams, J. R. & Marcus, C. M. Gate-Defined Graphene Quantum Point Contact in the Quantum Hall Regime. *Phys. Rev. Lett.* **107,** 036602 (2011).

204. Abanin, D. A. & Levitov, L. S. Quantized Transport in Graphene p-n Junctions in a Magnetic Field. *Science* **317,** 641–643 (2007).

205. Long, W., Sun, Q. & Wang, J. Disorder-Induced Enhancement of Transport through Graphene p-n Junctions. *Phys. Rev. Lett.* **101,** 166806 (2008).

206. Li, J. & Shen, S.-Q. Disorder effects in the quantum Hall effect of graphene *p-n* junctions. *Phys. Rev. B* **78,** 205308 (2008).

207. Chen, J.-C., Yeung, T. & Sun, Q.-F. Effect of disorder on longitudinal resistance of a graphene pn junction in the quantum Hall regime. *Phys. Rev. B* **81,** 245417 (2010).

208. Chen, J.-C., Zhang, H., Shen, S.-Q. & Sun, Q.-F. Dephasing effect on transport of a graphene pn junction in a quantum Hall regime. *Journal of Physics: Condensed Matter* **23,** 495301 (2011).

209. Amet, F., Williams, J. R., Watanabe, K., Taniguchi, T. & Goldhaber-Gordon, D. Selective Equilibration of Spin-Polarized Quantum Hall Edge States in Graphene. *Phys. Rev. Lett.* **112,** 196601 (2014).

210. Morikawa, S. *et al.* Edge-channel interferometer at the graphene quantum Hall pn junction. *Appl. Phys. Lett.* **106,** 183101 (2015).

211. Zimmermann, K. Quantum point contact in high mobility graphene. *PhD thesis, Université Grenoble Alpes* (2016).

212. Wei, D. S. *et al.* Mach-Zehnder interferometry using spin- and valley-polarized quantum Hall edge states in graphene. *Science Advances* **e1700600** (2017).

213. Makk, P. *et al.* Coexistence of classical snake states and Aharonov-Bohm oscillations along graphene p-n junctions. *Phys. Rev. B* **98,** 035413 (2018).

214. Jo, M. *et al.* Quantum Hall valley splitters in a graphene PN junction. *arXiv,* 2011.04958 (2020).

215. Brasseur, P. Mach Zehnder interferometry and coherent manipulation of the valley in a graphene PN junction. *PhD thesis, Université Paris-Saclay* (2020).

216. Zhang, G. *et al.* Coulomb-dominated oscillations in a graphene quantum Hall Fabry–Pérot interferometer. *Chinese Physics B* **28,** 127203 (2019).

217. Veyrat, L. *et al.* Low-Magnetic-Field Regime of a Gate-Defined Constriction in High-Mobility Graphene. *Nano letters* **19,** 635–642 (2019).

218. Fariha Ahmad, N. *et al.* Effect of gap width on electron transport through quantum point contact in hBN/graphene/hBN in the quantum Hall regime. *Appl. Phys. Lett.* **114,** 023101 (2019).

219. Fariha Ahmad, N. *et al.* Fabry–Pérot resonances and a crossover to the quantum Hall regime in ballistic graphene quantum point contacts. *Scientific Reports* **9** (2019).

220. Young, A. F. & Kim, P. Quantum interference and Klein tunnelling in graphene heterojunctions. *Nature Physics* **5,** 222–226 (2009).

221. Amet, F., Williams, J. R., Watanabe, K., Taniguchi, T. & Goldhaber-Gordon, D. Insulating Behavior at the Neutrality Point in Single-Layer Graphene. *Phys. Rev. Lett.* **110,** 216601 (2013).

222. Giovannetti, G. *et al.* Doping Graphene with Metal Contacts. *Phys. Rev. Lett.* **101,** 026803 (2008).

223. Gu, N., Rudner, M., Young, A., Kim, P. & Levitov, L. Collapse of Landau Levels in Gated Graphene Structures. *Phys. Rev. Lett.* **106,** 066601 (2011).

224. Rickhaus, P. and Maurand, R. and Liu, M.H. and Weiss, M. and Richter, K. and Schönenberger, C. Ballistic interferences in suspended graphene. *Nature Communications* **4,** 2342 (2013).

225. Grushina, A., Ki, D. & Morpurgo, A. A ballistic pn junction in suspended graphene with split bottom gates. *Appl. Phys. Lett.* **102,** 223102 (2013).

226. Rickhaus, P. and Makk, P. and Liu, M.H. and Tóvári, E. and Weiss, M. and Maurand, R. and Richter, K. and Schönenberger, C. Snake trajectories in ultraclean graphene p–n junctions. *Nature Communications* **6,** 6470 (2015).

227. Kim, K. K. *et al.* Synthesis and Characterization of Hexagonal Boron Nitride Film as a Dielectric Layer for Graphene Devices. *ACS Nano* **6,** 8583–8590 (2012).

228. Liu, M. Theory of carrier density in multigated doped graphene sheets with quantum correction. *Phys. Rev. B* **87,** 125427 (2013).

229. Evans, A. K., Glazman, L. I. & Shklovskii, B. I. Coulomb blockade in the quantum-Hall-effect state. *Phys. Rev. B* **48,** 11120 (1993).

230. McClure, D. T. *et al.* Edge-state velocity and coherence in a quantum Hall Fabry-Pérot interferometer. *Phys. Rev. Lett.* **103,** 206806 (2009).

231. Yamauchi, Y. *et al.* Universality of bias- and temperature-induced dephasing in ballistic electronic interferometers. *Phys. Rev. B* **79,** 161306 (2009).

232. Ngo Dinh, S. Bosonization of Nonequilibrium Quantum Wire Networks (2013).

233. Litvin, L. V., Helzel, A., Tranitz, H.-P., Wegscheider, W. & Strunk, C. Edge-channel interference controlled by Landau level filling. *Phys. Rev. B* **78,** 075303 (2008).

234. Roulleau, P. *et al.* Finite bias visibility of the electronic Mach-Zehnder interferometer. *Phys. Rev. B* **76,** 161309 (2007).

235. Roulleau, P. *et al.* Noise Dephasing in Edge States of the Integer Quantum Hall Regime. *Phys. Rev. Lett.* **101,** 186803 (2008).

236. Roulleau, P. Quantum coherence in the integer quantum Hall regime. *PhD thesis, Université Pierre et Marie Curie - Paris VI* (2008).

237. Bieri, E. *et al.* Finite-bias visibility dependence in an electronic Mach-Zehnder interferometer. *Phys. Rev. B* **79,** 245324 (2009).

238. Roulleau, P. *et al.* Direct Measurement of the Coherence Length of Edge States in the Integer Quantum Hall Regime. *Phys. Rev. Lett.* **100,** 126802 (2008).

239. Gurman, I., Sabo, R., Heiblum, M., Umansky, V. & Mahalu, D. Dephasing of an electronic two-path interferometer. *Phys. Rev. B* **93,** 121412 (2016).

240. Altimiras, C. *et al.* Tuning Energy Relaxation along Quantum Hall Channels. *Phys. Rev. Lett.* **105,** 226804 (2010).

241. Huynh, P. *et al.* Quantum Coherence Engineering in the Integer Quantum Hall Regime. *Phys. Rev. Lett.* **108,** 256802 (2012).

242. Duprez, H. *et al.* Macroscopic Electron Quantum Coherence in a Solid-State Circuit. *Phys. Rev. X* **9,** 021030 (2019).

243. Ronen, Y. *et al.* Aharonov Bohm Effect in Graphene Fabry Pérot Quantum Hall Interferometers. *Nature Nanotechnology* **16,** 563–569 (2021).

244. Sivan, I. *et al.* Interaction-induced interference in the integer quantum Hall effect. *Phys. Rev. B* **97,** 125405 (2018).

245. Frigeri, G., Scherer, D. D. & Rosenow, B. Sub-periods and apparent pairing in integer quantum Hall interferometers. *EPL* **126** (2019).

246. Das Sarma, S., Freedman, M. & Nayak, C. Topologically Protected Qubits from a Possible Non-Abelian Fractional Quantum Hall State. *Phys. Rev. Lett.* **94,** 166802 (2005).

247. Wen, X. G. Edge transport properties of the fractional quantum Hall states and weak-impurity scattering of a one-dimensional charge-density wave. *Phys. Rev. B* **44,** 5708.

248. Milliken, F., Umbach, C. & Webb, R. Indications of a Luttinger Liquid in the Fractional Quantum Hall Regime. *Solid State Commun.* **97,** 309–313 (1996).

249. Roddaro, S., Pellegrini, V. & Beltram, F. Nonlinear Quasiparticle Tunneling between Fractional Quantum Hall Edges. *Phys. Rev. Lett.* **90,** 046805 (2003).

250. Radu, I. P. *et al.* Quasi-Particle Properties from Tunneling in the ν= 5/2 Fractional Quantum Hall State. *Science* **320,** 899–902 (2008).

251. Lin, X., Dillard, C., Kastner, M. A., Pfeiffer, L. N. & West, K. W. Measurements of quasiparticle tunneling in the ν=5/2 fractional quantum Hall state. *Phys. Rev. B* **85,** 165321 (2012).

252. Baer, S. *et al.* Experimental probe of topological orders and edge excitations in the second Landau level. *Phys. Rev. B* **90,** 075403 (2014).

253. Khanna, U., Goldstein, M. & Gefen, Y. Fractional edge reconstruction in integer quantum Hall phases. *Phys. Rev. B* **103,** L121302 (2021).

254. Huang, X. L. & Nazarov, Y. Interaction-induced supercurrent in quantum Hall setups. *Phys. Rev. B* **100,** 155411 (2019).

255. Ishigami, M., Chen, J. H., Cullen, W. G., Fuhrer, M. S. & Williams, E. D. Atomic Structure of Graphene on SiO_2. *Nano Lett.* **7,** 1643–1648 (2007).

256. Ando, T. Screening Effect and Impurity Scattering in Monolayer Graphene. *Journal of the Physical Society of Japan* **75,** 074716 (2006).

257. Hwang, E. H., Adam, S. & Das Sarma, S. Carrier Transport in Two-Dimensional Graphene Layers. *Phys. Rev. B* **98,** 186806 (2007).

258. Du, X., Skachko, I., Barker, A. & Andrei, E. Y. Approaching ballistic transport in suspended graphene. *Nature Nanotechnology* **3,** 491–495 (2008).

259. Bolotin, K. I., Sikes, K. J., Hone, J., Stormer, H. L. & Kim, P. Temperature-Dependent Transport in Suspended Graphene. *Phys. Rev. Lett.* **101,** 096802 (2008).

260. Barrier, J. *et al.* Long-range ballistic transport of Brown-Zak fermions in graphene superlattices. *Nature Communications* **11,** 5756 (2020).

261. Couto, N. J. G. *et al.* Random Strain Fluctuations as Dominant Disorder Source for High-Quality On-Substrate Graphene Devices. *Phys. Rev. X* **4,** 041019 (2014).

262. Wang, L. *et al.* Mobility Enhancement in Graphene by in situ Reduction of Random Strain Fluctuations. *Phys. Rev. Lett.* **124,** 157701 (2020).

263. Zihlmann, S. *et al.* Out-of-plane corrugations in graphene based van der Waals heterostructures. *Phys. Rev. B* **102,** 195404 (2020).

264. Novoselov, K. S. *et al.* Two-dimensional atomic crystals. *PNAS* **102,** 10451–10453 (2005).

265. Taniguchi, T. & Watanabe, K. Synthesis of high-purity boron nitride single crystals under high pressure by using Ba-BN solvent. *J. Cryst. Growth* **303,** 525–529 (2007).

266. Blake, P. *et al.* Making graphene visible. *Appl. Phys. Lett.* **91,** 063124 (2007).